Komposite aus Aluminium-basierten Metall-organischen Gerüstverbindungen und deren Anwendung in der Gassorption

Inaugural – Dissertation

zur Erlangung des Doktorgrades
Dr. rer. nat.
der Mathematisch-Naturwissenschaftlichen Fakultät
der Heinrich-Heine-Universität Düsseldorf

vorgelegt von

Ülkü Kökçam-Demir
aus Holzminden

Düsseldorf, Oktober 2021

aus dem Institut für Anorganische Chemie und Strukturchemie I
der Heinrich-Heine-Universität Düsseldorf

Gedruckt mit der Genehmigung der
Mathematisch-Naturwissenschaftlichen Fakultät der
Heinrich-Heine-Universität Düsseldorf

Berichterstatter:

1. Prof. Dr. Christoph Janiak

2. Prof. Dr. Christian Ganter

Tag der mündlichen Prüfung: 21.12.2021

Eidesstattliche Erklärung

Ich versichere an Eides statt, dass die Dissertation von mir selbstständig und ohne unzulässige fremde Hilfe unter der Beachtung der „Grundsätze zur Sicherung guter wissenschaftlicher Praxis“ an der Heinrich-Heine-Universität Düsseldorf erstellt worden ist. Die aus fremden Quellen direkt oder indirekt übernommenen Gedanken sind als solche kenntlich gemacht. Die Arbeit wurde bisher weder im Inland noch im Ausland in gleicher oder ähnlicher Form einer anderen Prüfungsbehörde vorgelegt. Es wurden keine früheren erfolglosen Promotionsversuche unternommen.

Ort, Datum

Unterschrift

Die vorliegende Dissertation wurde zum einen im Rahmen des vom Bundesministerium für Bildung und Forschung (BMBF) geförderten Verbundprojekts „Optimierung von neuartigen Materialien für zyklische Adsorptionsprozesse“ (OptiMat, 03SF0492C) und zum anderen im Rahmen der Deutschen Forschungsgemeinschaft (DFG) geförderten Projekts (Ja466/40-1, Projektnummer 396890929/GRK 2482) angefertigt.

Teilnehmende Verbundprojektpartner im Projekt OptiMat waren das Fraunhofer-Institut für Solare Energiesysteme (ISE) Freiburg, die DencoHappel GmbH Herne (später FläktGroup) und die Heinrich-Heine-Universität Düsseldorf (HHU).

„Der Fortschritt lebt vom Austausch des Wissens."

Albert Einstein

Danksagung

An erster Stelle gebührt ein ganz besonderer Dank Herrn Prof. Dr. Christoph Janiak für die Möglichkeit meine Dissertation in seinem Arbeitskreis anzufertigen. Vielen Dank für die konstruktiven Diskussionen, die hilfreichen Anregungen, die Korrekturen der Manuskripte und für die Freiheit, die Sie mir in der Gestaltung der Projekte gewährt haben. Besonders möchte ich mich für die Möglichkeit zur Teilnahme am Projekt OptiMat, die interessante Themenvergabe im Rahmen der Projekte und die Teilnahme an Projekttreffen und internationalen Konferenzen danken.

Herrn Prof. Dr. Christian Ganter danke ich für die Übernahme des Korreferates und der hilfreichen Anregungen in den Seminarvorträgen.

Ein weiterer besonderer Dank geht an Marco Bengsch, Dr. Anna Goldman, Alex Spieß, Dr. Niels Tannert und allen anderen Projektpartnern für die enge Zusammenarbeit. Des Weiteren möchte ich mich bei meinen ehemaligen Büro- und Laborkollegen, Dr. Subarna Dey, Dr. Irina Gruber, Dr. Serkan Gökpınar, Olga Koikolainen, Daniel Komisarek, Dr. Tobie Matemb Ma Ntep, Saskia Menzel, Dr. Simon Millan und Dr. Shang Hua Xing bedanken. Danke für das angenehme Arbeitsklima, die freundliche Unterstützung und Hilfsbereitschaft sowie für die vielen netten Gespräche. In gleicher Weise danke ich Dr. Emrah Hastürk und Christian Jansen und allen anderen Doktoranden, Bachelor- und Masterstudenten des Arbeitskreises. Darüber hinaus möchte ich mich bei den festangestellten Mitarbeitern des Arbeitskreises, Jutta Bourgeois, Marcell Demandt, Annette Ricken und Birgit Tommes bedanken.

Mein allergrößter Dank geht an **meine liebe Familie**.
Ich danke meinen Eltern und meinen Schwestern, die mich immer unterstützt und an mich geglaubt haben. Danke für Alles! Von ganzem Herzen und am allermeisten danke ich meinem Ehemann Ing. Adem Demir. Danke, dass Du immer für mich da bist. Danke fürs Zuhören, für deine ehrliche Meinung, für deine Geduld und für deine bedingungslose Unterstützung. Du hast mir den Rücken gestärkt, immer weiter zu machen. Ich liebe Dich!

Für meine Familie

I. Kurzzusammenfassung

Die vorliegende kumulative Dissertation beschäftigt sich mit zwei Forschungsschwerpunkten im Bereich der Metall-organischen Gerüstverbindungen (MOFs). Ein Ziel war es, neue mikroporöse, wasserstabile Komposite aus Aluminium-basierten MOFs (Al-MOFs) mit Graphitoxid (GO) herzustellen und verbesserte Sorptionseigenschaften hinsichtlich der Porosität und der Wasseraufnahmekapazität gegenüber den reinen Al-MOFs zu erzielen. Ein weiteres Ziel bestand darin, eine umfassende Übersicht zu dem Thema „MOFs mit offenen Metallstellen“ (*open metal sites*, OMS) anhand der Fachliteratur in Form eines Reviews zusammenzustellen.

Im Rahmen einer Veröffentlichung wurden neue Al-MOF-GO Komposite vorgestellt. Diese Komposite bestehen aus zwei literaturbekannten Al-MOFs, MIL-100 und CAU-10-H, mit verschiedenen Anteilen an Graphitoxid (von 2 bis 16 Gew.-%). Die Darstellung der Al-MOF-GO Komposite erfolgte durch *in situ* MOF-Synthesen. Die Komposite wurden als mikrokristalline Pulver erhalten und anschließend umfassend charakterisiert. Ihre Porosität wurde mittels Stickstoffsorption und ihre Wasseraufnahmekapazität mittels Wassersorption untersucht. Im Vergleich zu reinen Al-MOFs konnten höhere spezifische BET-Oberflächen, (Mikro-) Porenvolumina und Wasseraufnahmen erreicht werden. Dies lässt sich auf eine gute Wechselwirkung zwischen dem Al-MOF und GO mit der Bildung einer zusätzlichen Grenzfläche zurückführen. Vor allem das MIL-100(Al)-GO Komposit mit nur 2 Gew.-% GO zeigte eine 12% höhere BET-Oberfläche, einen 10% höheren Gesamtporenvolumen und eine um 23% erhöhte Wasseraufnahme gegenüber dem reinem MIL-100(Al) auf. Bei höheren GO-Anteilen (4, 9, 16 Gew.-%) resultierten ebenfalls verbesserte Sorptionsergebnisse. Im Gegensatz dazu wurde im Fall von CAU-10-H-GO Kompositen mit 2, 5, 8, 15 Gew.-% GO nur eine geringe Zunahme der Porosität und der Wasseraufnahme festgestellt. Andererseits wurden in allen vier CAU-10-H-GO Kompositen eine hydrophile Verschiebung der steilen Wasseraufnahme der S-förmigen Isotherme zu einem niedrigen relativen Druck ($p \cdot p_0^{-1}$ = ~0.15) im Vergleich zu reinem CAU-10-H ($p \cdot p_0^{-1}$ = ~0.17) beobachtet. Die hydrothermale Stabilität der Al-MOF-GO Komposite konnte mittels Wasseradsorptions- und Wasserdesorptionszyklen belegt werden.

Im Rahmen einer weiteren Veröffentlichung wurde eine umfangreiche theoretische Zusammenfassung zu MOFs mit offenen Metallstellen (*open metal sites*, OMS) gegeben. Dieses Review kombiniert alle bisherigen Aspekte der Fachliteratur zu OMS in MOFs. MOFs mit offenen Metallstellen können durch die Entfernung von koordinierten labilen Lösungsmittelmolekülen mithilfe von Synthesestrategien generiert werden. Die erhaltenen OMS-MOFs können mittels analytischer Methoden auf die Beibehaltung der Kristallinität und Porosität und auf das Vorhandensein von offenen Metallstellen untersucht werden. Die relative Menge an Lewis-Säure Stellen oder OMS in MOFs kann anhand weiterer Methoden wie Gas- oder Dampfadsorption, Infrarot-Spektroskopie und temperaturprogrammierter Desorption quantifiziert werden. In theoretischen Studien werden die Auswirkungen von offenen Metallstellen auf Wirt-Gast-Wechselwirkungen thematisiert. OMS in MOFs führen zu einer Verstärkung der Wechselwirkungen zwischen den freien Metallstellen und den Gastmolekülen. Beispielsweise besitzen MOFs mit offenen Metallstellen eine höhere Affinität gegenüber diversen Gasen wie Wasserstoff, Kohlenstoffdioxid oder Stickstoffmonoxid im Vergleich zu MOFs ohne OMS.

II. Abstract

The present cumulative thesis consists of two main parts in the field of metal-organic frameworks (MOFs). One objective was to produce microporous, water stable composites of aluminum-based MOFs (Al-MOFs) with graphite oxide (GO) and to enhance the gas sorption properties with regard to the porosity and the water uptake capacity compared to the neat Al-MOFs. Another objective was to compile a complete overview on the subject “MOFs with open metal sites” (OMS) based on the literature in form of a review.

In one publication, new Al-MOF-GO composites were presented. These composites consist of two known Al-MOFs MIL-100 and CAU-10-H with different GO loadings (from 2 to 16 wt%) and were prepared by *in situ* MOF synthesis. The composites were obtained as microcrystalline powders and then fully characterized. The porosity was investigated by nitrogen sorption and the water uptake capacity by water sorption. Compared to the neat Al-MOFs, it was possible to archive higher specific BET surface areas, (micro) pore volumes and water uptakes. This can be explained by the good interaction of Al-MOF and GO with the formation of an additional interface with surface area and void volume. In particular, the MIL-100(Al)-GO composite with only 2 wt% GO showed an increase of 12% in BET surface area, an increase of 10% in total pore volume and an increase of 23% in water uptake, in comparison to neat MIL-100(Al). Higher GO loadings (4, 9, 16 wt%) also resulted in an increase in sorption properties. To the contrary, in the CAU-10-H-GO composites with 2, 5, 8, 15 wt% GO the porosities and water uptakes increase only slightly. On the other hand, a hydrophilic shift of the steep water uptake of the S-shaped isotherm to slightly lower relative pressure ($p \cdot p_0^{-1}$ = ~0.15) was observed in all four CAU-10-H-GO composites, in comparison to neat CAU-10-H ($p \cdot p_0^{-1}$ = ~0.17). The hydrothermal stability of the composites has been proven by water adsorption and desorption cycles.

In an additional publication, an extensive theoretical summary on MOFs with open metal sites (OMS) was given. This review combines all previous aspects of the literature on OMS in MOFs. MOFs with open metal sites can be generated by the removal of coordinated labile solvent ligand molecules by using synthetic strategies. OMS-MOFs can be examined by analytical methods to show the retention of crystallinity, porosity and presence of open metal sites. Several other techniques such gas or vapor adsorption, infrared spectroscopy and temperature-programmed desorption can be used to quantify the relative amount of Lewis acid sites or OMS in MOFs. The effect of open metal sites with host-guest interactions are discussed in theoretical studies. The presence of OMS in MOFs causes enhanced interactions between the metal site and guest molecules. For example, MOFs with open metal sites provide higher affinity for various gases such as hydrogen, carbon dioxide or nitrogen monoxide compared to MOFs without OMS.

III. Publikationsliste

Erstautorenschaften

Ülkü Kökçam-Demir, Niels Tannert, Marco Bengsch, Alex Spieß, Carsten Schlüsener, Sandra Nießing, Christoph Janiak,
Improving porosity and water uptake of Al-MOFs as graphite oxide composites;
Microporous Mesoporous Mater, 2021, **326**, 111352.
DOI: 10.1016/j.micromeso.2021.111352

Ülkü Kökçam-Demir, Anna Goldman, Leili Esrafili, Maniya Gharib, Ali Morsali, Oliver Weingart, Christoph Janiak,
Coordinatively unsaturated metal sites (open metal sites) in metal–organic frameworks: design and applications;
Chem. Soc. Rev., 2020, **49,** 2751–2798.
DOI: 10.1039/C9CS00609E

Co-Autorenschaften

Mathias Getzlaff, Miriam Leifels, Paula Weber, Ülkü Kökçam-Demir, Christoph Janiak,
Magnetic nanoparticles in toner material;
Nano-Structures & Nano-Objects, 2020, **22**, 100462.
DOI: 10.1016/j.nanoso.2020.100462

Phillipe Belle Ebandaa Kedi, Chick Christian Nanga, Awawou Paboudam Gbambie, Vandi Deli, Francois Eya'ane Meva, Hamza Elsayed Ahmed Mohamed, Agnes Antoinette Ntoumba, Moise Henri Julien Nko'o, Ülkü Kökçam-Demir, Bastian Moll, Houatchaing Kouemegne Armelle Michelle, Peter Teke Ndifon, Emmanuel Albert Mpondo Mpondo, Alain Bertrand Dongmo, Christoph Janiak, Malik Maaza,
Biosynthesis of Silver Nanoparticles from Microsorum Punctatum (L.) Copel Fronds Extract and an In-Vitro Anti-Inflammation Study;
J. Nanotechnol. Res., 2020, **2**, 025–041.
DOI: 10.26502/jnr.2688-85210014

Dana Bejan, Lucian Gabriel Bahrin, Sergiu Shova, Narcisa Laura Marangoci, Ülkü Kökçam-Demir, Vasile Lozan, Christoph Janiak,
New Microporous Lanthanide Organic Frameworks. Synthesis, Structure, Luminescence, Sorption, and Catalytic Acylation of 2-Naphthol;
Molecules, 2020, **25**, 3055.
DOI: 10.3390/molecules25133055

Phillipe Belle Ebandaa Kedi, Berthe Ngangue Etah, Vandi Deli, Awawou Paboudam Gbambie, Agnes Antoinette Ntoumba, Ülkü Kökçam-Demir, Bastian Moll, Hamza Elsayed Ahmed Mohamed, Judith Caroline Ngo Nyobe, Chick Christian Nanga, Jean Yves Sikapi Fouda, Loick Pradel Kojom Foko, Emmanuel Edmond Tchoumbi, Armelle Michelle Houatchaing, Yvon Kevin Dimitri Manfred Kotto Modi, Francois Eya'ane Meva, Peter Teke Ndifon, Alain Bertrand Dongmo, Malik Maaza, Siegfried Didier Dibong, Emmanuel Albert Mpondo Mpondo, Christoph Janiak,
In vitro and in vivo anti-inflammatory activity of green synthesized silver nanoparticles from the aqueous bark extract of Mangifera indica Linn. (Anacardiaceae);
Int. J. Green Herbal Chem., 2020, **9**, 345–360.
DOI: 10.24214/IJGHC/HC/9/3/34560

Mohammed Enamullah, Kazi Saima Banu, Mohammed Anwar Hossain, Ülkü Kökçam-Demir,
High-spin bis[(S or R)-N-1-(Ar)ethyl-salicylaldiminato-κ^2N,O]-Λ/Δ-iron(II): Combined studies of syntheses, spectroscopy, diastereoselection, electrochemistry, paramagnetic, thermal, PXRD and DFT/TDDFT;
J. Mol. Struct., 2020, **1199**, 126947.
DOI: 10.1016/j.molstruc.2019.126947

Mathias Getzlaff, Miriam Leifels, Paula Weber, Ülkü Kökçam-Demir, Christoph Janiak,
Nanoparticles in toner material;
SN Appl. Sci., 2019, **1:489**.
DOI: 10.1007/s42452-019-0501-9

Francois Eya'ane Meva, Joel Olivier Avom Mbeng, Cecile Okalla Ebongue, Carsten Schlüsener, Ülkü Kökçam-Demir, Agnes Antoinette Ntoumba, Phillipe Belle Ebanda Kedi, Etienne Elanga, Evrard-Rudy Njike Loudang, Moise Henri Julien Nko'o, Edmond Tchoumbi, Vandi Deli, Christian Chick Nanga, Emmanuel Albert Mpondo Mpondo, Christoph Janiak,
Stachytarpheta cayennensis Aqueous Extract, a New Bioreactor towards Silver Nanoparticles for Biomedical Applications;
J. Biomater. Nanobiotechnol., 2019, **10**, 102–119.
DOI: 10.4236/jbnb.2019.102006

Francois Eya'ane Meva, Agnes Antoinette Ntoumba, Philippe Belle Ebanda Kedi, Edmond Tchoumbi, Alexa Schmitz, Laura Schmolke, Maximilian Klopotowski, Bastian Moll, Ülkü Kökçam-Demir, Emmanuel Albert Mpondo Mpondo, Leopold Gustave Lehman, Christoph Janiak,
Silver and palladium nanoparticles produced using a plant extract as reducing agent, stabilized with an ionic liquid: sizing by X-ray powder diffraction and dynamic light scattering;
J. Mater. Res. Technol., 2019, **8**, 1991–2000.
DOI: 10.1016/j.jmrt.2018.12.017

Bernd Engelkamp, Mhamed El Achhab, Björn Fischer, Ülkü Kökçam-Demir, Klaus Schierbaum,
Combined Galvanostatic and Potentiostatic Plasma Electrolytic Oxidation of Titanium in Different Concentrations of H_2SO_4;
Metals, 2018, **8**, 386.
DOI: 10.3390/met8060386

Rana Dalapati, Ülkü Kökçam-Demir, Christoph Janiak, Shyam Biswas,
The effect of functional groups in the aqueous-phase selective sensing of Fe(III) ions by thienothiophene-based zirconium metal–organic frameworks and the design of molecular logic gates;
Dalton Trans., 2018, **47**, 1159–1170.
DOI: 10.1039/C7DT04130F

Teilnahme an Konferenzen

Postersession
EuroMOF 2017: 2nd European Conference on Metal Organic Frameworks and Porous Polymers, October 29th to November 1st – Delft, Netherlands;
Ülkü Kökçam-Demir, Christoph Janiak,
Al-based metal-organic frameworks for water sorption applications.

Organisationskomitee
International Workshop on Hierarchically Structured Materials: For a Green Environment (IWHSM), September 1st to 2nd 2016 – Düsseldorf, Germany;
Ülkü Kökçam-Demir, Niels Tannert, Christoph Janiak.

IV. Abkürzungsverzeichnis

AHPs	*Adsorption Heat Pumps* (Adsorptionswärmepumpen)
AHT	*Adsorption Heat Transformation* (Adsorptionswärmetransformation)
BET	Brunauer-Emmett-Teller
bspw.	Beispielsweise
bzw.	Beziehungsweise
ca.	Circa
CAU	Christian-Albrechts-Universität
CC	*Coupled Cluster* (gekoppelter Cluster)
CUS	*Coordinatively Unsaturated Sites* (koordinativ ungesättigte Stellen)
deion.	Deionisiert
DFT	*Density Functional Theory* (Dichtefunktionaltheorie)
et al.	*Et alia* (und andere)
FT-IR	Fourier-Transform-Infrarot
HHU	Heinrich-Heine-Universität
HKUST	*Hong Kong University of Science and Technology* (Universität für Wissenschaft und Technologie Hong Kong)
Gew.-%	Gewichtsprozent
IR	Infrarot
IUPAC	*International Union of Pure and Applied Chemistry* (Internationale Union für reine und angewandte Chemie)
MCM	*Mobil Composition of Matter* (mobile Zusammensetzung der Materie)
MIL	*Matériaux de l'Institut Lavoisier* (Materialien des Instituts Lavoisier)
MOF	*metal-organic framework* (Metall-organische Gerüstverbindung)
n/a	*Not available* (nicht verfügbar)
NMR	*Nuclear Magnetic Resonance* (Kernspinresonanz)
OMS	*Open Metal Sites* (offene Metallstellen)
p.a.	*Pro analysi* (analysenrein)
pcu	*Primitive cubic unit; topology* (kubisch-primitiv; Topologie)
PD	Privatdozent(in)

PXRD	*Powder X-Ray Diffraction* (Röntgenpulverdiffraktometrie; Röntgenpulverbeugung)
REM	Rasterelektronenmikroskopie
RT	Raumtemperatur
S_{BET}	BET-Oberfläche
SBU	*Secondary Building Unit* (sekundäre Baueinheit)
STP	*Standard Temperature and Pressure* (Standardtemperatur und -druck)
TDCs	*Thermally Driven adsorption Chillers* (thermisch angetriebene Adsorptionskältemaschinen)
TGA	Thermogravimetrische Analyse
THG	Treibhausgase
UiO	*Universitetet i Oslo* (Universität Oslo)
verd.	Verdünnt
wt%	Gewichtsprozent
z.B.	Zum Beispiel
ZIF	*Zeolitic Imidazolate Framework* (zeolitische Imidazolat-Gerüstverbindungen)

Abkürzungen chemischer Verbindungen

1,4-BDC	1,4-Benzoldicarbonsäure (Terephthalsäure)
1,4-H_2BDC	1,4-Benzoldicarbonsäure (Terephthalsäure)
H_2TDC	2,5-Thiophendicarbonsäure
H_3BTC	1,3,5-Benzoltricarbonsäure (Trimesinsäure)
H_4(*m*-DOBDC)	4,6-Dihydroxyisophthalsäure
Alfum	Aluminiumfumarat
AlPO	Aluminophosphat
AP	Aeroperl®
AS	Aerosil®
BTC	1,3,5-Benzoltricarbonsäure (Trimesinsäure)
BTT	1,3,5-Tri(1H-tetrazol-5yl)benzol

DCM	Dichlormethan
DEF	*N*,*N*-Diethylformamid
DMF	*N*,*N*-Dimethylformamid
EtOH	Ethanol
GO	*Graphite oxide* (Graphitoxid)
m-DOBDC	4,6-Dihydroxyisophthalsäure
MeOH	Methanol
SAPO	Silica-Aluminophosphat
TDC	2,5-Thiophendicarbonsäure
TRGO	Thermisch reduziertes GO

Abkürzungen physikalischer Größen

°C	Grad Celsius (Temperatureinheit)
Å	Ångström (1 Å = 10^{-10} m)
cm	Zentimeter
cm^{-1}	Reziproke Zentimeter, Wellenzahl
cm^3	Volumeneinheit Kubikzentimeter
g	Gewichtseinheit Gramm
$g \cdot g^{-1}$	Gramm pro Gramm
$g \cdot L^{-1}$	Gramm pro Liter
h	Stunde
K	Temperatureinheit Kelvin
L	Volumeneinheit Liter
m	Längeneinheit Meter
mg	Gewichtseinheit Milligramm (10^{-3} g)
$mg \cdot g^{-1}$	Milligramm pro Gramm
min	Zeiteinheit Minute
mL	Volumeneinheit Milliliter
mmol	Stoffmengeneinheit Millimol (10^{-3} mol)
nm	Längeneinheit Nanometer (10^{-9} mol)
$p \cdot p_0^{-1}$	Relativer Druck

Inhaltsverzeichnis

1 Einleitung

1.1 Metall-organische Gerüstverbindungen

Metall-organische Gerüstverbindungen (engl. *metal-organic frameworks*, MOFs) sind potentiell poröse Materialien aus anorganischen Metallknotenpunkten und verbrückenden organischen Liganden, die zu zwei- oder drei-dimensionalen Koordinationsnetzwerken (engl. *porous coordination networks*, PCNs) verknüpft sind.[1,2,3] Diese Netzwerke sind eine Untergruppe der Koordinationspolymere und werden daher auch als poröse Koordinationspolymere (engl. *porous coordination polymers*, PCPs) bezeichnet.[4,5,6] Nach der IUPAC-Definition (engl. *International Union of Pure and Applied Chemistry*) werden MOFs wie folgt definiert:

„Eine Metall-organische Gerüstverbindung ist ein Koordinationsnetzwerk mit organischen Liganden und potenziellen Hohlräumen."[7,8]

Aus der Definitionserläuterung geht hervor, dass MOFs nicht notwendigerweise kristallin vorliegen müssen. Die Gründe dafür sind, dass viele Systeme dynamisch sind und ihre Materialstruktur abhängig von physikalischen Größen wie Temperatur, Druck oder anderen externen Stimulationen ist, was wiederum zur Änderung der potentiellen Porosität und der Porenblockierung durch Lösungsmittelmoleküle führen kann.[7,8]

Die Eigenschaften der MOFs, wie die hohe spezifische Oberfläche (bis 7000 $m^2 \cdot g^{-1}$),[9] der modulare Aufbau durch die Einstellung von Porengrößen und Topologien[10,11] und ihr damit einhergehender breiter Anwendungsbereich, wie bspw. Gasspeicherung,[3,12,13,14] Separation,[15,16] (heterogene) Katalyse[3,17,18,19,20,21,22] etc., übertreffen die traditionellen porösen Adsorbentien, wie Aktivkohle[23] und Zeolithe.[24,25,26,27,28,29,30,31,32,33,34,35] In Abbildung 1 werden einige anwendungsorientierte Eigenschaften von MOFs aufgezeigt.[36]

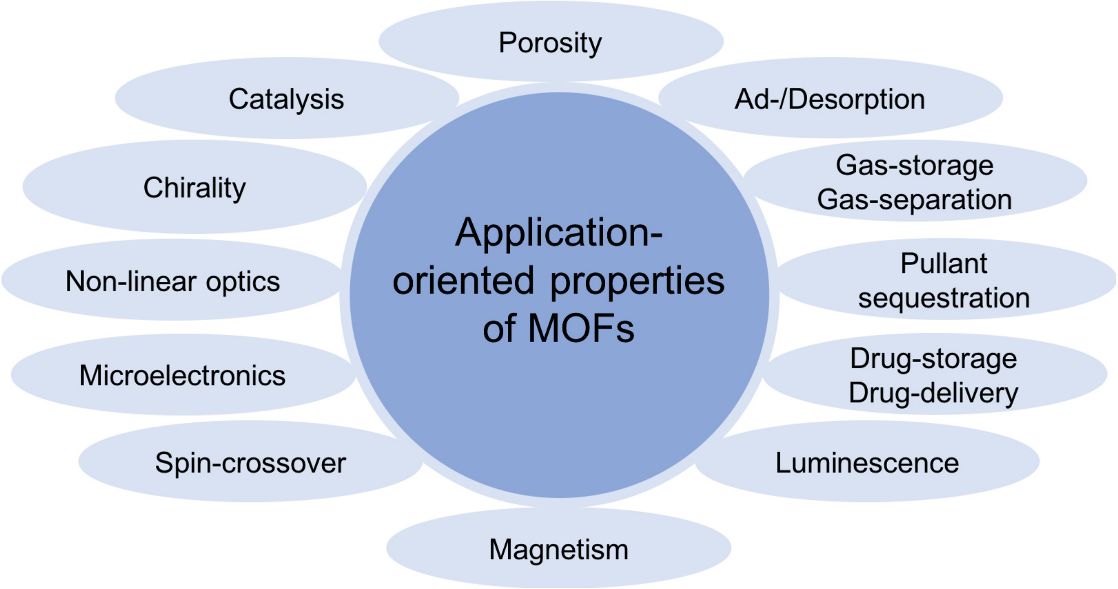

Abbildung 1 Schematische Darstellung einiger anwendungsorientierter Eigenschaften von MOFs. Reproduziert von Ref. 36 mit Genehmigung, The Royal Society of Chemistry, © 2012.

Poröse Materialien – MOFs für die Energiewende

Seit einigen Jahren wird zudem vermehrt ihr Einsatz in der Gas-Abscheidung und Gas-Speicherung, insbesondere der Gase Wasserstoff (H_2),[37,38] Kohlenstoffdioxid (CO_2)[39,40] und Methan (CH_4), im Rahmen der Energiewende diskutiert.[41,42,43,44,45,46,47,48]

Im Hinblick auf den Klimawandel berichtet das Weltklimarat IPCC (*Intergovernmental Panel on Climate Change*) von einer globalen Erwärmung von etwa 1 °C gegenüber dem Niveau vor Beginn der Industrialisierung und einer Steigerung auf 1.5 °C zwischen den Jahren 2030 und 2052.[49] Die Hauptverursacher für die globale Erderwärmung sind unumstritten die menschlichen Aktivitäten.[49,50] Große Mengen an anthropogenen Treibhausgasemissionen (THG-Emissionen), wie CO_2, entstehen in der Energiebranche (Kraftwerke), in der Industrie (Stahlwerke, Raffinerien, chemische Industrie) und im Verkehr (Fahrzeug- und Luftfahrtbranche) durch Einsatz und Verbrennung von großen Mengen an fossilen Brennstoffen, wie Kohle, Erdgas und Erdöl.[50,51,52,53,54] Auch die Landwirtschaft setzt durch die Massentierhaltung und Bodenbearbeitung Emissionen, wie CH_4 und Lachgas (N_2O), frei.[50,52,53,54,55] Somit reichern sich unterschiedliche Anteile an anthropogener THG-Emissionen in der Atmosphäre an und verstärken die Wirkung des natürlichen Treibhauseffektes, was zur Erwärmung des Erdklimas führt.[56,57,58]

Als Maßnahme gegen den Klimawandel wurde im Rahmen der internationalen Klimakonferenz im Dezember 2015 das Pariser Klimaschutzabkommen mit dem zentralen Ziel, die globale Erderwärmung auf 1.5 °C zu begrenzen verabschiedet.[59,60,61,62] Daraufhin hat die Bundesregierung im Klimaschutzplan vom November 2016 das Ziel „weitgehende THG-Neutralität bis 2050“, d.h. die THG um 95% im Vergleich zu 1990 zu reduzieren, festgelegt.[63,64,65,66,67,68] Um dieses Langfristziel zu erreichen, sind eine Reihe von Maßnahmen, wie Dekarbonisierung (Substitution von fossilen Brennstoffen), Nutzung von Biomasse, CO_2-Abscheidung und -Speicherung, Wärmedämmungen von Gebäuden, Nutzung öffentlicher Verkehrsmittel, Einführung eines generellen Tempolimits auf Autobahnen etc., erforderlich.[65,67] Betrachtet man nur die chemische Industrie, so ist sie für 7% der globalen THG-Emissionen verantwortlich.[69] In der Studie „*Enabling for Future*“ berichtet der Weltchemieverband ICCA (*International Council of Chemical Associations*), dass die chemische Industrie mit technologischen Innovationen zur Einsparung von THG beitragen kann.[70] In dieser Studie wurden insgesamt 17 Technologiecluster zu den Bereichen wie Stromerzeugung und -speicherung, Industrie und Produktion, Mobilität und Verkehr, Bauen und Wohnen, Ernährung und Landwirtschaft aufgestellt und untersucht. Schätzungen zufolge wäre durch die Zusammenarbeit dieser Bereiche eine THG-Reduzierung von 5 bis 10 $GtCO_2eq$/Jahr (Gigatonne CO_2-Äqivalent pro Jahr) bis 2050 möglich.[70] Im Auftrag des Verbands der Chemischen Industrie e.V. (VCI) haben zudem DECHEMA (Gesellschaft für Chemische Technik und Biotechnologie) und FutureCamp (Beratungsunternehmen) 2019 eine Studie über die Realisierung des Ziels „treibhausgasneutrale chemische Industrie bis 2050“ durchgeführt. Diese berichten, dass die THG-Ausstöße mithilfe neuer Produktionstechnologien reduziert werden können, wenn zudem große Mengen emissionsfreien Stroms aus erneuerbaren Quellen zu niedrigen Preisen bezogen werden.[71,72,73] Um diese Bedingungen zur THG-Neutralität entsprechend gestalten zu können, hat die VCI ergänzend mit dem Verein Deutscher Ingenieure e.V. (VDI) die Plattform *Chemistry4Climate* eingerichtet.[73]

Um auf das Thema MOFs für die Energiewende zurückzukommen, wurde bspw. in einer Publikation im Jahr 2018 von Long et al.[37] die volumetrische H_2-Speicherkapazität in

MOFs dargestellt. Dabei erwies sich das [Ni_2(*m*-DOBDC)] MOF (H_4(*m*-DOBDC) = 4,6-Dihydroxyisophthalsäure) als das leistungsstärkste Speichermaterial. [Ni_2(*m*-DOBDC)] zeigt Adsorptionskapazitäten von 11.0 $g{\cdot}L^{-1}$ bei 25 °C und 23.0 $g{\cdot}L^{-1}$ in einem Temperaturbereich zwischen −75 und 25 °C. Laut Long et al. können diese Art von MOFs für die Anwendung in Kraftfahrzeugen (*on-board storage in motor vehicles)* relevant sein.[37] Im Rahmen eines EU-finanzierten Projekts berichten Freek Kapteijn et al.[74] über ihre Forschung zum Thema „*Mixed-Matrix* Membranen". Sie entwickelten ein energieeffizientes CO_2-Filtersystem auf der Grundlage einer M^4-Membran (M^4 = Membrantyp) mit dem Ziel, eine CO_2-Emissionsreduktion um 90% bei weniger als 25 Euro pro Tonne CO_2 zu realisieren. Die Kosten für die M^4-CO_2-Abtrennung vor der Verbrennung wurden auf weniger als 20 Euro pro Tonne CO_2 geschätzt und könnten in einem speziellen Prozess auf 16 Euro pro Tonne CO_2 gesenkt werden. Die Kosten nach der Verbrennung wurden auf 28 Euro pro Tonne CO_2 kalkuliert.[74] Der Einsatz von MOFs in der Energiespeicherung wurde auch in der oben genannten „*Enabling for Future*" Studie aus dem Jahr 2019 dargelegt.[70] Des Weiteren berichten Nasruddin et al.[75] über die industrielle Anwendung von recycelbaren MOFs, auch Bio-MOFs (bio: biologisch) genannt, zur CO_2-Adsorption. Bio-MOFs weisen für diesen Anwendungsbereich geeignete Eigenschaften, wie Gastbindung, Chiralität, starre oder flexible Netzwerkstruktur, auf.[75] Zur Herstellung von Bio-MOFs werden Bioliganden aus Biomolekülen, wie Aminosäuren, Proteine, Peptide und Porphyrine, verwendet.[75] Bspw. zeigt das Bio-MOF NH_2-*β*-CD-MOF[76] (CD = Cyclodextrine) eine CO_2-Adsorptionskapazität von 12.3 $cm^3{\cdot}g^{-1}$ und eine hohe selektive Adsorption von CO_2/N_2 (974.52) im Vergleich zu bereits bekannten MOFs, Aktivkohle oder Zeolithe.[75] In einer weiteren Publikation (2021) wurde ein Photokatalysator vorgestellt, der selektiv aus CO_2 mithilfe von sichtbarem Licht CH_4 als Kraftstoff umwandeln und CO_2-Emissionen senken kann.[77,78] Der Photokatalysator, $Cu_2O@Cu_3(BTC)_2$, wurde durch die Einkapselung der eindimensionalen Kupferoxid-Nanodrähten (Cu_2O) mit einer HKUST-1-Hülle (HKUST-1 = *Hong Kong University of Science and Technology* oder MOF-199, kommerziell erhältlich als Basolite® C300 von BASF, [$Cu_3(BTC)_2(H_2O)_2$], H_3BTC = 1,3,5-Benzoltricarbonsäure) hergestellt.[77,78]

Aufbau und Eigenschaften

Die Bezeichnung *„metal-organic framework*, MOF“ wurde erstmals im Jahr 1995 von Omar M. Yaghi verwendet.[1,2] In den darauffolgenden Jahren wurden über die ersten wohl bekanntesten MOFs, wie das Cu-basierte MOF HKUST-1 von Ian D. Williams und die Zn-basierten MOFs, MOF-2 bis MOF-5, von Omar M. Yaghi berichtet.[10,79,80,81] Heute sind mehr als tausend MOF-Strukturen mit permanenter Porosität bekannt.[82] Diese Verbindungen setzen sich aus zwei Bestandteilen zusammen: einer anorganischen Baueinheit (engl. *secondary building units*, SBUs),[83,84,85,86] wie isolierte Metallatome, Metall-Sauerstoff-Cluster, -Ketten oder -Schichten, die als Konnektoren im Netzwerk dienen und einer bi-, tri- oder multifunktionellen organischen Baueinheit (organischer Ligand, engl. *linker*), der die Zähligkeit und Topologie des Konnektors bestimmt (Abbildung 2).[82,87,88]

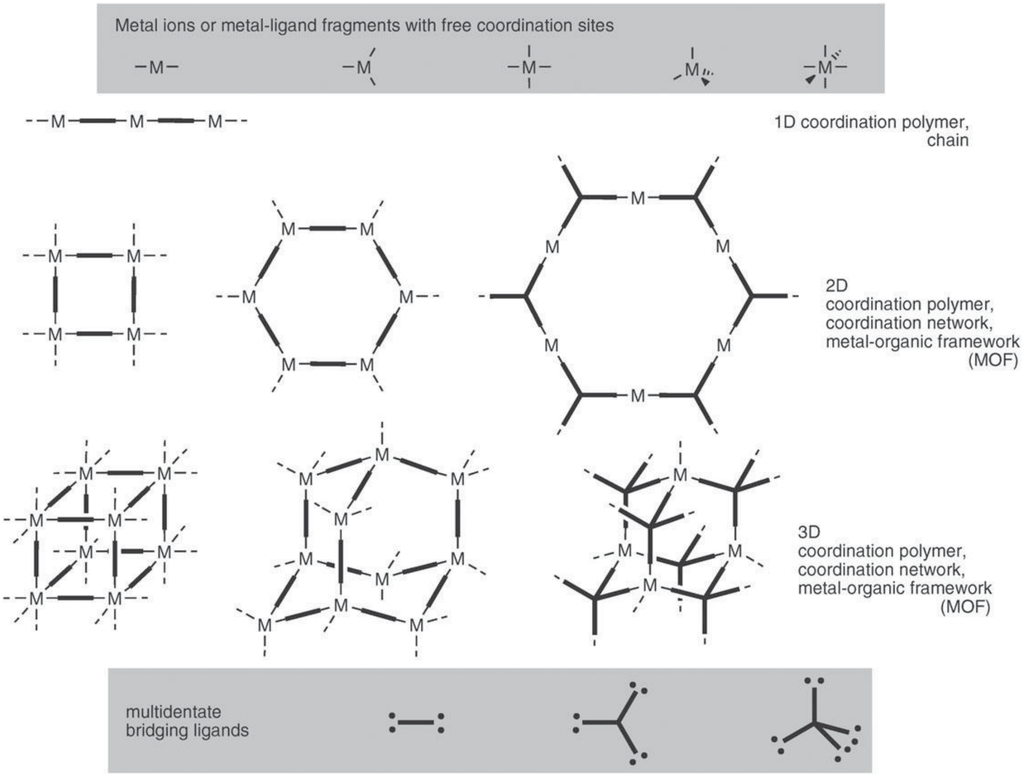

Abbildung 2 Schematische Darstellung über den Aufbau von ein-, zwei- und dreidimensionalen Koordinationspolymeren aus möglichen Metallionen (oben) und mehrzähnigen, verbrückenden Liganden (unten). Nachdruck von Ref. 88 mit Genehmigung, Centre de la Recherche Scientifique (CNRS), The Royal Society of Chemistry, © 2010.

Diese beiden Baueinheiten sind über Metall-Ligand-Bindungen miteinander verbunden und verknüpfen sich zu einem ein-, zwei- oder dreidimensionalen Gerüst (Abbildung 2).[88,89,90]

MOFs können aus einer starren (z.B. MIL-101(Cr),[91] MIL = *Matériaux de l´Institut Lavoisier*) oder flexiblen (z.B. MIL-53(Al),[92,93] siehe Kapitel 1.2) Netzwerkstruktur bestehen.[94] Betrachtet man die flexiblen Netzwerke, so weisen diese den sogenannten Atmungseffekt (engl. *breathing effect*) auf. Das „Atmen" ist hierbei abhängig von Temperatur, Druck und Gastmolekülen.[95]

Die Porengröße oder die Porenfunktionalität der MOFs wird durch den modularen Aufbau, ohne dabei die Netzwerktopologie zu verändern, eingestellt. Dabei werden topologisch identische anorganische Baueinheiten mit organischen Liganden unterschiedlicher Länge und funktioneller Gruppen (Alkyl-, Amino, Alkohol-, oder Säuregruppen) verknüpft.[11,87,96] Diese Verbindungen werden auch als isoretikuläre MOFs (IRMOFs) bezeichnet.[11,87,96] Die retikuläre Synthese von MOFs wurde im Jahr 2002 von Omar M. Yaghi eingeführt.[11,90,97] Der bekannteste Vertreter der IRMOF-Reihe ist das kubische MOF-5 ($Zn_4O(BDC)_3\cdot(DMF)_8(C_6H_5Cl)$, IRMOF-1, Abbildung 3), welches aus dem Terephthalat-Liganden (1,4-Benzoldicarbonsäure: 1,4-H_2BDC, Abbildung 4) und dem $\{ZnO(\text{-}COO)_6\}$-Cluster (Abbildung 5) aufgebaut ist und eine BET-Oberfläche (Brunauer-Emmett-Teller)[98,99] von 2205 $m^2\cdot g^{-1}$ besitzt.[10,96] Durch die Substitution der organischen Liganden können weitere IRMOFs mit der gleichen **pcu**-Topologie, höherer Porosität und hoher chemischer Stabilität für unterschiedliche Anwendungsbereiche erhalten werden (Abbildung 3).[11,87,96]

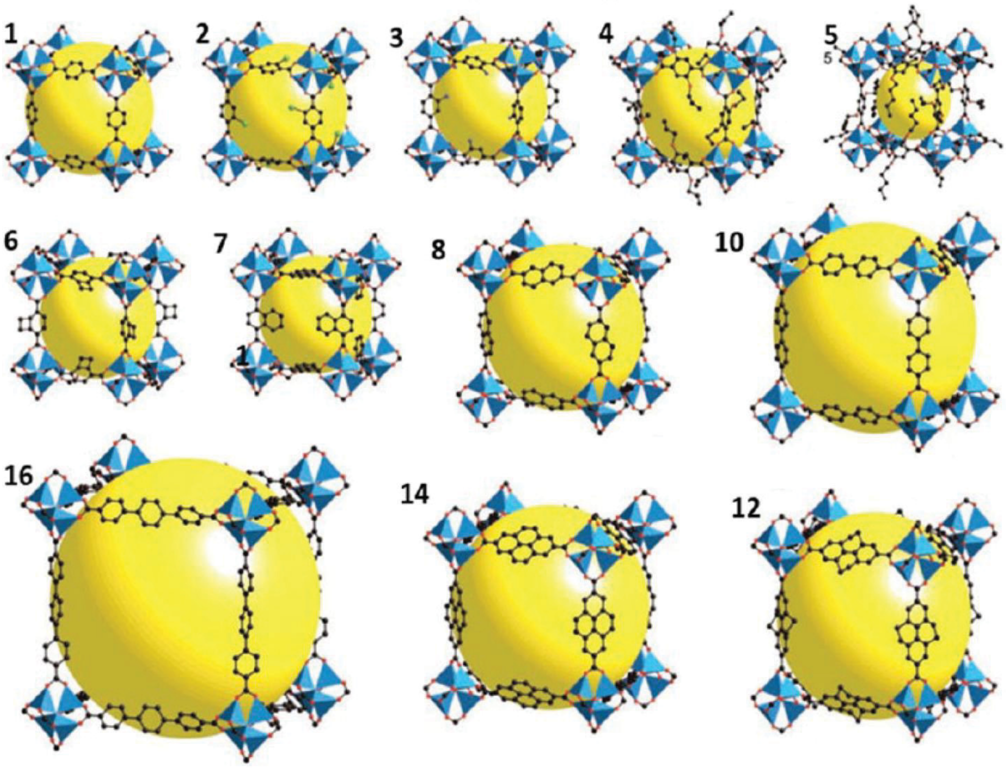

Abbildung 3 Darstellung des IRMOF-n (n = 1 bis 8, 10, 12, 14, 16) ohne Interpenetration. Nachdruck von Ref. 96 mit Genehmigung, American Chemical Society, © 2019.

In Abbildung 4 sind einige zwei- und mehrzähnige, verbrückende organische Liganden wie die Carbonsäure-Liganden und die Stickstoff-Liganden dargestellt. Mithilfe unterschiedlicher anorganischer Baueinheiten, SBUs, die je nach eingesetztem Metallatom und Ligand resultieren, können zahlreiche MOFs-Strukturen erhalten werden. Abbildung 5 zeigt verschiedene SBUs wie bspw. die paddle-wheel SBU $[M_2(CO_2)_4]$.[43]

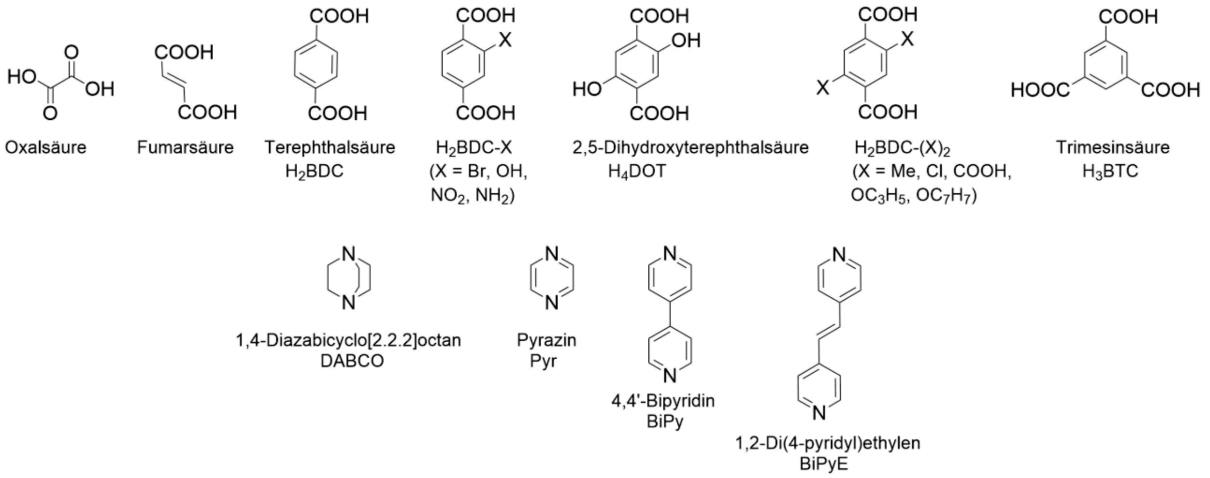

Abbildung 4 Darstellung einiger ausgewählter Beispiele für Carbonsäure-Liganden (oben) und Stickstoff-Liganden (unten), die in der Synthese von MOFs verwendet werden.

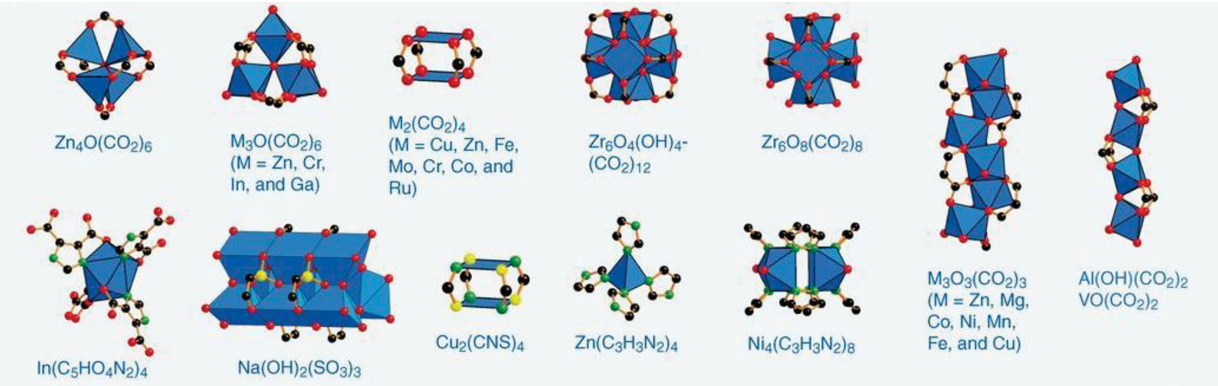

Abbildung 5 Darstellung verschiedener SBUs zum Aufbau von MOFs. Farbschema: C schwarz; O rot; N grün; S gelb; P lila; Cl hellgrün; Metallionen blaue Polyeder. Wasserstoffatome sind der Übersichtlichkeit halber weggelassen. Nachdruck von Ref. 43 mit Genehmigung, American Association for the Advancement of Science, © 2013.

Synthese

In der Regel werden MOFs unter konventionellen Synthesemethoden, wie der hydro- oder solvothermalen Methode hergestellt.[100] Hierbei finden die Synthesen in geschlossenen Gefäßen (Autoklaven) unter autogenem Druck und in polaren Lösungsmitteln, wie Wasser (H_2O), *N*,*N*-Dimethylformamid (DMF), *N*,*N*-Diethylformamid (DEF), Alkoholen (Methanol = MeOH, Ethanol = EtOH) oder Acetonitril, statt.[101] Die Reaktionstemperatur liegt dabei zwischen 80 bis 260 °C und hängt vom Siedepunkt des Lösungsmittels ab.[102,103,104] Die hydro- und solvothermale Synthesen sind zwar die meist verwendeten Synthesemethoden, allerdings sind diese Methoden durch lange Reaktionszeiten und Einsatz von teuren und umweltschädlichen Lösungsmitteln (bei der solvothermalen Methode) bekannt.[101,105]

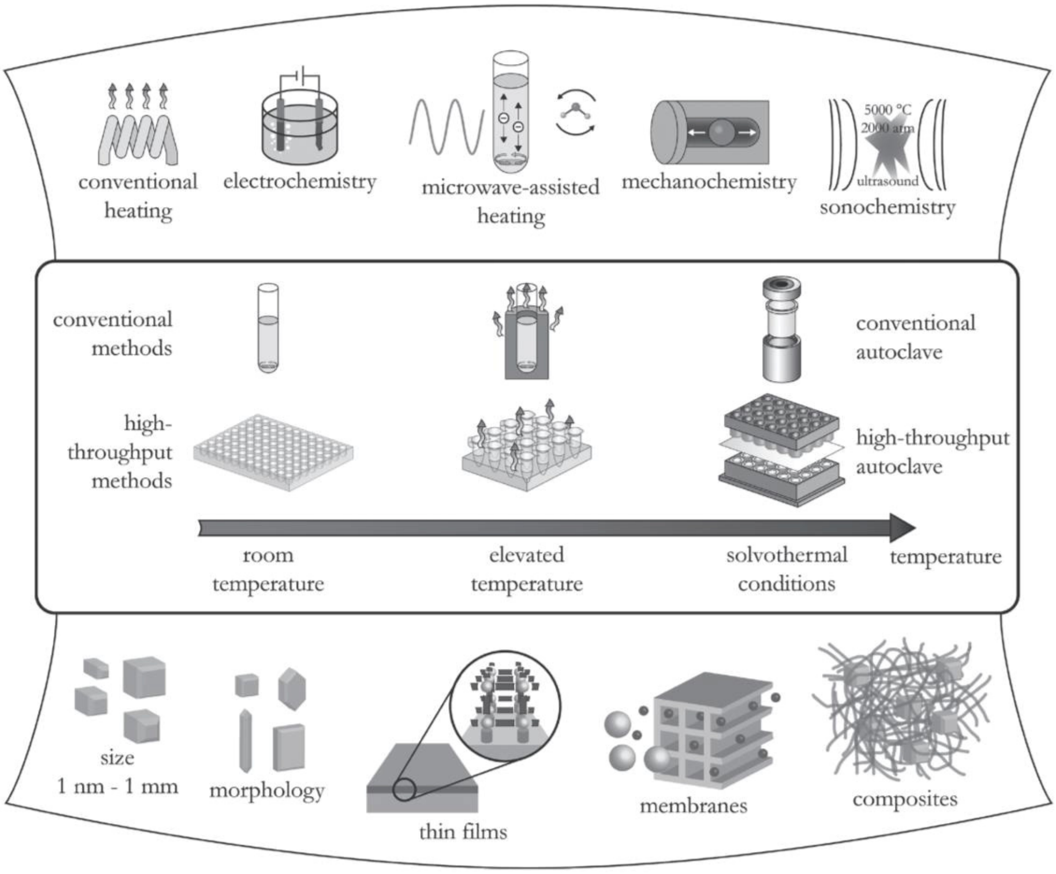

Abbildung 6 Übersicht der Synthesemethoden, mögliche Reaktionstemperaturen und -produkte in der MOF-Synthese. Nachdruck von Ref. 101 mit Genehmigung, American Chemical Society, © 2011.

Im Zuge der MOF-Forschung haben sich infolgedessen verschiedene Synthesemethoden, wie z.B. die Mikrowellen-unterstützte, Rückfluss-, Trocken-Gel-[106,107,108] und mechanochemische Synthese, entwickelt und etabliert (Abbildung 6).[101,109,110,111] Das Ziel bestand darin, die Ausbeute, Partikelgröße und Morphologie zu steuern sowie schnellere (d.h. kürzere Reaktionszeiten), effizientere und umweltfreundlichere Methoden bereitzustellen.[101] Im Gegensatz zu den konventionellen Methoden zeichnen sich insbesondere die Mikrowellen-unterstützte,[112] elektro-,[104] mechano-[113] und sonochemische[104] Synthesen durch kürzere Reaktionszeiten und keinen bis geringen Einsatz von Lösemitteln aus.[101]

Die Mikrowellen-unterstützte Synthese bietet neben der Kontrolle über die Reaktionsparameter, wie Druck, Leistung, Reaktionszeit und -temperatur auch kurze Kristallisationszeiten, enge Partikelgrößenverteilung, einfache Morphologiekontrolle und Phasenselektivität.[102,112,114] Bei der Mikrowellen-unterstützten Synthese werden elektromagnetische Wellen von einem Magnetron – bestehend aus einer metallischen Vakuumröhre mit einem Dauermagneten – erzeugt und der Hochspannungs-Gleichstrom in hochfrequente Strahlung umgewandelt (Abbildung 7).[101,102,112,114,115,116]

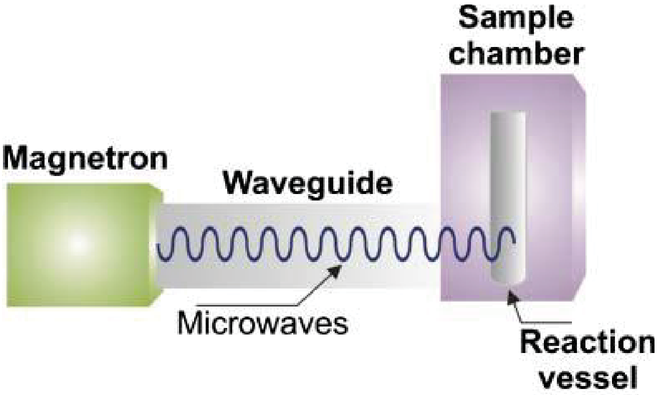

Abbildung 7 Schematische Darstellung der Grundkomponenten einer Monomode-Mikrowelle. Nachdruck von Ref. 112 mit Genehmigung, The Royal Society of Chemistry, © 2011.

Die erzeugte Mikrowellenenergie wird auf die Probe übertragen und von innen erhitzt. Es erfolgt eine dielektrische Erwärmung, welches auf der Wechselwirkung nichtleitender Stoffe, Dielektrika, mit dem elektrischen Wechselfeld der elektromagnetischen Schwingungen beruht.[101,102,112,114,115,116] Für die Wärmeerzeugung ist die Polarisation verantwortlich. Beim Bestrahlen der Probe richten sich die Dipole im angelegten Feld aus. Das Dipolfeld versucht sich mit dem wechselnden elektrischen Feld neu auszurichten, sodass das Feld oszilliert. Dabei wird durch die Molekularreibung und den dielektrischen Verlust Energie in Form von Wärme frei.[101,102,112,114,115,116]

Zur Aktivierung des MOF-Gerüstes, d.h. die Entfernung von Lösemittelmolekülen aus den Poren, werden die synthetisierten MOFs thermisch unter Vakuum behandelt.[87] Jedoch ist die Aktivierung mittels thermischer Behandlung unter vermindertem Druck bei manchen MOFs aufgrund der thermischen Instabilität nicht immer möglich. Um die Gefahr des Kollabierens und folglich den Verlust der Kristallinität und Porosität der Gerüststruktur zu vermeiden, sind schonende Aktivierungsmethoden, wie überkritische CO_2-Trocknung (engl. *supercritical* CO_2 *drying*) oder Lösungsmittelaustausch (engl. *solvent exchange*), auszuwählen (Abbildung 8).[102]

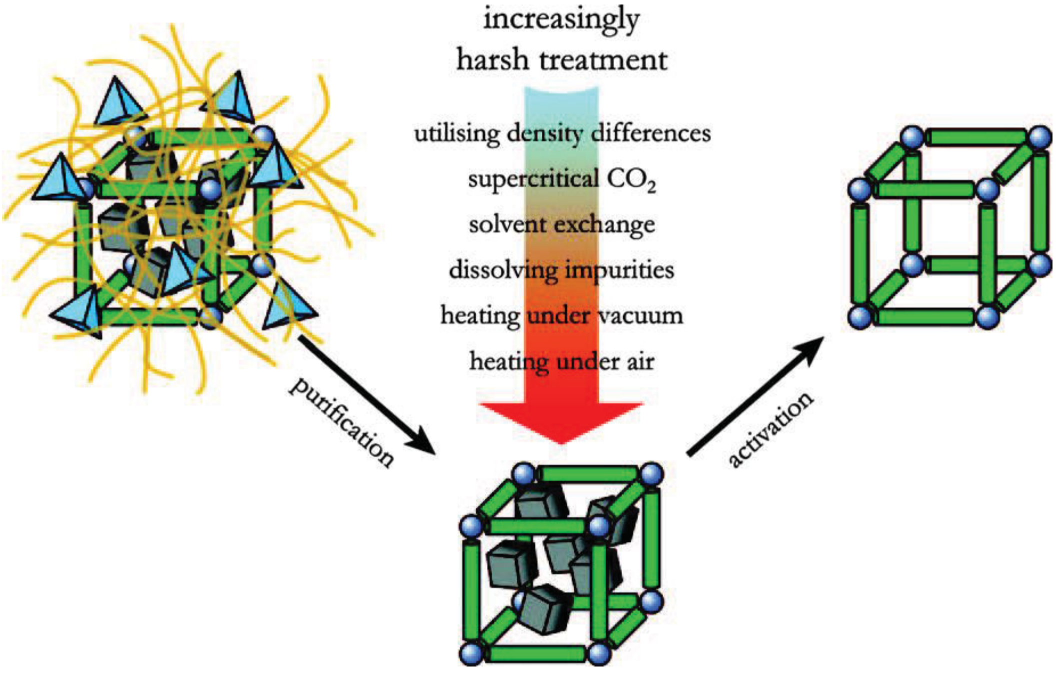

Abbildung 8 Schematische Darstellung der Aktivierung eines MOF-Gerüstes. Tetraeder und gelbe Schnüre symbolisieren Verunreinigungen und Würfel Lösemittelmoleküle in den Poren. Nachdruck von Ref. 102 mit Genehmigung, The Royal Society of Chemistry, © 2011.

Bei der Entfernung von labilen terminalen Liganden, d.h. von koordinierten Lösungsmittelmolekülen wie Wasser, Alkoholen (MeOH, EtOH), Acetonitril oder DMF, können offene Metallstellen (engl. *open metal sites*, OMS) durch Lösungsmittelaustauch und thermische, chemische oder photochemische Aktivierung erzeugt werden.[117,118,119,120] Um stabile OMS-MOFs generieren zu können, ist es wichtig, dass die MOF-Struktur nach der Aktivierung nicht kollabiert und ihre Kristallinität und Porosität beibehält.[121,122] Eines der bekanntesten OMS-MOF ist z.B. das paddle-wheel MOF HKUST-1 mit offenen Cu^{2+} Stellen.[79]

Charakterisierung mittels analytischer Methoden

Zur Bestimmung der charakteristischen Eigenschaften von porösen Materialien, MOFs, werden analytische Methoden wie die Röntgenpulverdiffraktometrie (engl. *Powder X-Ray Diffraction*, PXRD) und die Gasadsorption eingesetzt.

Röntgenpulverdiffraktometrie (PXRD)

Die Röntgenpulverdiffraktometrie ist eine Methode zur strukturellen Charakterisierung von kristallinen Materialien. Diese Methode basiert auf der Beugung von Röntgenstrahlung an geordneten Strukturen wie Kristallen. 1912 wurde die Bragg´sche Gleichung $n\cdot\lambda=2\cdot d\cdot \sin\theta$ (n: natürliche Zahl (0, 1, 2, 3, ...) – Ordnung der Interferenz, λ: Wellenlänge der Röntgenstrahlung, d: Netzebenenabstand, θ: Glanz- oder Braggwinkel) von William L. Bragg zur Erklärung der Röntgenbeugung entwickelt.[123]

Treffen Röntgenstrahlen – elektromagnetische Wellen – auf einen Kristall mit regelmäßiger Gitterstruktur, so reflektieren sie an der obersten und an folgenden Netzebenen des Kristallgitters (Abbildung 9).[123] Dadurch kommt es zu Interferenzen. Der Einfallswinkel (θ_0) des einfallenden Strahls (S_0) ist hierbei gleich dem Ausfallswinkel (θ) des ausfallenden/reflektierten Strahls (S). Der Winkel zwischen einfallendem und ausfallendem Strahl beträgt 2θ und wird auch als Beugungswinkel bezeichnet. Eine konstruktive Interferenz liegt vor, wenn der Gangunterschied $\delta=2\cdot d\cdot \sin\theta$ ein ganzzahliges Vielfaches der Wellenlänge $n\cdot\lambda$ ist. Es entstehen Reflexe, die im Diffraktogramm zu sehen sind.[123]

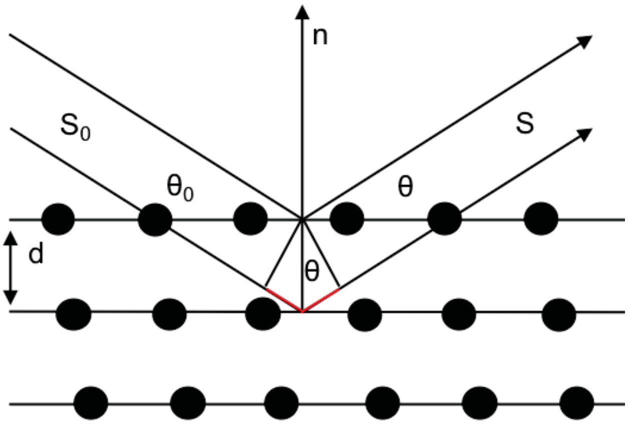

$$\delta = 2 \cdot d \cdot \sin\theta$$

Abbildung 9 Beugungsvorgang an einer Netzebenenschar nach W. L. Bragg (θ_0: Einfallswinkel, θ: Ausfallswinkel, S_0: einfallender Strahl, S: ausfallender Strahl). Reproduziert von Ref. 123 mit Genehmigung, © Springer-Verlag Berlin Heidelberg, 2003.

Physisorption und Porosität

MOFs zeichnen sich durch sehr hohe spezifische Oberflächen bzw. hohe Porosität aus. Diese Eigenschaft ermöglicht die Sorption von verschiedenen inerten Gasen. IUPAC definiert die Porendurchmesser für poröse Materialien wie folgt: Mikroporen bis 2 nm, Mesoporen zwischen 2 bis 50 nm und Makroporen ab 50 nm.[124]

Bei der Gasadsorption wechselwirken die Gasmoleküle (Adsorptiv) mit der Oberfläche des zu untersuchenden porösen Materials (Adsorbens) miteinander. Bei der Wechselwirkung handelt es sich um Van-der-Waals-Kräfte. Die Anlagerung der Gasmoleküle (Adsorbat) an der Oberfläche eines Materials erfolgt mittels physikalischer Adsorption, auch Physisorption genannt. Die Physisorption stellt im Gegensatz zur Chemisorption einen reversiblen Prozess dar, d.h. die adsorbierten Gasmoleküle können unverändert wieder entfernt werden. Dieser Umkehrprozess wird Desorption genannt.[99]

Für die Oberflächenbestimmung der mikro- und mesoporösen MOFs wird häufig die Stickstoffsorption (N_2, bei 77 K) herangezogen.[99,125] Da das Stickstoffmolekül aber ein Quadrupolmoment aufweist, d.h. eine Wechselwirkung mit funktionellen Oberflächen-gruppen und Ionen eingehen kann, die wenn möglich unterdrückt werden sollte, ist Argon (Ar, bei 87 K) als Adsorptiv zu bevorzugen. Argon besitzt kein Quadrupolmoment und ist weniger reaktiv als das zweiatomige Stickstoffmolekül. Insbesondere für die Mikroporenanalyse ist die Argonmessung bei 87 K, mithilfe eines Kryostats oder Kryokühlers um die Temperatur konstant zu halten, vorteilhaft.[99,125]

Nach der IUPAC-Empfehlung werden Physisorptionsisothermen in sechs Isothermentypen unterteilt (Abbildung 10).[99]

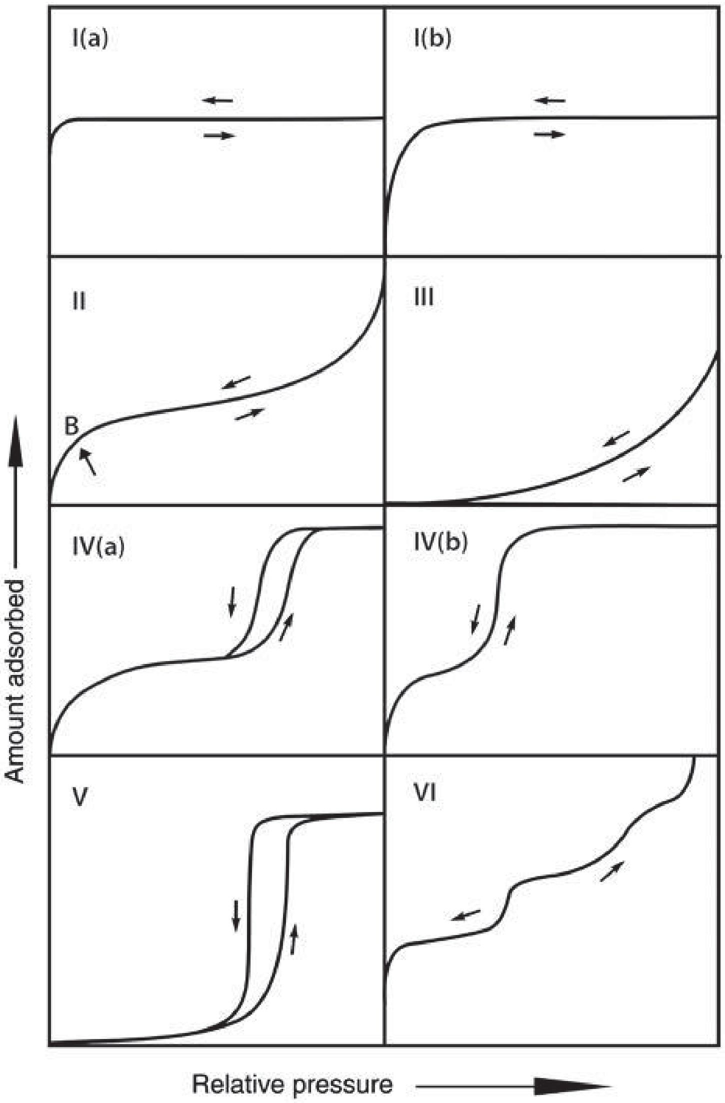

Abbildung 10 Darstellung der verschiedenen Physisorpsionsisothermentypen nach IUPAC. Nachdruck von Ref. 99 mit Genehmigung, De Gruyter, IUPAC, © 2015.

Die reversible **Typ I**-Isotherme wird den mikroporösen Feststoffen, wie Aktivkohle und Zeolithe, die eine geringe äußere Oberfläche besitzen, zugeordnet. Die geringe Aufnahme ist nicht von der inneren Oberfläche, sondern von dem zugänglichen Mikroporenvolumen abhängig. Der steile Anstieg der Isotherme bei niedrigem Relativdruck lässt auf eine frühe Mikroporenfüllung schließen, welche auf die verstärkte Adsorbens-Adsorptiv-Wechselwirkung bei kleineren Poren beruht. Typ I(a)-Isothermen sind charakteristisch für Materialien mit Porendurchmesser bis zu 1 nm und Typ I(b)-Isothermen für Materialien mit Porendurchmesser bis zu 2.5 nm.[99] Die reversiblen **Typ II**-Isothermen sind spezifisch für nicht-poröse oder makroporöse Adsorbentien. Der zunächst steile Verlauf der Isotherme beschreibt die Ausbildung einer Monolage, welche bei hohem relativem Druck in Multilagen übergeht.[99] Bei **Typ III**-Isothermen handelt es sich ebenfalls um nicht-poröse oder makroporöse Feststoffe. In diesem Fall ist die Adsorbens-Adsorbat-Wechselwirkung schwächer, sodass keine Monolagen gebildet werden. In Typ II- und Typ III-Isothermen werden bei hohen Relativdrücken keine Plateaus erreicht.[99] **Typ IV**-Isothermen sind charakteristisch für mesoporöse Materialien, wie Oxidgele, industrielle Adsorbentien und Molekularsiebe. Das Adsorptionsverhalten wird durch die Adsorbens-Adsorbat-Wechselwirkung und der Adsorbat-Absorbat-Wechselwirkung bestimmt. Wie auch in Typ II-Isotherme erfolgt zunächst die Bildung einer Monolage, welche anschließend bei hohem relativem Druck durch Porenkondensation in Multilagen übergeht. Durch die Sättigung der Poren bei hohen Relativdrücken werden Plateaus in Typ IV(a)- und (b)-Isothermen erreicht. Im Fall von Typ IV(a)-Isotherme bildet sich eine Hysterese aufgrund einer Kapillarkondensation, welche bei der Stickstoff- oder Argonadsorption in Abhängigkeit der Temperatur und Porendurchmesser größer 4 nm auftritt, aus. Typ IV(b) zeigt einen reversiblen Verlauf der Isotherme.[99] **Typ V**-Isothermen werden bei der Wassersorption an hydrophoben mikro- bzw. mesoporösen Materialien beobachtet. Sie verläuft im niedrigen relativen Druckbereich ähnlich wie die Typ III-Isotherme und weist schwache Adsorbens-Absorbat-Wechselwirkungen auf. Bei höheren Relativdrücken findet die Bildung von Clustern und die Porenfüllung statt. Analog zu Typ IV(a)-Isotherme kann sich auch hier eine Hysterese aufgrund einer Kapillarkondensation ausbilden.[99] Die reversible **Typ VI**-Isotherme zeigt die schichtweise Adsorption an einem nicht-porösen Material.[99]

Die Einteilung der Hysteresetypen richtet sich ebenfalls nach der IUPAC-Empfehlung (Abbildung 11).[99] Die Form der Hysterese, wie in Typ IV(a)-Isotherme und Typ V-Isotherme zu sehen ist (Abbildung 10), hängt stark von der Kapillarkondensation in den Poren ab.[99]

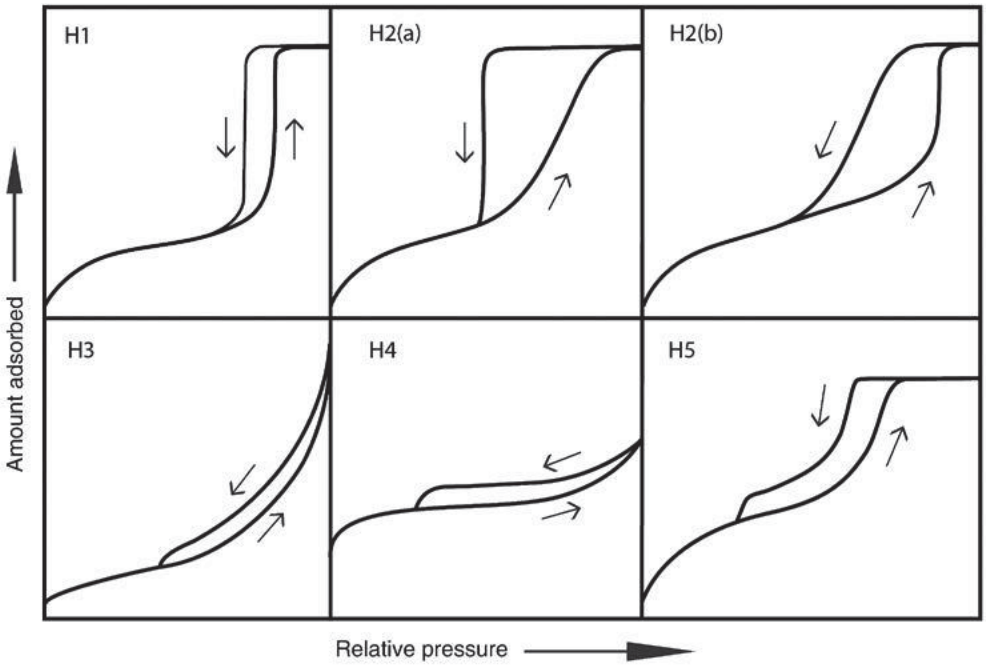

Abbildung 11 Darstellung der verschiedenen Hysteresetypen nach IUPAC. Nachdruck von Ref. 99 mit Genehmigung, De Gruyter, IUPAC, © 2015.

Typ **H1**-Hysteresen sind charakteristisch für Materialien mit einheitlichen Mesoporen, wie bspw. Kieselsäuren (z.B. MCM-41, MCM = *Mobil Composition of Matter*). Typ **H2**-Hysteresen werden bei Materialien mit komplexer Porenstruktur, in denen Netzwerkeffekte wie Porenblockierung/Perkolation oder Kavitation auftreten, beobachtet. Der Unterschied zwischen Typ H2(a)- und Typ H2(b)-Hysteresen ist die unterschiedliche Porenweitenverteilung, welche in Typ H2(b) größer ist als in Typ H2(a). Typ **H3**-Hysteresen zeigen sich bei Typ II-Isothermen makroporöser Materialien oder Aggregaten mit plättchenförmigen Partikeln. Typ **H4**-Hysteresen sind charakteristisch für mikro- und mesoporöse Materialien. Hierbei ist die Adsorption eine Mischung aus Typ I- und Typ II-Isothermen. Die ausgeprägte Aufnahme bei niedrigen Relativdrücken lässt auf die Mikroporenfüllung schließen. Typ **H5**-Hysteresen sind typisch für mesoporöse Materialien mit offenen und teilweise blockierten Poren.[99]

Bestimmung der spezifischen Oberfläche mit der BET-Methode

Die Brunauer-Emmett-Teller-Methode, kurz BET-Methode, wird zur Bestimmung der spezifischen Oberfläche nichtporöser, meso- und makroporöser Materialien aus Typ II- und Typ IV(a)-Isothermen im relativen Druckbereich von 0.05 bis 0.30 verwendet.[98,99] Diese Methode wurde 1938 von Stephen Brunauer, Paul H. Emmet und Edward Teller entwickelt und basiert auf der Mehrschichtenadsorption.[98] Bei der Mehrschichtenadsorption wird zunächst eine Monolage an Adsorbat, welche an freien Adsorptionsstellen des Adsorbens absorbiert, ausgebildet. Jedes adsorbierte Molekül kann wiederum als Adsorptionsstelle dienen, sodass weitere Moleküle adsorbieren und zu einer Multilagen-Ausbildung führen können.[98]

Die BET-Gleichung zur Berechnung der spezifischen Oberfläche setzt sich aus der spezifischen Aufnahmekapazität n, der spezifischen Monolagenkapazität n_m, der positiven C-Konstante, die ein Parameter für die Energie der Monolagenadsorption ist und im Wertebereich zwischen 2 bis 150 liegt, und dem Relativdruck $p \cdot p_0^{-1}$ zusammen. Siehe die Gleichung (1).[99]

$$\frac{p/p_0}{n\left(1-p/p_0\right)}=\frac{1}{n_m C}+\frac{C-1}{n_m}\left(\frac{p}{p_0}\right) \qquad (1)$$

Die Ermittlung der spezifischen Monolagenkapazität n_m erfolgt durch die Auftragung des BET-Plots, $(p/p_0)/n(1-p/p_0)$ gegen den relativen Druck p/p_0. Aus der spezifischen Monolagenkapazität n_m, der Avogadrokonstante L, der Querschnittsfläche des verwendeten Gases σ_m und der Masse des Adsorbens m lässt sich die spezifische BET-Oberfläche a_s(BET) berechnen. Siehe die Gleichung (2).[99]

$$a_s(\mathrm{BET})=\frac{n_m \cdot L \cdot \sigma_m}{\mathrm{m}} \qquad (2)$$

1.2 Aluminium-basierte MOFs

Aluminium-basierte MOFs, kurz Al-MOFs, bestehend aus dreiwertigen Metall-Ionen (Al^{3+}-Kationen), haben in den vergangenen Jahren aufgrund ihrer hohen chemischen und thermischen Stabilität zunehmend an Interesse gewonnen.[126] Sie bestehen weitgehend aus $AlO_4(OH)_2$-Oktaedern, die sich in Abhängigkeit der verwendeten Liganden und Synthesebedingungen zu unterschiedlichen SBUs verknüpfen können.[127] In Abbildung 12 sind bspw. drei anorganische Baueinheiten in Al-MOFs, CAU-1, CAU-3 und CAU-6 (CAU = Christian-Albrechts-Universität) dargestellt.[128]

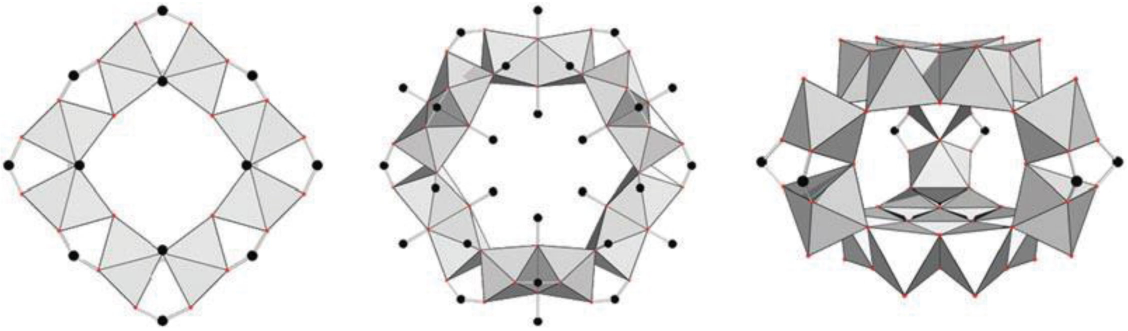

Abbildung 12 Darstellung der anorganischen Baueinheit (SBU) in CAU-1 (links), CAU-3 (mitte) und CAU-6 (rechts). Nachdruck von Ref. 128 mit Genehmigung, The Royal Society of Chemistry, © 2012.

Eines der ersten Al-MOF ist das MIL-53(Al) (kommerziell erhältlich als Basolite® A100 von BASF) mit der allgemeinen Formel [Al(OH)(1,4-BDC)] und wurde im Jahr 2004 von Gérard Férey et al.[92] beschrieben. In MIL-53(Al) sind die Terephthalat-Liganden mit eindimensionalen rautenförmigen Kanälen zu einem dreidimensionalen Gerüststruktur verknüpft, welche aus unendlichen Ketten *trans*-eckenverknüpfter AlO_6-Polyeder bestehen. Zu den Eigenschaften gehören zum einen die hohe thermische Stabilität bis zu einer Temperatur von über 400 °C und zum anderen die reversible Gerüstflexibilität (Abbildung 13).[92,93] Mit Änderung der Gerüststruktur verändern sich auch die Zellparameter in Abhängig der Gastmoleküle.[87,92]

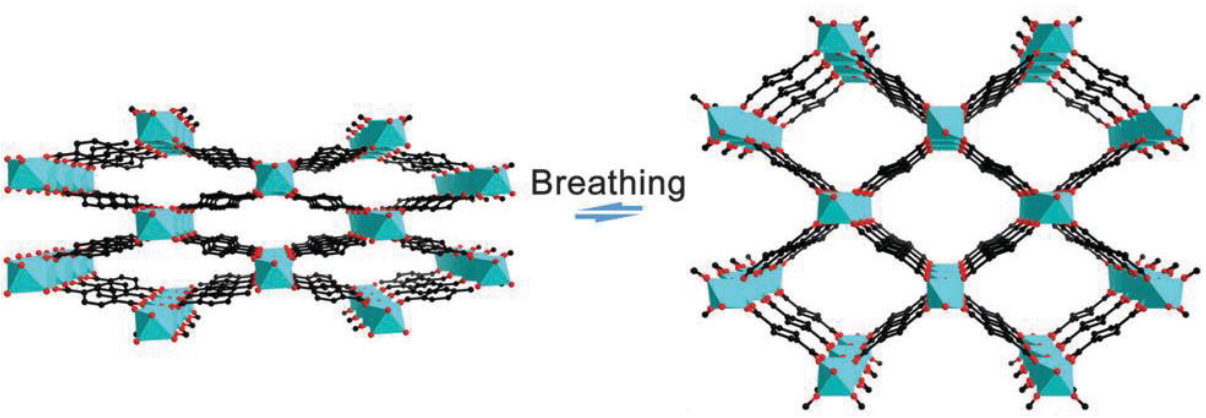

Abbildung 13 MIL-53 – Atmungseffekt. Farbschema: C schwarz; O rot; Metall türkis. Nachdruck von Ref. 93 mit Genehmigung, The Royal Society of Chemistry, © 2014.

MOFs, insbesondere Al-MOFs wie Aluminiumfumarat (Alfum, kommerziell erhältlich als Basolite® A520 von BASF)[30,129], CAU-10,[29,130,131,132,133,134,135] MIL-53-TDC (H_2TDC = 2,5-Thiophendicarbonsäure)[136,137] und MIL-160,[138] haben eine hohe Affinität zu Wasser. Sie sind vielversprechende Adsorptionsmaterialien für die Verwendung in wasserbasierten Adsorptionswärmepumpen (engl. *adsorption heat pumps*, AHPs) oder thermisch angetriebenen Adsorptionskältemaschinen (engl. *thermally driven adsorption chillers*, TDCs).[27,28,139,140,141,142,143,144,145,146,147,148] In AHPs besitzen MOFs vergleichsweise zu anderen Sorptionsmaterialien, wie Silica Gele, Zeolithe, SAPO und AlPO (Silica-Aluminophosphat und Aluminophosphat), eine hohe Wasseraufnahme (Abbildung 14).[139]

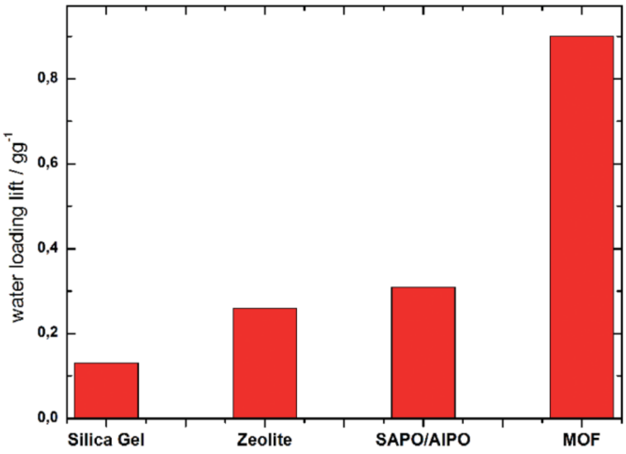

Abbildung 14 Darstellung der Wasseraufnahmemengen verschiedener Sorptionsmaterialien in AHPs. Nachdruck von Ref. 139 mit Genehmigung, Wiley-VCH Verlag GmbH & Co. KGaA, © 2012.

Einsatzfähige Adsorptionsmaterialien für die Verwendung in AHPs sind solche, die einen hydrophilen Charakter, eine S-förmige Sorptionsisotherme, eine hohe Wasseraufnahme in einem engen Partialdruckbereich (zwischen 0.1 bis 0.3 $p \cdot p_0^{-1}$) und eine hohe Anzahl an Adsorptions- und Desorptionszyklen aufweisen.[27,28,140,141,142,146,149,150,151] Im Allgemeinen erfolgt die Wasseradsorption und -desorption nach drei Mechanismen: (1) Adsorption am Metall-Cluster (irreversibel), (2) Adsorption in den Poren (reversibel) und (3) Kapillarkondensation in den Poren (irreversibel).[28,152]

Die Arbeitsweise eines Adsorptionswärmeumwandlung-Prozesses (engl. *adsorption heat transformation*, AHT) ist in Abbildung 15 dargestellt.[146]

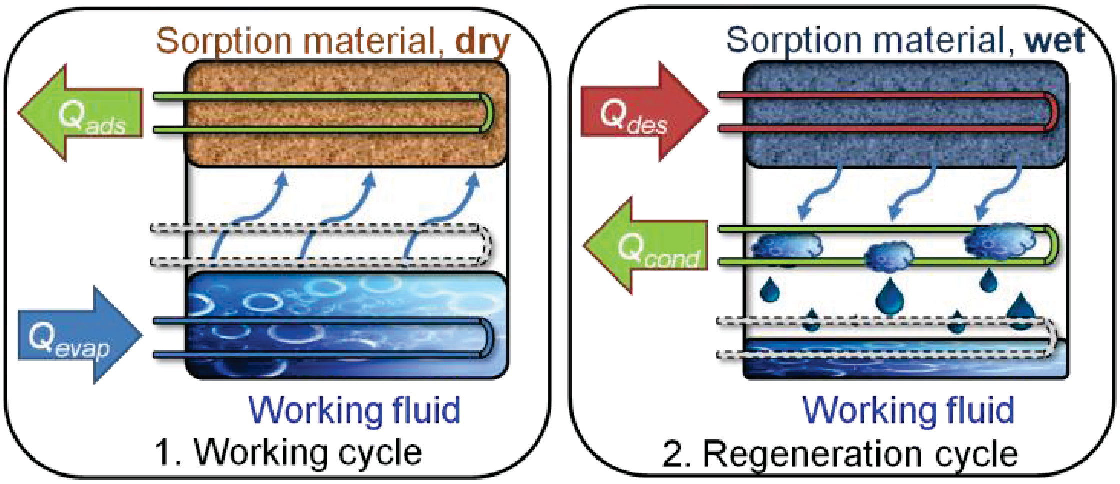

Abbildung 15 Arbeitsschema eines AHT-Prozesses während des Arbeitszyklus und Regenrationszyklus. Nachdruck von Ref. 146 mit Genehmigung, The Royal Society of Chemistry, © 2012.

Im Arbeitszyklus wird eine Arbeitsflüssigkeit, vorzugweise Wasser aufgrund seiner hohen Verdampfungsenthalpie und Ungefährlichkeit, bei niedrigem Druck verdampft und die Verdampfungswärme Q_{evap} aufgenommen. Während der Anlagerung der Moleküle an der Oberfläche eines porösen Materials wird die Adsorptionsenthalpie Q_{ads} freigesetzt. Im Regenerationszyklus wird die Antriebswärme Q_{des} für den Übergang der Moleküle von der Oberfläche des porösen Materials in die Gasphase aufgenommen. Die gasförmige Arbeitsflüssigkeit kondensiert auf mittlerem Temperaturniveau und setzt die Kondensationsenthalpie Q_{cond} frei. Je nach Betätigungsrichtung kann das Gerät als Adsorptionswärmepumpe oder Adsorptionskältemaschine verwendet werden.[146]

1.3 MOF-Graphitoxid Komposite

Die Sorptionseigenschaften der MOFs, insbesondere die Zunahme der spezifischen Oberfläche und der Adsorptionskapazität, kann durch die Zugabe eines Kompositmaterials, wie bspw. Polymer,[153,154] Aluminiumoxid,[155,156,157,158] Oxide,[159] Kohlenstoffnanoröhrchen,[160] funktionalisierter Graphit[161] oder Graphitoxid,[162,163,164,165,166] durch die Herstellung von MOF Kompositen verbessert werden.

Graphitoxid (engl*.* *graphite oxide*, GO) ist ein nicht-stöchiometrisches Material, welches aus planaren Kohlenstoffschichten mit sp^2- und sp^3-hybridisierten Kohlenstoffatomen besteht.[167,168,169,170] GO mit der Summenformel $C_8O_{3.7}H_{2.5}$ wird über die Oxidation von Graphit nach der Methode von William S. Hummers und Richard E. Offeman erhalten.[171,172] Nach dieser Methode wird Graphit unter Einsatz von Natriumnitrat, Schwefelsäure und Kaliumpermanganat oxidiert. Die Oxidation von Graphit führt zu funktionellen Hydroxy- und Epoxy-Gruppen an den sp^2-hypridisierten Kohlenstoffatomen.[171] Aufgrund seines hydrophilen Charakters kann Graphitoxid in Wasser und polaren Lösungsmittel dispergiert und zur Herstellung von hydrophilen Kompositen verwendet werden.[173]

Die Bildung des MOFs an GO-Schichten ist in Abbildung 16 vereinfacht dargestellt.[174] Demnach geht das MOF, MOF-5, eine Reaktion mit den Epoxidgruppen des GOs ein. Diese Reaktion wird der Wechselwirkung zwischen Wassermolekülen und MOF-5 gleichgesetzt. Es wird davon ausgegangen, dass die Sauerstoffatome der Epoxygruppen des GOs die gleiche Rolle wie die Sauerstoffatome in Wasser spielen. Jedoch kommt es nicht, wie bei der Zersetzung von MOF-5 in Wasser (Zersetzung, d.h. Austausch von Sauerstoffatomen in ZnO_4-Tetraedern durch die Sauerstoffatomen in Wasser), zu einem Kollaps der MOF-5-Struktur, da nur eine begrenzte Anzahl an Epoxidgruppen vorliegt. Des Weiteren führen die Wasserstoffbrückenbindungen zwischen den Hydroxygruppen (Donor) des GOs und den Sauerstoffatomen (Akzeptor) in ZnO_4-Tetreadern zur Verstärkung der Wechselwirkungen zwischen den GO-Schichten und MOF.[162,165,174]

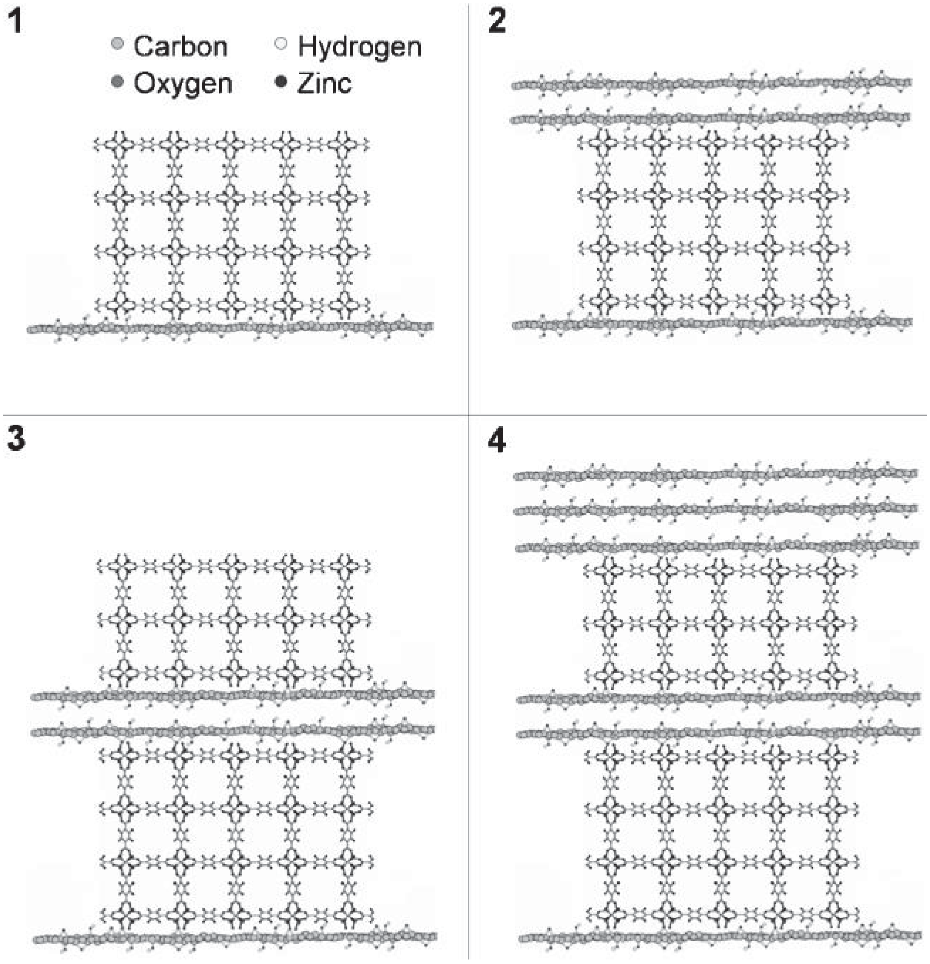

Abbildung 16 Schematische Darstellung der Bildung von MOF-5-GO Kompositen. Nachdruck von Ref. 174 mit Genehmigung, WILEY-VCH Verlag GmbH & Co. KGaA, © 2009.

Im Gegensatz zu reinen MOFs weisen MOF-GO-Komposite, wie z.B. in Chrom-,[166,175,176] Kupfer-[170,177,178] und Zink-basierten MOFs,[179,180] eine verbesserte Porosität und Adsorptionskapazitäten auf. Im Vergleich zum Chrom-basierten MOF, MIL-101(Cr), wurde für das MIL-101(Cr)-GO Komposit mit einem GO-Anteil von 2 Gew.-% eine 10% höhere BET-Oberfläche und ein 22% erhöhtes Porenvolumen erzielt.[175] In einer weiteren Veröffentlichung wurde für das MIL-101(Cr)-GO Komposit mit einem höheren Anteil von 6 Gew.-% GO eine Erhöhung der BET-Oberfläche um ca. 22% und des Porenvolumens um 35% realisiert.[166] Des Weiteren erzielten Sung H. Jhung et al. für das MIL-101(Cr)-GO Komposit mit einem GO-Anteil von 0.25% eine 22% höhere BET-Oberfläche (Abbildung 17a), eine ca. 11% erhöhtes Porenvolumen und eine 30% höhere Adsorptionskapazität (Abbildung 17b).[176]

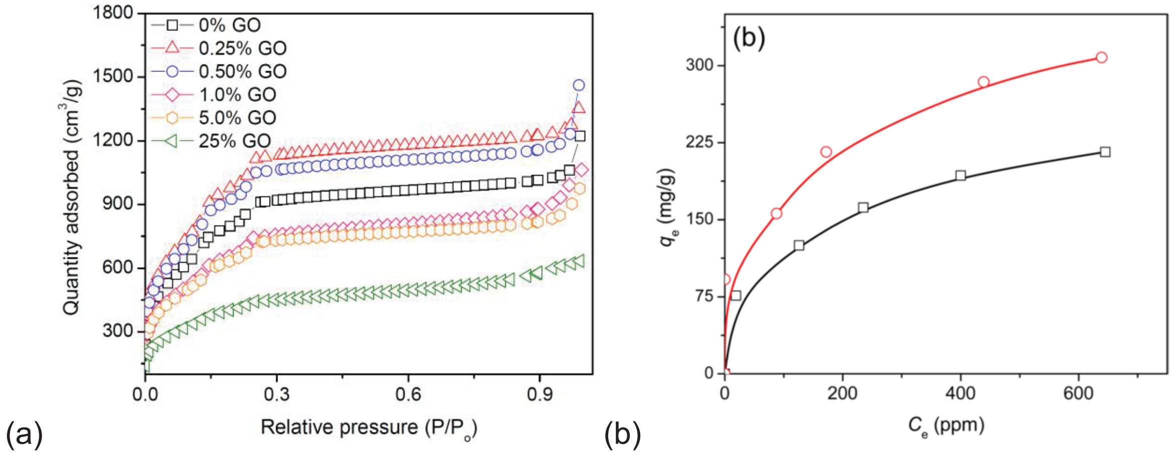

Abbildung 17 N_2-Sorptionsisothermen (a) und Adsorptionsisothermen – Indol (b) von MIL-101(Cr) und MIL-101(Cr)-GO Kompositen. Nachdruck von Ref. 176 mit Genehmigung, American Chemical Society, © 2013.

Bei einer Erhöhung des GO-Anteils über 10 Gew.-% lässt sich jedoch ein negativer Trend, wie auch in Abbildung 17a zu sehen, beobachten.[164,165,170,174,176,181,182] In Tabelle 1 sind weitere MOF-GO Komposite und ihr Einsatz in der Gasspeicherung und -separation zusammengefasst.

Tabelle 1 MOFs-GO Komposite für den Einsatz in der Gasspeicherung und -separation.

MOF-GO Komposite	Gasspeicherung und -separation	Referenzen
HKUST-1-GO	H_2 Adsorption CO_2 Adsorption H_2S Adsorption NH_3 Adsorption CO_2/N_2 Separation	170,183,184 185,186,187,188 189 177,190 191
MIL-53(Cr)-GO	CO_2/CH_4 Separation	192
MIL-101(Cr)-GO	CO_2, CH_4, Methylmercaptan Adsorption Acetone Adsorption Adsorption von n-Alkanen Adsorption von n-Hexan CO_2/CH_4 Separation	193 194 195 196 197
MOF-5-GO	CO_2 Adsorption H_2S Adsorption NH_3 Adsorption	179 198 162,199
UiO-66-GO	CO_2 Adsorption H_2/CH_4 und CO_2/CH_4 Separation	200,201 202
ZIF-8-GO	H_2 Adsorption	203,204

2 Zielsetzung

Die vorliegende Dissertation setzt sich mit zwei Themengebieten, der Synthese und Charakterisierung von MOF Kompositen und dem Verfassen eines Reviews zu dem Thema „MOFs mit offenen Metallstellen“, auseinander.

Der erste Teil dieser Dissertation wird im Rahmen des Projekts „Optimierung von neuartigen Materialien für zyklische Adsorptionsprozesse“, kurz OptiMat, angefertigt. Das Ziel des Projekts OptiMat ist die Entwicklung neuer, hydrothermal stabiler, mikroporöser, schwammartiger Materialien und Komposite für den Einsatz in thermisch angetriebenen Wärmepumpen und Klimaanlagen. Relevant sind bspw. Materialien aus der Klasse der MOFs, die einen hydrophilen Charakter, eine S-förmige Wassersorptionsisotherme, eine hohe Wasseraufnahme in einem engen Partialdruckbereich und eine hohe Anzahl an Wasseradsorptions- und Wasserdesorptionszyklen aufweisen.[143,146] Al-MOFs erfüllen die Anforderungen an Stabilität und S-förmige Wassersorptionsisotherme, lediglich könnte versucht werden, ihre Wasseraufnahmekapazitäten zu steigern.[27,144,146]

In Abbildung 18 werden die HHU-relevanten Arbeitspakete im Projekt OptiMat dargestellt.

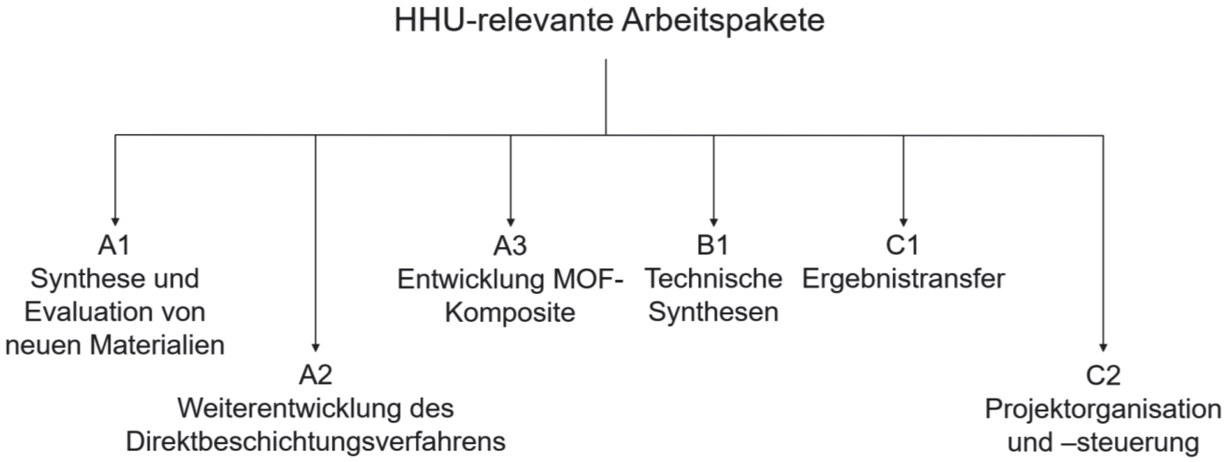

Abbildung 18 Die HHU-relevanten Arbeitspakete im Projekt OptiMat.

Das Ziel dieser Dissertation liegt dabei in der Synthese von MOF Kompositen. Hierbei sollen neue MOF Komposite aus literaturbekannten Al-MOFs mit ca. 2 bis 20 Gew.-% GO hergestellt werden. Des Weiteren wird das Ziel der Steigerung der Gasaufnahmen, insbesondere der Wasseraufnahmen im Vergleich zu reinen Al-MOFs verfolgt. Aus der Fachliteratur ist bekannt, dass im Vergleich zu reinen MOFs bei den MOF-GO Kompositen durch den Einsatz von GO höhere spezifische Oberflächen und Gasaufnahmen erzielt werden können.[166,170,179] Anschließend sollen die hergestellten Materialien anhand analytischer Methoden wie IR-Spektroskopie (Infrarot-Spektroskopie), PXRD und REM (Rasterelektronenmikroskopie) umfassend charakterisiert werden. Ferner sind Sorptionsuntersuchungen, insbesondere die Wassersorption über mehrere Adsorptions- und Desorptionszyklen und Stickstoffsorption, durchzuführen.

Der zweite Teil dieser Dissertation wird im Rahmen des Projekts „OMS-Review“ erstellt. Das Ziel des Reviews „*Coordinatively unsaturated metal sites (open metal sites) in metal–organic frameworks: design and applications*“ ist es, anhand der Fachliteratur eine umfangreiche Zusammenfassung über MOFs mit offenen Metallstellen (engl. *open metal sites*, OMS) zu geben.

Abbildung 19 zeigt den schematischen Aufbau des OMS-Reviews.

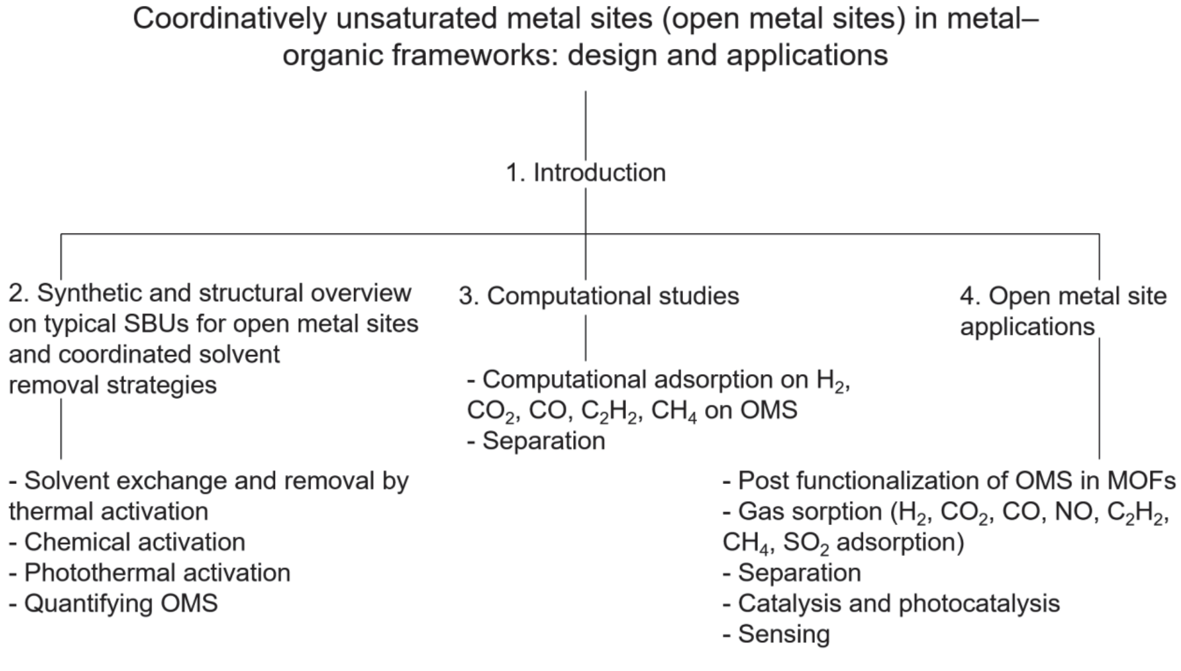

Abbildung 19 Schematische Darstellung des OMS-Review-Aufbaus.

Zu Beginn des Reviews soll eine detaillierte Übersicht der unterschiedlichen Synthesestrategien zur Generierung von OMS-MOFs vorgestellt werden. Im Anschluss sollen die Auswirkungen von offenen Metallstellen auf Wirt-Gast-Wechselwirkung, die in zahlreichen theoretischen Studien in der Fachliteratur thematisiert worden sind, gezeigt werden. Anschließend sollen die verschiedenen potentiellen OMS-MOF Anwendungen dargestellt werden.

Das Ziel dieser Dissertation liegt darin, die folgenden Abschnitte zu verschriftlichen: Einleitung, Kapitel 2 (ausgenommen die SBU bezogenen Abschnitte; Unterabschnitt *Quantifying OMS* in Zusammenarbeit) und Kapitel 4 (*Post functionalization of OMS in MOFs*, H_2 *adsorption*, NO *adsorption*, SO_2 *adsorption*, *Catalysis and photocatalysis*, *Sensing*). Zudem sollen Abbildungen dargestellt und Tabellen angefertigt werden.

3 Kumulativer Teil

In diesem Kapitel werden alle Veröffentlichungen als Erst- und Co-Autorin aufgezeigt.

Das Kapitel 3.1 beinhalt die wesentlichen Ergebnisse dieser Dissertation, die in Form von Veröffentlichungen in internationalen Fachjournalen publiziert wurden. Jede Publikation ist in sich geschlossen und enthält einen einleitenden Teil und ein separates Literaturverzeichnis. Zu den Publikationen werden eine kurze Zusammenfassung und eine Beschreibung der Eigenanteile gegeben. Die Publikationen[205,206] werden in zeitlich chronologischer Reihenfolge aufgezeigt.

In Kapitel 3.2 folgt ein kurzer Einblick in weitere Veröffentlichungen als Co-Autorin. Zu diesen Publikationen werden eine kurze Zusammenfassung und eine Beschreibung der Eigenanteile gegeben. Die Publikationen[207,208,209,210,211,212,213,214,215,216] werden in zeitlich chronologischer Reihenfolge aufgezeigt.

3.1 Veröffentlichungen als Erstautorin

3.1.1 Improving porosity and water uptake of aluminum metal-organic frameworks (Al-MOFs) as graphite oxide (GO) composites

Ülkü Kökçam-Demir, Niels Tannert, Marco Bengsch, Alex Spieß, Carsten Schlüsener, Sandra Nießing, Christoph Janiak*,

Microporous Mesoporous Mater., 2021, **326**, 111352.
DOI: 10.1016/j.micromeso.2021.111352, Referenz [205]

Impact Faktor: 4.157 (2019)

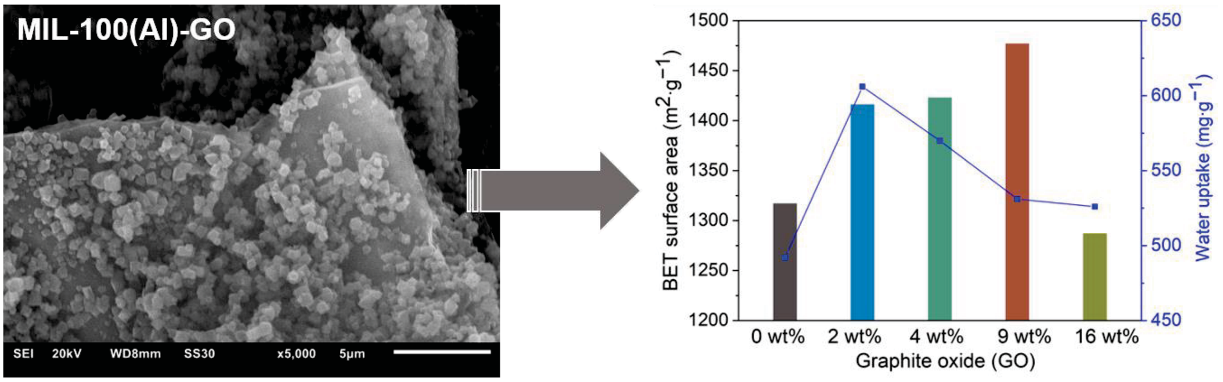

Zusammenfassung

In dieser Arbeit werden Komposite aus zwei Al-basierten Metall-organischen Gerüstverbindungen (Al-MOFs) mit Graphitoxid (GO) vorgestellt. Im Vergleich zu reinen Al-MOFs konnten MIL-100(Al)-GO und CAU-10-H-GO Komposite mit höherer spezifischer Oberfläche und Wasseraufnahme hergestellt werden. Dabei wurden Komposite aus 2 bis 16 Gew.-% GO synthetisiert. Es wird gezeigt, dass das MIL-100(Al)-GO Komposit mit 2 Gew.-% GO eine um 23% erhöhte Wasseraufnahme gegenüber dem reinen MIL-100(Al) aufweist. Des Weiteren wurde eine hydrophile Verschiebung der S-förmigen Wasseraufnahme in CAU-10-H-GO Kompositen beobachtet. Darüber hinaus wird gezeigt, dass die Al-MOF-GO Komposite nach fünf Wasseradsorptions- und Wasserdesorptionszyklen unveränderte Wasseraufnahmen besitzen.

Anteile an der Publikation:

- Die Idee zum Projekt ist in Zusammenarbeit mit Herrn Dr. Niels Tannert und Herrn Prof. Dr. Christoph Janiak entstanden.
- Die Synthesen von MIL-100(Al) und MIL-100(Al)-GO Kompositen wurden eigenständig und die Synthesen von CAU-10-H und CAU-10-H-GO Kompositen wurden von Herrn Marco Bengsch (Bachelorarbeit) durchgeführt. Die Auswertung, Darstellung und Verschriftlichung der Ergebnisse wurden eigenständig vorgenommen.
- Die GO-Synthese wurde von Herrn Dr. Niels Tannert durchgeführt. Die Auswertung, Darstellung und Verschriftlichung der Ergebnisse wurden eigenständig vorgenommen. Die GO-Analyse erfolgte mittels PXRD, IR-Spektroskopie, Stickstoff- und Wassersorption (Marco Bengsch, Bachelorarbeit) und Elementaranalyse (eigenständig). Die Auswertung, Darstellung und Verschriftlichung der Ergebnisse wurden eigenständig vorgenommen.
- Die eigenständige Durchführung, Auswertung, Darstellung und Verschriftlichung der PXRD- und Sorptions-Ergebnisse.
- Die eigenständige Konzipierung, Erstellung der Abbildungen und Tabellen, Aufarbeitung und Verschriftlichung der kompletten experimentellen Ergebnisse und Verschriftlichung der theoretischen Zusammenhänge in Form einer wissenschaftlichen Publikation.
- Die umfassende und eigenständige Literaturrecherche.
- Die REM Untersuchungen wurden von Frau Dr. Sandra Nießing, Herrn Dr. Carsten Schlüsener und Herrn Alex Spieß durchgeführt und dargestellt. Die Auswertung und Verschriftlichung der Ergebnisse wurden eigenständig vorgenommen.
- Im Rahmen ihrer Bachelorarbeit haben Herr Marco Bengsch und Herr Alex Spieß an dem Projekt zeitweise mitgewirkt.

- Die Einreichung in dem internationalen Journal „*Microporous and Mesoporous Materials*“ und finale Überarbeitung des Manuskriptes erfolgten in Zusammenarbeit mit Herrn Prof. Dr. Christoph Janiak.
- Die finale Überarbeitung des Manuskriptes, auch nach der Durchsicht der Gutachter (Revision) und die Anfertigung des Revisionsscheins erfolgten in Zusammenarbeit mit Herrn Prof. Dr. Christoph Janiak.

Microporous and Mesoporous Materials 326 (2021) 111352

Contents lists available at ScienceDirect

Microporous and Mesoporous Materials

journal homepage: www.elsevier.com/locate/micromeso

Improving porosity and water uptake of aluminum metal-organic frameworks (Al-MOFs) as graphite oxide (GO) composites

Ülkü Kökçam-Demir, Niels Tannert, Marco Bengsch, Alex Spieß, Carsten Schlüsener, Sandra Nießing, Christoph Janiak *

Institut für Anorganische Chemie und Strukturchemie, Heinrich-Heine-Universität Düsseldorf, 40204, Düsseldorf, Germany

ARTICLE INFO

Keywords:
Metal-organic frameworks (MOFs)
Graphite oxide
Water sorption
Composite
Aluminum MOFs

ABSTRACT

Composites of the aluminum metal-organic frameworks (Al-MOFs) MIL-100(Al) and CAU-10-H and graphite oxide (GO) have been synthesized (by in-situ MOF formation) with four different GO loadings (from 2 to 16 wt%) for enhanced porosity and water uptake capacity. These composite materials MIL-100(Al)-GO and CAU-10-H-GO were examined by powder X-ray diffraction to show the retention of crystallinity and by scanning electron microscopy to show the retention of the morphology. Nitrogen and water sorption isotherms indicate no loss of mass-weighted surface areas, porosity and uptake capacity. In case of MIL-100(Al)-GO composites, the BET surface areas and porosities from nitrogen sorption data even reveal an increase of 8–12% in surface area with the GO increase from 2 to 9 wt% and an increase of 7–10% in total pore volume with GO loading from 9 to 2 wt %, in comparison to neat MIL-100(Al). In the 2 and 5 wt% CAU-10-H-GO composites, a 4% and 7% increase, respectively, in total pore volume was observed. The water uptake in the MIL-100(Al)-GO composites increased 23% over neat MIL-100(Al) with only 2 wt% GO but dropped again to a small 7% increase upon higher GO loadings up to 16 wt%. To the contrary, in the CAU-10-H-GO composites, the water uptake increases only slightly by 4–6% with 2–8 wt% GO. In particular, the MIL-100(Al)-GO composites showed an increase in the porosities and water uptake due to the synergistic effect from the interaction of MOF and GO with the formation of an additional interface with surface area and void volume. Furthermore, a hydrophilic shift of the water uptake to lower relative pressure $p \cdot p_0^{-1}$ was observed in the 2, 5, 8, 15 wt% CAU-10-H-GO composites. The MOF-GO composites showed essentially unchanged water sorption data after five water ad- and desorption cycles together with retention of crystallinity, morphology and porosity as verified by powder X-ray diffraction, scanning electron microscopy and by nitrogen sorption isotherm analysis, respectively.

1. Introduction

Metal-organic frameworks (MOFs) are infinitely extended coordination networks with metal nodes and bridging organic linkers [1–5]. They are promising candidates for applications such as gas sorption, including gas separation [6] and storage [6–8], catalysis [9–11], heat transformation [12–16].The adsorption performance of MOFs, such as its gas uptake capacity, can be still further improved by formulating them as composites with e.g. polymers [17,18], alumina [19–22], oxides [23], carbon nanotubes [24], functionalized graphite [25], or graphite oxide [26–31]. Graphite oxide (GO) is obtained by the oxidation of graphite [32]. It consists of graphene layers bearing various oxygen groups (carboxyl, hydroxyl, epoxy) on the basal planes and the edges of the layers [33,34]. Due to its hydrophilic character, GO disperses well in water or in some other polar solvents [35]. This carbon-based compound can be used for the preparation of hydrophilic composite materials.

MOF-GO composite materials (see Table S1, SI for a summary of applications) feature enhanced porosity and adsorption capacities of gases (compared to the pristine MOF and GO materials) for example in zinc [36,37], chromium [38,39] and copper [26,40,41]-based MOFs. For example, Elsayed et al. [38] achieved with MIL-101(Cr)-GO composites (2 wt% GO loading) a 10% higher BET surface area and a 22% increase in pore volume. In comparison, Yan et al. [31] reported for MIL-101(Cr)-GO composites (6 wt% GO loading) an approximately 26% higher BET surface area and a 35% increase in pore volume over neat MIL-101(Cr). Chen et al. [42] described an increase in the CO_2 uptake capacity and in the CO_2/CH_4 and CO_2/N_2 adsorption selectivities for MOF-505-GO composites with maximum values at 5 wt% GO loading.

---

* Corresponding author.
E-mail address: Christoph.Janiak@uni-duesseldorf.de (C. Janiak).

https://doi.org/10.1016/j.micromeso.2021.111352
Received 20 May 2021; Received in revised form 5 August 2021; Accepted 7 August 2021
Available online 12 August 2021

Wu et al. [43] synthesized MIL-68(Al)-GO composites for the removal of methyl orange (MO). They also showed that the MIL-68(Al) crystals grow between the planes of GO constructing a sandwich structure, which reflects a chemical interaction between MIL-68(Al) and GO. The composites exhibited better adsorption of MO than did both parent materials [43,44]. Notably, the adsorption performances of the MOF-GO composites are improved at low GO wt%, but higher GO loadings of over 10 wt% tend to have a detrimental effect [26,29,30,33,44,45].

For the MOF-GO composite formation an interaction between the oxygen groups of GO and the metal centers of MOFs at the outer MOF-particle surface is assumed [30]. In addition, hydrogen bonding from the donor hydroxyl groups on the GO to acceptor oxygen atoms in the MOF linker increases the degree of interaction between GO layers and MOF (Fig. S1, SI) [27,45]. In case of cubic MOF-5 and HKUST-1, perpendicular and parallel GO layers can coordinate to the MOF crystallites. Thereby the MOF crystallite can continue to grow in the non-GO-coordinated direction (Fig. S1, SI). In contrast, around the spherical MIL-100(Fe) crystallites, the GO layers coordinate with an angle larger or smaller than 90°. In the latter case, this coordination blocks the growth of the crystallites (Fig. S1, SI).

Water-based adsorption heat pumps (AHPs) and thermally driven adsorption chillers (TDCs) are recently advocated for the integration of MOFs in these applications [12,16,46–48]. AHPs and TDCs use adsorptive heat transformation and are based on the cycling adsorption and desorption of a working fluid at a highly porous substrate (Fig. S2, SI). Water is a desirable working fluid because of its non-harmful nature and large enthalpy change upon evaporation and condensation. MOFs used in AHPs/TDCs must be of extraordinary stability against the cycling sorption of the adsorbate, have an appropriate S-shaped sorption isotherm [47,49–51] and as high as possible adsorbate loading. Al-MOFs fulfill the requirements of stability and S-shaped isotherm [52,53] but their water uptake capacity of 300–400 mg g^{-1} is borderline for the desired application where the material should have an uptake of at least 300 mg g^{-1} [12,16,52,54]. Hence, measures or formulations to improve the water uptake capacity of Al-MOFs would be warranted.

In this work, we report on two Al-MOF-GO composites with the Al-MOFs MIL-100(Al) (MIL = Matériaux de l'Institute Lavoisier) and CAU-10-H (CAU = Christian-Albrechts-University) for improved H_2O adsorption relative to the individual components.

2. Experimental section

2.1. Materials and methods

All materials and solvents were commercially obtained and used without further purification. $AlCl_3 \cdot 6H_2O$ (99%) was purchased from Janssen Chemicals, $Al(NO_3)_3 \cdot 9H_2O$ (98–102%), basic aluminum acetate $Al(OH)(O_2CCH_3)_2 \cdot H_2O$, graphite powder (99%) and isophthalic acid (H_2ipa, 99%) from Alfa Aesar, $Al_2(SO_4)_3 \cdot 18H_2O$ (>98%) from Sigma Aldrich, ethanol (p.a.) and H_2O_2 (30%) from Aldrich and Chemsolute, *N*, *N*′-dimethylformamide (DMF, p.a.) from Fischer Chemical, $KMnO_4$ (99%) from Grüssing GmbH, H_2SO_4 (95–97%) and $NaAlO_2$ (50–56%) from VWR Chemicals, $NaNO_3$ (99%) from PanReac AppliChem, SAPO-34 (silicoaluminiumphosphate) provided by Clarinat and trimesic acid (H_3btc, 98%) from abcr GmbH.

Elemental analyses (CHN) were performed using an Elementar Analysensysteme vario MICRO cube.

Fourier-transform infrared (FT-IR) measurement were carried out on a Bruker Tensor 37 IR spectrometer (Bruker Optics, Ettlingen, Germany) in the range of 4000 to 500 cm^{-1} with an ATR/KBr unit (Platinum ATR-QL, Diamond).

Scanning electron microscopy (SEM) images were acquired on a JEOL JSM-6510LV QSEM advanced electron microscope (Jeol, Akishima, Japan) using a LaB_6 cathode at 5–20 keV. The microscope was equipped with a Bruker XFlash 410 silicon drift detector (Bruker, Billerica, US) for energy-dispersive X-ray spectrometric (EDX) elemental analysis. Additional SEM images were acquired on a ZEISS LEO-1430 VP standard scanning electron microscope (Carl Zeiss AG, Jena, Germany) using a tungsten cathode.

Powder X-ray diffraction (PXRD) patterns were obtained at ambient temperature on a Bruker D2 phaser (Bruker, Billerica, US) using Cu-Kα radiation ($\lambda = 1.54182$ Å) between $5^\circ < 2\theta < 50^\circ$ with a scan rate of 0.1502 down to 0.0142°/s, depending on the desired diffractogram quality (300 W, 30 kV, 10 mA). The diffractograms were obtained on a flat low-background silicon sample holder, for which the beam spot is strongly broadened at low angle so that only a fraction of the reflected radiation reaches the detector, hence the low relative intensities measured at $2\theta < 7^\circ$. The analyses of the diffractograms were carried out with the "Match! 3.3.0" software.

Supercritical drying was carried out using a Leica EM CPD300 – automated critical point dryer which was set to perform 99 exchange cycles of CO_2.

Nitrogen (purity 99.9990%, 5.0) physisorption isotherms were measured on a Nova 4000e from Quantachrome at 77 K within the relative pressure range of $p \cdot p_0^{-1} = 10^{-3}$–1. Before the measurement the samples were degassed under vacuum ($<10^{-2}$ mbar) at 120 °C for approx. 3 h (neat MIL-100(Al)), at 180 °C for approx. 3 h (neat CAU-10-H), at 60 °C for approx. 3 h plus a supercritical drying with CO_2 (99 cycles) (MOF-GO composite). All Brunauer-Emmett-Teller (BET [55]) surface areas were calculated from five adsorption points by applying Roquerol plots (r > 0.998). In this work we designate the surface areas from microporous MOFs which feature Type I isotherms as 'apparent S (BET)' based on the aforementioned reference [55], where it is noted that 'the BET-area derived from a Type I isotherm must not be treated as a realistic probe accessible surface area' but 'represents an apparent surface area, which may be regarded as a useful adsorbent "fingerprint" '. Total pore volumes were calculated from the nitrogen sorption isotherm at $p \cdot p_0^{-1} = 0.95$. Non-local density functional theory (NLDFT) calculations for the pore size distribution curves were done with the native 'NovaWin 11.03' software using the 'N_2 at 77 K on carbon, slit pore, NLDFT equilibrium' model [56–58].

Water sorption isotherms were obtained on a Quantachrome VStar4 device at 293 K within the partial pressure range of $p \cdot p_0^{-1} = 10^{-3}$–0.9. Before measuring of the isotherms, samples were degassed under vacuum ($<10^{-3}$ mbar) at 120 °C for approx. 3 h (neat MIL-100(Al)), at 180 °C for approx. 3 h (neat CAU-10-H), at 60 °C for approx. 3 h (MOF-composite), using a FloVac degasser.

2.2. Synthesis of Al-based MOFs-GO composites

2.2.1. Preparation of GO

GO was synthesized by the Hummers and Offeman method as described in the literature [32], see SI. The resulting dark grey material is referred to as GO. For details see Figs. S3 and S4 and Tables S2, S3, SI.

2.2.2. Preparation of MIL-100(Al)

The microwave-assisted synthesis of MIL-100(Al) is based on the publication of Qiu et al. [59]. The parameters for the microwave synthesis were modified from this literature source. In a 10 mL microwave vessel, 132 mg (0.35 mmol) $Al(NO_3)_3 \cdot 9H_2O$, 61.2 mg (0.29 mmol) trimesic acid (H_3btc) and 3.1 mg (0.05 mmol) SAPO-34 were dissolved in 2 mL of distilled H_2O and stirred for 5 min. Then the reaction vessel was sealed, placed in a microwave reactor (CEM Discover, maximum power 300 W) and heated from room temperature (RT) to 190 °C within a few minutes (instrument operation: power of 150 W; autogenic pressure up to 20 bar). This temperature was maintained for 10 min. After cooling to RT, the as-synthesized product was centrifugated and washed with DMF (3 × 2 mL) and then the solvent was exchanged with ethanol (3 × 2 mL). The resulting material was dried in a vacuum oven at 120 °C for 3 h until a white powder was obtained. For details see Table S4, SI.

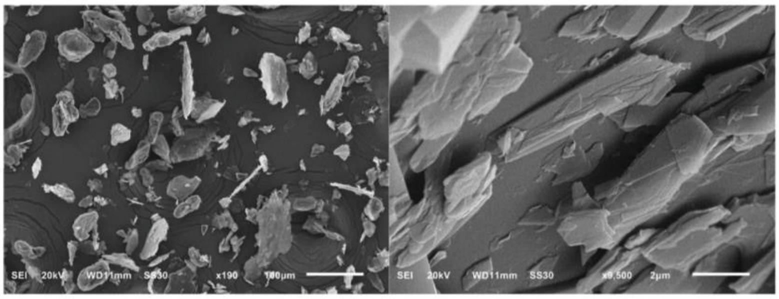

Fig. 1. SEM images of GO sheets at different magnifications.

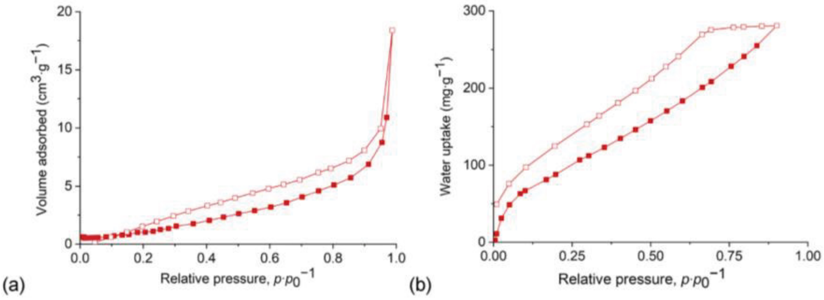

Fig. 2. N_2 (a) and H_2O (b) sorption isotherms of GO (at 77 K and 293 K, respectively).

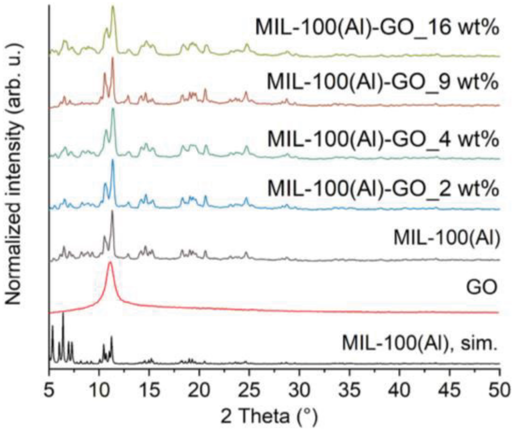

Fig. 3. Powder X-ray diffraction patterns of simulated MIL-100(Al) (CCDC no. 789872, CSD-Refcode BUSPIP) [66], GO, neat MIL-100(Al) and MIL-100(Al)-GO_2, 4, 9, 16 wt% composites. The diffractograms were obtained on a flat "low background sample holder", for which the beam spot is strongly broadened at low angle so that only a fraction of the reflected radiation reaches the detector, hence the low relative intensities measured at 2θ < 7°.

2.2.3. *Preparation of MIL-100(Al)-GO composites*

The MIL-100(Al)-GO composites were synthesized under microwave irradiation method as described before. Hereby, GO (0.35, 1.05, 2, 3.6 mg) was added to the mixture of $Al(NO_3)_3 \cdot 9H_2O$ (132 mg, 0.35 mmol), H_3btc (61.2 mg, 0.29 mmol), SAPO-34 (3.1 mg, 0.05 mmol), and distilled H_2O (2 mL) and stirred at RT for 5 min (in 10 mL microwave vessel). Then the reaction vessel was sealed, placed in a microwave reactor (CEM Discover, maximum power 300 W) and heated from RT to 190 °C within a few minutes (instrument operation: power of 150 W; autogenic pressure up to 20 bar). This temperature was maintained for 10 min. After cooling to RT, the as-synthesized product was centrifugated and washed with DMF (3 × 2 mL) and then the solvent was exchanged with ethanol (3 × 2 mL). The resulting material was dried overnight in a vacuum oven at 60 °C until a light grey powder was obtained. GO (wt%) was calculated as follows: $(mass\ GO)\ /(mass\ MOF - GO) \times 100\%$. The added GO consisted of approx. 2, 4, 9, 16 wt% of the final materials. The resulting samples are referred to as MIL-100(Al)-GO_*x* (*x* = approx. 2, 4, 9, 16 wt%). For details see Scheme S1 and Table S4, SI.

2.2.4. *Preparation of CAU-10-H*

The synthesis of CAU-10-H is based on the publication of Reinsch et al. [60]. $AlCl_3 \cdot 6H_2O$ (482 mg, 2 mmol) and isophthalic acid (H_2ipa) (334 mg, 2 mmol) were reacted in a round bottom flask in distilled H_2O and DMF mixture (4:1, 10 mL) and refluxed at 135 °C for 24 h. After cooling to RT, the as-synthesized product was centrifugated and washed with DMF (40 mL) and then the solvent was exchanged with distilled water (2 × 40 mL). The resulting material was dried overnight in a vacuum oven at 60 °C until a white powder was obtained. For details see Table S5, SI.

2.2.5. *Preparation of CAU-10-H-GO composites*

The CAU-10-H-GO composites were synthesized under reflux. Hereby, GO (7, 20, 33, 66 mg) was added to the mixture of $AlCl_3 \cdot 6H_2O$ (483, 482, 484, 482 mg, 2 mmol), H_2ipa (335, 334, 335, 334 mg, 2 mmol) and distilled H_2O/DMF (10 mL; 4:1) solution. Then the round bottom flask was heated for 24 h at 135 °C under reflux. After cooling to RT, the as-synthesized product was centrifugated and washed with DMF (40 mL) and then the solvent was exchanged with distilled water (2 × 40 mL). The resulting material was dried overnight in a vacuum oven at 60 °C until a light grey powder was obtained. GO (wt%) was calculated

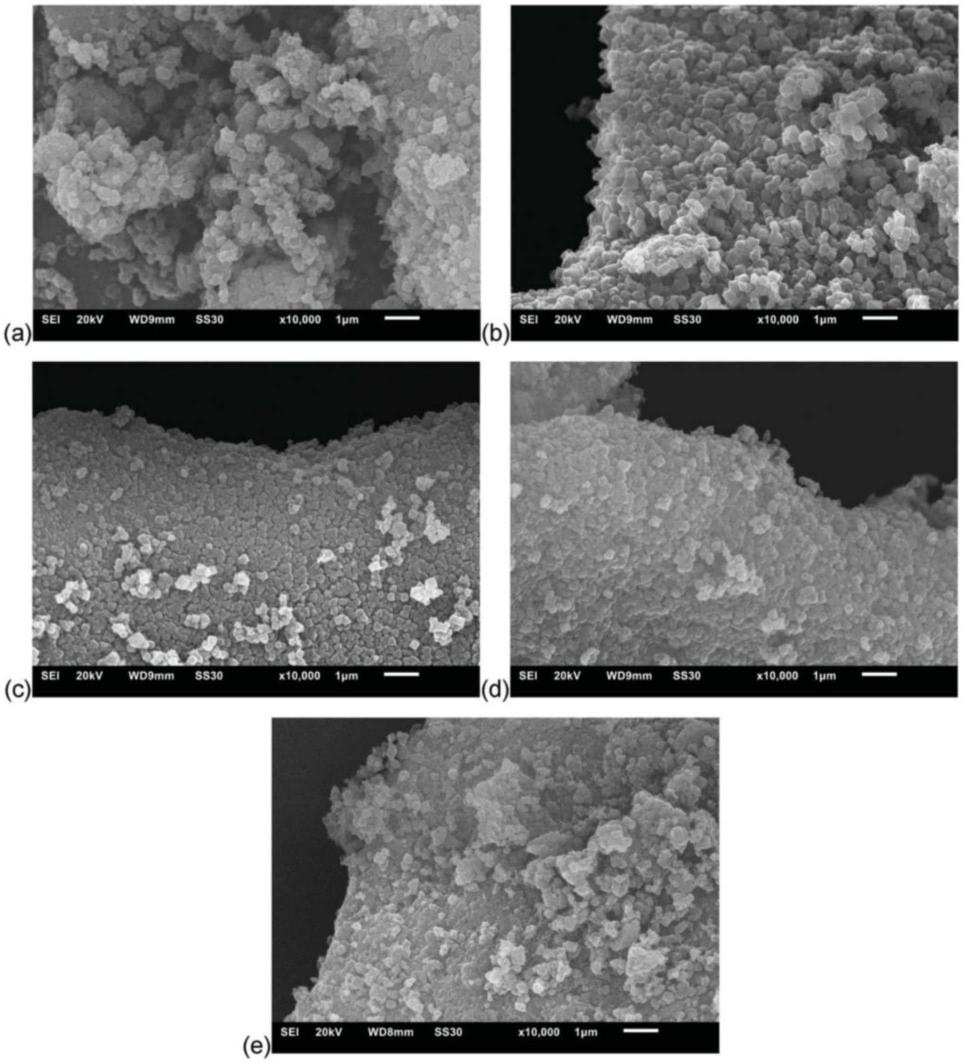

Fig. 4. SEM images of (a) neat MIL-100(Al), (b) MIL-100(Al)-GO_2 wt%, (c) MIL-100(Al)-GO_4 wt%, (d) MIL-100(Al)-GO_9 wt% and (e) MIL-100(Al)-GO_16 wt% (all scale bars 1 μm).

as follows: $(mass\ GO)\ /(mass\ MOF - GO) \times 100\%$. The added GO consisted of approx. 2, 5, 8, 15 wt% of the final materials. The resulting samples are referred to as CAU-10-H-GO_*x* (*x* = approx. 2, 5, 8, 15 wt%). For details see Scheme S2 and Table S5, SI.

3. Results and discussion

3.1. Graphite oxide, GO

Graphite oxide is a non-stoichiometric compound, which consists of planar carbon layers with sp^2 and sp^3 hybridized carbon atoms [26, 61–63]. GO can be generated from graphite by the Hummers and Offeman method [32] through the addition of sodium nitrate, sulfuric acid and potassium permanganate. The oxidation of graphite introduces hydroxyl and epoxy functional groups at the formerly sp^2-hybridized graphite carbon atoms (Fig. S3, SI) [32]. Fig. 1 visualizes the morphology of the GO particles.

GO is thermally relatively unstable [64]. When GO is heated to above 150 °C the functional groups decompose into CO and CO_2 gas which exfoliates the layered GO structure into functionalized (thermally) reduced graphite oxide (TRGO, rGO) (see SI for details) [64,65]. Therefore, the final Al-MOF-GO composites were subsequently activated only at 60 °C for 3 h under vacuum.

GO has low micro- and mesoporosity. A Type III nitrogen adsorption isotherm with a Type H3 hysteresis (Fig. 2a) gives a BET surface area of 8 $m^2\ g^{-1}$. Type H3 loops are given by non-rigid aggregates of plate-like particles and also if the pore network consists of macropores [55]. The water adsorption isotherm (Fig. 2b) shows an uptake of 281 mg g^{-1} with an adsorption isotherm curvature indicative of a moderately hydrophilic meso-to macroporous material [16]. Noteworthy, the water adsorption isotherm at $p \cdot p_0^{-1} = 1$ still has a high positive slope and has not leveled off, which indicates an adsorption curve far from saturation, which will be reached only at higher pressures.

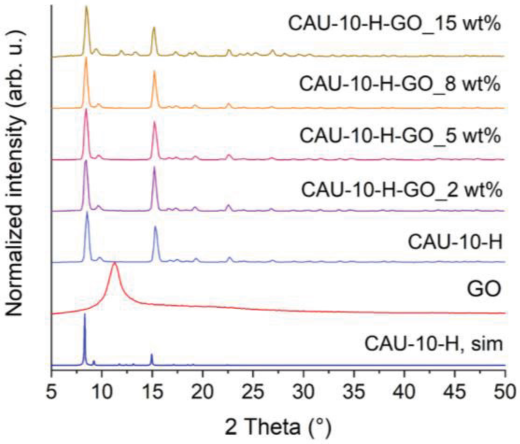

Fig. 5. Powder X-ray difraction patterns of simulated CAU-10-H (CCDC no. 1454066, CSD-Refcode OQOBUT) [67], GO, neat CAU-10-H and CAU-10-H-GO_2, 5, 8, 15 wt% composites. The diffractograms were obtained on a flat "low background sample holder", for which the beam spot is strongly broadened at low angle so that only a fraction of the reflected radiation reaches the detector, hence the lower relative intensities measured at 2θ < 7°.

3.2. MOF-GO composites

The MIL-100(Al)-GO composites were synthesized under microwave irradiation from GO, $Al(NO_3)_3{\cdot}9H_2O$, H_3btc, SAPO-34 and distilled water (see Exp. Section and Scheme S1, SI). From the photographic images in Fig. S6, SI, it can be seen that the colorless MIL-100(Al) and dark-grey GO combined to a grey to dark grey MIL-100(Al)-GO composites depending on the GO fraction. The PXRD patterns of the MIL-100(Al)-GO composite materials (Fig. 3) verify the formation of MIL-100(Al) with identical crystallinity as neat MIL-100(Al). The characteristic broad peak of GO at 2-theta = 11° is not visible in the patterns of the MIL-100(Al)-GO composites due to the low content of GO and the superposition of the relatively weak reflex from amorphous GO with the strong MIL-100(Al) reflections in this 2-theta region.

The SEM images of MIL-100(Al) and MIL-100(Al)-GO composites (Fig. 4, Fig. S7, SI) reveal similar tiny octahedrally-shaped crystals of 0.2–0.5 μm size [59] which for the MIL-100(Al)-GO composites, were grown on top of the GO particles, which can be viewed as a template for MOF crystallization (Fig. S7). Other work found that the hydroxyl, carboxyl, epoxy, ketone groups of GO can coordinate to the metal ions intended for the MOF and thus induce the growth of the MOF crystallites onto the GO layers [27]. It can be noted that the MIL-100(Al) crystallites form a dense layer on the GO which speaks for a powerful seeding action of the GO and a good adhesion of the formed MOF particles to the GO.

The CAU-10-H-GO composites were synthesized under reflux conditions from GO, $AlCl_3{\cdot}6H_2O$, H_2bdc and H_2O/DMF solution (see Exp. Section and Scheme S2, SI). The PXRD patterns of the CAU-10-H-GO composite materials (Fig. 5) indicate the formation of CAU-10-H with a crystallinity identical to neat CAU-10-H. The reflexes were retained unchanged and the characteristic broad peak of GO at 2-theta = 11° (Fig. 5) does not show in the composites, due to their low content of GO and the concomitant low intensity of the broad peak from amorphous GO (cf. Fig. 3).

The SEM images of the CAU-10-H-GO composites indicate that the CAU-10-H crystals were not exclusively grown on top of the GO particles (Fig. 6, Fig. S10, SI). In comparison with the SEM images of the MIL-100(Al)-GO composites it is evident that the GO particles are not densely covered by the CAU-10-H crystallites. A significant amount of CAU-10-H also forms free from GO or does not adhere well and falls off afterwards (Fig. S10, SI). The particle size of the CAU-10-H composites is smaller than that of neat CAU-10-H.

3.2.1. Nitrogen sorption of MOF-GO composites

The isotherms of the composites and neat MIL-100(Al) are largely of Type Ib (Fig. 7) [55] according to the IUPAC (International Union of Pure and Applied Chemistry) classification, with the characteristic step for MIL-100(Al) before $p{\cdot}p_0^{-1} = 0.2$ indicating microporous windows and mesopores (Fig. S5, SI). The increase in gas sorption above $p{\cdot}p_0^{-1} = 0.9$ in a Type II or III branch is due to the filling of interparticle voids (Fig. 4). Among the MIL-100(Al)-GO composites the ones with 2, 4 and 9 wt% GO content had a higher BET surface area and a higher micropore volume than neat MIL-100(Al) which was prepared under the same conditions in this work (Table 1). The total pore volumes for the 2, 4 and 9 wt% MIL-100(Al)-GO composites were also slightly larger than for the MOF itself. Only the composite MIL-100(Al)-GO with 16 wt% GO content shows a lower porosity (Table 1) than neat MIL-100(Al). As GO has a negligible porosity, its content should decrease the porosity in a purely physical mixture. The counterintuitively observed increase in porosity from 2 to 9 wt% GO must be due to the interaction of the MIL and GO with the formation of an additional interface with surface area and void volume at this interface. Also, a composite of MIL-101(Cr)-GO had a higher BET surface area and pore volume compared to the neat MIL-101 sample which was ascribed to new pores formed between the graphene layers and MOF crystallites [69].

The isotherms of the CAU-10-H-GO composites and neat CAU-10-H at low relative pressure are of Type I [55] (Fig. 8), which is indicative of the microporous character. At $p{\cdot}p_0^{-1} > 0.9$ the isotherms show a Type II or Type III behavior [55], which indicates mesopores from interparticle voids. The BET surface areas of the composites CAU-10-H-GO with 2 and 5 wt% GO content appear slightly higher than for neat CAU-10-H but are still within experimental error. The CAU-10-H composites with 8 and 15 wt% GO content exhibit lower porosities than the MOF alone (Table 1). Different from the MIL-100(Al)-GO composites the formation of an interface surface area and pore volume is not evident in the CAU-10-H-GO composites.

3.2.2. H_2O-sorption

Fig. 9 depicts the S-shaped H_2O sorption isotherms of the MIL-100(Al)-GO composites in comparison to neat MIL-100(Al). The characteristic two-step water-sorption isotherm of MIL-100(Al) with the steep and two-step rise is retained in the GO composites. The two-step curvature is due to the consecutive filling of to the two different mesopore sizes, first the 25 Å mesopores and then the 29 Å mesopores. The inflection point between the two pores is at $p{\cdot}p_0^{-1} \approx 0.36$ Fig. 9b) [50]. The composites with 2, 4, 9 and 16 wt% GO content have significantly higher water uptakes at $p{\cdot}p_0^{-1} = 0.5$, immediately after the loading lift, and at $p{\cdot}p_0^{-1} = 0.9$ than neat MIL-100(Al) (Fig. 9, Table 1). However, before $p{\cdot}p_0^{-1} \approx 0.31$ the water uptake of the composites is slightly less than that of neat MIL-100(Al) (Fig. 9b). The water adsorption performance of the MIL-100(Al)-GO composites is improved but most prominently with small GO loadings of 2 and 4 wt%, whereas for higher GO loadings of 9 and 16 wt% the improvement is less prominent and water uptake approaches the one of the neat MIL-100(Al) again. The PXRD patterns (Fig. S9, SI) and SEM images (Fig. S10, SI) indicate that the MIL-100(Al)-GO composites were unchanged after water sorption.

Over the interesting uptake region starting from $p{\cdot}p_0^{-1} = 0.25$ GO takes up less water (due to its low porosity) than MIIL-100(Al) (Fig. 2, Fig. S8, SI). Hence, if one would estimate the water loading for a purely physical mixture as the sum of the mass-weighted vapor uptakes of MIL-100(Al) and GO such a physical mixture should have a lower water uptake than the neat MIL until $p{\cdot}p_0^{-1} = 0.9$. In the literature the adsorption of water vapor by MIL-101(Cr)-GO [31] and CO_2 by MOF-505-GO composites [42] was found to be enhanced over the neat MOFs. As was already seen for the porosity from N_2 sorption there is a synergistic effect from the interaction of the MOF with GO which

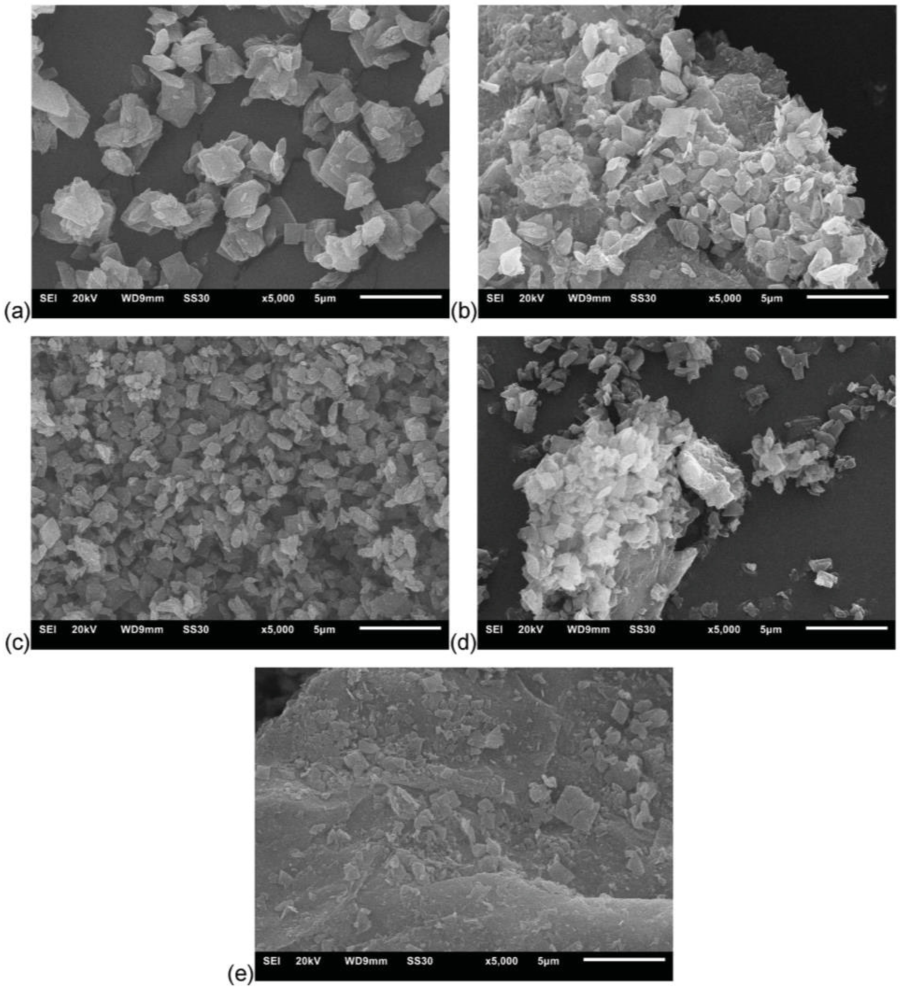

Fig. 6. SEM images of (a) neat CAU-10-H, (b) CAU-10-H-GO_2 wt%, (c) CAU-10-H-GO_5 wt%, (d) CAU-10-H-GO_8 wt% and (e) CAU-10-H-GO_15 wt% (all scale bars 5 μm).

amounts to additional pore volume available for water sorption above $p\cdot p_0^{-1} \approx 0.31$. Together the increase in porosity (by BET surface areas and pore volumes, see above) and water uptake of the MIL-100(Al)-GO composites can be reasoned by the apparently good interaction of MIL-100(Al) and GO without pore-blocking phenomena.

To analyze the effect of cycling water sorption on the MIL-100(Al)-GO composites, five water ad- and desorption cycles were performed using especially MIL-100(Al)-GO_2 and 4 wt% as examples. The water uptake values at $p\cdot p_0^{-1} = 0.5$ and 0.9 are the same within experimental error before and after the cycling (Fig. S13, Table S5). There is a slight increase in water uptake at $p\cdot p_0^{-1} = 0.3$ which may be attributed to hydrophilic sites becoming available, possibly due to very slight changes in the MOF structure, even if not reflected in the PXRD patterns (Fig. S11, SI), SEM (Fig. S12, SI) and N_2 sorption data (Table S5, SI) which remain rather identical. Only in case of MIL-100(Al)-GO_2 wt%, the BET surface area from nitrogen sorption data shows a positive increase of 12% after water sorption cycling. Hence, cycling water sorption may also have removed residual DMF or ethanol solvent from the synthesis.

Fig. 10 shows the S-shaped H_2O sorption isotherms of the CAU-10-H-GO composites in comparison to neat CAU-10-H. The curvature of the neat MOF is well retained in the composites. All isotherms exhibit a steep increase at $0.14 < p\cdot p_0^{-1} < 0.19$. The low hysteresis confirms the microporosity of the composites [55]. The composites with 2, 5, 8 wt% GO content have only very slightly higher water uptakes at $p\cdot p_0^{-1} = 0.9$, essentially still within experimental error to neat CAU-10-H (Table 1). Only the composite with 15 wt% GO content has again a significantly lower value (275 $m^2\ g^{-1}$) than neat CAU-10-H. Interestingly, the presence of GO shifts the steep increase in the S-shaped water adsorption isotherm from $p\cdot p_0^{-1} = \sim 0.17$ for neat CAU-10-H to $p\cdot p_0^{-1} = \sim 0.15$ with 2–15 wt% GO content. Consequently, the water uptake at $p\cdot p_0^{-1} = 0.15$ of these composites is significantly higher than that of neat CAU-10-H (Fig. 10b). Further, the steep water uptake of these composites is already mostly finished at $p\cdot p_0^{-1} = \sim 0.16$ before the uptake of neat CAU-10-H had even significantly started. The hydrophilic shift of the water uptake to lower relative pressure $p\cdot p_0^{-1}$ in the composites with 2–15 wt% GO content, compared to the neat MOF can be reasoned through the higher GO hydrophilicity in the low relative pressure region (Fig. S11, SI). Other than the small hydrophilic shift to slightly lower relative pressure there was no significant enhancement effect (also not

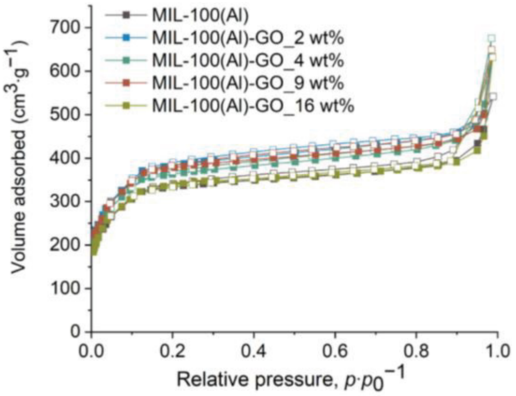

Fig. 7. N_2 sorption isotherms of neat MIL-100(Al) and MIL-100(Al)-GO_2, 4, 9, 16 wt% composites (at 77 K). Adsorption is depicted with filled, desorption with empty symbols.

for the porosity, see above) through the composite formation of the MOF CAU-10-H with GO. At present, possible amplification effects of MOF-GO composites cannot be predicted or necessarily expected. On the other hand, GO did not exert a negative effect, that is, no pore blocking on the MOF part.

Cycling water sorption on the CAU-10-H-GO composites was performed with the examples CAU-10-H-GO_2 and 5 wt%. Again, the water uptake values remain essentially identical after five water ad- and desorption cycling, except for a slight decrease at $p \cdot p_0^{-1} = 0.5$ for the 2 wt% composite (Fig. S21, Table S7, SI). After single and cycling water sorption (Fig. S17 and S19, SI), the PXRD patterns for the CAU-10-H-GO composites exhibit additional weak reflections which are due to residual water in the hydrophilic MOF, which was not dried before the PXRD measurements. The BET surface area from nitrogen sorption data remains within experimental error, which can be around ±50 m^2 g^{-1} (Table S7, SI), however the curvature of the N_2 sorption isotherms after five water sorption cycles indicate additional mesoporosity, which is also reflected in an increased total pore volume. It is suggested that repeated water sorption enhances the interface or void volume between CAU-10-H and GO.

Table 1
Results from N_2 and H_2O sorption measurements of MIL-100(Al)-GO and CAU-10-H-GO composites.

Sample[a]	S (BET) (m^2•g^{-1})[b]	$V_{pore(total)}$ (cm^3•g^{-1})[c]	$V_{pore(micro)}$ (cm^3•g^{-1})[d]	Water uptake (mg•g^{-1}) at $p \cdot p_0^{-1}$ =		
				0.1/ 0.3	0.5	0.9
GO	8	0.01	–	67/ 112	158	281
				0.3	**0.5**	**0.9**
MIL-100 (Al) Lit.	1576 [59]	n/a [59]	n/a [59]	≤200 [50]	≤400 [50]	500 [12, 50]
MIL-100 (Al)	1317	0.67	0.44	273	429	492
MIL-100 (Al)-GO_2	1416	0.74	0.49	234	543	606
MIL-100 (Al)-GO_4	1423	0.73	0.46	268	503	570
MIL-100 (Al)-GO_9	1477	0.72	0.49	211	465	531
MIL-100 (Al)-GO_16	1287	0.65	0.46	213	458	526
				0.15	**0.3**	**0.9**
CAU-10-H Lit.	635 [60]	n/a [60]	0.25[e] [60]	≤5 [68]	≤270 [68]	340 [67, 68]
CAU-10-H	666	0.28	0.24	8	275	331
CAU-10-H-GO_2	671	0.29	0.23	181	278	345
CAU-10-H-GO_5	689	0.30	0.24	83	260	350
CAU-10-H-GO_8	589	0.28	0.20	146	255	345
CAU-10-H-GO_15	564	0.26	0.19	127	219	272

All values are rounded.

[a] In MIL-100(Al)-GO_*x* or CAU-10-H-GO_*x* "*x*" refers to the wt% of GO in the composite (see Exp. Section). For example, MIL-100(Al)-GO_2 has 2 wt% loading of GO in the composite.

[b] Apparent *S*(BET) values were determined from N_2 sorption isotherms at 77 K. *S*(BET) were obtained from five adsorption points in the pressure range of $0.04 < p \cdot p_0^{-1} < 0.1$ for MIL-100(Al), $0.01 < p \cdot p_0^{-1} < 0.4$ for MIL-100(Al)-GO_*x* composites, $0.01 < p \cdot p_0^{-1} < 0.02$ for CAU-10-H and $0.01 < p \cdot p_0^{-1} < 0.4$ for CAU-10-H-GO_*x* composites.

[c] Total pore volume, $V_{pore(total)}$ calculated from N_2 sorption isotherm at 77 K ($p \cdot p_0^{-1} = 0.95$ for MIL-100(Al) corresponding composites, and $p \cdot p_0^{-1} = 0.90$ for CAU-10-H and corresponding composites) for pores ≤ 20 nm.

[d] Micropore volume, $V_{pore(micro)}$ refers to the volume that originates only from micropores, obtained by the $V-t$ method with thickness method "DeBoer" in the range of $0.2 < p \cdot p_0^{-1} < 0.4$ for MIL-100(Al), MIL-100(Al)-GO_*x* composites, CAU-10-H and CAU-10-H-GO_*x*. All correlation coefficients (*r*) within calculations were ≥0.999.

[e] Micropore volume determined by single point calculation at $p \cdot p_0^{-1} = 0.5$.

4. Conclusions

In this work, two novel MIL-100(Al)-GO and CAU-10-H-GO composites with graphite oxide (GO) contents from 2 to 16 wt% were prepared with in-situ MOF synthesis from the metal salts and linker in the presence of preformed GO under microwave irradiation (MIL-100(Al) and composites) and under reflux conditions (CAU-10-H and composites). Due to the good interaction of MIL-100(Al) and GO, the MIL-100 (Al)-GO composites largely showed an increase in adsorption capacity of nitrogen, in BET surface areas and (micro-)pore volumes and increased water uptakes. For the MOF CAU-10-H an effect of compounding with GO in terms of improved porosity and enhanced water uptake is minimal and hardly visible. Most prominently for the CAU-10-H-GO composites was a hydrophilic shift to slightly lower relative pressure $p \cdot p_0^{-1}$ of ~0.15 for the steep water uptake of the S-shaped isotherm compared to neat CAU-10-H with $p \cdot p_0^{-1}$ of ~0.17. Thus, an effect of GO on MOF porosity or sorption behavior cannot be generalized or predicted beforehand. MOF seeding and crystallite growth on the GO surface together with good MOF adhesion is suggested as crucial for a positive synergistic effect. Formation of an interface surface area, an interface volume and additional interparticle porosity is further suggested as the basis of a positive synergistic effect with enhanced porosity and guest uptake. Furthermore, the exemplifying MIL-100(Al)-GO_2 and 4 wt% as well as CAU-10-H-GO_2 and 5 wt% composites exhibit unchanged water uptakes without performance loss over more than five water ad- and desorption cycles.

Credit authorship contribution statement

Ülkü Kökçam-Demir: performed the experiments, collected and interpreted the data, wrote and revised the manuscript, outlined the idea together. **Niels Tannert:** carried out preliminary experiments, outlined

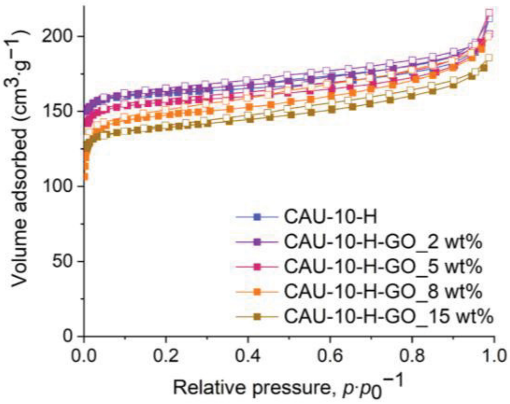

Fig. 8. N_2 sorption isotherms of neat CAU-10-H and CAU-10-H-GO_2, 5, 8, 15 wt% composites (at 77 K). Adsorption is depicted with filled, desorption with empty symbols.

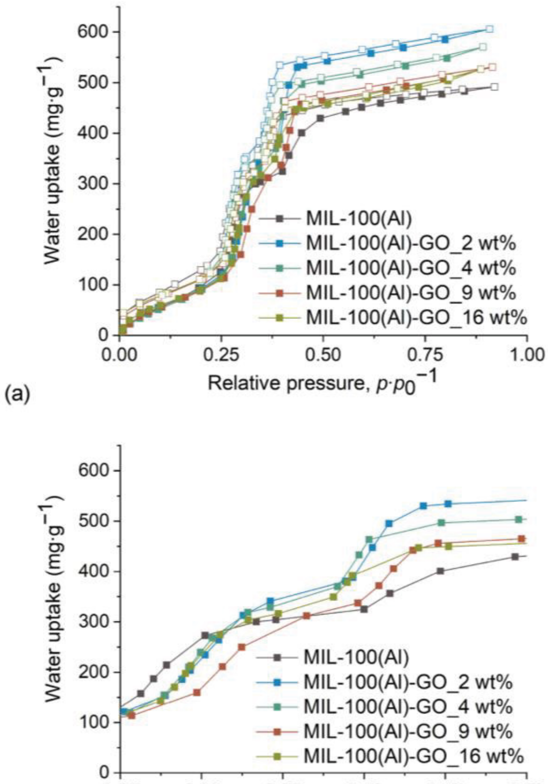

Fig. 9. Water sorption isotherms of neat MIL-100(Al) and MIL-100(Al)-GO_2, 4, 9, 16 wt% composites (at 293 K). Adsorption is depicted with filled, desorption with empty symbols. (a) Full region from $p \cdot p_0^{-1} = 0$–1, (b) expanded adsorption region from $p \cdot p_0^{-1} = 0.25$–0.5 (for clarity, only the adsorption isotherms are shown).

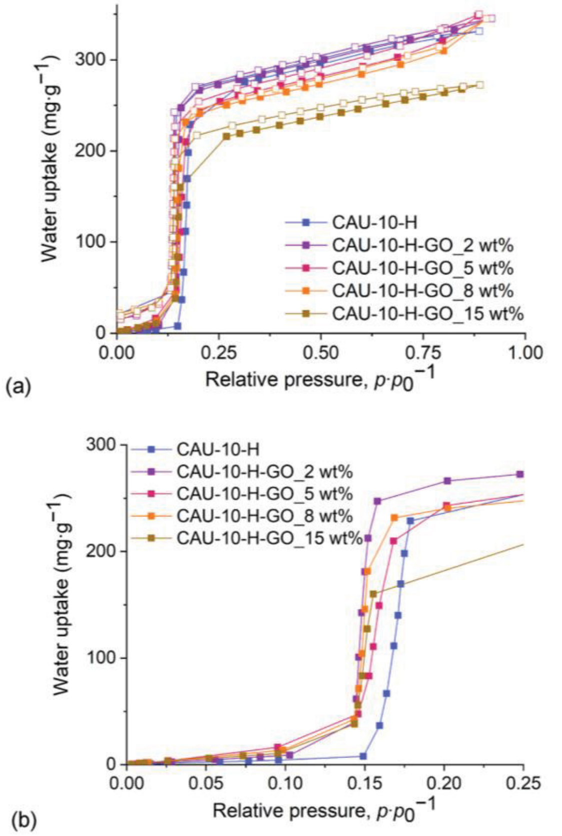

Fig. 10. Water sorption isotherms of neat CAU-10-H and CAU-10-H-GO_2, 5, 8, 15 wt% composites (at 293 K). Adsorption is depicted with filled, desorption with empty symbols. (a) Full region from $p \cdot p_0^{-1} = 0$–1, (b) expanded adsorption region from $p \cdot p_0^{-1} = 0.25$–0.5 (for clarity, only the adsorption isotherms are shown).

the idea together. **Marco Bengsch:** carried out preliminary experiments. **Alex Spieß:** collected the SEM images. **Carsten Schlüsener:** collected the SEM images. **Sandra Nießing:** collected the SEM images. **Christoph Janiak:** outlined the idea together.

Declaration of competing interest

The authors declare that they have no known competing financial interests or personal relationships that could have appeared to influence the work reported in this paper.

Acknowledgement

The authors gratefully acknowledge the financial support of the Federal German Ministry of Education and Research (BMBF) in the project Optimat under grant no. 03SF0492C.

Appendix A. Supplementary data

Supplementary data to this article can be found online at https://doi.org/10.1016/j.micromeso.2021.111352.

References

[1] S.R. Batten, N.R. Champness, X.-M. Chen, J. Garcia-Martinez, S. Kitagawa, L. Öhrström, M. O'Keeffe, M.P. Suh, J. Reedijk, Pure Appl. Chem. 85 (2013) 1715–1724.
[2] C. Janiak, J.K. Vieth, New J. Chem. 34 (2010) 2366–2388.
[3] C. Janiak, Dalton Trans. (2003) 2781–2804.
[4] H. Furukawa, N. Ko, Y.B. Go, N. Aratani, S.B. Choi, E. Choi, A.Ö. Yazaydin, R. Q. Snurr, M. O'Keeffe, J. Kim, O.M. Yaghi, Science 329 (2010) 424–428.
[5] O.K. Farha, A.Ö. Yazaydin, I. Eryazici, C.D. Malliakas, B.G. Hauser, M. G. Kanatzidis, S.T. Nguyen, R.Q. Snurr, J.T. Hupp, Nat. Chem. 2 (2010) 944–948.
[6] A.U. Czaja, N. Trukhan, U. Müller, Chem. Soc. Rev. 38 (2009) 1284–1293.
[7] J. Dechnik, J. Gascon, C.J. Doonan, C. Janiak, C.J. Sumby, Angew. Chem. Int. Ed. 56 (2017) 9292–9310.
[8] B. Li, H.-M. Wen, W. Zhou, B. Chen, J. Phys. Chem. Lett. 5 (2014) 3468–3479.
[9] J.Y. Lee, O.K. Farha, J. Roberts, K.A. Scheidt, S.T. Nguyen, J.T. Hupp, Chem. Soc. Rev. 38 (2009) 1450–1459.
[10] Y.-B. Huang, J. Liang, X.-S. Wang, R. Cao, Chem. Soc. Rev. 46 (2017) 126–157.
[11] A. Herbst, C. Janiak, CrystEngComm 19 (2017) 4092–4117.
[12] F. Jeremias, D. Fröhlich, C. Janiak, S.K. Henninger, New J. Chem. 38 (2014) 1846–1852.
[13] X. Liu, X. Wang, F. Kapteijn, Chem. Rev. 120 (2020) 8303–8377.
[14] C. Janiak, S.K. Henninger, Chimia 67 (2013) 419–424.
[15] S.K. Henninger, F.P. Schmidt, H.-M. Henning, Appl. Therm. Eng. 30 (2010) 1692–1702.
[16] D.M. Steinert, S.-J. Ernst, S.K. Henninger, C. Janiak, Eur. J. Inorg. Chem. (2020) 4502–4515.
[17] L.D. O'Neill, H. Zhang, D. Bradshaw, J. Mater. Chem. 20 (2010) 5720–5726.
[18] M.D. Rowe, D.H. Thamm, S.L. Kraft, S.G. Boyes, Biomacromolecules 10 (2009) 983–993.
[19] M. Arnold, P. Kortunov, D.J. Jones, Y. Nedellec, J. Kärger, J. Caro, Eur. J. Inorg. Chem. (2007) 60–64.
[20] J. Gascon, S. Aguado, F. Kapteijn, Microporous Mesoporous Mater. 113 (2008) 132–138.
[21] Y. Liu, Z. Ng, E.A. Khan, H.-K. Jeong, C.-B. Ching, Z. Lai, Microporous Mesoporous Mater. 118 (2009) 296–301.
[22] Y. Yoo, H.-K. Jeong, Chem. Commun. (2008) 2441–2443.
[23] S. Hermes, D. Zacher, A. Baunemann, C. Wöll, R.A. Fischer, Chem. Mater. 19 (2007) 2168–2173.
[24] S.J. Yang, J.Y. Choi, H.K. Chae, J.H. Cho, K.S. Nahm, C.R. Park, Chem. Mater. 21 (2009) 1893–1897.
[25] M. Jahan, Q. Bao, J.-X. Yang, K.P. Loh, J. Am. Chem. Soc. 132 (2010) 14487–14495.
[26] C. Petit, B. Mendoza, T.J. Bandosz, ChemPhysChem 11 (2010) 3678–3684.
[27] C. Petit, T.J. Bandosz, Adv. Funct. Mater. 21 (2011) 2108–2117.
[28] C. Petit, T.J. Bandosz, Dalton Trans. 41 (2012) 4027–4035.
[29] D. Bradshaw, A. Garai, J. Huo, Chem. Soc. Rev. 41 (2012) 2344–2381.
[30] I. Ahmed, S.H. Jhung, Mater. Today 17 (2014) 136–146.
[31] J. Yan, Y. Yu, C. Ma, J. Xiao, Q. Xia, Y. Li, Z. Li, Appl. Therm. Eng. 84 (2015) 118–125.
[32] W.S. Hummers, R.E. Offeman, J. Am. Chem. Soc. 80 (1958) 1339.
[33] X. Liu, H. Zhou, Y. Zhang, Y. Liu, A. Yuan, Chin. J. Chem. 30 (2012) 2563–2566.
[34] O.C. Compton, S.T. Nguyen, Small 6 (2010) 711–723.
[35] S. Park, J. An, I. Jung, R.D. Piner, S.J. An, X. Li, A. Velamakanni, R.S. Ruoff, Nano Lett. 9 (2009) 1593–1597.
[36] Y. Zhao, H. Ding, Q. Zhong, Appl. Surf. Sci. 284 (2013) 138–144.
[37] C. Petit, T.J. Bandosz, Adv. Funct. Mater. 20 (2010) 111–118.
[38] E. Elsayed, H. Wang, P.A. Anderson, R. Al-Dadah, S. Mahmoud, H. Navarro, Y. Ding, J. Bowen, Microporous Mesoporous Mater. 244 (2017) 180–191.
[39] I. Ahmed, N.A. Khan, S.H. Jhung, Inorg. Chem. 52 (2013) 14155–14161.
[40] C. Petit, T.L. Huang, J. Jagiello, J. Kenvin, K.E. Gubbins, T.J. Bandosz, Langmuir 27 (2011) 13043–13051.
[41] Y. Li, J. Miao, X. Sun, J. Xiao, Y. Li, H. Wang, Q. Xia, Z. Li, Chem. Eng. J. 298 (2016) 191–197.
[42] Y. Chen, D. Lv, J. Wu, J. Xiao, H. Xi, Q. Xia, Z. Li, Chem. Eng. J. 308 (2017) 1065–1072.
[43] S.-C. Wu, L.-L. Yu, F.-F. Xiao, X. You, C. Yang, J.-H. Cheng, J. Alloys Compd. 724 (2017) 625–632.
[44] Y. Zheng, S. Zheng, H. Xue, H. Pang, Adv. Funct. Mater. 28 (2018) 1804950.
[45] C. Petit, T.J. Bandosz, Adv. Mater. 21 (2009) 4753–4757.
[46] M.F. de Lange, K.J.F.M. Verouden, T.J.H. Vlugt, J. Gascon, F. Kapteijn, Chem. Rev. 115 (2015) 12205–12250.
[47] E. Hastürk, S.-J. Ernst, C. Janiak, Curr. Opinion Chem. Eng. 24 (2019) 26–36.
[48] S. Gökpinar, S.-J. Ernst, E. Hastürk, M. Möllers, I. El Aita, R. Wiedey, N. Tannert, S. Nießing, S. Abdpour, A. Schmitz, J. Quodbach, G. Füldner, S.K. Henninger, C. Janiak, Ind. Eng. Chem. Res. 58 (2019) 21493–21503.
[49] Y.I. Aristov, Appl. Therm. Eng. 50 (2013) 1610–1618.
[50] F. Jeremias, A. Khutia, S.K. Henninger, C. Janiak, J. Mater. Chem. 22 (2012) 10148–10151.
[51] C. Schlüsener, M. Xhinovci, S.-J. Ernst, A. Schmitz, N. Tannert, C. Janiak, Chem. Mater. 31 (2019) 4051–4062.
[52] N. Tannert, C. Jansen, S. Nießing, C. Janiak, Dalton Trans. 48 (2019) 2967–2976.
[53] C. Schlüsener, D.N. Jordan, M. Xhinovci, T.J. Matemb Ma Ntep, A. Schmitz, B. Giesen, C. Janiak, Dalton Trans. 49 (2020) 7373–7383.
[54] A. Khutia, H.U. Rammelberg, T. Schmidt, S.K. Henninger, C. Janiak, Chem. Mater. 25 (2013) 790–798.
[55] M. Thommes, K. Kaneko, A.V. Neimark, J.P. Olivier, F. Rodriguez-Reinoso, J. Rouquerol, K.S. Sing, Pure Appl. Chem. 87 (2015) 1051–1069.
[56] A. Vishnyakov, P. Ravikovitch, A.V. Neimark, Langmuir 16 (2000) 2311–2320.
[57] L.D. Gelb, K.E. Gubbins, R. Radhakrsihan, M. Sliwinska-Bartowiak, Rep. Prog. Phys. 62 (1999) 1573–1659.
[58] N.A. Sedron, J.P.R.B. Walton, N. Quirke, Carbon 27 (1989) 853–861.
[59] M. Qiu, Q. Guan, W. Li, Cryst. Growth Des. 16 (2016) 3639–3646.
[60] H. Reinsch, M.A. van der Veen, B. Gil, B. Marszalek, T. Verbiest, D. de Vos, N. Stock, Chem. Mater. 25 (2013) 17–26.
[61] F. Barroso-Bujans, S. Cerveny, A. Alegría, J. Colmenero, Carbon 48 (2010) 3277–3286.
[62] A. Buchsteiner, A. Lerf, J. Pieper, J. Phys. Chem. B 110 (2006) 22328–22338.
[63] B. Kartick, S.K. Srivastava, J. Nanosci. Nanotechnol. 11 (2011) 8586–8592.
[64] E. Tegou, G. Pseiropoulos, M.K. Filippidou, S. Chatzandroulis, Microelectron. Eng. 159 (2016) 146–150.
[65] D.R. Dreyer, S. Park, C.W. Bielawski, R.S. Ruoff, Chem. Soc. Rev. 39 (2010) 228–240.
[66] C. Volkringer, D. Popov, T. Loiseau, G. Férey, M. Burghammer, C. Riekel, M. Haouas, F. Taulelle, Chem. Mater. 21 (2009) 5695–5697.
[67] D. Fröhlich, E. Pantatosaki, P.D. Kolokathis, K. Markey, H. Reinsch, M. Baumgartner, M.A. van der Veen, D.E. De Vos, N. Stock, G.K. Papadopoulos, J. Mater. Chem. A 4 (2016) 11859–11869.
[68] D. Fröhlich, S.K. Henninger, C. Janiak, Dalton Trans. 43 (2014) 15300–15304.
[69] X. Zhou, W. Huang, J. Miao, Q. Xia, Z. Zhang, H. Wang, Z. Li, Chem. Eng. J. 266 (2015) 339–344.

Supporting Information

Improving porosity and water uptake of aluminum metal-organic frameworks (Al-MOFs) as graphite oxide (GO) composites

Ülkü Kökçam-Demir, Niels Tannert, Marco Bengsch, Alex Spieß, Carsten Schlüsener, Sandra Nießing, Christoph Janiak*

Institut für Anorganische Chemie und Strukturchemie, Heinrich-Heine-Universität Düsseldorf, 40204 Düsseldorf, Germany. E-Mail: Christoph.Janiak@uni-duesseldorf.de

Email addresses:
Uelkue.Koekcam@uni-duesseldorf.de, Tannert@hhu.de, Marco.Bengsch@uni-duesseldorf.de, Alex.Spiess@hhu.de, Carsten.Schluesener@uni-duesseldorf.de, Sandra.Niessing@uni-duesseldorf.de

Table S1. MOFs-graphite oxide composite materials with applications.

Application	MOF-GO	MOF-rGO*	MOF-aminated GO	MOF-exfoliated graphene
Batteries	MIL-101(Cr): lithium ion battery [1]	MIL-101(Cr): lithium sulfur battery [2]		
Gas separation / storage	HKUST-1: H_2 adsorption [3,4], CO_2 adsorption [5,6,7,8], H_2S adsorption [9,10], NH_3 adsorption [11,12], CO_2/N_2 separation [13] MIL-53(Cr): CO_2/CH_4 separation [14] MIL-101(Cr): CO_2, CH_4, methyl mercaptane adsorption [15], acetone adsorption [16], adsorption of n-alkanes [17], adsorption of n-hexane [18], CO_2/CH_4 separation [19] MOF-5: CO_2 adsorption [20], H_2S adsorption [21], NH_3 adsorption [22,23] UiO-66: CO_2 adsorption [24,25], H_2/CH_4 and CO_2/CH_4 separation [26] ZIF-8: H_2 storage [27,28]	Zr-MOF: H_2 storage [29]	HKUST-1: CO_2 adsorption [30] MOF-5: CO_2 adsorption [20]	MIL-101(Fe): H_2O adsorption [31]
Photo- / Catalysis	Cu-MOF: catalysts [32] MIL-88(Fe): photocatalysts [33] MIL-88B(Fe): photocatalysts [34] MIL-101(Fe): catalysts [35,36]	MIL-53(Fe): photocatalysts [37,38] MIL-125(Ti): photocatalysts [39]		
Sensing / Chemical Sensors	Cu-tpa: electrochemical sensor [40] HKUST-1: electrochemical sensor [41] ZIF-8: electrochemical sensor [42]	Co-and Cd-based MOFs: lithium / sodium ion batteries [43] HKUST-1: electrochemical nitrite sensor [44]		
Super-capacitors		HKUST-1: supercapacitor electrode material [44]		
Water purification (Removal of in-/organic pollutants	Cu-tpa: adsorption of toxic metal ion [45] HKUST-1: adsorption of organic dye pollutants [46] MIL-68(Al): adsorption of dye (methyl orange) [47] MIL-68(In): adsorption of dye (rhodamine B) [48] MIL-101(Fe): adsorption of organic dyes [49] Ni-MOF: adsorption of dye (Congo red) [50] UiO-66: water purification [51] ZIF-8: adsorption of dye (malachite green) [52]	MIL-68(Al): adsorption of dye (p-nitrophenol) [53]		

* rGO: reduced GO

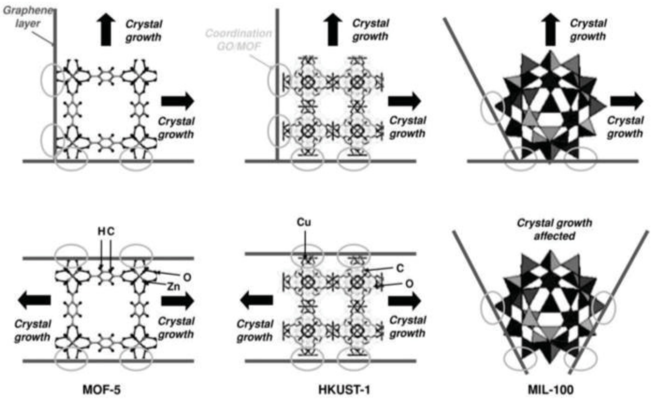

Figure S1. Schematic comparison of the coordination between GO layers to MOF crystallites for e.g. cubic MOF-5, cubic HKUST-1 and spherical MIL-100(Fe). Reprinted from ref. [22] with permission from Wiley-VCH Verlag GmbH & Co. KGaA, Weinheim, copyright 2011.

Principle of heat transformation processes in adsorption heat pumps (AHPs) and thermally driven adsorption chillers (TDCs)

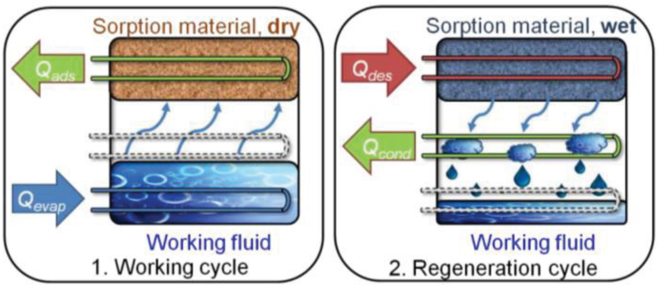

Figure S2. In the working cycle, a working fluid (favorably water due to its high evaporation enthalpy and nontoxicity) is evaporated at a low pressure, taking up evaporation heat Q_{evap}. During incorporation into a porous material, heat of adsorption Q_{ads} is released. In the regeneration cycle, driving heat Q_{des} for desorption is applied, and further condensation takes place at a medium temperature level and releases condensation heat Q_{cond}. Depending on the operation direction, the device can be used as a chiller or a heat pump. Reprinted from ref. [54] with permission from the author. The Royal Society of Chemistry, copyright 2012.

Graphite Oxide (GO)

Preparation: The synthesis of graphite oxide is based on the publication of Hummers et al. [55]. Hereby, graphite powder (5.0 g) and sodium nitrate ($NaNO_3$, 5.0 g) were dispersed in sulfuric acid (H_2SO_4, >230 mL). The suspension was stirred and cooled to 0 °C in an ice bath. Then, potassium permanganate ($KMnO_4$, 30.1 g) was slowly added to the suspension over a time of 30 min. After 60 min stirred in an ice bath, the suspension was stirred for 48 h at room temperature. At the end of the time, deionized water (1500 mL) and hydrogen peroxide (H_2O_2, 120 mL) were added and further stirred overnight. The mixture was separated by centrifugation. After several time washing with water (5x), centrifugations (5x) and Soxhlet extraction with water the resulting material was obtained.

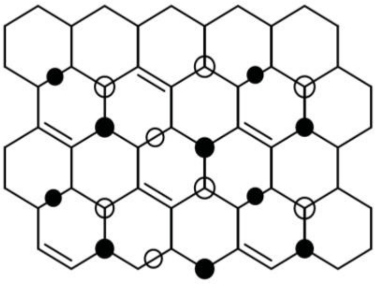

Figure S3. Structure of a single layer of GO. The carbon atoms are arranged as six-membered rings as in graphite. The hydroxy groups are represented as circles on the corners and the epoxy groups as circles on the edges of the six-membered rings. The filled (hollow) circles represent groups that are situated above (below) the carbon layer. Reproduced from ref. [56] with permission from the American Chemical Society, copyright 2006.

The oxygen groups in GO can significantly affect the van der Waals interactions between the graphene layers [57]. Buchsteiner et al. [56] reported that three different distances are known between the layers of GO: 5.5–5.6 Å resulting from Brodie's procedure [58] (carbon content 62 wt%), 6.3–6.5 Å resulting from Staudenmaier's procedure [59] (52 wt%) and 6.7–6.9 Å resulting from Hummers' procedure [55] (57 wt%) [56]. At the sorption of water, the interlayer distances increase from 5.5 Å [58] to 8.6 Å [60], and the first peak in the powder XRD shifts to smaller 2-theta angles [60].

GO was heated under vacuum at 60, 100, 135 and at 180 °C for three hours, to check for the decomposition of GO and to find the optimal activation temperature of the final Al-based MOFs-GO composites for sorption measurements. Figure S4a shows the IR-spectra of GO with the characteristic bands of hydroxyl (O-H), carbonyl (C=O) and epoxy (C-O-C) groups. This indicated that the oxygen-containing functional groups exist on the surface of GO. The broad band at approx. 3500 cm^{-1} to 3000 cm^{-1} can be caused by water, which keeps due to the dispersive forces also until 135 °C between the

GO layers. Thus, above an activation temperature of 100 °C the functional groups start to get lost and from 180 °C on the functional groups disappeared completely and (thermally) reduced GO (TRGO, rGO) was formed [61]. Jeong et al. [62] showed by TGA that at a temperature of about 200 °C the covalent bonds between carbon and oxygen atoms dissociated. Figure S4b shows the PXRDs of GO by activation at different temperatures. The characteristic peak of GO at RT is at 11° 2-theta and thus corresponds to the literature-known GO [20,63]. By increasing the temperature, it can be seen that the peak of GO shifts to higher 2-theta values. This can be explained by a decrease in the distances of the GO layers with increasing temperature. The PXRDs of GO at 100 °C and 135 °C show a peak broadening. In the diffractogram of GO at 185 °C the band of GO at ~12° has completely disappeared and another broad band has emerged. This low intensity this signal can already be seen in the diffractogram of GO at 135 °C. This band at 23° 2-theta represents the [100] reflection of rGO and corresponds to a lattice spacing of the graphene planes of 3.8 Å (from the Bragg equation $n\lambda = 2d \sin\theta$ with $\lambda = 1.54182$ Å) [64].

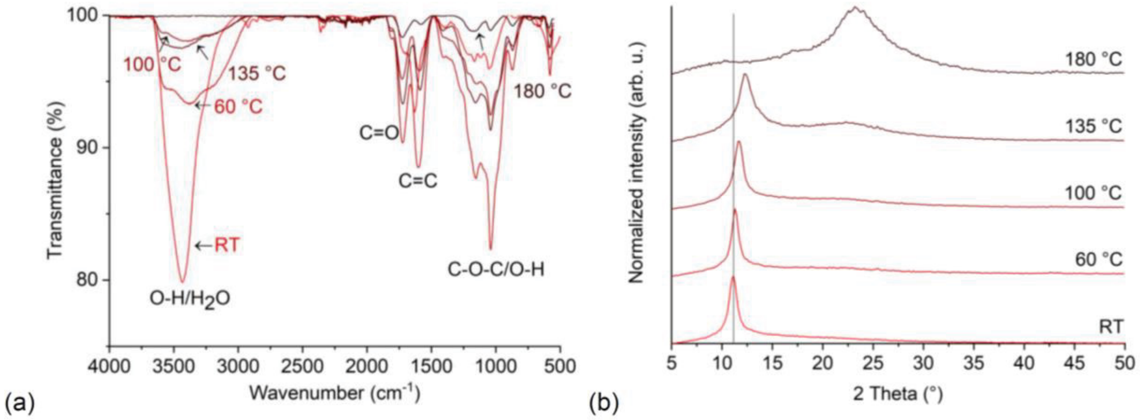

Figure S4. IR spectra (a) and powder X-ray diffraction patterns (b) of GO at different temperatures.

Table S2 gives the interlayer distances (d) and 2-theta angles of the GO layers at different temperatures. With rising activation temperature, the interlayer distance decreases, due to the loss of the separating functional groups, and the band in the PXRD pattern shifts to higher 2-theta angles (Figure S4b). These distances are in the range of those usually observed for graphite oxide and graphite in the literature [65].

Table S2. Interlayer distances of GO synthesized at different temperatures.

	RT	60 °C	100 °C	135 °C	>180 °C
2Θ [°]	11.1	11.3	11.6	12.2	23.2
d [Å]	7.95	7.80	7.62	7.24	3.83

The elemental analysis data in Table S3 of GO illustrates the carbon and sulfur content increase and the hydrogen content decrease with rising temperature.

Table S3. Elemental analysis of GO synthesized at different temperatures.

	RT	60 °C	100 °C	>180 °C
% C (41.5) [66]	42.3	48.5	49.7	62.5
% H (3.11) [66]	2.65	1.91	1.72	0.900
% S	3.81	4.25	4.45	4.58

In summary, the structural changes of GO start to occur at temperatures above 60 °C. Higher temperatures reduce GO so that the functional O/H-containing groups are lost, which could adversely affect the hydrophilicity and possible interaction with the MOF.

MIL-100(Al)

The microporous MOF MIL-100(Al) has the empirical formula 3D-$[Al_3O(OH)(H_2O)_2[btc]_2 \cdot 24H_2O]$ and was first synthesized by Volkringer et al. [67] in a hydrothermal synthesis from a mixture of aluminum nitrate, trimethyl trimesate (Me_3btc) linker and nitric acid. The reaction takes place at high temperature (210 °C, 3.5 h) and a pH range of 0.5 to 0.7, possible by-products are MIL-96(Al) and MIL-110(Al) [67]. The controllable synthesis of MIL-100(Al) is feasible in a microwave [68,69]. Hence, Qiu et al. [68] reported that MIL-100(Al) can be formed after five minutes, whereas MIL-96(Al) occurs after a longer reaction time. Therefore, it is assumed that MIL-100(Al) is the kinetically controlled product and MIL-96(Al) the thermodynamically controlled product [68]. MIL-100(Al) is built from μ_3-oxido-centered trinuclear $[Al_3O]$ units. Four of such $[Al_3O]$ units, form a supertetrahedra in which the $[Al_3O]$ units are linked by four btc ligands, which cover the faces of the tetrahedron [67]. MIL-100(Al) is isostructural to MIL-100(Fe). The structure exhibits two mesoporous cages of approx. 25 and 29 Å diameter, accessible through microporous windows of 5.5 and 8.6 Å diameter (Figure S5) [54].

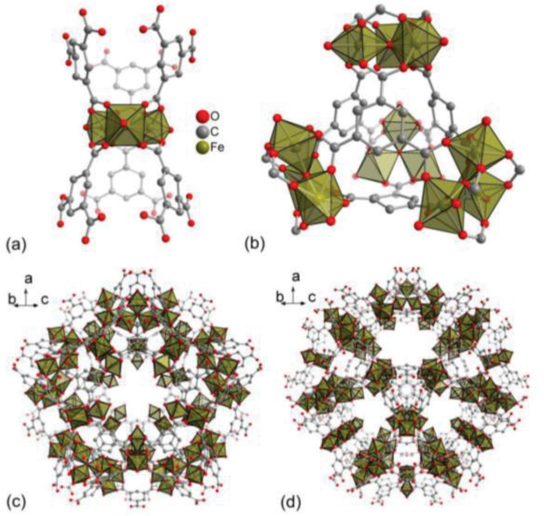

Figure S5. (a) SBU, (b) supertetrahedra, (c) small S cage and (d) large L cage in MIL-100(Fe) (different objects are not drawn to scale). Hydrogen atoms and solvent molecules of crystallization are not shown. MIL-100(Al) is isostructural with Al instead of Fe. Reprinted from ref. [54] with permission from the author. The Royal Society of Chemistry, copyright 2012.

MIL-100(Al)-GO composites

Syntheses of the MIL-100(Al)-GO composites in CEM Discover microwave

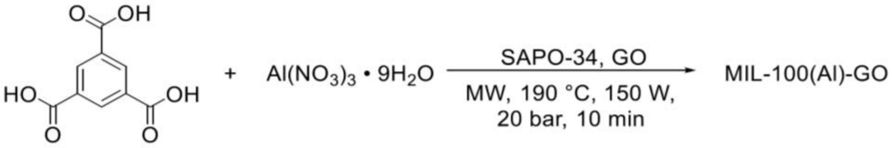

Scheme S1. Synthesis of MIL-100(Al)-GO composites. SAPO-34 was used as an inducing agent for rapid and controllable synthesizing of MIL-100(Al) [68] (see the explanation below). The amounts of the starting materials and yields are given in Table S4.

Explanation on the use of SAPO-34 in the synthesis of MIL-100(Al):

SAPO-34 is used as an inducing reagent for the targeted formation of MIL-100(Al) based on the publication of Qiu et al. [70]. SAPO-34 allows to induce the formation of MIL-100(Al) over its framework isomer MIL-96(Al). Poorly soluble phosphates are decomposed in the microwave reaction, releasing a tetrahedral PO_4^{3-} anion that promotes the formation of the basic building unit of MIL-100(Al). It could be shown that zeolite $AlPO_4$ or SAPO-34 allowed for the rapid and controllable synthesis of single-phase MIL-100(Al). The gradual release of phosphate from the solid surface during the early stage of synthesis plays a crucial role in the inducing action.

SAPO-34 does not remain in the product and was therefore not considered for the calculation of the GO content in Table S4.

Figure S6. Photographs of parent MIL-100(Al) (colorless) and MIL-100(Al)-GO_16 wt% (dark gray).

Table S4. Synthesis data of neat MIL-100(Al) and MIL-100(Al)-GO composites.

Sample[a]	Educt	Amount (mg)	Yield (mg; %)[b]	GO (wt%)[c]
MIL-100(Al)	$Al(NO_3)_3 \cdot 9H_2O$	132	22.3; 27	–
	H_3btc	61.2		
	SAPO-34	3.1		
MIL-100(Al)-GO_2	$Al(NO_3)_3 \cdot 9H_2O$	132	21.1; 26	1.66 = 2
	H_3btc	61.2		
	SAPO-34	3.1		
	GO	0.35		
MIL-100(Al)-GO_4	$Al(NO_3)_3 \cdot 9H_2O$	132	23.9; 29	4.39 = 4
	H_3btc	61.2		
	SAPO-34	3.1		
	GO	1.05		
MIL-100(Al)-GO_9	$Al(NO_3)_3 \cdot 9H_2O$	132	23.0; 28	8.70 = 9
	H_3btc	61.2		
	SAPO-34	3.1		
	GO	2		
MIL-100(Al)-GO_16	$Al(NO_3)_3 \cdot 9H_2O$	132	22.5; 28	16.0 = 16
	H_3btc	61.2		
	SAPO-34	3.1		
	GO	3.6		

[a] In MIL-100(Al)-GO_*x* "*x*" refers to the wt% of GO in the composite (*x* = 2, 4, 9, 16 wt%).

[b] All syntheses are reproducible. Each synthesis in this Table was carried out at least twice. See the explanation below for the small scale.

[c] GO (wt%) was calculated by dividing the amount of GO (mg) by the yield of MIL-100(Al)-GO_*x* (mg).
All values are rounded. In the main text the GO wt% is given as the rounded value for clarity.

Explanation on the small-scale synthesis of MIL-100(Al) and its composites:

The syntheses took place in a *Discover* lab microwave with a reaction vessel of 10 mL. We performed several experiments to optimize the yield of MIL-100(Al). Yet, it was always around 20 mg. Unfortunately, a transfer to a microwave with larger reaction vessels was not successful. The problem with MIL-100(Al) synthesis is the purity. In the solvothermal method, MIL-100(Al) rapidly converts to the thermodynamic product MIL-96. Microwave synthesis always yields pure MIL-100(Al). Therefore, all work on MIL-100(Al) and its composites with different amounts of GO were carried out in the lab microwave from *Discover* using the 10 mL reaction vessels.

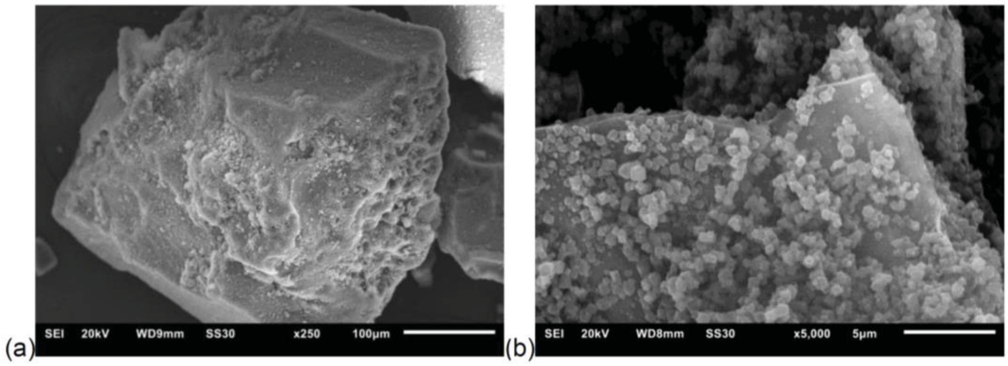

Figure S7. SEM images of (a, b) MIL-100(Al)-GO_2 wt% at different magnifications.

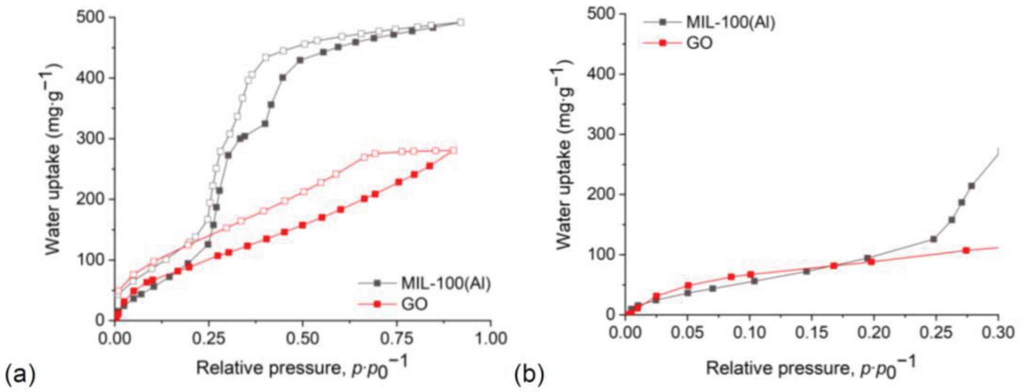

Figure S8. Water sorption isotherms of neat MIL-100(Al) and GO (at 293 K). Adsorption is depicted with filled, desorption with empty symbols. (a) Full region from $p \cdot p_0^{-1} = 0 - 1$, (b) expanded adsorption region from $p \cdot p_0^{-1} = 0 - 0.3$ (for clarity, only the adsorption isotherms are shown).

After water sorption: PXRD, SEM

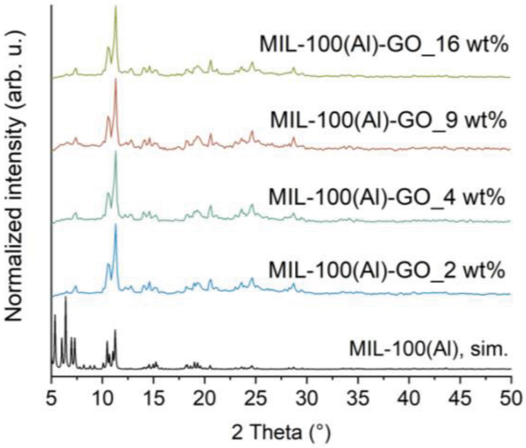

Figure S9. Powder X-ray diffraction patterns of simulated MIL-100(Al) (CCDC no. 789872, CSD-Refcode BUSPIP) [67] and MIL-100(Al)-GO_2, 4, 9, 16 wt% composites after water ad- and desorption without further drying.

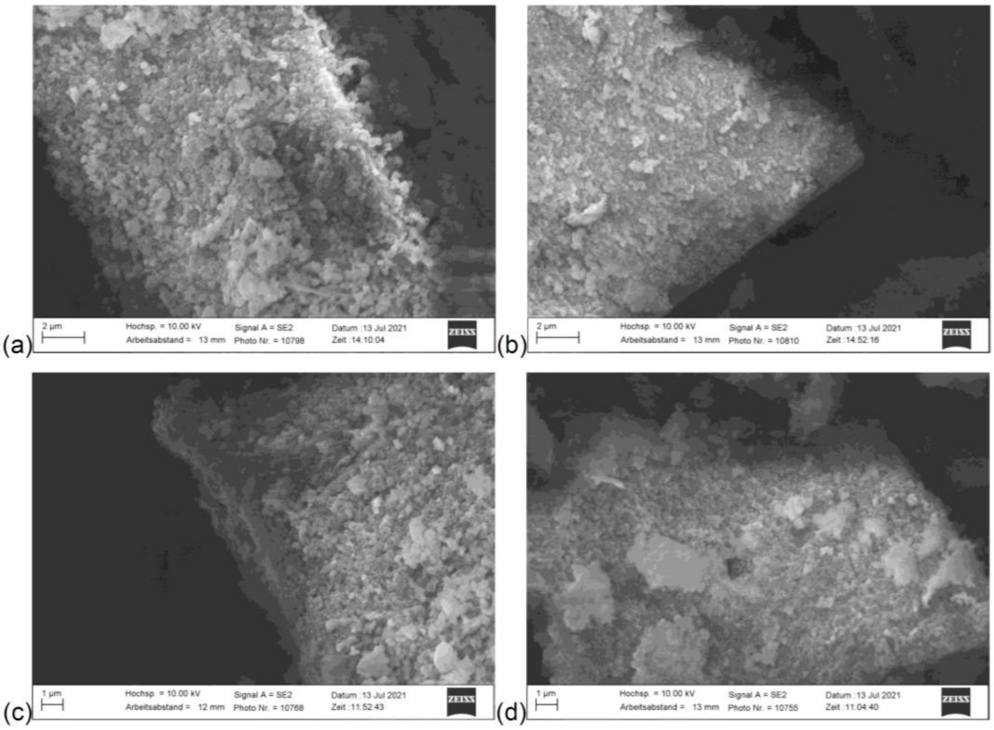

Figure S10. SEM images of (a) MIL-100(Al)-GO_2 wt%, (b) MIL-100(Al)-GO_4 wt%, (c) MIL-100(Al)-GO_9 wt% and (d) MIL-100(Al)-GO_16 wt% after water sorption at different magnifications.

After water sorption cycling (five cycles): PXRD, SEM, N_2 and water sorption isotherms

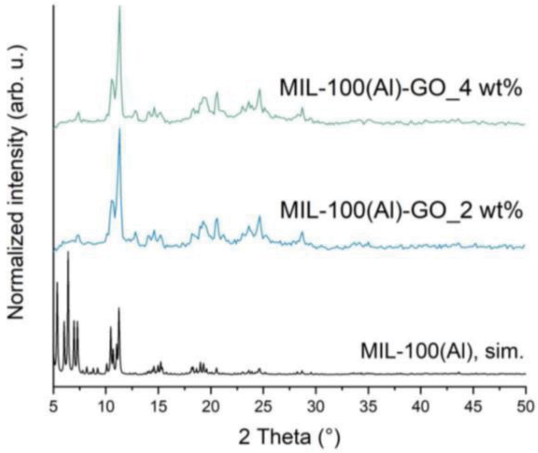

Figure S11. Powder X-ray diffraction patterns of simulated MIL-100(Al) (CCDC no. 789872, CSD-Refcode BUSPIP) [67] and MIL-100(Al)-GO_2, 4 wt% composites after five water ad- and desorption cycles without further drying.

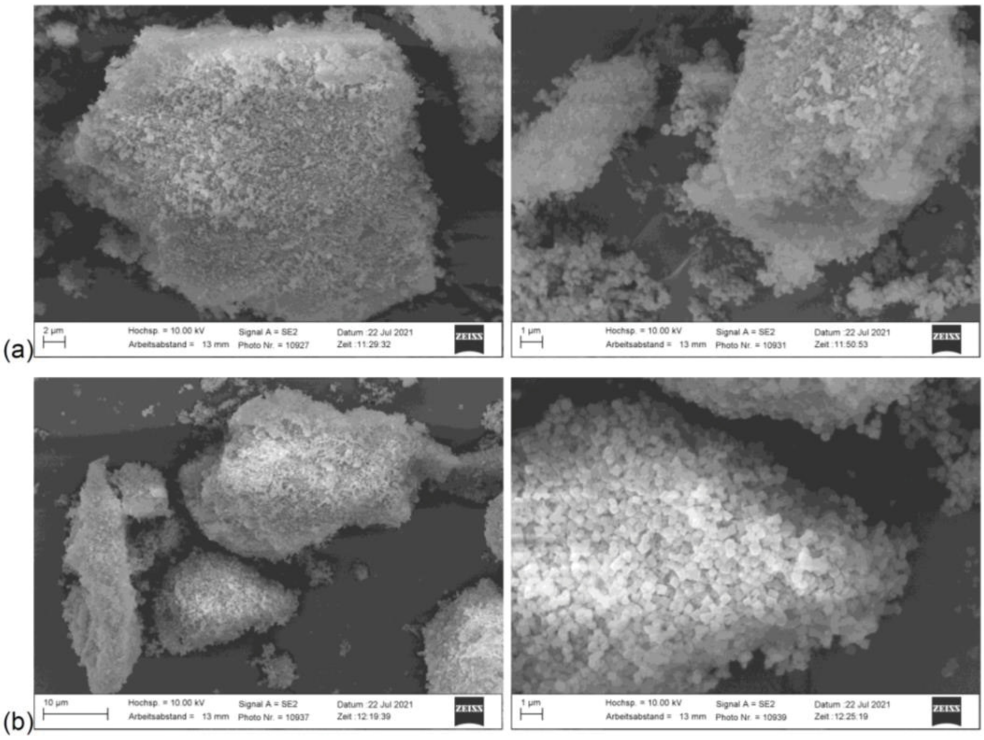

Figure S12. SEM images of (a) MIL-100(Al)-GO_2 wt% and (b) MIL-100(Al)-GO_4 wt% after five water ad- and desorption cycles at different magnifications.

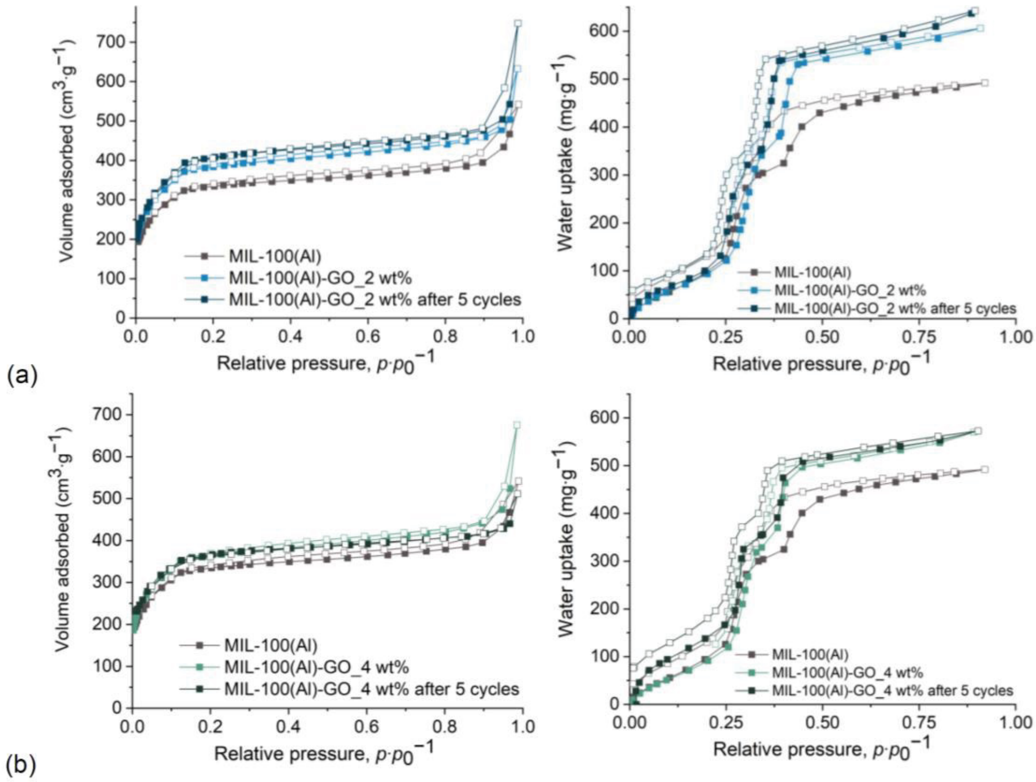

Figure S13. Nitrogen (left) and water (right) sorption isotherms of (a) MIL-100(Al)-GO_2 wt% and (b) MIL-100(Al)-GO_4 wt% after five water ad- and desorption cycles.

Table S5. N_2 and water sorption data of MIL-100(Al)-GO_2, 4 wt% composites before and after five water ad- and desorption cycles.

Sample[a]	*S* (BET) ($m^2 \cdot g^{-1}$)[b]	$V_{pore(total)}$ ($cm^3 \cdot g^{-1}$)[c]	$V_{pore(micro)}$ ($cm^3 \cdot g^{-1}$)[d]	Water uptake ($mg \cdot g^{-1}$) at $p \cdot p_0^{-1}$ =		
				0.3	**0.5**	**0.9**
MIL-100(Al)-GO_2 (before 5 cycles)	1416	0.74	0.49	234	543	606
MIL-100(Al)-GO_2 (after 5 cycles)	1579	0.78	0.53	321	559	642
MIL-100(Al)-GO_4 (before 5 cycles)	1423	0.73	0.46	268	503	570
MIL-100(Al)-GO_4 (after 5 cycles)	1423	0.66	0.49	325	518	573

[a] In MIL-100(Al)-GO_x "x" refers to the wt% of GO in the composite (x = 2, 4 wt%).

[b] Apparent *S*(BET) values were determined from N_2 sorption isotherms at 77 K. *S*(BET) were obtained from five adsorption points in the pressure range of $0.04 < p \cdot p_0^{-1} < 0.1$ for MIL-100(Al), $0.01 < p \cdot p_0^{-1} < 0.4$ for MIL-100(Al)-GO_*x* composites.

[c] Total pore volume, $V_{pore(total)}$ calculated from N_2 sorption isotherm at 77 K ($p \cdot p_0^{-1} = 0.95$ for MIL-100(Al) corresponding composites) for pores ≤ 20 nm.

[d] Micropore volume, $V_{pore(micro)}$ refers to the volume that originates only from micropores, obtained by the *V*−*t* method with thickness method "DeBoer" in the range of $0.2 < p \cdot p_0^{-1} < 0.4$ for MIL-100(Al)-GO_*x* composites. All correlation coefficients (*r*) within calculations were ≥ 0.999.

CAU-10-H

Another Al-based and extremely water stable MOF is CAU-10-H – with a stability for over 10 000 water ad- and desorption cycles – with the empirical formula $[Al(OH)(ipa)\cdot 1.7H_2O]$ (ipa^{2-} = isophthalate). CAU-10-H was first synthesized by Stock and co-workers [71]. This microporous MOF is prepared from aluminum sulfate octadecahydrate with the isophthalate linker. The framework structure is formed by the interconnection of fourfold helical chains of *cis*-corner sharing $[AlO_6]$ octahedra by isophthalate linker molecules. Four oxygen atoms in each polyhedron originate from four different coordinating carboxylate groups while two cis positioned hydroxide ions induce the helical shape of the inorganic building unit (Figure S14a). The organic moieties connect each chain to four adjacent inorganic units and, thus, square shaped one-dimensional channels are formed (Figure S14b) [72].

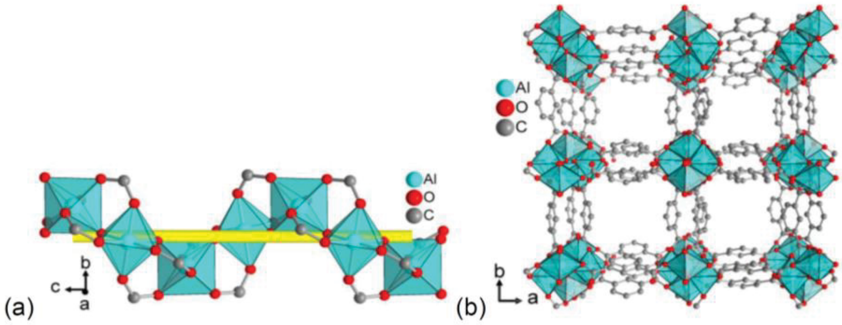

Figure S14. The inorganic building unit (a) and the 3D framework structure (b) of CAU-10-H. Reprinted from ref. [72] with permission from the author. The Royal Society of Chemistry, copyright 2016.

CAU-10-H-GO composites

Syntheses of the CAU-10-H-GO composites under reflux conditions

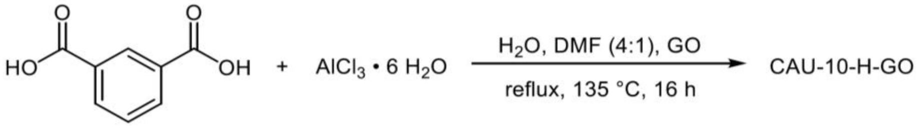

Scheme S2. Synthesis of the CAU-10-H-GO composites. The amounts of the starting materials and yields are given in Table S6.

Table S6 Syntheses data of neat CAU-10-H and CAU-10-H-GO composites.

Sample[a]	Educt	Amount (mg)	Yield (mg; %)	GO (wt%)[b]
CAU-10-H	$AlCl_3 \cdot 6\ H_2O$	482	400; 96	–
	H_2ipa	334		
CAU-10-H-GO_2	$AlCl_3 \cdot 6\ H_2O$	483	397; 94	1.76 = 2
	H_2ipa	335		
	GO	7		
CAU-10-H-GO_5	$AlCl_3 \cdot 6\ H_2O$	482	395; 90	5.06 = 5
	H_2ipa	334		
	GO	20		
CAU-10-H-GO_8	$AlCl_3 \cdot 6\ H_2O$	484	406; 90	8.13 = 8
	H_2ipa	335		
	GO	33		
CAU-10-H-GO_15	$AlCl_3 \cdot 6\ H_2O$	482	441; 83	15.0 = 15
	H_2ipa	334		
	GO	66		

[a] In CAU-10-H-GO_*x* “*x*” refers to the wt% of GO in the composite, (*x* = 2, 5, 8, 15 wt%).
[b] GO (wt%) was calculated by dividing the amount of used GO (mg) by the yield of CAU-10-H-GO_*x* (mg). All values are rounded. In the main text the GO wt% is given as the rounded value for clarity.

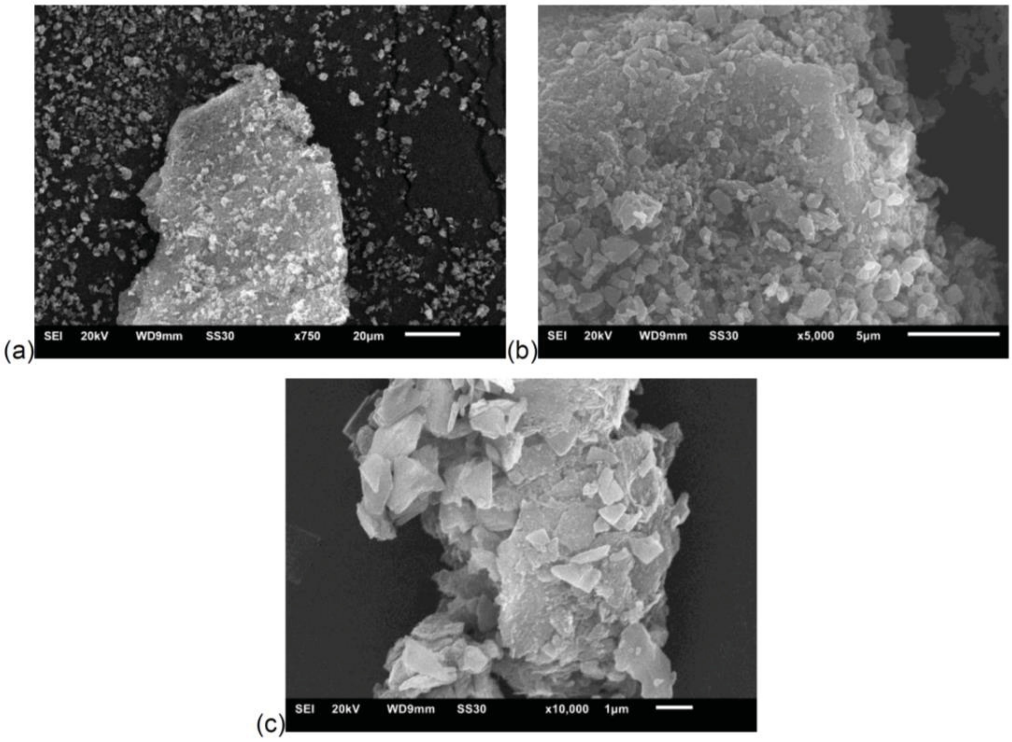

Figure S15. SEM images of (a) CAU-10-H-GO_2 wt% (overview), (b) CAU-10-H-GO_5 wt% and (c) CAU-10-H-GO_8 wt% at different magnifications.

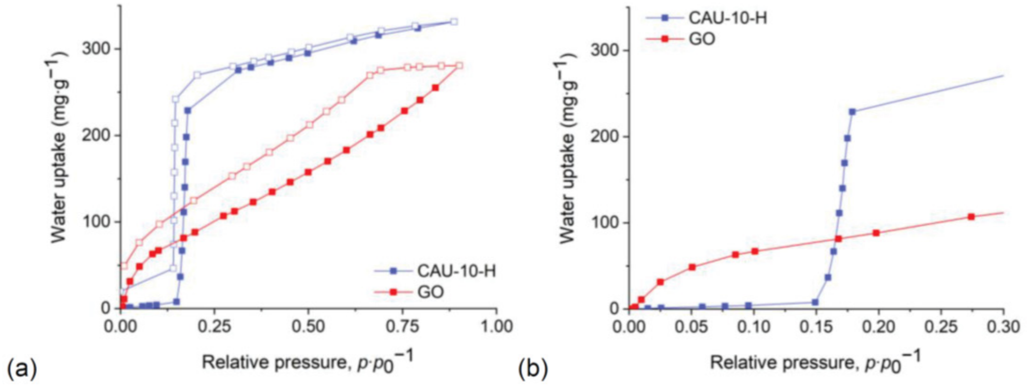

Figure S16. Water sorption isotherms of neat CAU-10-H and GO (at 293 K). Adsorption is depicted with filled, desorption with empty symbols. (a) Full region from $p \cdot p_0^{-1} = 0 – 1$, (b) expanded adsorption region from $p \cdot p_0^{-1} = 0 – 0.3$ (for clarity, only the adsorption isotherms are shown).

After water sorption: PXRD, SEM

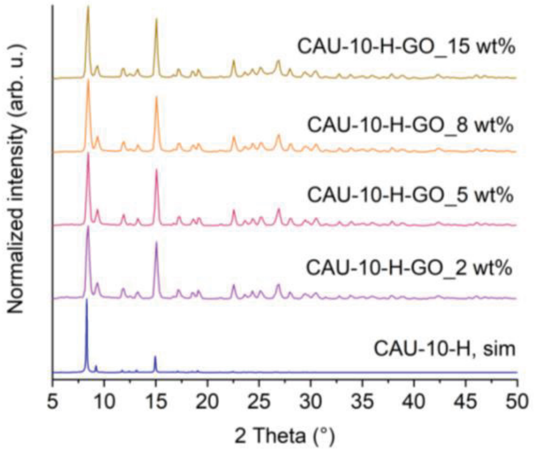

Figure S17. Powder X-ray difraction patterns of simulated CAU-10-H (CCDC no. 1454066, CSD-Refcode OQOBUT) [72] and CAU-10-H-GO_2, 5, 8, 15 wt% composites after water ad- and desorption without further drying.

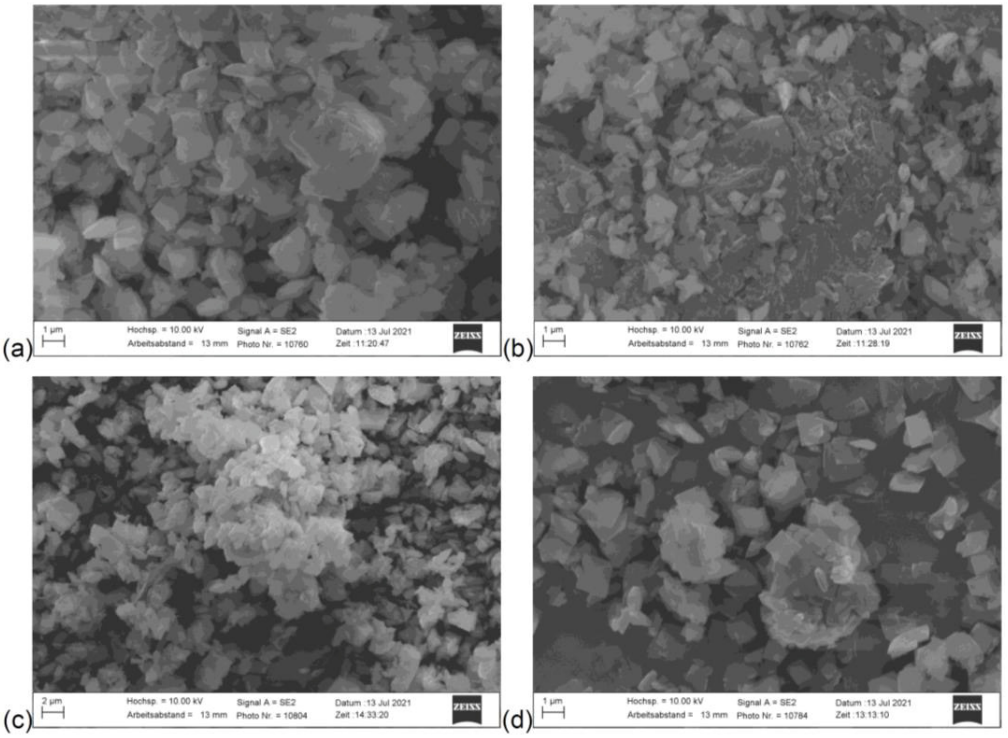

Figure S18. SEM images of (a) CAU-10-H-GO_2 wt%, (b) CAU-10-H-GO_5 wt%, (c) CAU-10-H-GO_8 wt% and (d) CAU-10-H-GO_15 wt% after water sorption at different magnifications.

After water sorption cycling (five cycles): PXRD, SEM, N_2 and water sorption isotherms

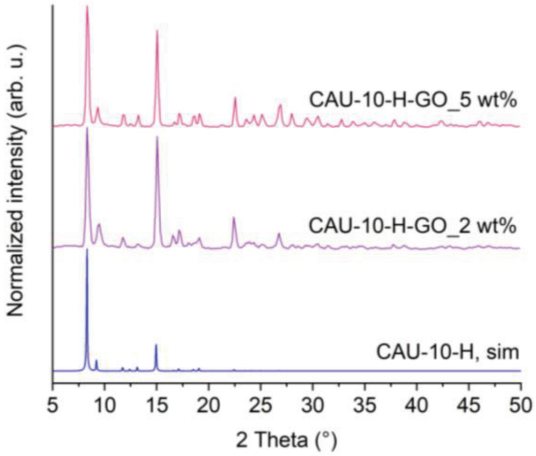

Figure S19. Powder X-ray diffraction patterns of simulated CAU-10-H (CCDC no. 1454066, CSD-Refcode OQOBUT) [72] and CAU-10-H-GO_2, 5 wt% composites after five water ad- and desorption cycles without further drying.

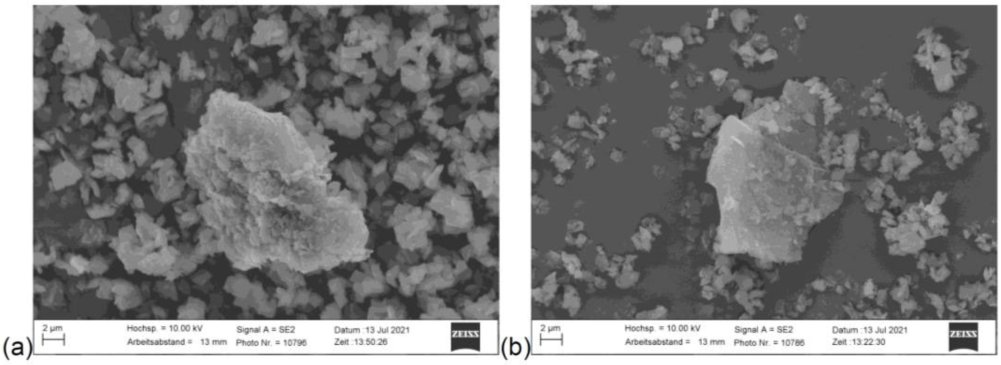

Figure S20. SEM images of (a) CAU-10-H-GO_2 wt% and (b) CAU-10-H-GO_5 wt%, after five water ad- and desorption cycles (all scale bars 2 µm).

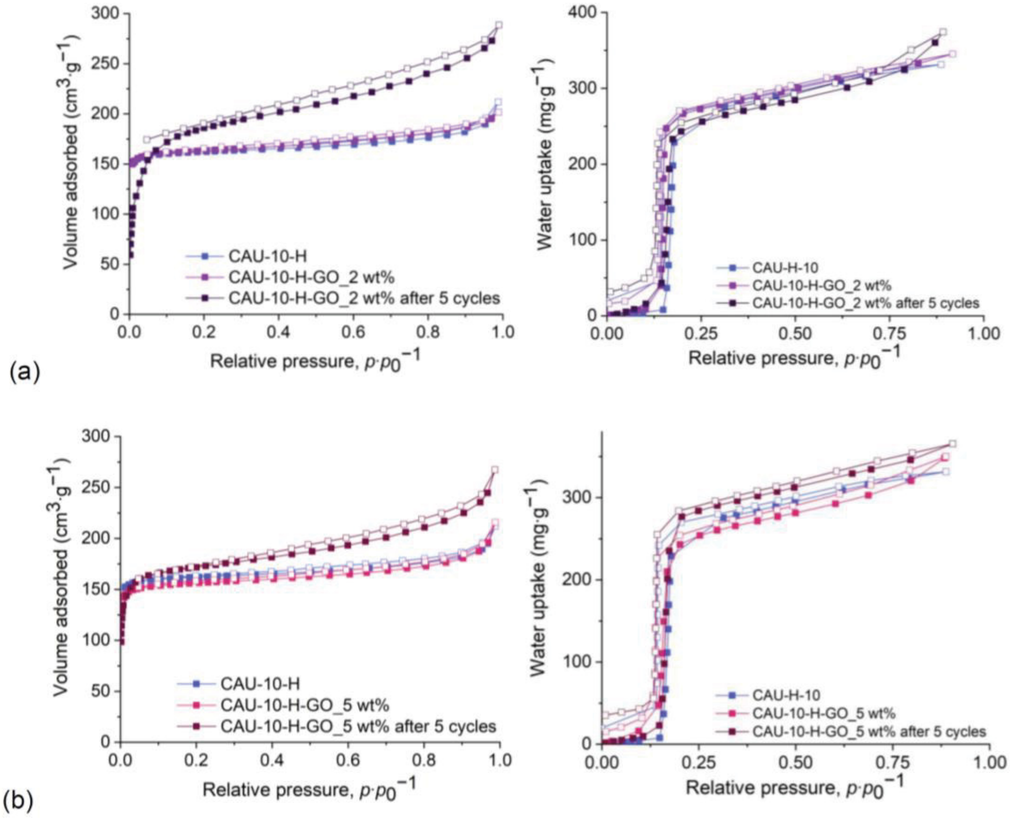

Figure S21. Nitrogen (left) and water (right) sorption isotherms of (a) CAU-10-H-GO_2 wt% and (b) CAU-10-H-GO_5 wt% after five water ad- and desorption cycles.

Table S7. N_2 and water sorption data of CAU-10-H-GO_2, 5 wt% composites before and after five water ad- and desorption cycles.

Sample[a]	S (BET) ($m^2 \cdot g^{-1}$)[b]	$V_{pore(total)}$ ($cm^3 \cdot g^{-1}$)[c]	$V_{pore(micro)}$ ($cm^3 \cdot g^{-1}$)[d]	Water uptake ($mg \cdot g^{-1}$) at $p \cdot p_0^{-1}$ =		
				0.15	**0.3**	**0.9**
CAU-10-H-GO_2 (before 5 cycles)	671	0.29	0.23	181	278	345
CAU-10-H-GO_2 (after 5 cycles)	741	0.41	0.21	81	270	374
CAU-10-H-GO_5 (before 5 cycles)	689	0.30	0.24	83	260	350
CAU-10-H-GO_5 (after 5 cycles)	681	0.36	0.21	55	290	365

[a] In CAU-10-H-GO_*x* "*x*" refers to the wt% of GO in the composite, (*x* = 2, 5 wt%).

[b] Apparent *S*(BET) values were determined from N_2 sorption isotherms at 77 K. *S*(BET) were obtained from five adsorption points in the pressure range of $0.01 < p \cdot p_0^{-1} < 0.02$ for CAU-10-H and $0.01 < p \cdot p_0^{-1} < 0.4$ for CAU-10-H-GO_*x* composites.

[c] Total pore volume, $V_{pore(total)}$ calculated from N_2 sorption isotherm at 77 K ($p \cdot p_0^{-1} = 0.90$ for CAU-10-H and corresponding composites) for pores ≤ 20 nm.

[d] Micropore volume, $V_{pore(micro)}$ refers to the volume that originates only from micropores, obtained by the *V–t* method with thickness method "DeBoer" in the range of $0.2 < p \cdot p_0^{-1} < 0.4$ for CAU-10-H and CAU-10-H-GO_*x*. All correlation coefficients (*r*) within calculations were ≥ 0.999.

References

[1] G. Li, F. Li, H. Yang, F. Cheng, N. Xu, W. Shi, P. Cheng, Inorg. Chem. Commun. 64 (2016) 63–66.
[2] W. Bao, Z. Zhang, Y. Qu, C. Zhou, X. Wang, J. Li, J. Alloys Compd. 582 (2014) 334–340.
[3] C. Petit, J. Burress, T.J. Bandosz, Carbon 49 (2011) 563–572.
[4] S. Liu, L. Sun, F. Xu, J. Zhang, C. Jiao, F. Li, Z. Li, S. Wang, Z. Wang, X. Jiang, H. Zhou, L. Yang, C. Schick, Energy Environ. Sci. 6 (2013) 818–823.
[5] Z. Bian, J. Xu, S. Zhang, X. Zhu, H. Liu, J. Hu, Langmuir 31 (2015) 7410–7417.
[6] A. Policicchio, Y. Zhao, Q. Zhong, R.G. Agostino, T.J. Bandosz, ACS Appl. Mater. Interfaces 6 (2014) 101–108.
[7] W. Huang, X. Zhou, Q. Xia, J. Peng, H. Wang, Z. Li, Ind. Eng. Chem. Res. 53 (2014) 11176–11184.
[8] Z. Bian, X. Zhu, T. Jin, J. Gao, J. Hu, H. Liu, Microporous Mesoporous Mater. 200 (2014) 159–164.
[9] C. Petit, B. Mendoza, T.J. Bandosz, ChemPhysChem 11 (2010) 3678–3684.
[10] A.M. Ebrahim, J. Jagiello, T.J. Bandosz, J. Mater. Chem. A 3 (2015) 8194–8204.
[11] C. Petit, L. Huang, J. Jagiello, J. Kenvin, K.E. Gubbins, T.J. Bandosz, Langmuir 27 (2011) 13043–13051.
[12] C. Petit, B. Mendoza, T.J. Bandosz, Langmuir 26 (2010) 15302–15309.
[13] F. Xu, Y. Yu, J. Yan, Q. Xia, H. Wang, J. Li, Z. Li, Chem. Eng. J. 303 (2016) 231–237.
[14] X. Zhou, W. Huang, J. Liu, H. Wang, Z. Li, Chem. Eng. Sci. 167 (2017) 98–104.
[15] A. Taheri, E.G. Babakhani, J.T. Darian, Energy Fuels 31 (2017) 8792–8802.
[16] X. Zhou, W. Huang, J. Shi, Z. Zhao, Q. Xia, Y. Li, H. Wang, Z. Li, J. Mater. Chem. A 2 (2014) 4722–4730.
[17] X. Sun, Y. Li, H. Xi, Q. Xia, RSC ADV. 4 (2014) 56216–56223.
[18] X. Sun, Q. Xia, Z. Zhao, Y. Li, Z. Li, Chem. Eng. J. 239 (2014) 226–232.
[19] X. Zhou, W. Huang, J. Miao, Q. Xia, Z. Zhang, H. Wang, Z. Li, Chem. Eng. J. 266 (2015) 339–344.
[20] Y. Zhao, H. Ding, Q. Zhong, Appl. Surf. Sci. 284 (2013) 138–144.
[21] Z.H. Huang, G. Liu, F. Kang, ACS Appl. Mater. Interfaces 4 (2012) 4942–4947.
[22] C. Petit, T.J. Bandosz, Adv. Funct. Mater. 21 (2011) 2108–2117.
[23] C. Petit, T.J. Bandosz, J. Mater. Chem. 19 (2009) 6521–6528.
[24] A.R. Noorpoor, S. Nazari Kudahi, J. Environ. Chem. Eng. 4 (2016) 1081–1091.
[25] Y. Cao, Y. Zhao, Z. Lv, F. Song, Q. Zhong, J. Ind. Eng. Chem. 27 (2015) 102–107.
[26] S. Castarlenas, C. Téllez, J. Coronas, J. Membr. Sci. 526 (2017) 205–211.
[27] H. Zhou, J. Zhang, J. Zhang, X. Yan, X. Shen, A. Yuan, Int. J. Hydrog. Energy 40 (2015) 12275–12285.
[28] J. Zhang, D. Ji, H. Zhou, X. Yan, A. Yuan, J. Nanosci. Nanotechnol. 17 (2017) 1400–1406(7).

[29] N.M. Musyoka, J. Ren, H.W. Langmi, B.C. North, M. Mathe, D. Bessarabov, J. Alloys Compd. 724 (2017) 450–455.

[30] Y. Zhao, M. Seredych, J. Jagiello, Q. Zhong, T.J. Bandosz, Chem. Eng. J. 239 (2014) 399–407.

[31] S.A.M. Said, N.U. Qadir, R.B. Mansour, K. Mezghani, H.M. Irshad, RSC Adv. 7 (2017) 17353–17356.

[32] M. Jahan, Z. Liu, K.P. Loh, Adv. Funct. Mater. 23 (2013) 5363–5372.

[33] Y. Wu, H. Luo, H. Wang, RSC Adv. 4 (2014) 40435–40438.

[34] T.A. Vu, G.H. Le, H.T. Vu, K.T. Nguyen, T.T.T. Quan, Q.K. Nguyen, H.T.K. Tran, P.T. Dang, L.D. Vu, G.D. Lee, Mater. Res. Express 4 (2017) 035038.

[35] J. Tang, J. Wang, RSC Adv. 7 (2017) 50829–50837.

[36] C. Bao, L. Zhou, Y. Shao, Q. Wu, H. Zhu, K. Li, J. Ind. Eng. Chem. 38 (2016) 132–140.

[37] Y. Zhang, G. Li, H. Lu, Q. Lv, Z. Sun, RSC Adv. 4 (2014) 7594–7600.

[38] R. Liang, L. Shen, F. Jing, N. Qin, L. Wu, ACS Appl. Mater. Interfaces 7 (2015) 9507–9515.

[39] X. Yuan, H. Wang, Y. Wu, G. Zeng, X. Chen, L. Leng, Z. Wu, H. Li, Appl. Organometal. Chem. 30 (2016) 289–296.

[40] X. Wang, Q. Wang, Q. Wang, F. Gao, F. Gao, Y. Yang, H. Guo, ACS Appl. Mater. Interfaces 6 (2014) 11573–11580.

[41] Q. Chen, X. Li, X. Min, D. Cheng, J. Zhou, Y. Li, Z. Xie, P. Liu, W. Cai, C. Zhang, J. Electroanal. Chem. 789 (2017) 114–122.

[42] Y.Y. Zheng, C.X. Li, X.T. Ding, Q. Yang, Y.M. Qi, H.M. Zhang, L.T. Qu, Chin. Chem. Lett. 28 (2017) 1473–1478.

[43] C. Dong, L. Xu, ACS Appl. Mater. Interfaces 9 (2017) 7160–7168.

[44] M. Saraf, R. Rajak, S.M. Mobin, J. Mater. Chem. A 4 (2016) 16432–16445.

[45] E. Rahimi, N. Mohaghegh, Environ. Sci. Pollut. Res. 24 (2017) 22353–22360.

[46] V. Jabbari, J.M. Veleta, M. Zarei-Chaleshtori, J. Gardea-Torresdey, D. Villagrán, Chem. Eng. J. 304 (2016) 774–783.

[47] S.-C. Wu, L.-L. Yu, F.-F. Xiao, X. You, C. Yang, J.-H. Cheng, J. Alloys Compd. 724 (2017) 625–632.

[48] C. Yang, S. Wu, J. Cheng, Y. Chen, J. Alloys Compd. 687 (2016) 804–812.

[49] S. Luo, J. Wang, Environ. Sci. Pollut. Res. 25 (2018) 5521–5528.

[50] S. Zhao, D. Chen, F. Wei, N. Chen, Z. Liang, Y. Luo, Ultrason. Sonochem. 39 (2017) 845–852.

[51] J. Ma, X. Guo, Y. Ying, D. Liu, C. Zhong, Chem. Eng. J. 313 (2017) 890–898.

[52] J. Abdi, M. Vossoughi, N.M. Mahmoodi, I. Alemzadeh, Chem. Eng. J. 326 (2017) 1145–1158.

[53] Z. Wu, X. Yuan, H. Zhong, H. Wang, G. Zeng, X. Chen, H. Wang, L. Zhang, J. Shao, Sci. Rep. 6 (2016) 25638.

[54] F. Jeremias, A. Khutia, S.K. Henninger, C. Janiak, J. Mater. Chem. 22 (2012) 10148–10151.

[55] W.S. Hummers, R.E. Offeman, J. Am. Chem. Soc. 80 (1958) 1339.

[56] A. Buchsteiner, A. Lerf, J. Pieper, J. Phys. Chem. B 110 (2006) 22328–22338.

[57] Y. Wu, H. Luo, H. Wang, C. Wang, J. Zhang, Z. Zhang, J. Colloid Interf. Sci. 394 (2013) 183–191.

[58] B.C. Brodie, Ann. Chim. Phys. 59 (1860) 466.

[59] L. Staudenmaier, Ber. Dtsch. Chem. Ges. 31 (1899) 1481–1487.

[60] F. Barroso-Bujans, S. Cerveny, A. Alegría, J. Colmenero, Carbon 48 (2010) 3277–3286.

[61] E. Tegou, G. Pseiropoulos, M.K. Filippidou, S. Chatzandroulis, Microelectron. Eng. 159 (2016) 146–150.

[62] H.-K. Jeong, Y.P. Lee, M.H. Jin, E.S. Kim, J.J. Bae, Y.H. Lee, Chem. Phys. Lett. 470 (2009) 255–258.

[63] E. Elsayed, H. Wang, P.A. Anderson, R. Al-Dadah, S. Mahmoud, H. Navarro, Y. Ding, J. Bowen, Microporous Mesoporous Mater. 244 (2017) 180–191.

[64] R. Allmann, Röntgenpulverdiffraktometrie, Rechengestützte Auswertung, Phasenanalyse und Strukturbestimmung, ISBN: 978-3-540-43967-7, e-ISBN: 978-3-642-56079-8, Springer-Verlag Berlin Heidelberg, 2003, DOI: 10.1007/978-3-642-56079-8.

[65] S.C. Ray, Chapter 2 – application and uses of graphene oxide and reduced graphene oxide, in Appl. Graphene Graphene-Oxide Based Nanomater., William Andrew Publishing Oxford (2015) 39–55.

[66] https://www.sigmaaldrich.com/technical-documents/articles/technology-spotlights/carbon-nanomaterials.html, 17.05.2021.

[67] C. Volkringer, D. Popov, T. Loiseau, G. Férey, M. Burghammer, C. Riekel, M. Haouas, F. Taulelle, Chem. Mater. 21 (2009) 5695–5697.

[68] M. Qiu, Q. Guan, W. Li, Cryst. Growth Des. 16 (2016) 3639–3646.

[69] A. García Márquez, A. Demessence, A.E. Platero-Prats, D. Heurtaux, P. Horcajada, C. Serre, J.-S. Chang, G. Férey, V. A. de La Peña-O'Shea, C. Boissière, Eur. J. Inorg. Chem. 2012 (2012) 5165–5174.

[70] M. Qiu, Q. Guan, W. Li, Cryst. Growth Des. 16 (2016) 3639–3646.

[71] H. Reinsch, M.A. van der Veen, B. Gil, B. Marszalek, T. Verbiest, D. de Vos, N. Stock, Chem. Mater. 25 (2013) 17–26.

[72] D. Fröhlich, E. Pantatosaki, P.D. Kolokathis, K. Markey, H. Reinsch, M. Baumgartner, M.A. van der Veen, D.E. De Vos, N. Stock, G.K. Papadopoulos, J. Mater. Chem. A 4 (2016) 11859–11869.

3.1.2 Coordinatively unsaturated metal sites (open metal sites) in metal–organic frameworks: design and applications

Ülkü Kökçam-Demir,‡a Anna Goldman,‡a Leili Esrafili,b Maniya Gharib,b Ali Morsali,‡*b Oliver Weingartc, Christoph Janiak‡*a,

Chem. Soc. Rev., 2020, **49**, 2751–2798.
DOI: 10.1039/c9cs00609e, Referenz [206]

Impact Faktor: 40.443 (2018/2019)

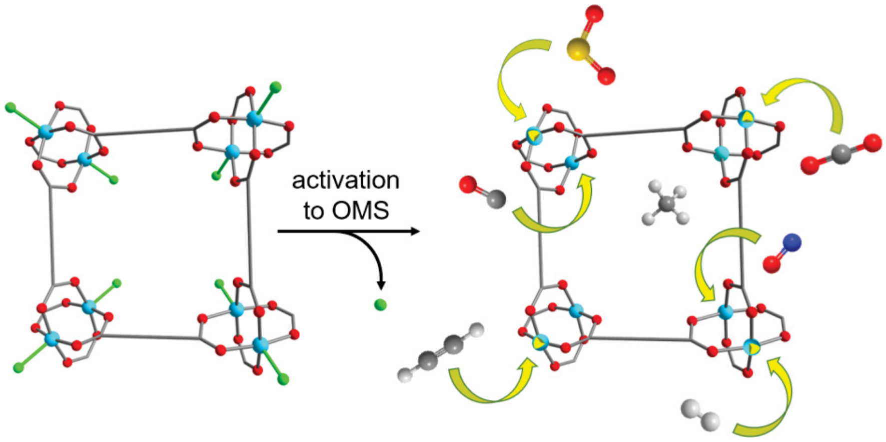

Zusammenfassung

In dieser Arbeit werden eine Vielzahl an Metall-organischen Gerüstverbindungen mit offenen Metallstellen (*open metal sites*, OMS), wie bspw. HKUST-1, MOF-74 oder MIL-101, gezeigt. MOFs können OMS oder koordinativ ungesättigte Stellen (*coordinatively unsaturated sites*, CUS) oder offene Koordinationsstellen (*open coordination sites*, OCS) enthalten, wenn freie Lewis-Säure-Stellen auf den Metallionen oder Clusterknoten erzeugt werden. Dieses Review gibt eine umfangreiche Zusammenfassung über die verschiedenen Synthesestrategien, über die theoretischen Studien und über die verschiedenen OMS-MOF Anwendungen. Im experimentellen Teil dieser Arbeit liegt der Fokus auf MOFs mit nachgewiesener OMS-Bildung, die durch gezielte Methoden eindeutig analysiert wurden.

Anteile an der Publikation:

- Die Projektidee erfolgte durch Herrn Prof. Dr. Ali Morsali.
- Die Konzipierung, umfassende Literaturrecherche, der Aufbau, die Verschriftlichung und kontinuierliche Überarbeitung des Manuskriptes erfolgte in Zusammenarbeit mit Frau Dr. Anna Goldman zu gleichen Anteilen.
- Die Verschriftlichung der Einleitung, des Kapitels 2 sowie des Kapitels 4 mit den folgenden Abschnitten „*Post functionalization of OMS in MOFs*”, „H_2 *adsorption*”, „NO *adsorption*”, „SO_2 *adsorption*”, „*Catalysis and photocatalysis*” und „*Sensing*”. Die Darstellung der Abbildungen 1 und 3 und die Anfertigung der Tabellen 2 und 3.
- Die Verschriftlichung des Abschnitts 2.IV erfolgte in Zusammenarbeit mit Frau Dr. Anna Goldman und Herrn Prof. Dr. Christoph Janiak.
- Die SBU bezogene Abschnitte in Kapitel 2, Kapitel 3 sowie in Kapitel 4 die Abschnitte „*Gas sorption*“, „CO_2 *adsorption*“, „CO *adsorption*“, „C_2H_2 *sorption*“, „CH_4 *adsorption*“, „SO_2 *adsorption*“ und „*Separation*“ wurden von Frau Dr. Anna Goldman verfasst. Die Darstellung der SBUs anhand von kristallographischen Daten und Anfertigung der Tabellen 1 und S1 bis S3 erfolgte durch Frau Dr. Anna Goldman.
- Die Überarbeitung und Korrektur des Kapitels 3 erfolgte durch Herrn PD Dr. Oliver Weingart.
- Die Literaturrecherche und Durchsicht des Manuskriptes erfolgte durch Frau Leili Esrafili, Frau Maniya Gharib und Herrn Prof. Dr. Ali Morsali.
- Die Überarbeitung und Korrektur des Manuskriptes erfolgten durch Herrn Prof. Dr. Christoph Janiak.
- Die Einreichung in dem internationalen Journal „*Chemical Society Reviews – Royal Society of Chemistry*“ erfolgte in Zusammenarbeit mit Frau Dr. Anna Goldman und Herrn Prof. Dr. Christoph Janiak.
- Die finale Überarbeitung und Anfertigung des Revisionsscheins erfolgten in Zusammenarbeit mit Frau Dr. Anna Goldman und Herrn Prof. Dr. Christoph Janiak.

Chem Soc Rev

REVIEW ARTICLE

Cite this: *Chem. Soc. Rev.*, 2020, 49, 2751

Coordinatively unsaturated metal sites (open metal sites) in metal–organic frameworks: design and applications†

Ülkü Kökçam-Demir,[‡a] Anna Goldman,[‡a] Leili Esfarili,[b] Maniya Gharib,[b]
Ali Morsali,[‡*b] Oliver Weingart[c] and Christoph Janiak[‡*a]

Received 6th December 2019

DOI: 10.1039/c9cs00609e

rsc.li/chem-soc-rev

Metal–organic frameworks (MOFs) can contain open metal sites (OMS) or coordinatively unsaturated sites (CUS) or open coordination sites (OCS) when vacant Lewis acid sites on the metal ions or cluster nodes have been generated. This review combines for the first time all aspects of OMS in MOFs, starting from different preparation strategies over theoretical studies on the effects of OMS with host–guest interactions up to distinct OMS-MOF applications. In the experimental part the focus of this review is on MOFs with proven OMS formation which are not only invoked but are clearly verified by analytical methods.

1. Introduction

Metal–organic frameworks are three-dimensional coordination networks containing potential voids.[1,2] This subcategory of coordination polymers is built from metal ions or metal clusters linked together by organic ligands. A key characteristic of MOFs should be their crystallinity for structure determination together with proven (micro-)porosity. An important feature of MOFs over other porous materials such as zeolites and porous carbons[3,4] is the ability to widely design the physiochemical inner surface properties, and thereby establish a large variety in topologies and structures by the deliberate design and selection of organic and inorganic molecular building blocks.[5] MOFs have been considered to be promising candidates for a diversity of potential applications such as gas sorption, including gas separation[6] and storage,[7–9] catalysis,[10–13] photocatalysis,[14] sensing,[15] drug delivery,[16] optical applications[17] and heat transformation.[18–21]

In classical coordination chemistry or organometal chemistry the concept of free coordination sites was already well established. A free coordination site exists in complexes with a lower than the normal coordination number of the metal atom. For those

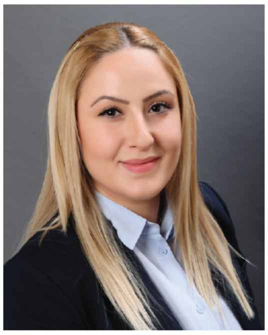

Ülkü Kökçam-Demir

Ülkü Kökçam-Demir graduated from Heinrich-Heine University of Düsseldorf with a BSc and an MSc degree in Business Chemistry. Currently, she is pursuing her PhD under the guidance of Prof. Dr Christoph Janiak at the Institute of Bioinorganic Chemistry and Catalysis at the University of Düsseldorf. Her research focuses on the synthesis, characterization and application of new metal–organic framework-based materials for gas adsorption.

Anna Goldman

Anna Goldman graduated from Heinrich-Heine University of Düsseldorf with a MSc degree in Chemistry. She is currently a PhD student at the Institute of Bioinorganic Chemistry and Catalysis under the supervision of Prof. Christoph Janiak. Her research focuses on the synthesis, characterization and application of new monoalkylphosphonate-carboxylate coordination polymer/metal–organic framework-based materials for gas adsorption.

---

[a] *Institut für Anorganische Chemie und Strukturchemie, Heinrich-Heine-Universität Düsseldorf, D-40204 Düsseldorf, Germany. E-mail: janiak@hhu.de*

[b] *Department of Chemistry, Faculty of Sciences, Tarbiat Modares University, P.O. Box 14115-175, Tehran, Islamic Republic of Iran. E-mail: morsali_a@modares.ac.ir*

[c] *Institut für Theoretische Chemie und Computerchemie, Heinrich-Heine-Universität Düsseldorf, D-40204 Düsseldorf, Germany. E-mail: Oliver.Weingart@hhu.de*

† Electronic supplementary information (ESI) available. See DOI: 10.1039/c9cs00609e

‡ These authors contributed equally.

3d metal atoms for which an octahedron with coordination number six would be expected, a missing ligand and only fivefold coordination would establish a free coordination site. Square-planar metal complexes which are often found for d^8 metal atoms have inherently two free coordination sites.[22,23] In ligand substitution reactions with metal complexes the dissociative pathway proceeds through a lower coordination number/free coordination site as the intermediate or transition state. Oxidative addition needs open metal sites with possibility to increase the coordination (and oxidation) number by two. A free coordination site is required *e.g.* for π-coordination of an olefin prior to insertion in the metal–carbon bond of the polymer chain end for olefin polymerization. Many metalloproteins and -enzymes have free coordination sites before the substrate coordination, *e.g.* the iron atom in hemoglobin is five-fold coordinated before the dioxygen coordination.[24] The ''free coordination site'' can be temporarily occupied by a labile water (aqua) ligand. Different to open metal sites in MOFs, the ''free coordination sites'' in classical coordination chemistry often present only intermediary or transition states. This is due to the presence of solvent molecules as coordination chemistry or catalysis is often conducted in solution. Hence, the potential free coordination sites will then be occupied by labile solvent molecules.[22,25]

Overall, the M–L bond in metal–ligand coordination complexes is often kinetically labile. Thus, in solution there will often be an equilibrium between the desired ligand and competing coordinating solvent molecules like water, alcohols, *etc.*[24] The lability of the metal–ligand bond is an inherent necessity of the use of metal atoms as catalytic centers in metallo-enzymes or technical catalysts. When the thermally activated ligand exchange will be very slow as for kinetically stable (inert) metal complexes, *e.g.* of Co^{3+} in $[\mathrm{Co(CN)_6}]^{3-}$ or $[\mathrm{Co(NH_3)_6}]^{3+}$ excitation with light can lead to an effective (fast) ligand exchange through the population of a photoactive excited state. When the light irradiation of the complexes is carried out in water, the CN$^-$ or NH$_3$ ligand will initially be replaced by an aqua ligand (photoaquation).[22,25]

From left to right: Leili Esrafili and Maniya Gharib

Leili Esrafili was born in Shabestrar, Iran in 1991 and she received her BS degree in 2014 from Tabriz University. Maniya Gharib was born in Tehran in 1990 and earned her BS and MS degree in 2013 and 2015, respectively, at Tehran University. They joined Tarbiat Modares University in 2014 and 2015 to pursue her graduate studies under the supervision of Prof. Ali Morsali. Their research interest focuses on design and engineering of 2D and 3D MOFs and investigate their applications in environmental redemption catalysis and sensing. In particular, they are interested in the synthesis of mixed-metal MOFs and materials with flexibility.

Ali Morsali

Professor Ali Morsali received his BS and MS degree from Tarbiat Moallem University and Zanjan University. He then attended Tarbiat Modares University, Tehran and earned his PhD in 2003 and he began his independent career at the Tarbiat Modares University where he has been a Professor in the Department of Chemistry since 2012. He spent two sabbatical periods in the groups of Prof. Hupp and Prof. Farha, Northwestern University in 2016 and with Prof. Omar Yaghi, Berkeley in 2017. Also, in 2019, he spent three months as a scientific visitor at Düsseldorf University in Prof. Christoph Janiak's group. His research interests are primarily in the area of inorganic chemistry, CPs and MOFs.

Oliver Weingart

Oliver Weingart received his PhD in Theoretical Chemistry at Duisburg University, Germany in 2005 under the guidance of Prof. V. Buss, working on excited state molecular dynamics of polyene Schiff bases. In 2010, he joined Prof. Walter Thiel's group at the Max-Planck-Institute for Coal Research in Mülheim, Germany. Since 2012 he is a researcher at the Institute of Theoretical and Computational Chemistry at Heinrich-Heine-University Düsseldorf in Prof. Christel Marian's group, where he did his habilitation in Computational Photodynamics in 2017. He develops and applies quantum mechanical/molecular mechanical (QM/MM) methods to investigate ground- and excited-state reactions of molecules in complex environments.

The M–L bond dissociation energy of the coordinative bond is usually lower than that of a covalent C–C or C–O bond.[24] From coordination chemistry principles, the thermodynamic stability of the M–L bond can be increased with high valence metal ions, such as Cr^{3+}, Fe^{3+}, and Zr^{4+}. With the coordination environments being equal, an increased charge will increase the electrostatic interaction between the metal ions and the ligands. A measure of the complex stability is the stability constant, which typically is not very large for monodentate ligands.[24,26]

In MOFs the metal ion which will be considered for the generation of the open metal site should be part of the metal node or metal secondary building unit. There are also MOFs which have metal ions as part of the linker, in so-called metallo-ligands.[27–30] The formation or presence of open metal sites in these metallo-ligands will not be the topic of this review as this is even more closely related to classical coordination chemistry.

In MOF structures any change to the metal ions in the metal SBU must ensure the integrity of the network. Importantly, the MOF structure must not collapse, and their crystallinity and porosity should be preserved, that is, a labile terminal ligand should be removed without damage to the framework. The obtained not fully coordinated metal ions are termed open metal sites (OMS) or coordinatively unsaturated sites (CUS) or occasionally also open coordination sites (OCS). Open metal site chemistry based on MOFs started in 1999, when HKUST-1 (Hong Kong University of Science and Technology, commercially available as Basolite C300 from BASF) was reported by Williams *et al.*[31] as the first MOF with an obviously easily obtainable OMS. The first report of a Zn-MOF with an open metal site was confirmed in 2000 by Yaghi *et al.*[32,33] with $[Zn_2(btc)(NO_3)(C_2H_5OH)_3]\cdot(C_2H_5OH)_2(H_2O)$, also named as MOF-4 which is converted to $[Zn_2(btc)(NO_3)]$ after activation.[34,35]

We note that this review is only on MOFs with proven OMS formation. Thus, we solely considered work in which OMS are not only invoked but are clearly verified by analytical methods. The large number of publications which refer to OMS with no definitive proof were not assessed for this review.

Christoph Janiak

Christoph Janiak is full professor for Bioinorganic Chemistry and Catalysis at the University of Düsseldorf since 2010, with research interests in the synthesis and properties of metal–organic frameworks (MOFs) and porous organic polymers, mixed-matrix membranes, metal nanoparticles, ionic liquids and catalysis. Until 2018 he was a visiting professor at Wuhan University of Technology and currently he is a guest professor at the Hoffmann Institute of Advanced Materials at Shenzhen Polytechnic in China. He has (co-)authored about 500 research papers and is a Fellow of the Royal Society of Chemistry (FRSC).

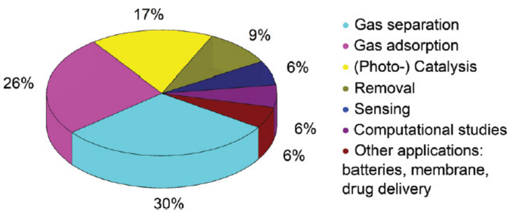

Fig. 1 Most commonly associated potential applications to open metal site MOFs in percent [%] of its number of publications. Taken from SciFinder – CAS by literature search. (Source: https://sso.cas.org/as/jUgiM/resume/as/authorization.ping. Search term: metal–organic frameworks, open metal sites (486 hits, approx. 100%): gas separation (146 hits, 30%), gas adsorption (125 hits, 26%), (photo-) catalysis (84 hits, 17%), removal (46 hits, 9%), sensing (30 hits, 6%), computational studies (27 hits, 6%), other applications: batteries, membrane and drug delivery (28 hits, 6%). Search day: 17.06.2019).

The activation of open metal sites in MOFs is often seen as a key in applications. The OMS in MOFs represent often the strongest binding sites, which leads to an increased interaction with different sorbate molecules, compared to MOFs where the metal sites are fully occupied.[36,37] Hence, such OMS-MOFs are very promising candidates for applications, like catalysis,[38–40] sensing,[41] gas separation (*e.g.* alkene/alkane,[42–45] C_2H_2/CO_2,[46–48] CO_2/CH_4,[47] C_2H_2/CH_4,[48,49] C_2H_4/CH_4,[49] CO_2/CH_4,[49,50] 1-butene from other butene isomers[51]),[52–54] and gas sorption, *e.g.* H_2,[55–65] CO_2,[49,66–71] O_2,[72] CO,[73] NO,[74] N_2O,[75] acetylene C_2H_2,[49,76–78] SO_2,[79] CH_4,[80,81] olefins (ethylene,[49,82] propylene[82]) and alkanes (ethane,[82] propane[82]), ammonia,[83] sulfonamide,[84] phosphine.[85] The most commonly associated potential applications to open metal sites are shown in Fig. 1. The largest number of potential applications in connection with OMS by the number of publications is gas separation and adsorption. The first connection of OMS to gas adsorption for H_2 was reported in 2005 by Yaghi *et al.*[86] Following the already well-established coordination chemistry and catalysis principles for free coordination sites (see above) OMS-MOFs show an increase in H_2 uptake capacity and improved isosteric heat of adsorption (Q^0_{st}), due to the dihydrogen affinity of the metal atom (akin to the formation of metal–H_2 complexes).[87–92]

Furthermore, OMS can give π-interactions with olefins (formation of metal–olefin complexes) and feature a high adsorption enthalpy of CO_2 which is advantageous for its gas sorption, and separation.[52,93–97] In addition, OMS of electron-deficient metal atoms can act as Lewis acid sites, *e.g.* in catalytic reactions.[32,39] The post-functionalization of OMS, in other words ligand substitution through first formation of an OMS followed by a new ligand coordination to the OMS in MOFs, can be used to postsynthetically functionalize MOFs in general.[98]

In this review, we focus on the synthetic strategies for the verified formation of OMS in MOFs and on applications where a strong evidence for the effect of OMS was provided. Moreover, we also summarize computational studies, because they are an important foundation for studying and predicting sorption properties and applications of OMS-MOFs. Therefore, this overview should help to advance the design of OMS-MOFs for desired applications.

2. Synthetic and structural overview on typical SBUs for open metal sites and coordinated solvent removal strategies

From the initial MOF synthesis, the (remaining) metal coordination sites and the MOF pores will be filled by the solvent which was used in the synthesis. This solvent will be a ligand at the metal atoms to reach their stable coordination number and act as a porogen for the formation of the framework structure. The stability of the SBU and thus the entire framework depends upon the coordination chemistry of the metal atom. A metal atom has a preferred or typical coordination geometry governed by coordination chemistry principles, such as the metal atom size and d-electron configuration (see above in Introduction). If the metal ions are not solely coordinated to the donor atoms of the bridging ligands, their coordination sphere is usually saturated with coordinating unidentate solvent molecules derived from the synthesis medium.

The as-synthesized MOF will have initially all metal ions in the SBU in their fully coordinatively saturated state, that is, most stable coordination environment according to their usual coordination numbers, which are typically six (octahedral) or four (tetrahedral) for most 3d transition metal ions. In order to obtain open metal sites in the metal SBUs of MOFs (Table 1) an initial labile terminal ligand which may typically be a solvent molecule needs to be removed from its coordinating metal atom (Fig. 2). The procedure for this ligand removal with OMS generation is usually solvent exchange and removal, which may be generally termed "activation"[68,96,99,100] and can be further differentiated into thermal, chemical[101–104] or photothermal[105] activation (Fig. 3).

The synthesis of OMS in MOFs by the general removal of coordinated solvent molecules must proceed without causing a collapse of the network structure.[106,107] It should be noted, however that the salient features of MOFs, namely crystallinity and proven porosity must be retained upon OMS formation which is not always verified in the literature.

In general, the removal of these coordinated solvent molecules is accompanied by a change in the coordination geometry of the metal center.

The open metal sites in MOFs can be generated by the removal of coordinated labile solvent ligand molecules like water, alcohols (methanol and ethanol), acetonitrile, and DMF (*N*,*N*′-dimethylformamide). The attempt to simply remove the coordinated solvent ligand (and the solvent from the pores) by heating under vacuum, however, may often fail and result in framework degradation or complete decomposition. Some of the solvent ligands are low volatile (*e.g.* DMF), therefore require high temperature or long evacuation times. Others are more strongly coordinated to the network (*e.g.* water through stronger metal coordination or hydrogen-bonding to the ligand donor atoms) and have a high surface tension in their liquid state and may lead to cavitation effects, that is, network collapse upon their removal.[108]

In order to ensure network retention there are several strategies and procedures in the literature to remove the coordinated solvent molecules (Fig. 3):[101–104,106]

(I) Solvent exchange and removal by thermal activation.[86,92] A less-volatile (higher boiling) solvent ligand is first exchanged with a more volatile (lower boiling) solvent. At the same time the less volatile solvent is thereby washed from the pores of the MOF. This solvent exchange procedure is then followed by thermal activation,[83,98–100,109–116] that is, by applying heat energy and/or (high) vacuum.

(II) Chemical activation.[101–104] A less-volatile solvent is first exchanged by a (washing) treatment with highly volatile and only very weakly coordinating halogenated solvents. Different from (I) the final halogenated solvent removal occurs upon air-drying without using extra thermal energy (accept the energy provided by room temperature). Thereby, the final drying procedure is simpler and faster than in (I).

(III) Photothermal activation.[105] Especially for kinetically stable (inert) metal ions (*e.g.* Cr^{3+}) solvent ligand exchange and thermal ligand exchange will be very slow. Instead irradiation with (UV-vis) light then leads to a fast ligand exchange or removal through the population of a photoactive excited state. Selected papers will be presented, which describe the removal of the coordinated solvent molecules to form open metal sites in their MOFs, by using these three synthetic strategies. Table 2 gives an overview of the OMS-MOFs with their removal strategies in detail, which are reported in this review.

In the following we only reference work where OMS formation was confirmed in combination with framework stability.

2.I Solvent exchange and removal by thermal activation

The most used strategy for forming OMS is by removing the coordinated solvent molecules from the metal atoms in MOFs by the solvent exchange (SE) method, followed by thermal activation (TA).[86,87,93,98–100,109–114,116]

Dinuclear paddle-wheel SBUs. The dinuclear paddle-wheel metal unit $[M_2(COO)_4(solvent)_2]$ is of great interest, because these structures can be systematically tuned by carboxylate linkers of different lengths and geometries.[117–122] This unit is surrounded by four carboxylate groups in a 4-c square planar fashion (Fig. 4). The labile solvent molecules terminate the two axial positions of the metal handle.

For Cu^{2+} the easy removal is due to the Jahn–Teller effect for the d^9-ion which leads to weakly-bound apical ligands with long M–L bonds and a tendency towards formation of a square-planar geometry.[123–125]

The first MOF, that was examined for open Cu^{2+} sites, was HKUST-1, $[Cu_3(btc)_2(H_2O)_2]$. The framework is constructed of these dicopper paddle-wheel SBUs linked by trigonal 1,3,5-btc (H_3btc = 1,3,5-benzentricarboxylate) linkers.[31] During the activation step the color changed from pale blue to dark blue due to the loss of the water molecules coordinated to the Cu centers as the coordination number of the Cu atoms decreased from five (square-pyramidal) to four (square planar).[126,127] Sometimes the dark-blue color of activated HKUST-1 is also referred to as deep-purple.[105]

Table 1 Overview presentation of selected prototypical OMS-MOFs with their linkers and SBUs discussed in this review[a]

Ligand	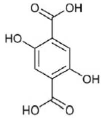 H_2dobdc	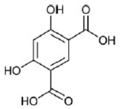 H_4(*m*-dobdc)	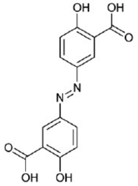 H_4olz	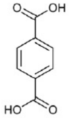 H_2bdc	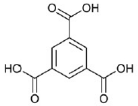 H_3btc	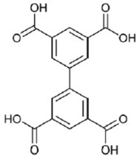 H_2bptc	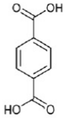 H_2bdc	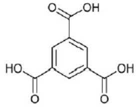 H_3btc
Selected MOF M with OMS	M-MOF-74 Mg^{2+}, Mn^{2+}, Fe^{2+}, Co^{2+}, Ni^{2+}, Cu^{2+}, Zn^{2+}, Cd^{2+}	$[M_2(m\text{-dobdc})]^*$ Mg^{2+}, Mn^{2+}, Fe^{2+}, Co^{2+}, Ni^{2+}	$[M_2(olz)]$ Mg^{2+}, Fe^{2+}, Co^{2+}, Ni^{2+}, Zn^{2+}	MOF-2 Cu^{2+}	HKUST-1 Cr^{2+}, Cu^{2+}	MOF-505 Cu^{2+}	MIL-101 V^{3+}, Cr^{3+}, Fe^{3+}	MIL-100 Sc^{3+}, V^{3+}, Cr^{3+}, Fe^{3+}
SBU		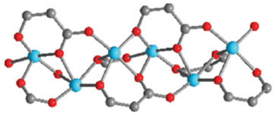			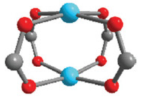		 (● = F, OH)	

Ligand	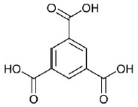 H_3btc	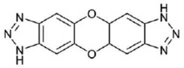 H_2btdd	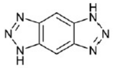 H_2bbta	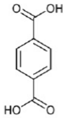 H_2bdc	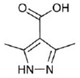 H_2dmcapz
Selected MOF M with OMS	$[Eu(btc)]$ Eu^{3+}	$[M_2Cl_2btdd]$ Mn^{2+}, Co^{2+}, Ni^{2+}	MAF-X27-Cl Mn^{2+}, Co^{2+}	UiO-66 Zr^{4+}	$[Cu_2(dmcapz)]$ Cu^{2+}
SBU	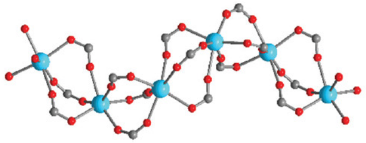	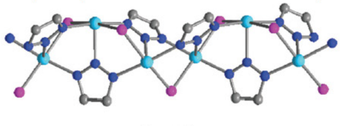 (● = Cl)		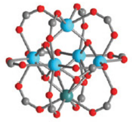	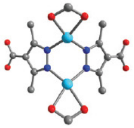

Table 1 (continued)

Ligand	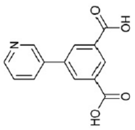 H_2pyip	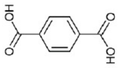 H_2bdc 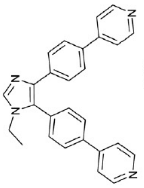 L**	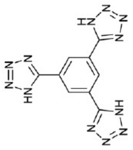 H_3btt
Selected MOF	NJU-Bai33	$[Co_3(L)(bdc)_{2.5}(OAc)]$	M-btt
M with OMS	Mn^{2+}	Co^{2+}	Cr^{2+}, Mn^{2+}, Fe^{2+}, Co^{2+}, Cu^{2+}, Cd^{2+}
SBU	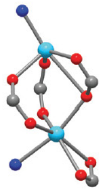	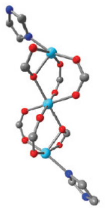	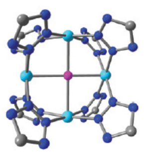 (● = Cl)

[a] The coordinated solvent molecules on the metal nodes, present in the X-ray structure, and the ligand hydrogen atoms are not shown for clarity. Atom color scheme: C grey; O red; N dark-blue; metal atoms pale blue; Cl, F, OH purple. Crystal structure information for the respective compounds was taken from the Cambridge crystallographic data center (CCDC). For a deciphering of the used acronyms such as HKUST, MIL, UiO, NJU, *etc.* See abbreviations at the end of this review.*For $[M_2(m\text{-dobdc})]$ and $[M_2(olz)]$, the SBU of M-MOF-74 is representatively shown, since both compounds are isostructural.**L = 4,5-bis[4(4-pyridyl)phenyl]1-ethyl-1*H*-imidazole.

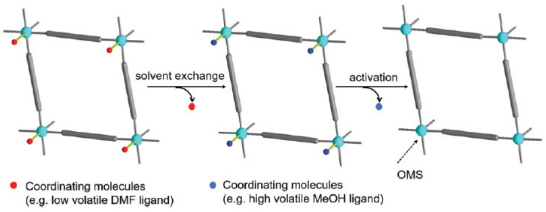

Fig. 2 Schematic presentation of the generation of unsaturated coordination environments on metal atoms in MOFs by replacing a low-volatile ligand (*e.g.* DMF) by a higher-volatile ligand (*e.g.* MeOH) through "solvent exchange" for the subsequent activation, that is, solvent removal.

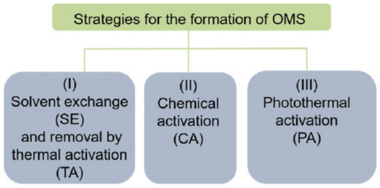

Strategies for the formation of OMS

(I) Solvent exchange (SE) and removal by thermal activation (TA)

(II) Chemical activation (CA)

(III) Photothermal activation (PA)

Fig. 3 Overview on the synthetic strategies for the formation of OMS in MOFs.

Nair *et al.*[93] reported on the SE method to activate the Cu^{2+} sites in HKUST-1 for olefin/paraffin separation. They analyzed the removal of the solvent molecules and the availability of open metal sites in detail by *in situ* Fourier transform infrared spectroscopy (FT-IR), *in situ* mass spectrometry, and vapor-phase binary breakthrough experiments. The Cu-bound water exchange was based on removal and replacement by acetone through washing three times with fresh dry acetone over two days. Acetone was finally removed by drying at 70 °C for 1 h and evacuating at room temperature (RT) for 24 h in a vacuum oven to yield the solvent-exchanged and thermally activated sample (sample S2).[93]

For comparison, an only thermally activated sample (sample S1) was prepared by drying at 70 °C for 2 h and evacuating at RT for 24 h in a vacuum oven at 7×10^{-4} bar without previous SE. Nair *et al.* found that sample S2 had a 29% higher BET (Brunauer–Emmett–Teller) surface area of 1600 $m^2\ g^{-1}$ with a pore volume of 0.71 $cm^3\ g^{-1}$ than sample S1, which gave only 1240 $m^2\ g^{-1}$ with 0.55 $cm^3\ g^{-1}$ pore volume.[93]

Fig. 5 shows the powder X-ray diffractions patterns (PXRD) of sample S1 and sample S2 at RT and the PXRDs at different temperatures of the thermally activated sample S1, where, the reflection at 6.5° disappeared, which was seen as a proof for the removal of the aqua ligands on Cu^{2+}.[93]

Furthermore, Nair *et al.* found that the total adsorption capacity and the equilibrium olefin selectivity in sample S2 was 44–55% and 10% higher, respectively, than in the thermally-only activated sample S1. The authors explained these results by using *in situ* FT-IR measurements to show that sample S2 has very few free carboxyl groups, hence, much less structure defects than sample S1. For the availability of OMS, they measured the amount of water desorbed from a known mass

Table 2 Open metal sites in metal–organic frameworks, which are reported in this review

				Formation of OMS			
OMS	Ligand	MOF-formula with solvent ligands (without pore solvent)	MOF-acronym	Removal strategies	Temp. [°C] (time [h], vac)	Verification methods	Ref.
Mg	H_4dobdc	$[Mg_2(dobdc)(H_2O)_2]$	Mg-MOF-74	SE,^{f} TA, PA	200 (vac) 136 (30 min)	PXRD, TGA	70, 105 and 172
	H_4olz	$[Mg_2(olz)(solvent)_2]$	$[Mg_2(olz)]$	SE,^{c,f} TA	180 (12, vac)	PXRD, TGA	310
Sc	H_3btc	$[Sc_3(O)X_3(btc)_2(H_2O)_2]$	MIL-100(Sc)	SE^{e}	RT	PXRD	140 and 162
Zr	H_2bdc	$[Zr_6O_4(OH)_4(bdc)_6]$	UiO-66	TA	300 (vac); 300 (2, calcination)	PXRD, TGA	105, 114, 162 and 163
				PA	57 (30 min)		
	H_2bdc-NH_2	$[Zr_6O_4(OH)_4(NH_2\text{-bdc})_6]$	UiO-66-NH_2	SE,^{c,f} TA	150 (5, vac), 200 (16, vac)	—	164 and 284
V	H_2bdc	$[V_3(O)X(bdc)_3(H_2O)_2]$	MIL-101(V)	SE,^{c} TA	100 (12, vac), 150 (5, vac)	PXRD	143
	H_3btc	$[V_3(O)X_3(btc)_2(H_2O)_2]$	MIL-100(V)	SE^{e,g}	100	PXRD	140 and 143
Cr	H_2bdc	$[Cr_3(O)X(bdc)_3(H_2O)_2]$	MIL-101(Cr)	TA	150 (24, vac); 150 (12, vac)	—	113 and 143–148
	H_3btc	$[Cr_3(btc)_2(H_2O)_2]$	$[Cr_3(btc)_2]$	SE,^{f} TA	160 (48, vac)	—	134
	H_3btc	$[Cr_3(O)X_3(btc)_2(H_2O)_2]$	MIL-100(Cr)	SE,^{e,g} TA	RT (16), 120–140 (12, vac); 200 (1, vac)	FTIR, NMR, PXRD, SEM	112, 138, 140 and 141
	H_3btt	$Cr_3[(Cr_4Cl)_3(btt)_8(DMF)_{12}]_2$	Cr-btt	SE,^{c,f} TA	150 (12, vac)	PXRD	159
Mn	H_2bbta	$[Mn_2Cl_2(bbta)(H_2O)_2]$	MAF-X25-Cl	SE,^{f,g} TA	100 (12, vac)	PXRD, TGA	183 and 184
	H_2btdd	$[Mn_2Cl_2(btdd)(H_2O)_2]$	$[Mn_2Cl_2(btdd)]$	SE,^{f} TA	100 (vac)	PXRD, TGA	83
	H_2pyip	$[Mn_2(pyip)_2DMF]$	NJU-Bai33	SE,^{a} TA	110 (10, vac)	PXRD, TGA, FTIR	137
	H_3btt	$Mn_3[(Mn_4Cl)_3(btt)_8(MeOH)_{12}]_2$	Mn-btt	SE,^{d} TA	150 (2, vac)	PXRD, TGA	160
	H_3tatb	$2H_3O^{+}\cdot[Mn_4O(tatb)(H_2O)_4]_{8/3}$	PCN-9(Mn)	SE,^{b,f} TA	RT (12, vac), 60 (1, vac)	—	56 and 57
Fe	H_3btc	$[(Fe_3(O)F_{0.81}(OH)_{0.19})(btc)_2(H_2O)_2]$	MIL-100(Fe)	SE,^{e,g} TA	100 (12, vac) 150–250 (12, vac)	PXRD, FTIR	143
	H_3btt	$Fe_3[(Fe_4Cl)_3(btt)_8(MeOH)_{12}]_2$	Fe-btt	SE,^{f} TA	135 (24, vac)	TGA	157
	H_3tatb	$2H_3O^{+}\cdot[Fe_4O(tatb)(H_2O)_4]_{8/3}$	PCN-9(Fe)	SE,^{b,f} TA	RT (12, vac), 60 (1, vac)	—	57
	H_4dobdc	$[Fe_2(dobdc)(DMF)_2]$	Fe-MOF-74	SE,^{f} TA	160 (48, vac)	PXRD, TGA	167
	H_4olz	$[Fe_2(olz)(solvent)_2]$	$[Fe_2(olz)]$	SE,^{c,f} TA	120 (vac)	PXRD, TGA	310
Co	H_2bbta	$[Co_2Cl_2(bbta)(H_2O)_2]$	MAF-X27-Cl	SE,^{f,g} TA	100 (12, vac)	PXRD, TGA	182 and 184
	H_2bdc L = 4,5-bis[4(4-pyridyl)phenyl]1-ethyl-1*H*-imidazole	$[Co_3L(CH_3OH)_{0.5}(H_2O)_{0.5}(bdc)_{2.5}(OAc)]$	$[Co_3(L)(bdc)_{2.5}(OAc)]$	TA	70 (2)	PXRD, TGA	99
	H_2btdd	$[Co_2Cl_2(btdd)(H_2O)_2]$	$[Co_2Cl_2(btdd)]$	SE,^{f} TA	100 (vac)	PXRD, TGA	83
	H_3btt	$Co_3[(Co_4Cl)_3(btt)_8(MeOH)_{12}]_2$	Co-btt	SE,^{f} TA	135 (24, vac)	FTIR, PXRD, TGA	155
	H_3tatb	$2H_3O^{+}\cdot[Co_4O(tatb)(H_2O)_4]_{8/3}$	PCN-9(Co)	SE^{b,f}	RT (12, vac), 60 (1, vac)	PXRD	57
	H_3tzpa	$[Co_2(tzpa)(OH)(H_2O)_2]$	$[Co_2(tzpa)(\mu_3\text{-OH})]$	SE,^{f} TA	220 (vac)	PXRD, TGA, FTIR	181
	H_4dobdc	$[Co_2(dobdc)(H_2O)_2]$	Co-MOF-74	SE,^{f} TA	200 (vac)	SCXRD, TGA	70 and 173
	H_4olz	$[Co_2(olz)(solvent)_2]$	$[Co_2(olz)]$	SE,^{c,f} TA	180 (12, vac)	PXRD, TGA	310
	H_8tdcppy	$[Co_3(\mu_3\text{-O})(tdcppy)_6(solvent)_3]$	$[Co_3(\mu_3\text{-O})(tdcppy)_6]$	SE,^{f} TA	65 (12, vac)	PXRD, TGA	67
Ni	H_2bdc Hna	$[(Ni_2(H_2O)_2)_{1.5}(Ni_3OH)_2(bdc)_6(na)_6]$	—	SE,^{b,c} TA	100 (vac)	PXRD, TGA	58
	H_2btdd	$[Ni_2Cl_2(btdd)(H_2O)_2]$	$[Ni_2Cl_2(btdd)]$	SE,^{f} TA	100 (vac)	PXRD, TGA	83
	H_4dobdc	$[Ni_2(dobdc)(H_2O)_2]$	Ni-MOF-74	SE,^{f} TA TA CA PA	200 120 (1, vac) — 167 (30 min)	NMR, PXRD, TGA	70, 101–105, 174 and 326
	H_4olz	$[Ni_2(olz)(solvent)_2]$	$[Ni_2(olz)]$	SE,^{c,f} TA	180 (12, vac)	PXRD, TGA	310
	H_2sip	$[NaNi_3(OH)(sip)_2]$	—	TA	300–350 (vac)	PXRD, TGA	59

Table 2 (*continued*)

				Formation of OMS			
OMS	Ligand	MOF-formula with solvent ligands (without pore solvent)	MOF-acronym	Removal strategies	Temp. [°C] (time [h], vac)	Verification methods	Ref.
Cu	H_2bdc	[Cu_2(bdc)$_2$(DMF)$_2$]	Cu-bdc/MOF-2	SE,^{f} TA CA	60 (12), 120 (vac) —	FTIR, SEM, NMR, PXRD	98 and 101–104
	H_2dmcapz	[Cu_2(dmcapz)$_2$(H_2O)]	[Cu_2(dmcapz)$_2$]	SE,^{g} TA	150 (7, vac), −196 (vac)	PXRD, TGA	100
	H_2sp5-BF_4	[Cu-sp5-MeOH]	[Cu-sp5]	TA	120 (15, vac)	PXRD, TGA	332
	H_3btc	[Cu_3(btc)$_2$(H_2O)$_2$]	HKUST-1/MOF-199	SE,^{a,f,g} TA CA PA	RT (24, vac), 70 (1–2) 100 (12, vac), 170–280 120–150 (vac) 150 (10, vac) — 125 (30 min)	DSC, FTIR, NMR, PXRD, TGA, SEM	93, 101–105, 109, 111, 313 and 334
	H_3btt	HCu[(Cu_4Cl)$_3$(btt)$_8$(H_2O)$_{12}$]	Cu-btt	SE,^{f} TA	120 (24, vac)	FTIR, PXRD, TGA	158
	H_3btt$_{ri}$	H_3[(Cu_4Cl)$_3$(btt$_{ri}$)$_8$(DMF)$_{12}$]	Cu-btt$_{ri}$	SE,^{f} TA	180 (12, vac); RT (3, vac), 180 (3, vac)	PXRD, TGA	278, 287, 288 and 300
	H_3L = [1,1′:4′,1″-terphenyl]-3,4″,5-tricarboxylic acid	[Cu_2(L)$_2$(HCOO)$_2$(H_2O)$_2$] [Cu_6(L)$_4$(H_2O)$_6$]	PCP-31; PCP-32	SE,^{a} TA	RT (6), 60 (6), 120 (24, vac)	PXRD	119
	H_3tzi	[Cu_6O(tzi)$_3$(H_2O)$_9$(NO_3)]	—	SE,^{e} TA	RT (vac), 85 (6, vac)	PXRD	60
	H_4adip	[Cu_2(adip)(H_2O)$_2$]	PCN-14	SE,^{b,f} TA	RT (12, vac), 120 (4, vac)	PXRD, TGA	121
	H_4aobtc	[Cu_2(abtc)(H_2O)$_2$]	PCN-10(Cu)	SE,^{b,f} TA	RT (12, vac), 120 (4, vac)	PXRD, TGA	63
	H_4bptc	[Cu_2(bptc)(H_2O)$_2$]	MOF-505/NOTT-100	SE,^{a} TA	RT (15, vac); 70 (15, vac); 120 (12, vac)	PXRD, TGA	86 and 87
	H_4dobdc	[Cu_2(dobdc)(DMF)$_2$]	Cu-MOF-74	SE,^{d} TA CA	70 (vac), 150-225 (5, vac) —	NMR, PXRD	101–104 and 175
	H_4L = 4′,4‴-(pyridine-3,5-diyl)bis([1,1′-biphenyl]-3,5-dicarboxylic acid)	[Cu_2($C_{33}H_{17}NO_8$)(H_2O)$_{0.65}$]	MFM-170	SE,^{a} TA	423 (24, vac)	PXRD, TGA	122
	H_4mbdpb	[Cu_6(mbdpb)$_3$(H_2O)$_6$]	NJFU-3	SE,^{c,f} TA	90 (20, vac)	PXRD	118
	H_4mdip	[Cu_6(C_s-mdip)$_2$(C_{2v}-mdip)(H_2O)$_6$]	PCN-12(Cu)	SE,^{b,f} TA	RT (12, vac), 150 (4, vac)	PXRD, TGA	117
	H_4sbtc	[Cu_2(sbtc)(H_2O)$_2$]	PCN-11(Cu)	SE,^{b,f} TA	RT (12, vac), 120 (4, vac)	PXRD, TGA	63
	H_5n	[Cu_2(*n*)(H_2O)$_2$]	NEM-4	SE,^{f} TA	90 (12, vac)	NMR, PXRD	110
	H_6bhb	[Cu_3(bhb)(H_2O)$_3$]	UTSA-20	SE,^{a} TA	120 (24, vac)	PXRD	177 and 360
	H_6tdpat	[Cu_3(tdpat)(H_2O)$_3$]	Cu-tdpat	SE,^{f} TA	120 (24, vac); 120 (10, vac)	PXRD, TGA	333 and 334
	H_6L = $C_{54}H_{30}O_{12}$	[Cu_3($C_{54}H_{24}O_{12}$)(H_2O)$_3$]	NOTT-116/ PCN-68	SE,^{a} TA	RT (vac), 100 (12, vac)	PXRD, TGA	62 and 87
	H_6L = H_6btat	[Cu_3(L)(H_2O)$_3$]	NOTT-112/MFM-112a	SE,^{a} TA	115 (16, vac)	PXRD, TGA	61, 62 and 120
	H_4L = tetracarboxylic acid ligands with different functionalities at the aromatic core	[Cu_2(L)(H_2O)$_2$]	NOTT-101/ZJU-24; NOTT-102/MFM-102; -103; -105; -106; -107	SE,^{a} TA	140 (20, vac)	PXRD, TGA	87 and 312
Zn	H_3btc	[Zn_2(btc)(NO_3)(EtOH)$_3$]	MOF-4	TA	RT (48, vac), 72 (16, vac)	—	32 and 33
	H_4dobdc	[Zn_2(dobdc)(DMF)$_2$]	Zn-MOF-74	PA	145 (30 min)	PXRD	105, 173 and 340
	H_4olz	[Zn_2(olz)(solvent)$_2$]	[Zn_2(olz)]	SE,^{c,f} TA	100 (12, vac)	PXRD, TGA	310
Cd	H_3btt	Cd_3[(Cd_4Cl)$_3$(btt)$_8$(MeOH)$_{12}$]$_2$	Cd-btt	SE,^{f} TA	135 (24, vac)	FTIR, PXRD, TGA	155
	H_4dobdc	[Cd_2(dobdc)(H_2O)$_2$]	Cd-MOF-74	SE,^{f} TA	100 (18, vac)	FTIR, PXRD, TGA	176
Eu	H_3btc	[Eu(btc)(H_2O)]	[Eu-btc]	TA	140 (24, vac)	TGA	180

[a] Solvent exchange (SE) with acetone. [b] SE with DCM. [c] SE with DMF. [d] SE: solvent not given. [e] SE with ethanol. [f] SE with methanol. [g] SE with water. For a deciphering of the used acronyms such as HKUST, MIL, UiO, NJU, *etc.* see abbreviations at the end of this review.

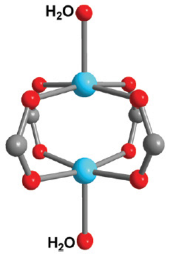

Fig. 4 Representation of the paddle-wheel unit of HKUST-1 [$Cu_3(btc)_2(H_2O)_3$], where the axial or apical sites of the Cu^{2+} ions are coordinated by water molecules. Crystal structure information from ref. 128 (CSD-Refcode DIHVIB01). The Cu···Cu distance is in the range of 2.5 Å.

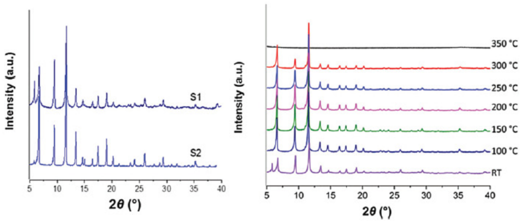

Fig. 5 Left: Powder X-ray diffraction patterns of thermally-only activated HKUST-1 (sample S1) and solvent-exchanged plus thermally-activated HKUST-1 (sample S2) at RT. Right: Powder X-ray diffraction patterns of a thermally-only activated HKUST-1 (sample S1) at different temperatures. Reproduced from ref. 93 with permission from the American Chemical Society, copyright 2016.

of completely dehydrated HKUST-1 and estimated the percentage of generated open metal sites (Fig. 6). Nair *et al.* found that the availability of OMS increases with the activation temperature, *e.g.*, after activating at 70 °C for 12 h under a vacuum of 7×10^{-4} bar, the percentage of open metal sites in sample S1 was 69%. The fraction of 93% of OMS could be made available by TA up to 230 °C before the framework began to collapse. It was also concluded that the presence of defects in the material due to incomplete coordination of btc^{3-} linkers to the metal centers, led to stronger binding of the aqua ligands on the defective metal sites.[93] The percentage of OMS in samples S2 was already 78% after activating at 50 °C for 12 h, 9% higher than in sample S1 and increased further to 98% at 200 °C.[93]

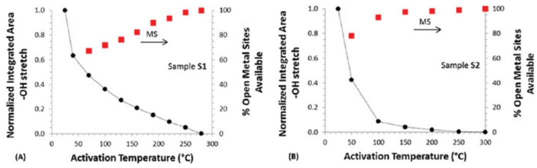

Fig. 6 Normalized mass of water lost from sample and percentage of OMS available for (A) sample S1 and (B) sample S2 at each activation step. Reproduced from ref. 93 with permission from the American Chemical Society, copyright 2016.

Hong *et al.*[111] reported also on the activation of HKUST-1 at different temperatures. The as-synthesized HKUST-1 was dried at 378 K for 12 h under vacuum and activated in a nitrogen flow at different temperatures, 443, 473, 503, 523, and 553 K, to remove the coordinated water molecules. Hong and his co-workers followed this removal using thermogravimetric analysis (TGA) and differential scanning calorimetry (DSC). The first weight loss from room temperature to 378 K of 10.8 wt% was due to the loss of physisorbed H_2O and residual ethanol in the MOF channels. The second weight loss of 4.3 wt% from 378 and 473 K, and the third weight loss of 1.8 wt% from 473 and 558 K was eventually due to the dehydration of coordinated water in HKUST-1. The weight loss above 573 K represented the disintegration of the MOF structure. These experimental data were not in full agreement with the calculated mass change (4.1 wt% × 2) for two coordinated water molecules. Instead the two desorption steps for coordinated water molecules suggested the presence of two non-equivalent coordinated water molecules on the paddle-wheel unit. The authors also reported that the crystallite size and morphology of the as-synthesized and the all-activated HKUST-1 MOFs did not show any changes in the PXRD and of the morphology under the SEM (scanning electron microscope) until HKUST-1-553 K. From nitrogen adsorption measurements at 77 K the BET surface areas increased from 1382 (for HKUST-1-443 K) over 1441 (for HKUST-1-503 K) to 1449 $m^2\ g^{-1}$ (for HKUST-1-523 K). We critically note that these differences are still within experimental error of about ±50 $m^2\ g^{-1}$ and values of 1441 and 1449 $m^2\ g^{-1}$ can be considered identical.[111] In 2016, Abbasi *et al.*[109] prepared microbelts of HKUST-1 as a heterogeneous catalyst for selective organic sulfide oxidation. After synthesis, the resulting solid was washed with water and methanol and dried under vacuum between 120 and 150 °C. Based on the TGA of these microbelts the removal of the coordinated water was assigned from the weight loss below 160 °C (Fig. 7).[129,130]

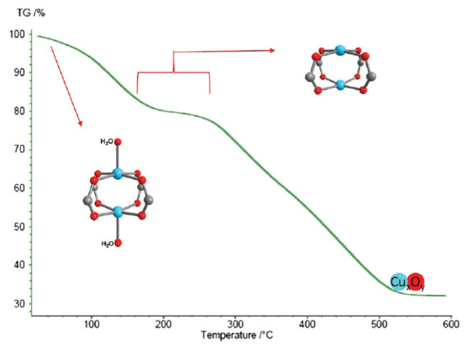

Fig. 7 Thermogravimetric analysis of HKUST-1 microbelts with the assigned weight losses for the aqua ligands giving the OMS-HKUST-1 network after 160 °C and before ~280 °C where the organic linkers start to degrade. Crystal structure information from ref. 128 (CSD-Refcode DIHVIB01). Reproduced from ref. 109 with permission of John Wiley & Sons, Ltd, copyright 2016.

In activated HKUST-1 the presence and co-existence of Cu^{1+} and Cu^{2+} was observed through the spectroscopic investigation of CO_2, CO or NO adsorbates (see in the application Section 4). Apparently, the oxidation state of copper can be reduced from Cu^{2+} and Cu^{1+} at higher temperature (approx. 473 K), for example by redox treatments, using vacuum and/or reducing gases at different sample temperatures.[127,131–133]

Other Cu MOFs that have been investigated for open metal sites are MOF-505 and MOF-2 ($[Cu_2(bdc)_2(DMF)_2]$).[86,98,134] Yaghi *et al.*[86] reported on the Cu-MOF MOF-505, which is isoreticular to HKUST-1 with the 3,3′,5,5′-biphenyltetracarboxylic acid (H_4bptc) ligand. Accordingly, the as-synthesized MOF-505 was activated by soaking in fresh acetone three times for 24 h each (72 h total) to remove the DMF molecules from the pores. After that, the acetone-containing material was carefully evacuated at $<1 \times 10^{-6}$ bar in three steps to remove the coordinated water molecules. In the first step, the solid kept at room temperature loses 42 wt% over 15 h and changes its color from blue-green to light blue. In the second step, at 70 °C for 15 h, the weight decrease continues (5.3 wt%), and the color changes to dark blue. In the third step, the solid, kept at 120 °C for 12 h, loses 4.7 wt% and changes its color to purple. Subsequently, the nitrogen uptake of MOF-505 increased over the three different activation steps. The nitrogen uptake in step I increased from 278 mg g^{-1} to 386 mg g^{-1} in step II, with a final increase to 526 mg g^{-1} in step III. The authors analyzed the stability of the framework under SE conditions using powder X-ray diffraction patterns and thermogravimetric analysis. They reported that the X-ray diffraction patterns of the simulated, as-synthesized, and acetone-exchanged scenarios showed nearly the same pattern and the PXRD of the desolvated material showed a decrease in the intensities and broader reflections with an additional broader reflection at around 7° 2-theta. The thermogravimetric analysis showed a weight loss of 30.8% below 250 °C, which agrees with the calculated value of 30.5% from the liberation of 2.5 acetone and three water molecules per Cu_2bptc formula unit. Furthermore, they explained that the removal of non-coordinated DMF/water molecules and coordinated water molecules have two positive effects, due to a decrease of sample mass and an increase of available micropore volume and specific surface area, on the H_2 adsorption capacity. The OMS enhance the hydrogen-framework (SBU) interaction. The authors also reported that MOF-505 has a high hydrogen uptake capacity due to the availability of open metal sites. The hydrogen uptake, which is 14.1 mg g^{-1} (1.41 wt%) after the first activation step, increased to 19.7 mg g^{-1} (1.97 wt%) in the second step, and finally to 24.7 mg g^{-1} (2.47 wt%) after complete dehydration in the third step.[86]

Liu *et al.*[98] reported on the Cu-bdc MOF MOF-2 as a heterogeneous interfacial catalyst for a sustainable Suzuki coupling reaction. For this, the open Cu sites were grafted with pyridyl-salicylimine (Py-SI) to get Cu-bdc/Py-SI, and then palladium(II) chloride was added to produce Pd@Cu-bdc/Py-SI MOF. To remove the coordinated DMF solvent molecules, the SE and TA method was used. The as-synthesized Cu-bdc was washed one time with DMF, then with hot methanol (70 °C) for 4 h, filtered, dried at 60 °C overnight, and activated at 120 °C under vacuum. The DMF-characteristic IR band at 1663 cm^{-1} had disappeared after activation.[98] Guo *et al.*[110] investigated the Cu-MOF NEM-4 with open Cu^{2+} sites in hydrocarbon storage and separation. Before measuring the gas sorption, NEM-4 was activated by the SE method using methanol and under dynamic vacuum at 90 °C for 12 h. Hereby, the color of NEM-4 changed from pale blue to dark blue, similar to the situation of other Cu-MOFs in which open sites can be generated.[110]

The d^4-Cr^{2+} ion (high-spin) also shows the Jahn–Teller effect and typically exhibits a tetragonally distorted-octahedral or square-planar coordination environment. For example, $[Cr_3(btc)_2]$ was activated by SE with methanol and dried under vacuum at 160 °C for 48 h. The fully activated framework exhibits a short Cr–Cr distance of 2.06(2) Å within the paddle-wheel SBU, which is typically interpreted as a quadruple bond.[134] Consequently the Cr^{2+} ion has a decreased Lewis acidity.[135]

Dinuclear distorted SBUs. For Mn^{2+} the octahedral coordination is typical. Since the high-spin d^5-Mn^{2+} ion has no crystal field stabilization energy, different geometries are possible depending on the coordinated ligands.[136] Employing 5-(pyridin-3-yl)isophthalic acid (H_2pyip) as a bifunctional trigonal linker in a solvothermal reaction with $MnCl_2 \cdot 4H_2O$ leads to the construction of $[Mn_2(pyip)_2DMF]\cdot DMF\cdot MeOH$ (NJU-Bai33; Nanjing University) including dinuclear distorted $[Mn_2(COO)_4N_2]$ SBUs.[137] As shown in Fig. 8, two crystallographically independent Mn^{2+} ions (Mn1 and Mn2) are present in the $[Mn_2(COO)_4N_2]$ SBU. The Mn1 coordination consists of five carboxylate moieties and one N atom from different linkers. The coordination environment of Mn2 is completed by an oxygen atom from DMF. Based on the thermogravimetric analysis the removal of the coordinated DMF molecules was achieved after SE with acetone followed by TA at 110 °C for 10 h under vacuum.[137]

In 2012, Kitagawa *et al.*[100] reported on the Cu-MOF $[Cu_2(dmcapz)_2(H_2O)]\cdot DMF_{1.5}$, obtained from CuX_2 (X = Cl, NO_3) salts with 3,5-dimethyl-4-carboxypyrazole (H_2dmcapz). This compound consists of a dinuclear SBU were the Cu^{2+} ions are surrounded by two N-donor atoms from two pyrazolate groups and by two carboxylate groups in a bidentate coordination mode each from different linkers. Further, the Cu^{2+} ions are bridged by a μ_2-OH_2 water ligand achieving a distorted square-pyramidal geometry (Fig. 9). The presence of bridging water molecules in a MOF SBU is unusual.[100]

To obtain open metal sites they used a reversed combination of TA and SE method and described a stepwise removal. In the

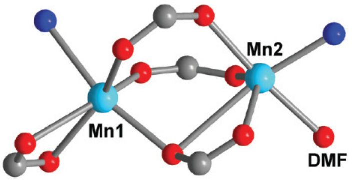

Fig. 8 Ball and stick presentation of the distorted $[Mn_2(COO)_4N_2(DMF)]$ cluster. Crystal structure information from ref. 137 (CSD-Refcode GASTIG).

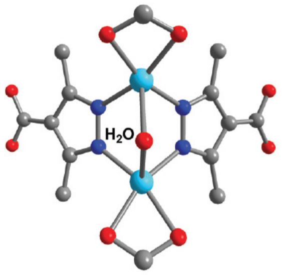

Fig. 9 SBU of [$Cu_2(dmcapz)_2(H_2O)$]. Crystal structure information from ref. 100 (CSD-Refcode ZECKID).

first step, the as-synthesized material [$Cu_2(dmcapz)_2(H_2O)$]·$DMF_{1.5}$ was evacuated at 120 °C for 7 h under high vacuum. The dark-blue TGA curve of [$Cu_2(dmcapz)_2(H_2O)$]·$DMF_{1.5}$ in Fig. 10, left shows a weight loss of 30% at around 100 °C, which stands for the removal of the DMF guest molecules and the aqua bridge, and a weight loss between 270 and 300 °C, due to framework decomposition. Then the sky blue [$Cu_2(dmcapz)_2(H_2O)$]·$DMF_{0.9}$ was soaked in water for 24 h to remove remaining DMF solvent molecules together with impurities of unreacted ligand or $CuCl_2$. In the next step, the water-exchanged pale blue [$Cu_2(dmcapz)_2(H_2O)$]·$H_2O_{4.5}$ was evacuated at 150 °C for 7 h under high vacuum. The pale blue TGA curve of [$Cu_2(dmcapz)_2(H_2O)$]·$H_2O_{4.5}$ in Fig. 10 shows a weight loss of 15% at around 80 °C, which means a loss of water guest molecules (calculated 16.1%), a small weight loss at around 120 °C, due to the loss of one water molecule per [$Cu_2(dmcapz)_2$] unit (experimental 3.8, calculated 4.3%) and a weight loss above 300 °C because of framework decomposition. The water removal is accompanied by a color change from pale blue to dark blue for which is akin to the color change in HKUST-1.[31] Therefore, the color change was also evidence to the loss of the water molecules coordinated to the Cu centers. The coordination number of the Cu atoms should have decreased from five (distorted square-pyramidal geometry) to four (distorted square planar), albeit it can be noted that no structural proof on the material [$Cu_2(dmcapz)_2$] was provided. The obtained dark-blue activated network [$Cu_2(dmcapz)_2$], returned its color to pale-blue within a few minutes under ambient moisture. Activated [$Cu_2(dmcapz)_2$] adsorbed ambient moisture and returned into [$Cu_2(dmcapz)_2(H_2O)$]·$H_2O_{4.5}$. If after the final activation step, [$Cu_2(dmcapz)_2$] was cooled to liquid-nitrogen temperature (77 K, under He atmosphere) a forest green (proven porous) material [$Cu_2(dmcapz)_2$], was obtained which was highly air- and moisture-stable at RT. The color change from dark blue to forest green at 77 K was interpreted to reflect a further change in the coordination of the metal centers. The authors assume a small twist of the dmcapz ligands concomitant with this change, so that a distortion from the initial square-planar geometry occurs to a distorted-tetrahedral coordination in [$Cu_2(dmcapz)_2$]. The higher hydrophobicity of the forest-green material compared with the dark-blue one seen as due to the structural reorganization which took place during the freezing process. To return forest-green [$Cu_2(dmcapz)_2$] into [$Cu_2(dmcapz)_2(H_2O)$]·$H_2O_{4.5}$, the former had to be soaked in deionized H_2O. The thermal stability of forest-green [$Cu_2(dmcapz)_2$] was followed by TGA (Fig. 10) with the green TGA curve indicating a fully activated material.[100]

Differences in the PXRDs at various temperature reflected the structural changes at the activation step from [$Cu_2(dmcapz)_2(H_2O)$]·$DMF_{1.5}$ to [$Cu_2(dmcapz)_2$]. From PXRD it was deduced that the μ_2-OH_2 bridge molecule is removed between 90 and 110 °C.[100]

Trinuclear SBUs. The solvothermal reaction of $Co(OAc)_2$ and 1,4-H_2bdc with the addition of imidazole as co-ligand (L = 4,5-bis[4(4-pyridyl)phenyl]1-ethyl-1*H*-imidazole), yielded a red-purple 3D-framework [$Co_3L(CH_3OH)_{0.5}(H_2O)_{0.5}(bdc)_{2.5}(OAc)$] solvent, which consists of Co_3-hourglass-like SBUs (Fig. 11).[99] The desolvated form [$Co_3(L)(bdc)_{2.5}$] with open Co^{2+} sites, was generated by heating at 70 °C for 2 h. During the activation, one of the six-coordinated {CoO_5N} chromophores changed to a coordinatively unsaturated five-coordinated one {CoO_4N}. For the other three types of Co^{2+} centers, no coordination-mode change was observed. After removing the coordinated methanol molecules, the solvent accessible void volume in [$Co_3L(bdc)_{2.5}(OAc)$] solvent increased to 1307 Å^3, that is to 41% of the total unit cell volume of 3181 Å^3. To regenerate [$Co_3L(CH_3OH)(bdc)_{2.5}(OAc)$] solvent without losing the single crystallinity, the activated form was soaked in methanol at room temperature for one day. Simulated and measured X-ray diffraction patterns were positively matched to further support the reversible methanol substitution-triggered single-crystal to single-crystal transformation. The thermogravimetric analysis of [$Co_3L(CH_3OH)_{0.5}(H_2O)_{0.5}(bdc)_{2.5}(OAc)$] solvent showed a weight loss of 4.8% at 150 °C, which indicates the removal of the MeOH/H_2O molecules. Based on TGA the desolvated OMS-containing Co^{2+}-MOF was stable up to 350 °C.[99]

It has to be noted that the coordination chemistry of Co^{2+} is a special case with its easy and reversible octahedral to tetrahedral transition. When two labile solvent ligands are present,

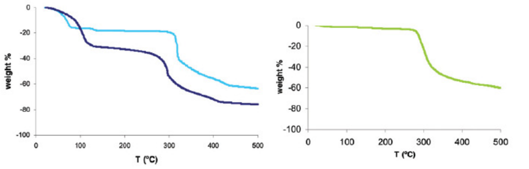

Fig. 10 Left: Thermogravimetric analyses of [$Cu_2(dmcapz)_2(H_2O)$]·$DMF_{1.5}$ (dark-blue), [$Cu_2(dmcapz)_2(H_2O)$]·$H_2O_{4.5}$ (pale blue) and right: of [$Cu_2(dmcapz)_2$] (green). Reproduced from ref. 100 with permission of Wiley-VCH Verlag GmbH & Co. KGaA, Weinheim, copyright 2012.

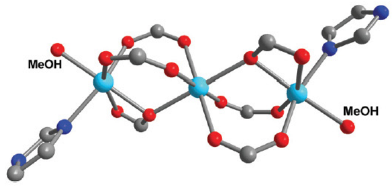

Fig. 11 Representation of the trinuclear Co^{2+} SBU in [$Co_3(L)(bdc)_{2.5}$]. Crystal structure information from ref. 99 (CSD-Refcode YUZRES).

then upon their removal the octahedral Co^{2+} environment changes to a tetrahedral Co^{2+} geometry, which can be identified through the concomitant color change from pink (octahedral) to blue (tetrahedral).[116] However, this well-known transition does not form OMS. Therefore, examples of such Co-MOFs were not included here as OMS-MOFs. It is also known that Co^{2+} forms low-spin compounds with strong-field ligands, which are often planar.

Open Cr^{3+}, Fe^{3+}, Sc^{3+}, $V^{3+/4+}$ and site MOFs with trinuclear $M_3O(CO_2)_6$ SBUs have been investigated in the 3D terephthalate (bdc) based structures MIL-101(Cr) and MIL-101(V) and in the trimesate (btc) based network MIL-100(Cr) (MIL = Materiaux de l'Institute Lavoisier). These MIL frameworks have the empirical formulae $[M_3(O)X(bdc_3/btc_2)(H_2O)_2]$ ($M = Cr^{3+}, Fe^{3+}, Sc^{3+}, V^{3+/4+}$; $X = OH^-$ or F^-).[112,113,138–142] Both MIL-100 and MIL-101 consist of three μ_3-oxido vertex-sharing M^{3+} octahedra, which are interconnected by bdc^{2-} or btc^{3-} ligands.[12] The trinuclear SBU $[M_3(\mu_3\text{-}O)(F/OH)(O_2C^-)_6(H_2O)_2]$ in MIL-101 and MIL-100 compounds has two terminal aqua ligands at two of the three octahedral M^{3+} ions (Fig. 12). The octahedral environment of the third metal atom is achieved through the coordination of an anionic ligand (OH^- or F^-), depending on the synthesis.[113,143–149]

In 2018, Mohsenzad *et al.*[112] reported on $MoO(O_2)_2$@En/MIL-100(Cr) as a new bifunctional Mo/Cr-MOF catalyst for selective thioether oxidation. To generate open metal sites, MIL-100(Cr) was activated in hot DMF at 110 °C, or in ethanol at 60 °C, or in water at 90 °C for 4 h, then it was dried at room temperature (for 16 h) and under vacuum between 120 and 140 °C for 12 h.[138] By comparison, MIL-100(Fe) was activated in hot water at 80 °C for 5 hours and then in hot ethanol at 60 °C for 3 h. After drying at 100 °C (overnight) and under vacuum the two aqua ligands were removed to form open Fe^{3+} sites (see dehydration, Fig. 13). When the sample was dried above 150 °C (12 h) and under vacuum increasing amounts of Fe^{2+} were observed by Mößbauer spectroscopy which reach 14 mol(Fe)% at 260 °C degassing for 90 h. The formation of Fe(II) is due to the removal of the anionic ligands OH^- or F^- (see partial reduction, Fig. 13).[142]

Several groups reported on MIL-101(Cr) for its catalysts, gas sorption, postsynthetic modification *etc.* In order to obtain OMS in activated MIL-101(Cr) the material is typically heated at 150 °C under vacuum for one day (24 h).[113,143–154]

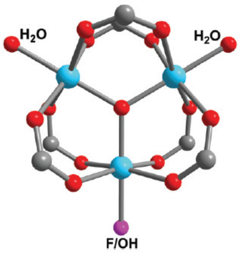

Fig. 12 Representation of the trinuclear SBU in MIL-101 and MIL-100 structures (pale blue metal atom = Cr^{3+}, Fe^{3+} or V^{3+}). Crystal structure information from ref. 149 (CSD-Refcode CIGXIA).

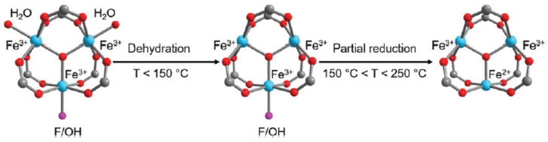

Fig. 13 Formation of open Fe^{3+} sites and Fe^{2+} site in an octahedral iron trimer of MIL-100(Fe) by dehydration and partial reduction through the removal of the anionic ligand (● = OH^- or F^-). Crystal structure information from ref. 149 (CSD-Refcode CIGXIA). Adapted from ref. 142 with permission of Wiley-VCH Verlag GmbH & Co. KGaA, Weinheim, copyright 2010.

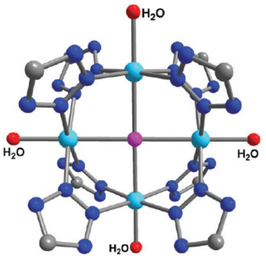

Fig. 14 Representation of the tetranuclear SBU in Fe-btt, where the axial Fe^{2+} sites are coordinated by water molecules. Crystal structure information from ref. 157 (CSD-Refcode GAGQAI).

Tetranuclear SBUs. A series of isostructural tetrazolate MOFs with the chemical formula $M_3[(M_4Cl)_3(btt)_8(solvent)_{12}]_2$, named M-btt ($Cr^{2+}$, Mn^{2+}, Fe^{2+}, Cu^{2+}; btt^{3-} = 1,3,5-benzenetristetrazolate) have been discussed in accordance to the presence of a high density of OMS.[155–158] A representative structure of the SBU in M-btt is given in Fig. 14. In general, these SBUs consist of chloride-centered square-planar $[M_4Cl]^{7+}$ units, which are connected by eight triangular btt^{3-} bridging ligands. The sixth coordination site on each M^{2+} ion is terminated by aqua ligands. These terminal aqua ligands can be removed through SE followed by TA to achieve OMS, verified with PXRD and TGA.[157–160] For example, Fe-btt, $Fe_3[(Fe_4Cl)_3(btt)_8(MeOH)_{12}]_2$, was washed with methanol and activated by heating at 135 °C for 24 h under a dynamic vacuum. Cr-btt, $Cr_3[(Cr_4Cl)_3(btt)_8(DMF)_{12}]_2$, was activated by soaking in fresh DMF, then washed with methanol and finally heating at 150 °C overnight under a dynamic vacuum. Cu-btt, $HCu[(Cu_4Cl)_3(btt)_8(H_2O)_{12}]$, was activated by a complete exchange of DMF for methanol and heating at 120 °C for approx. 24 h under reduced pressure. Mn-btt, $Mn_3[(Mn_4Cl)_3(btt)_8(MeOH)_{12}]_2$, was washed with DMF and methanol several times and activated at 150 °C for 2 h under dynamic vacuum.[157–160]

However, Queen *et al.*[156] showed that upon CO_2 loading a rapid drop in the isosteric heat of adsorption in Fe- and Mn-btt occurs, because some of the primary metal adsorption sites are still blocked by solvent molecules. Based on Rietveld refinement of the neutron diffraction data, the authors explained that the activated OMS M-btt frameworks showed that 23% (Cr), 65% (Fe) and 17% (Cu) of the metal sites (as potential OMS) were still occupied by coordinated solvent. For identically activated M-btt, the order for the amount of available OMS is Cu ≈ Cr > Fe > Mn. In this study the M-btt MOFs had been activated by the sequence soaking in DMF at 393 K for 24 h,

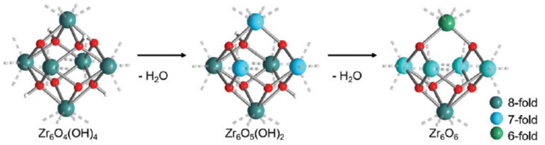

Fig. 15 Zr_6-SBU in UiO-MOFs without the carboxylate groups (for clarity) and a schematic two-step water-removal from the bridging OH^- and O^{2-} groups through TA under vacuum. The formed water consists of OH^- and H^+ from another OH^- group (transformed to O^{2-}). The different colors represent the coordination of the Zr atoms, with dark cyan = 8-fold, cyan = 7-fold and green = 6-fold coordination. Adapted from ref. 162 with permission from The Royal Society of Chemistry, copyright 2018. Crystal structure information from ref. 165 (CSD-Refcode RUBTAK02). For illustration purpose, the hydrogen atoms have been added manually with the "Add hydrogen atoms" function implemented in Mercury.[166]

decanting, soaking three times in (fresh) methanol at 343 K for 24 h, filtration, and heating under dynamic vacuum (<10 µbar) at 433 K for 24 h.[156]

Also, earlier *in situ* studies of D_2 adsorption yielded a significant number of metal sites in these MOFs that are still blocked by solvent molecules which had not been removed by normal activation procedures.[157,160] We note that these works clearly demonstrate that quantitative OMS generation cannot be taken for granted by "standard" activation protocols. It must be noted that more studies are needed to quantify the formed OMS.[157,160]

Hexanuclear SBUs. The class of UiO (University in Oslo) 3D frameworks consist of hexanuclear $[Zr_6(\mu_3\text{-}O_4)(\mu_3\text{-}OH)_4]$ clusters with eight-coordinated square-antiprismatic zirconium ions (Fig. 15, left). The prototypical UiO-66 has the formula unit $[Zr_6O_4(OH)_4(btc)_6]$.[161] The synthesis of open Zr^{4+} sites can be described with a gradual removal of two water molecules upon TA (Fig. 15). The loss of the first water molecule leads to a reduction in coordination number from eight to seven of three Zr^{4+} ions within the cluster. The lost water molecules originate from and are composed of a μ_3-OH group together with the H-atom of another μ_3-OH group. The removal of the second water molecule lowers the coordination number of two more Zr^{4+} ions to seven and one Zr^{4+} from seven to six.[105,114,162–164] Lamberti *et al.*[165] reported on a study of the hydroxylated and dehydroxylated forms of UiO-66. They used the TA method to remove the solvent molecules from the ordered $[Zr_6O_4(OH)_4]$ cluster and to generate a distorted Zr_6O_6 cluster. Based on the thermogravimetric analysis the loss of two water molecules per $[Zr_6O_4(OH)_4]$ cluster were obtained after heating above 250 °C (300 °C). IR data confirmed the full removal of OH groups and EXAFS (extended X-ray absorption fine structure) confirmed the loss of about one oxygen atom in the first coordination sphere of the Zr atoms.[165]

Gao *et al.*[114] reported also on the dehydration of UiO-66. They explained that the dehydrated UiO-66 with open Lewis-acid sites is a heterogeneous and size-selective catalyst for cyanosilylation reaction of aldehydes with trimethylsilylcyanide. To obtain the dehydrated UiO-66 with OMS Zr^{4+}, hydrous UiO-66 was calcinated at 300 °C for only two hours.[114]

In 2018, Speybroeck *et al.*[162] reported on the intrinsic dynamic nature of UiO-66. The structural deformation of UiO-66 can be explained through defect formation or removal of coordinated molecules. In their work UiO-66 was dehydrated between 523 and 573 K.[162]

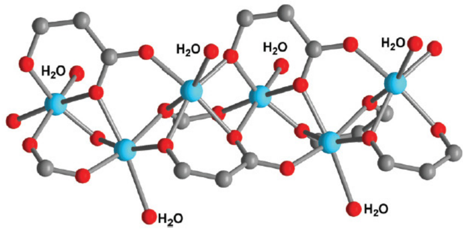

Fig. 16 Representation of the SBU in M-MOF-74 (left; M = Mg^{2+}, Mn^{2+}, Fe^{2+}, Co^{2+}, Ni^{2+}, Cu^{2+} and Zn^{2+}), with the labelled aqua ligands. Crystal structure information from ref. 179 (CSD-Refcode ORIVUI).

Infinite rod-shaped SBUs. The ligand *para*-2,5-dioxido-1,4-benzenedicarboxylate ($dobdc^{4-}$) with the metals Mg^{2+}, Mn^{2+}, Fe^{2+}, Co^{2+}, Ni^{2+}, Cu^{2+}, Zn^{2+} and Cd^{2+} leads to the formation of the isostructural series M-MOF-74, $[M_2(p\text{-dobdc})(\text{solvent})_2]$ (also known as CPO-27-M, solvent = H_2O or DMF) which have infinite rod-shaped SBUs.[167–176] Also the ligand 4,6-dioxido-1,3-benzene-dicarboxylate (m-$dobdc^{4-}$) leads to the same topology in $[M_2(m\text{-dobdc})(\text{solvent})_2]$ as a structural isomer to the M-MOF-74 series.[88] In M-MOF-74, edge connected $\{MO_6\}$ octahedra infinite linked rod shape SBUs with one coordinated water molecule per metal center (Fig. 16). The coordinated water or DMF molecule completes the octahedral coordination environment of each metal center. The bridging linkers then combine these parallel SBUs to give hexagonal, one-dimensional channels.

The OMS of Mg^{2+}, Mn^{2+}, Fe^{2+}, Co^{2+}, Ni^{2+}, Cu^{2+} and Zn^{2+} sites in the M-MOF-74 series can be generated by using SE followed by TA. Through desolvation of the coordinated solvent molecule the metal center converts to a distorted square pyramidal coordination environment with the OMS pointing into the channel.[70,88,101–105] The originally six-coordinated metal ions d^7-Co^{2+} (high spin) and d^9-Cu^{2+} feature the Jahn–Teller distortion. It should be noted that the pseudo-octahedral coordination environment of Co^{2+} and Cu^{2+} show an elongation along the axial bonds and this allows for an easier removal of the axially coordinated solvent molecule. At the same time the Jahn–Teller effect, impedes the approach and strong binding of molecules on the open metal site.[70,177]

Moreover, Moon *et al.*[178] reported on $[M_2(dobdc)(EG)_2]$ with coordinated ethylene glycol molecules (EG). To generate open Mg^{2+}, Co^{2+} and Ni^{2+} sites, the single crystals were soaked in anhydrous methanol and heated up to 200 °C. Based on single-crystal X-ray analysis (SCXRD) the coordinated and free EG molecules were replaced with methanol and based on the thermogravimetric analysis the coordinated methanol molecule was completely removed up to 250 °C.

Lobkovsky *et al.*[180] reported an Eu^{3+} MOF also with an infinite rod-shaped SBU, in which the OMS can be generated for the sensing of small molecules. $[Eu(btc)(H_2O)]$ is isostructural with MOF-76 and was achieved in a solvothermal reaction $Eu(NO_3)_3{\cdot}6H_2O$ and H_3btc in a solvent mixture of DMF, ethanol,

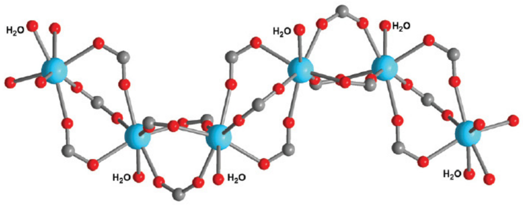

Fig. 17 Representation of the SBU in [Eu(btc)(H_2O)]. Crystal structure information from ref. 180 (CSD-Refcode OFEREX).

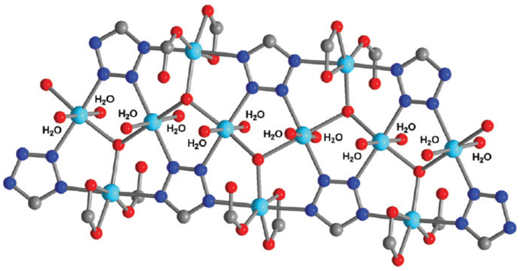

Fig. 18 Infinite ribbon-like SBU in [Co_2(tzpa)(OH)(H_2O)$_2$]. Crystal structure information from ref. 181 (CSD-Refcode SINTAN).

and water.[35] As shown in Fig. 17 the rod-shaped SBU consists of Eu^{3+} ions coordinated by six carboxylate oxygen atoms from the btc^{3-} linker and an oxygen atom from one water molecule in a seventh site. The as-synthesized [Eu(btc)(H_2O)]·1.5H_2O was activated at 140 °C under vacuum for one day and the removal of the free and Eu-bound water molecules was assessed by TGA where the water molecules were removed in the temperature range of 25 to 150 °C.[179]

The solvothermal reaction of $Co(NO_3)_2$·6H_2O with a T-shaped tetrazolyl-carboxyl ligand H_3tzpa (5-(4-(tetrazol-5-yl)phenyl)isophthalic acid) leads to the formation of the MOF [Co_2(tzpa)(OH)(H_2O)$_2$]·DMF based on infinite ribbon-like SBUs.[181] Which can be thought of being constructed from edge-sharing $Co_3(N_4C)_3(\mu_3\text{-}OH)$-metallacycles. As shown in Fig. 18, two of the three Co atoms have two aqua ligands each. The removal of these coordinated water molecules was achieved through SE with methanol followed by TA at 220 °C under vacuum, to yield the solvent-free framework [Co_2(tzpa)(μ_3-OH)].[181]

The group of Dincă *et al.*[83] demonstrated that the replacement of carboxylate moieties with triazolate ligands leads to the formation of networks with similar topology to the architecture of M-MOF-74. The solvothermal reaction of a bisbenzotriazole ligand, bis(1*H*-1,2,3-triazolo[4,5-*b*],[4′,5′-*i*])dibenzo[1,4]dioxin (H_2btdd) with hydrated Mn^{2+}, Co^{2+} and Ni^{2+} chlorides leads to the formation of the three isostructural MOFs, [Mn_2Cl_2(btdd)(H_2O)$_2$], [Co_2Cl_2(btdd)(H_2O)$_2$] and [Ni_2Cl_2(btdd)(H_2O)$_2$]. The octahedral coordination environment of the metal center was built by the coordination of three N-donor atoms from different $btdd^{2-}$ linkers, two bridging chloride ions and one terminal water molecule pointing into the channel (Fig. 19). The authors used Soxhlet extraction with methanol to remove the solvent molecules in the as-synthesized materials and then continued with TA (100 °C under dynamic vacuum) to create open Mn^{2+}, Co^{2+} and Ni^{2+} sites. They explained that upon activation, the color changed from red to green [Co_2Cl_2(btdd)] and from white to lime-green [Ni_2Cl_2(btdd)], due to the change in the metal-ion coordination number from six to five, while [Mn_2Cl_2(btdd)] remained off-white.[83] The MAF-X27 (M = Co^{2+}) and MAF-X25 (M = Mn^{2+}) MOFs with the 1*H*,5*H*-benzene(1,2-*d*:4,5-*d*′)bistriazole (H_2bbta) ligand have the same SBU as [M_2Cl_2(btdd)] (*cf.* Fig. 19).[182–184]

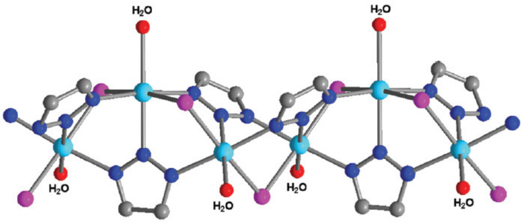

Fig. 19 Representation of the infinite rod-shaped SBU in [M_2Cl_2(btdd)(H_2O)$_2$]. Crystal structure information from ref. 83 (CSD-Refcode OVUNIE).

Open metal sites can be also obtained by using a so-called urothermal synthesis.[185] Hereby, various urea derivatives were used as solvents, which can be bound reversible to the metal sites, act as porogen, apparently aid in the crystallization and can be removed by SE to generate porosity and potential OMS. For example, the Y^{3+} sites in as-synthesized crystals in [Y_2(bdc)$_3$(e-urea)$_2$(H_2O)$_2$] are eight-coordinate, of which there are two urea solvent molecules for potential OMS.[185]

2.II Chemical activation

Chemical activation (CA) is a variant of "solvent exchange and removal by thermal activation" aims to allow for the final solvent removal at room temperature (RT), that is, without additional heating.

It can be noted that supercritical drying with CO_2 (scCO_2) would also belong to CA, since a stronger coordinating solvent together with the pore solvent would be replaced by CO_2 which is subsequently removed at or below RT. The supercritical carbon dioxide activation, which is performed by exchanging acetone or ethanol molecules, corresponds to the CA with halogenated solvents (see below), but is a much "greener" route, due to the use of the non-halogenated green solvent CO_2.[186,187] Upon CO_2 removal no (or little) surface tension or cavitation effects are expected – different to the removal of more strongly coordinating solvents. Freeze-drying is another solvent removal process, where the products are dried at temperatures below the freezing point of the solvent. This process has a direct solid-to-gas phase transition (sublimation), without the liquid phase.[188] Thus, both CA (including scCO_2 drying) and freeze-drying aim to prevent the framework collapse in the case of less-stable MOF structures. The only examples of the use of scCO_2 in connection with OMS reported a case with framework collapse.[189,190] Cases where scCO_2 or freeze-drying were used for the simple solvent removal

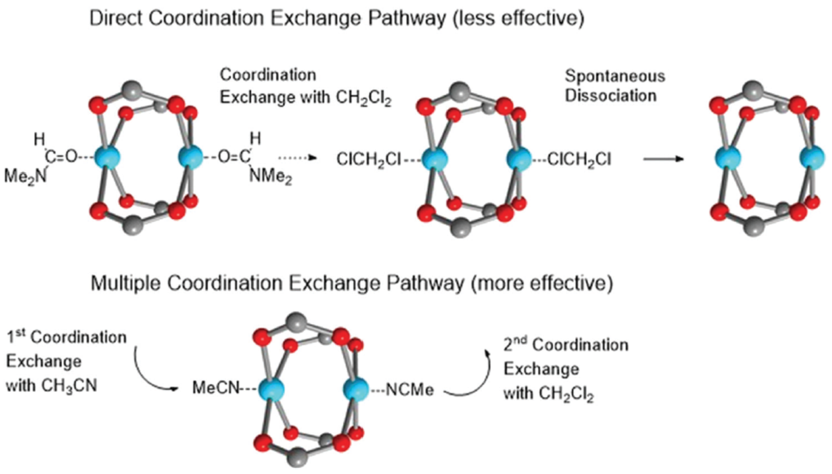

Fig. 20 Schematic illustration of the direct coordination exchange way for the CA of HKUST-1 by DCM (CH_2Cl_2) (top) and the multiple coordination exchange way by MeCN and DCM (bottom). Crystal structure information from ref. 128 (CSD-Refcode DIHVIB01). Reproduced from ref. 104 with permission from The Royal Society of Chemistry, copyright 2018.

from the pores, without dedicated OMS formation, are of course numerous.[191–194]

The mild CA by chlorinated solvents was described in detail for the activation of HKUST-1, but was also reported for MOF-2 and examples of M-MOF-74.[101–103] Jeong *et al.*[101–104] reported the CA route by treatment with halogenated solvents, like dichloromethane (DCM), without using extra thermal energy to remove the introduced halogenated solvent molecules in HKUST-1, MOF-2, M-MOF-74 (M = Cu, Ni). In contrast to the conventional TA route which is performed by applying heat energy to above room temperature and vacuum (possibly after SE), the CA proceeds by soaking the MOFs in halogenated solvents several times at room temperature and in a moisture-free argon-charged glove box.[101–103]

Fig. 20 shows schematically the CA route in ways of direct and multiple coordination exchange. The first step of the direct coordination exchange way is the exchange of DMF with DCM, and the second step is the spontaneous dissociation of the very weakly coordinated DCM at RT. As a variant, the multiple coordination exchange way proceeds by first exchanging the bound low-volatile DMF solvent with a more volatile one, such as MeCN, MeOH or EtOH followed by the final exchange with DCM.[101–104]

HKUST-1 was used as a proof of principle for the CA methodology. After synthesis, an activated solvent-free sample of HKUST-1 was prepared and loaded with DMF to prove the removal of the low-volatile DMF solvent through this method. The DMF coordinated and loaded HKUST-1 was soaked 30 times in DCM (30 × 10 min, RT) (direct exchange pathway, Fig. 20). The subsequent solution NMR analysis of the digested HKUST-1 showed no more signal of DMF (Fig. 21). Alternatively, the DMF-coordinated and -loaded HKUST-1 was soaked in MeOH, EtOH or MeCN (several times × 10 min, RT). Then the obtained MeOH, EtOH or MeCN coordinated HKUST-1 was soaked 30 times in DCM (30 × 10 min, RT) (multiple exchange pathway, Fig. 20). Again, the solution NMR analysis revealed the complete solvent removal (Fig. 21). Thereby, it is also shown that methanol, ethanol or acetonitrile can be removed by multiple soaking with DCM.[101–104]

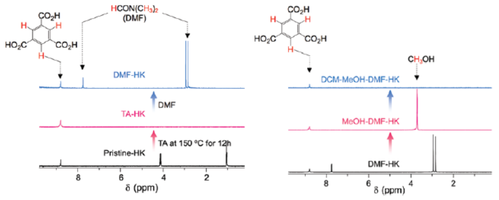

Fig. 21 Solution ^1H NMR spectra after HKUST-1 (HK) digestion of DMF-loaded HK before and after initial solvent treatment with MeOH and after final solvent treatment with DCM (CH_2Cl_2). Left: Reproduced from ref. 102 with permission from the American Chemical Society, copyright 2017. Right: Reproduced from ref. 104 with permission from The Royal Society of Chemistry, copyright 2018.

2.III Photothermal activation

In comparison to the above methods of solvent exchange and removal and chemical activation, which are performed by using solvents (and heat energy), the photothermal activation (PA) proceeds by only irradiation of the solid MOF sample. In 2018, Maspoch *et al.*[105] reported on this one-step activation method for MOFs by using UV-vis irradiation of 300–650 nm. The authors suggested that the light-to-heat conversion has significant potential in evaporation processes because of the local nature of the heat generated, thereby minimizing heat diffusion and energy loss. Under direct irradiation the MOFs experience a significant temperature increase (to 120–220 °C) in a few minutes (≤30 min) at atmospheric pressure, so that solvent molecules can be removed, and open metal sites can be generated. The MOFs exhibit absorption bands in the range 300–650 nm. The authors also pointed out that the MOF-to-light guide distance, "the distance of lamp to sample", is an

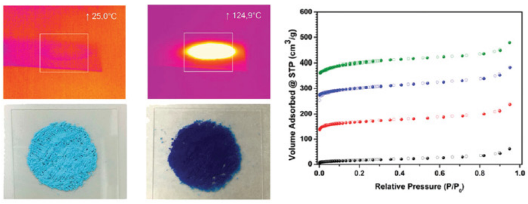

Fig. 22 Left, top: IR camera pictures of HKUST-1 before (left) and during UV-vis irradiation (right). Left, bottom: Pictures of HKUST-1 powder before (sky blue) and after (dark blue) irradiation. Right: N_2 sorption isotherms of HKUST-1. Black: as-synthesized sample. Red: thermal activated sample (120 °C, 30 min, S_{BET} = 655 m^2 g^{-1}), blue: photothermal activated sample (5 min, 500 mW cm^{-2}, S_{BET} = 1209 m^2 g^{-1}) and green (30 min, 500 mW cm^{-2}, S_{BET} = 1583 m^2 g^{-1}). Reproduced from ref. 105 with permission from the American Chemical Society, copyright 2018.

important factor that can influence the PA of MOFs. The authors used several verification methods, such as PXRD, N_2 sorption, UV-vis spectroscopy to analyze the successful activation.[105]

Evaluation of the activation parameters for HKUST-1, showed that the light distance and concomitant irradiance with the resulting temperature are crucial. A shorter distance induced a higher temperature. For example, when HKUST-1 was directly irradiated at 3 cm (2650 mW cm^{-2}, 5 min, ~250 °C), it turned amorphous and nonporous, and when it was irradiated at 5 cm (900 mW cm^{-2}, 5 min, ~187 °C), it remained crystalline and porous. Furthermore, they reported that the BET surface area increased from 1209 m^2 g^{-1} (7 cm, 500 mW cm^{-2}, 5 min), over 1583 (7 cm, 500 mW cm^{-2}, 30 min) to 1819 m^2 g^{-1} (5 cm, 900 mW cm^{-2}, 30 min). In comparison, the BET surface area of the conventionally activated HKUST-1 (through SE and TA) was between 1450 to 1800 m^2 g^{-1}.[105]

Fig. 22 shows that the color of the HKUST-1 powder changed from pale blue to dark blue (deep purple) after irradiation with the UV-vis lamp. The color change signaled the loss of the water molecules coordinated to the Cu^{2+} paddle-wheel clusters. The authors explained that the solid-state UV-vis spectrum of HKUST-1 showed a broad absorption band at 720 nm attributed to the d–d transition of the Cu^{2+} ion. The contribution of this absorption band was further studied by irradiating HKUST-1 in wavelength ranges of 320–390 nm (UV) and of 390–500 nm (visible). As expected, in both cases, lower temperatures (40 and 60 °C, respectively) were reached, demonstrating that the irradiation wavelengths close to the absorption maximum contributes significantly to the photothermal effect.[105] Using this PA process, Maspoch and co-workers[105] activated also Zn/Ni/Mg-MOF-74, by following conditions, Zn: 145 °C, 30 min; Ni: 167 °C, 30 min; and Mg: 136 °C, 30 min. Also, UiO-66, by these conditions: 57 °C, 30 min.

2.IV Quantifying OMS

The techniques gas or vapor adsorption, probe molecule infrared spectroscopy and temperature-programmed desorption (TPD) were used to quantify the relative amount (percentage) of Lewis acid sites or OMS in MOFs.[195,196]

OMS should be the primary adsorption site for suitable adsorbate molecules, such as H_2O, H_2, CO_2 and CO with significantly higher heats of adsorption than for the remaining pore walls. Thus, if the completed adsorption of such gas or vapor molecules to OMS identifies themselves through a step in the adsorption isotherm before adsorption continues at the pore walls, then the absolute gas uptake allows to quantify the amount of OMS in the given sample mass. Also, the step in the heat of adsorption curve *versus* the amount adsorbed can be used to quantify the OMS. Examples are H_2 isosteric heat of adsorption (Q_{st}) curves plotted against H_2 adsorbed/metal (see Section 4, H_2 sorption and Fig. 35, 37, 38 and 39, left). The isosteric heat of adsorption of H_2 is usually obtained using the Clausius–Clapeyron relation from H_2 isotherm data at 77 and 87 K which are fitted with appropriate isotherm equation, *e.g.*, a dual-site Langmuir–Freundlich equation or a trisite Langmuir equation.[88]

IR spectroscopy quantifies OMS through the increasing or decreasing absorbance of bands of adsorbed or desorbed probe molecules at the metal atoms. Used probe molecules are for example water, pyridine, deuterated acetonitrile, acetone and CO.[195,197,198]

TPD can identify the type and amount of Lewis-acid sites through the chemisorption of a chosen molecular probe at a low temperature followed by measuring the rate of its desorption as the temperature increases.[195] TPD of ammonia[11,199–204] and nitrogen oxide (NO)[205] were, for example, used to probe Lewis-acid sites. It has been pointed out, however, that the use of ammonia TPD in estimating MOF OMS densities presents two major drawbacks: First, the temperature range for desorption from different types of acid sites can often overlap, making peak deconvolution a necessary step in quantifying these different acid sites. Second, the temperatures required to desorb strong basic probe molecules such as ammonia may exceed the MOF thermal stability limit.[206] The methods of vapor adsorption and probe molecule IR spectroscopy are briefly explained with the following illustrative examples. Bollini *et al.*[206] used the quantity of irreversibly water adsorbed at room temperature on MIL-100(Cr) to measure the OMS density under a given set of activation conditions. Given the chemical binding of water molecules in the first coordination sphere of the metal as aqua ligands, it was assumed that adsorption of water onto open-metal sites at room temperature is irreversible under not too harsh activation condition. The type V adsorption isotherms of water onto the MOF exhibits three distinct steep regions (Fig. 23). Region I lies between approximately 0 and 1×10^{-4} bar and the water uptake corresponds roughly to 1 mol of water per mole chromium and the authors suggested that adsorption in this region of the isotherm may occur exclusively on open chromium sites (obtained when activated at 523 K).

The calculated open-metal site count close to a value of 1 mol H_2O per mol Cr was interpreted in that 523 K is a sufficiently high temperature under vacuum to render the vast majority (if not all) of the chromium in the MIL-100(Cr) material under investigation as open-metal chromium.[206] However, we note that an irreversible water uptake of 1 mol H_2O (mol Cr)$^{-1}$ cannot be rationalized with the empirical formula $[Cr_3(O)X(btc_2)(H_2O)_2]$ ($X = OH^-$ or F^-) of MIL-100(Cr) which has only 2 mol H_2O (3 mol Cr)$^{-1}$ or 0.66 mol H_2O (mol Cr)$^{-1}$.[141]

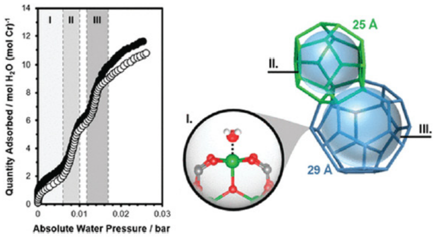

Fig. 23 H_2O adsorption isotherm (at 296 K) of MIL-100(Cr) evacuated ($P \approx 6.7 \times 10^{-5}$ bar) at 523 K for 6 h (●) and the repeat adsorption isotherm obtained immediately after evacuation for 12 h at the analysis temperature (○). Schematic representing the sequential adsorption of water onto the open Cr sites (I), filling of the smaller (25 Å) mesopores (II), and filling of the larger (29 Å) mesopores (II). Reproduced from ref. 206 with permission from the American Chemical Society, copyright 2020.

Still, increasing the activation temperature in MIL-100(Cr) from 303 to 523 K (at a given vacuum and time) clearly showed an increasing fraction of OMS (Fig. 24, left).[206]

In parallel, the relative infrared absorbance of hydroxyl vibrations was used for the quantification of OMS with increasing temperature. Aqua ligands at chromium in MIL-100(Cr) gave bands at 3672 and 3649 cm^{-1}. The areas for the aqua-ligand hydroxyl vibrations decrease upon activation between 303–523 K. The relative quantity of remaining coordinated water species was estimated by comparing the total area of the ν(OH) bands at 3672 and 3649 cm^{-1} for each activation temperature to that at 303 K, which in turn gave an estimate for the fraction of coordinated water removed (Fig. 24, right). We note that the equation for the estimation should be $H_2O\cdots Cr$ retained = area $(H_2O\cdots Cr)_{T=x}$/area $(H_2O\cdots Cr)_{T=303\,K}$ or $H_2O\cdots Cr$ removed = 1 − area $(H_2O\cdots Cr)_{T=x}$/area $(H_2O\cdots Cr)_{T\,=\,303\,K}$ where x is the temperature at which MIL-100(Cr) has been evacuated at for 1 h.[206]

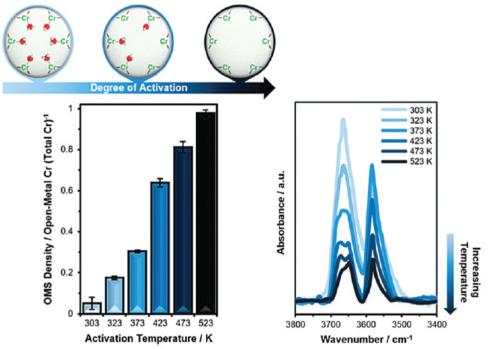

Fig. 24 Left: Estimated fraction of open Cr sites in MIL-100(Cr) as a function of activation temperature, determined using difference isotherms with H_2O as an adsorbate. Right: IR spectra of MIL-100(Cr) activated under vacuum (P = 8–11 × 10^{-5} bar) for 1 h at increasing temperature. Reproduced from ref. 206 with permission from the American Chemical Society, copyright 2020.

3. Computational studies

The focus of MOF synthesis lies on the design of MOFs with binding sites that are tuned to the adsorption of a preferred guest molecule. MOFs with OMS contain such stronger binding sites which lead to an increased interaction with different sorbate molecules (see Section 4), compared to MOFs where the metal sites are fully occupied. The knowledge, how various OMS interact with the guest molecules opens access to new materials that can be tailored to a desired property.[207] It should be noted, however, that these interactions cannot easily be deduced from experiments. Computational studies can help in these cases and are a main foundation for studying and predicting sorption and separation properties in MOFs.

For the computational description of MOFs, a variety of different approaches exist, which differ in computational demand and accuracy.[208] Force-field methods form a cost-efficient way to reproduce structural properties of periodic MOFs and, depending on their parametrization, allow for a fairly accurate prediction of geometry parameters. Simulations using standard force fields, however, often fail in reproducing the interaction of the sorbate molecules and OMS.[171,209–211] Here, an adjustment of those parameters which include adsorbate/OMS interactions is necessary to obtain a quantitative prediction of adsorption isotherms. Force fields derived from quantum mechanical (QM) calculations allow for a much better description of the interaction between guest molecules and OMS.[171,211] Thermodynamic data, as *e.g.* adsorption isotherms, is accessible through Grand-Canonical Monte Carlo (GCMC) simulations based on classical and QM-improved force fields.[212–219]

Density-functional theory (DFT) calculations have been most widely applied to predict the electrostatic interactions between the adsorbate molecules with OMS. The accuracy of the DFT method, however, depends on the employed exchange correlation functional.[220] Generally, most of the exchange–correlation functionals that neglect dispersion effects fail in describing the adsorbate/OMS interaction energy.[221,222] Here, pure generalized gradient approximation (GGA) functionals (*e.g.* PBE) and hybrid functionals (B3LYP, ωB97X)[211,220,222,223] mostly underestimate the dispersive interaction, while local density approximation (LDA) functionals[222] overestimate them, due to their inability to describe long-range electron correlation, which is responsible for van der Waals (vdW) or London dispersion forces.[221,223–228]

The inclusion of dispersion corrections has been proven to be crucial for improving the accuracy of the calculated results. To capture weak interactions and improve the accuracy in simulations, the implementation of vdW density and dispersion corrected functionals have been proposed.[70] These can be used in combination with the standard exchange–correlation functionals.

An approach to describe the dispersion forces by vdW empirical corrections has been introduced by Grimme *et al.* and the associated corrections are denoted as "-D" functionals.[224] Depending on the level of dispersion correction, the extended functionals are referred to as -D1,[229] -D2[224] and -D3.[230] Quantum mechanics (QM) methods based on *ab initio* wave function methods such as the Møller–Plesset Second-Order (MP2) level of theory and the coupled cluster (CC) approach have also been applied to study the gas adsorption on OMS.[222,231] In order to improve the accuracy of adsorption energies, a promising approach was found in combined QM/QM and QM/MM methods.[221,222,232,233] Nachtigall *et al.* showed that improved results can be achieved by employing a combined DFT-*ab initio* DFT/CC computational method.[232] Here, periodic DFT calculations with the PBE exchange correlation functional were employed to model the periodic crystal, while a subset of the structure (*i.e.* an embedded cluster) was described with the coupled cluster (CC) method including singles and doubles with perturbative triples (CCSD(T)).

Gas adsorption on OMS has been simulated for various gases using Grand-canonical Monte Carlo, DFT and *ab initio* methods of electronic structure. These studies have been employed to determine various sorption sites within the MOFs and to elucidate the role of the OMS related to the electronic interactions with different guest molecules. Using cluster models of HKUST-1 and a highly accurate coupled-cluster singles doubles (CCSD) approach, Rubeš *et al.* predicted that the OMS/adsorbate interactions can be classified into dispersion-driven interactions (CH_4), electrostatic and dispersion interactions (H_2, N_2, and CO_2), and the interaction with a partially covalent (dative) bonding character (CO).[221]

In this part, we consider computations on OMS-MOFs with gas and vapor adsorbates.[221] Hereby, we focus on the accuracy of the selected computational methods referring to the binding enthalpies in comparison to experimental data. It should be noted that some authors give the calculated binding energies (ΔE) as electronic energies. These cannot be directly compared with the experimental heats of adsorption (Q_{st}, ΔH_{ads}). To achieve a comparable value, the calculated electronic binding energies need to be adjusted by adding finite temperature and zero-point energy (ZPE) effects to approach the binding enthalpy (ΔH).[70,222,223,234,235] However, both the predicted ΔE and ΔH results provide information on how the adsorbate/OMS interaction can be tuned by metal substitution, thereby producing novel promising adsorbents for a particular adsorbate.

Computational adsorption of H_2 on OMS

In 2014, Space *et al.* performed GCMC simulations of H_2 adsorption in Mg-MOF-74 using the three-site Darkrim–Levesque (DL)[236] model (model 1) and the five-site charge–quadrupole Belof Stern Space (BSS)[237] model (model 2).[238] Both models include charge–quadrupole interactions, but no explicit terms to describe polarizability. Compared to the experimentally obtained H_2 sorption isotherm for Mg-MOF-74 at lower pressures ($<$10 kPa), these models show a significantly lower H_2 uptake and do not reproduce the sharp increase at lower pressures (Fig. 25, left). This and the calculated initial isosteric heats of adsorption of -6.5 kJ mol^{-1} and -6.0 kJ mol^{-1} indicate that these models do not capture the sorption on Mg^{2+} sites (Fig. 25, right). The total energy in these simulations was dominated by van der Waals contributions, hence sorption at open metal sites was not detected.[238]

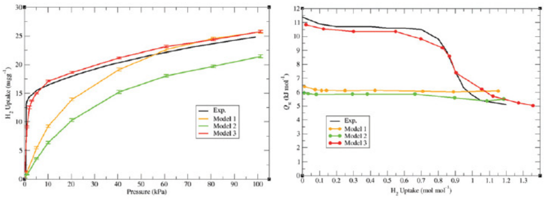

Fig. 25 Left: Low-pressure H_2 sorption isotherms at 77 K. Right: Isosteric heats of adsorption, Q_{st}, for H_2 in Mg-MOF-74 for experiment (black) and simulation using models 1 (orange), 2, (green), and 3 (red). Reproduced from ref. 238 with permission from the American Chemical Society, copyright 2014.

Space *et al.* showed that the BSSP model[237] (model 3) which includes explicit many-body polarization interactions, proves most suitable for an accurate reproduction of the experimental H_2 sorption isotherms and the resulting Q_{st} values for M-MOF-74 and the rht type MOFs, PCN-61 and NOTT-112.[238–240] In NOTT-112, two distinct environments for the Cu^{2+} metal sites within the paddle-wheel SBU were determined.[240] There are Cu^{2+} ions which face the cuboctahedral cage of the network and Cu^{2+} ions which are directed towards the linker. Simulations using the BSSP model indicated that the Cu^{2+} ions which face to the cuboctahedral cage of the network have a higher partial positive charge. Hence, these Cu^{2+} ions represent the main H_2 sorption sites.[240]

For Mg-MOF-74, the BSSP model produces an isotherm with a sharp increase at lower pressures ($<$5 kPa), which is also seen in the experiment (Fig. 25, left).[238]

Also, the calculated value for the heat of adsorption (-10.9 kJ mol^{-1}) is very close to the experiment (-11.4 kJ mol^{-1}), indicating the sorption of H_2 molecules on the Mg^{2+} OMS (Fig. 25, right and Table S2 in ESI†). Furthermore, a Mg^{2+}–H_2 center distance of 2.60 Å was calculated using the radial distribution function. Space *et al.* pointed out that this distance is an indication that the H_2 molecules are not directly coordinated to the open Mg^{2+} site, but rather are physisorbed around the site. In this regard, there is no direct interaction between the H_2 molecule and the open Mg^{2+} site. In comparison, no peak in this region was found with the models which lack explicit polarization. Here, the nearest interaction distance was found at 3.20 Å, indicating that the largest amount of H_2 molecules adsorbs in the area of the linker.[238]

One year later, the same group applied the BSSP model to the corresponding M-MOF-74 analogs with the metals Ni^{2+}, Co^{2+}, and Zn^{2+}.[177] The highest initial Q_{st}^0 value of -14.0 kJ mol^{-1} was calculated for Ni-MOF-74, followed by Co-MOF-74 with a Q_{st}^0 value of -12.4 kJ mol^{-1}, then for Zn-MOF-74, with the lowest Q_{st}^0 value for these MOFs at around -8.7 kJ mol^{-1}. This GCMC-calculated Q_{st}^0 values are in good agreement with the experimental results (see Table 3). Also, the inverse sigmoidal shape in the isosteric heat of adsorption, which then remains constant at higher loadings, could be reproduced for Ni-MOF-74 > Co-MOF-74 > Mg-MOF-74. This indicates that the OMS are already fully occupied at lower loadings and there is a large difference in the sorption energetics between the open-metal sites and the secondary adsorption sites, which were observed in the proximity of the neighboring metal-coordinated

Table 3 Experimental isosteric heats of adsorption of CO_2 and H_2 in OMS-MOFs

		$-Q^0_{st}$ [kJ mol^{-1}]
OMS	MOF	H_2
Zr	UiO-66-NH_2[164]	7.0[284]
	Mg$(acac)_2$@UiO-66-NH_2	7.9; 8.2[284]
	Ni$(acac)_2$@UiO-66-NH_2	9.3[284]
Cr	$[Cr_3(btc)_2]$	7.4[135,159]
	MIL-100	6.3[55]
	MIL-101	10.0[55]
Mn	PCN-9	8.7[56,57]
Fe	PCN-9	6.4[56,57]
Co	PCN-9	10.1[57,336]
Ni	$[(Ni_2(H_2O)_2)_{1.5}(Ni_3OH)_2(bdc)_6(na)_6]$	6.7[58]
	$[NaNi_3(OH)(sip)_2]$	10.4[59]
Cu	Cu-btt_{ri}	10.5[300]
	$[Cu_6O(tzi)_3(H_2O)_9(NO_3)]$	9.5[60]
	HKUST-1	4.5[313]
	MOF-505/NOTT-100	6.1[87,312]
	NJFU-3	6.27[118]
	NOTT-101	5.34[312]
	NOTT-102	~5.20[312]
	NOTT-103	5.71[312]
	NOTT-105	5.77[312]
	NOTT-106	6.34[312]
	NOTT-107	6.70[312]
	NOTT-112	5.64[61,62,87,240]
	NOTT-116/PCN-68	6.7[62,87]
	PCN-10	~7[63]
	PCN-11	~7[63]
	PCP-31	7.6[119]
	PCP-32	6.0[119]
Zn	$[Zn_3(\mu_3\text{-}OH)(H_2O)_4(L)(L\text{-}H_2)_2]$ L = tetrakis{3,5-bis[(4-carboxyl)phenyl]phenyl}methane	6.8[64]
In	In-*soc* MOF	6.5[65]

		$-Q^0_{st}$ [kJ mol^{-1}]	
MOF	OMS	CO_2	H_2
M-MOF-74 $[M_2(p\text{-dobdc})]$	Mg	47.0[52]	10.3[308]
		45.0[69]	10.6[309]
		44.0[178]	10.9[89]
		43.5[70]	
		42.0[220,378]	
		39.0[71]	
	Mn	31.9[220]	8.5[89]
		31.7[70]	8.8[88,89,309]
		28.0[378]	
	Fe	30.0[351]	9.5–10.0[89]
		33.2[70]	9.7[88,309]
	Co	37.0[52]	10.7[309]
		34.5[220]	10.8[88]
		34.4[178]	11.5[89]
		33.6[70]	
	Ni	41.0[52]	11.9[88]
		38.8[178]	12.9[309]
		38.7[220]	13.5[89]
		38.6[70]	
	Cu	22.1[70]	6.1[89]
	Zn	30.6[220]	8.3[241]
		30.0[69]	8.5[309]
		26.8[70]	8.8[89]
$[M_2(m\text{-dobdc})]$	Mn		10.3[88]
	Fe		11.1[88]
	Co		11.5[88]
	Ni		12.3[88]
$[M_2(dobpdc)]$	Mg		10.7[309]
	Mn		8.7[309]
	Fe		10.0[309]
	Co		11.3[309]
	Ni		12.0[309]
	Zn		8.4[309]
$[M_2(olz)]$	Mg		10.8[310]
	Fe		10.9[310]
	Co		11.4[310]
	Ni		12.1[310]
	Zn		7.3[310]
M-btt	Cr	36.7[156]	10.0[159]
	Mn	45.6[156]	10.1[157–160]
	Fe	51.2[156]	11.9[157,158]
	Cu	30.7[156]	9.5[157–159]

oxygen atoms. On the contrary, the experimental shape of the heat of adsorption for Zn-MOF-74 decreases only weakly with increasing loading, which is also reflected by the GCMC simulation. This behavior suggests that the energy for H_2 adsorption at the metal atoms is similar to the adsorption energy within the channels. Furthermore, a correlation between the H_2–M^{2+} distance and the Q^0_{st} values for the corresponding MOFs was found.[177]

The lowest Q_{st} value for H_2 was discovered in Cu-MOF-74. Space *et al.* performed electronic structure calculations for Cu-MOF-74 to investigate the reason for the low H_2 sorption ability and low isosteric heat of adsorption value in comparison to the M-MOF-74 analogs.[241] The results of this study indicate a lower positive partial charge for Cu-MOF-74, compared to the other transition metals, due to the Jahn–Teller effect. This leads to steric strains in the crystal structure and consequently to a weaker interaction of the open Cu^{2+} site and the H_2 molecule. GCMC calculations of H_2 sorption isotherms at 77 K and 87 K revealed a nearly constant Q_{st} value of -6.5 kJ mol^{-1} in Cu-MOF-74, which indicates similar energies for H_2 adsorbed onto the open Cu^{2+} sites and the secondary sites (defined as the oxido groups of the $dobdc^{4-}$ ligands).[241] The result that the open Cu^{2+} sites and the secondary adsorption sites are equally energetic in H_2 adsorption was supported by Dietzel *et al.*[89] This group has shown that the H_2 sorption properties can also be reproduced using DFT at the PBE level with and without dispersion corrections. In general, calculations at the pure DFT level exhibit an even weaker binding energy for the open Cu^{2+} site than for the secondary adsorption sites. If dispersion effects were included, a marginally stronger binding energy on the Cu^{2+} site than on the secondary adsorption sites was found. In summary, there is a decrease in the difference of the H_2 adsorption energy of the open metal site and the secondary adsorption sites according the following order $Ni^{2+} > Co^{2+} > Mg^{2+} > Fe^{2+} > Zn^{2+} \sim Mn^{2+} > Cu^{2+}$.[89]

For the DFT-simulation of H_2-bonding in MOFs, the range-separated, dispersion-corrected ωB97X-D functional has proven to be a suitable and accurate model.[242] In addition to thermochemistry and kinetics, it captures covalent and non-covalent interactions. Long *et al.* predicted differences in electronic structure at the open metal sites of M-MOF-74 ([M_2(*p*-dobdc)]) and [M_2(*m*-dobdc)] with the use of DFT calculations including the ωB97X-D functional.[88] While both frameworks have approximately the same surface area, their H_2 adsorption ability is different. For example, it was found that the open Ni^{2+} sites show stronger interaction with H_2 molecules in [Ni_2(*m*-dobdc)] compared to Ni-MOF-74. The binding strength in the M–H_2 system was examined by energy decomposition analysis (EDA). The advantage of using EDA calculations is that the interpretable physical components are considered individually. Otherwise, when comparing absolute energy differences, a single number is used to describe the H_2 bond strength. Based on absolutely localized molecular orbitals (ALMOs), the EDA was used to break down the entire binding energies into frozen energy, polarization and charge transfer components.[243] In the *p*-dobdc^{4-} linker MOFs in M-MOF-74, the H_2 binds in a linear end-on geometry while in the *m*-dobdc^{4-} MOFs the H_2 molecule is oriented bent end-on in the direction of the oxygen atom of the linker.[88]

DFT calculations with the PBE functional were performed for MOF-505.[244] Here, several localizations and orientations of the H_2 molecule were investigated around the paddle-wheel cluster. The strongest adsorption energy of −13.44 kJ mol^{-1} was calculated when the H_2 molecule was located perpendicularly in the direction of the open Cu^{2+} site.

Computational adsorption of CO_2 on OMS

Computational investigations applying DFT and GCMC methods predicted several adsorption sites for CO_2 in OMS-MOFs that result in different adsorption enthalpies. To study the interaction energy for CO_2 in relation to the different OMS, various computational approaches were used. At low coverage, the CO_2 molecules preferentially adsorb on the OMS.[155,232,234,245,246] Therefore, we will limit our discussion to the results achieved for the low-pressure regime.

Space *et al.* performed GCMC simulation studies to evaluate the sorption mechanism of CO_2 on open Cu^{2+} sites and to determine the heat of adsorption for CO_2 in UTSA-20.[210] For the CO_2 sorption simulation, three different potentials were used which are briefly described below: First, the non-polarizable TraPPe potential (transferable potentials for phase equilibria),[247] which is suitable for the description of explicit repulsion/dispersion as well as electrostatic interactions. It includes Lennard-Jones parameters and point partial charges at the atomic sites. Second, the five-site CO_2-PHAST-model[248] (PHAST = potentials with high accuracy, speed, and transferability), which determines bulk pressure–density data and potential energy curves for CO_2 dimers. And third, the analogous CO_2-PHAST*-model,[248] where the * stands for the inclusion of explicit polarization. With the inclusion of this parameter, explicit many-body polarization interactions are obtained which are important for the simulation in heterogeneous media with strongly charged and polar sites. It has been shown that the use of the TraPPe model is not suitable for the simulation of CO_2/OMS, as it does not detect the loading at the open Cu^{2+} sites and revealed significantly higher CO_2 uptakes compared to the experiment. The CO_2-PHAST- and CO_2-PHAST*-models are in better agreement, albeit slightly higher uptakes were received. However, the CO_2-PHAST model fails due to the lack of induced dipole parameters, as it detects only a weak proportion of CO_2 molecules near the Cu^{2+} sites. Using the CO_2-PHAST*-model, it was found that the inclusion of explicit many body polarization interactions makes an important contribution to capturing the sorption on the open Cu^{2+} sites. The heat of adsorption revealed an almost constant value as a function of loading in the range of −30 kJ mol^{-1}, calculated with TraPPE, CO_2-PHAST, and CO_2-PHAST* potentials, which is close to the experimental adsorption enthalpy of −29.0 kJ mol^{-1} at lowest loading.[232] A constant value of the heat of adsorption with increasing CO_2 loading can be attributed to the fact that the OMS and the adsorption sites within the pore have similar energies. This would also explain why the values for the heat of adsorption received from TraPPE and CO_2-PHAST are close to those of the CO_2-PHAST* model, even if they do not reproduce the CO_2/Cu^{2+} interaction.[210]

For M-MOF-74, DFT-D studies revealed that the adsorbed CO_2 molecule is end-on coordinated on the OMS and possesses an angular $M\cdots O{=}C{=}O$ orientation.[234,249] An orientation towards the linker was assigned to a secondary vdW interaction between the CO_2 molecule and the adjacent oxygen atom of the carboxylate group from the linker.[234,245] Here, Wang *et al.* confirmed that the CO_2 adsorption onto OMS has contributions from the Lewis acid and base interaction between O_{CO_2} and the metal ion as well as from the interaction between C_{CO_2} and the carboxylate oxygen in the square plane of the metal ion.[234] Based on various transition metals, Snurr *et al.* found an explanation for the relative CO_2 binding strengths in the effective charge of the metal atom.[222] The authors confirmed that a strong positive potential on the metal cation and a strong negative potential around the coordinated carboxylate oxygen atoms cause the angular geometry of the $Mg^{2+}\cdots O{=}C{=}O$ complex. Thus, due to the quadrupole moment of CO_2, there is a lateral interaction between the CO_2 molecule and the oxygen atom from the carboxylate group of the linker.[222]

DFT calculations including Grimme-dispersion (*e.g.* PBE-D2, PBE-D3, B3LYP-D, B3LYP-D*, ωB97X-D) were employed, with the intention of reproducing experimental heat of adsorption for CO_2 in OMS-MOFs.[171,220,223,249] Compared to the standard PBE functional, the Grimme D2 and D3 dispersion corrected PBE functional gives more accurate binding energies.[171,250] However, Siepmann *et al.* stated that PBE-D3 underestimates the magnitude of the experimental heats of adsorption for CO_2 in M-MOF-74 with a mean unsigned percentage error of 8.4%.[171] Smit *et al.* gave a percent deviation of ∼6% for the PBE-D3 functional and a slightly smaller deviation of 4.4% for PBE-D2.[223]

Bordiga *et al.*[249] achieved a ΔH^0 value of −37.9 kJ mol^{-1} for Mg-MOF-74 using the B3LYP-D* functional, which is somewhat underestimated compared to the experimental data (−39 to −47 kJ mol^{-1}).[52,69–71,178,222] Likewise, an improved value of −44.9 kJ mol^{-1} for Mg-MOF-74 was obtained with the ωB97X-D method.[220] Both, the ωB97X-D and the B3LYP-D functional, however, deliver underestimated ΔH values for MIL-101(Cr)

(-29.2 kJ mol^{-1} and -30.8 kJ mol^{-1} compared to the experimental enthalpy at zero coverage of about -44 kJ mol^{-1}).[220,251]

One of the latest computational studies by Yang *et al.* used DFT-D2 methodology to investigate CO_2 adsorption properties of several MOFs built from Cu^{2+} paddle-wheel units.[252] Since the investigated MOFs consist of the same paddle-wheel cluster but differ in the carboxylate ligands, the calculations were performed on a selected Cu^{2+} paddle-wheel cluster model derived from HKUST-1. The development of a combination of Coulomb potentials and vdW interactions (with Morse potential parameters derived from quantum calculations) was required to describe the interaction in the considered system. The DFT-D2 computed interaction energy for CO_2 of -21.2 kJ mol^{-1} is underestimated compared to the experimental Q_{st}^0 value of -29.0 kJ mol^{-1} (see Table 3).[232,252]

In addition to the Grimme approach, further adjustments of the standard exchange–correlation functionals were pursued by Lundqvist *et al.*[253] The authors include a nonlocal term to capture long-range interactions such as vdW-forces (vdW-DF functional). A second generation of this approach has been proposed, employing both, a semi-local exchange functional (PW86)[254] and a large-N asymptote gradient correction (vdW-DF2), where N refers to the number of electrons.[255] DF functionals such as optB88-vdW and optB86b-vdW were used to calculate the binding energies for CO_2 in M-MOF-74.[223] However, Smit *et al.* found that these functionals overestimate the experimental values by ~8 kJ mol^{-1}.[223]

Sayós *et al.* showed for Mg-MOF-74, that the calculated vdW-DF2 zero-coverage adsorption energy at 298 K for CO_2 adsorbed at the open Mg^{2+} sites (-47.9 kJ mol^{-1}) is in good agreement with the experimental result (-45 kJ mol^{-1}).[178,246]

Brown *et al.* indicated that the CO_2 adsorption ability is determined by the bond strength of the CO_2 molecule on the OMS.[70] The authors obtained the binding energies using the dispersion-correlation functional vdW-DF2+U. The inclusion of the Hubbard-like parameter U that relates single particle potentials to the magnetic and orbitals parameters was recommended to localize the d-states of the transition metals.

The CO_2 binding enthalpies ΔH (at loadings of 0.167 CO_2 per M^{2+}), which were obtained by including quantum zero-point energies (ZPEs) and finite-temperature thermal energies (TEs) at the level of a harmonic approximation, suggested the trend Mg^{2+} (-40.9 kJ mol^{-1}) > Ni^{2+} (-37.3 kJ mol^{-1}) > Fe^{2+} (-34.1 kJ mol^{-1}) > Mn^{2+} (-33.9 kJ mol^{-1}) > Co^{2+} (-33.8 kJ mol^{-1}) > Zn^{2+} (-30.2 kJ mol^{-1}) > Cu^{2+} (-27.1 kJ mol^{-1}). Here, the calculated values differed slightly from the experimental data (giving the trend Mg^{2+} (-43.5 kJ mol^{-1}) > Ni^{2+} (-38.6 kJ mol^{-1}) > Co^{2+} (-33.6 kJ mol^{-1}) > Fe^{2+} (-33.2 kJ mol^{-1}) > Mn^{2+} (-31.7 kJ mol^{-1}) > Zn^{2+} (-26.8 kJ mol^{-1}) > Cu^{2+} (-22.1 kJ mol^{-1})) and showed a deviating isosteric heat of adsorption for Mn^{2+}, Fe^{2+}, Co^{2+} and Zn^{2+}.[70]

In general, within the M-MOF-74-series, the largest affinity for CO_2 from computational studies was found for Mg-MOF-74, which agrees to the experimental data (see also Section 4, CO_2 adsorption).

The higher CO_2 uptake ability for Mg^{2+} in comparison to transition metals in the M-MOF-74 series could also be detected with the use of non-polarizable force fields derived from DFT calculations including periodic boundary conditions.[256] The calculated probability density plots for Mg-MOF-74 showed a lower mobility of the adsorbed CO_2 molecules as well as less obvious secondary adsorption sites (adjacent to the primary site) than in both Co- and Zn-MOF-74 (Fig. 26).

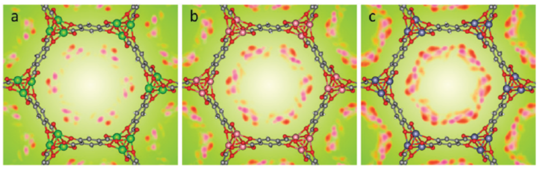

Fig. 26 Probability density plots obtained with a DFT-derived force field for CO_2 in (a) Mg-, (b) Co-, and (c) Zn-MOF-74, at 100 K. Orange dots indicate the density of the oxygen atoms in CO_2, whereas magenta dots correspond to the density of the carbon atoms. Darker colors refer to a higher probability of finding a guest at those positions. Each colored sphere corresponds to the following atoms: C, gray; O, red; H, white; Mg, lime green; Co, pink; Zn, slate. Reproduced from ref. 256 with permission from the American Chemical Society, copyright 2016. Direct link: http://pubs.acs.org/doi/10.1021/acs.jpcc.6b03393.

This lower mobility was attributed to the fact that Mg-MOF-74 has a large energetic difference between open metal and secondary adsorption sites. Therefore, all OMS are occupied first. Comparatively, in Co-MOF-74 and Zn-MOF-74 the secondary adsorption sites are more occupied, as here the computed binding energies of OMS and secondary adsorption sites are almost similar.[256] In further work, Smit *et al.* stated that in addition to the electrostatic interaction, the binding strength between CO_2 and the OMS is influenced by the hybridization between the metal d_{z^2} orbital and a lone pair on CO_2. For Mn^{2+} through Co^{2+}, the d_{z^2} orbital is singly occupied, while in Cu^{2+} and Zn^{2+} this orbital is doubly occupied, and the binding strength decreases.[223]

The lowest binding enthalpy within the M-MOF-74 series was found for Cu^{2+} and was related to the fact that the elongation along the axial ligand oxygen atom impedes the approach of CO_2 towards the Cu^{2+} site.

Brown *et al.* showed that the M···O(CO_2) distance correlates with the M–CO_2 binding strength, *i.e.* longer distances decrease the binding energy, albeit their vdW-DF2 calculated distances were overestimated compared to experimental data.[70]

Smit *et al.* furthermore found that for OMS-MOFs the vdW-DF2 functional overestimated the bond distances, resulting in a slightly higher binding energy (ΔE = +1.3 kJ mol^{-1}) compared to the experimental value. Therefore, the rev-vdW-DF2 has been applied to improve the geometries.[223] By using this functional the binding energy was overestimated by only 0.4 kJ mol^{-1}.

Queen *et al.* confirmed that the inclusion of vdW dispersion correlations in DFT calculations quantitatively support the structural features associated with the OMS as binding sites for CO_2.[156] The authors performed periodic DFT calculations using the dispersion corrected rev-vdW-DF2+U functional to study the CO_2 binding interaction in the M-btt (M = Cr^{2+}, Fe^{2+} and Cu^{2+}) series.

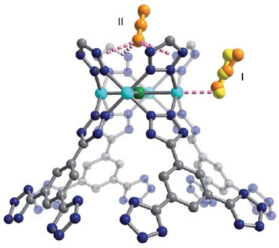

Fig. 27 Structure of Cu-btt showing the primary CO_2 adsorption site I (at right) and secondary site II (at top), as identified by DFT calculations (yellow ball-and-stick representations) and by *in situ* powder neutron diffraction (orange ball-and-stick representations). Cyan, grey, blue, and green spheres represent Cu, C, N, and Cl atoms, respectively; hydrogen atoms are omitted for clarity. Reproduced from ref. 156 with permission from The Royal Society of Chemistry, copyright 2018. (*cf.* to Fig. 47 for the experimental adsorption sites from Rietveld refinement).

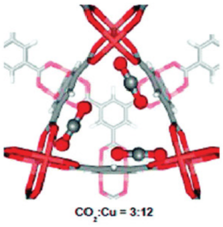

Fig. 28 Structure of the CO_2 adsorption complexes on the Cu^{2+} site for CO_2/Cu coverage of 3 : 12. Reproduced from ref. 232 with permission from the American Chemical Society, copyright 2011.

In this M-btt series, the primary adsorption sites were found at the OMS and secondary adsorption sites were above the $[M_4Cl]^{7-}$ cluster, arising through the interaction of the CO_2 molecule with the tetrazolate rings of the linker (Fig. 27).

An insight into the adsorptive behavior of the isostructural M-btt MOFs was provided by comparison of the DFT derived CO_2 binding energies for sites I (open metal site) and II (adsorption site above the $[M_4Cl]^{7-}$ cluster).[156] While the bond strength at site I depends mainly on the metal identity, the bond strength at site II is independent of the metal and is almost identical for the investigated species. The highest theoretical binding enthalpy on the primary site I was calculated for Fe-btt (as -51.7 kJ mol^{-1}), followed by Cr-btt (-36.6 kJ mol^{-1}) and then Cu-btt (-29.4 kJ mol^{-1}). These values are in very good agreement with the experimental isosteric heats of adsorption determined at zero coverage (see Table 3). The higher binding energy for Fe-btt was related to the shorter calculated Fe–O(CO_2) distance of 2.301 Å in comparison to the Jahn–Teller-elongated distances for Cu(II)···O(CO_2) (2.567 Å) and Cr(II)···O(CO_2) (2.625 Å). A shorter binding distance is normally correlated with a higher binding energy, hence the shorter Cu···O distance with lower binding energy is somewhat counter-intuitive. The smaller Cu···O than Cr···O distance can be explained by the shorter ionic radii of Cu^{2+} and Cr^{2+}.[156] The lower Cu···O binding may result from the stronger electronic repulsion of the doubly-occupied d_{z^2} orbital in d^9-Cu^{2+} relative to the singly-occupied d_{z^2} orbital in d^4-Cr^{2+}(high-spin).

Snurr *et al.* showed that calculations at the MP2-level give improved values for the binding energies compared to pure DFT methods.[222] For the M-MOF-74 series a more refined description of the binding energies for CO_2 molecules adsorbed at OMS was obtained with the use of relaxed structures obtained from B3LYP in combination with single point energies calculated at the MP2 level (Table S1 in ESI†).[222]

For HKUST-1, the most favorable orientation of the CO_2 molecule is linear and tilted away from the Cu–Cu axis of the paddle wheel SBU.[232] Here, Nachtigall *et al.* suggested that the interaction of CO_2 with Cu^{2+} is modulated by the additional electrostatic interaction with the hydrogen of the trimesic acid and the Cu^{2+} cation of the adjacent paddle-wheel SBU, as well as by the dispersion interaction with organic linkers (Fig. 28).

Using the DFT/CC method for HKUST-1, an interaction energy of -28.2 kJ mol^{-1} was calculated at low coverage with one CO_2 molecule per Cu^{2+} site, which is consistent with the findings by Rubeš *et al.* using the same method.[221,232] Nachtigall *et al.* added that at a coverage of three CO_2 molecules per 12 Cu^{2+} centers (3 : 12 coverage), the CO_2 molecules are not statistically distributed over the Cu^{2+} sites but are preferably adsorbed at the adjacent three Cu^{2+} sites within the triangular-shaped small cage forming one small opening (Fig. 28).[232] Here, an increased interaction energy of -35.9 kJ mol^{-1} for the third CO_2 molecule was calculated, because of an additional stabilization due to the T-shaped interaction of adjacent CO_2 molecules (as was also found in M-MOF-74, *cf.* Fig. 41b).

Computational adsorption of CO on OMS

The influence of open metal sites on the CO adsorption was investigated with periodic DFT and cluster models including various levels of correlation.[221,257–260]

Georgiev *et al.* applied cluster and periodic DFT calculations at the PBE level to study the CO adsorption at open Cu^{2+} sites in Cu-MOF-74 (Fig. 29).[73] Both models revealed a weak CO binding at the Cu^{2+} sites, which was mainly attributed to dispersive interactions. The calculated binding energies of -23.4 kJ mol^{-1} with the periodic model and -17.8 kJ mol^{-1} with the cluster model were in the range of the adsorption enthalpy of -20 kJ mol^{-1} obtained *via* variable-temperature IR (VTIR) experiments.[73]

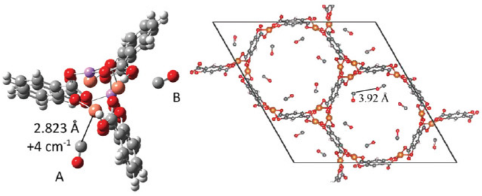

Fig. 29 Left: 92-atom cluster of Cu-MOF-74, with one CO molecule adsorbed at the open Cu^{2+} site, A, and a second CO molecule, B, adsorbed at the nearest Cu^{2+} adjacent site, which appears in the adjacent pore channel. Right: Periodic model of the Cu-MOF-74 structure. Reproduced from ref. 73 with permission from the American Chemical Society, copyright 2018.

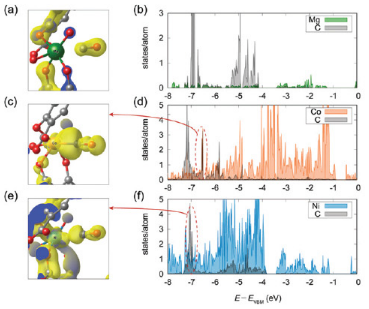

Fig. 30 Electronic properties calculated using DFT for CO adsorbed in (a and b) Mg-MOF-74, (c and d) Co-MOF-74 (e and f) Ni-MOF-74. Left: Isosurface of total charge density and right: partial density of states (PDOS). The partial charge densities in (c) and (e) were obtained from the states indicated by the red dashed ellipse. Reproduced from ref. 178 with permission from the American Chemical Society, copyright 2019.

DFT calculations for CO and the transition metal atoms Mg^{2+}, Co^{2+} and Ni^{2+} in M-MOF-74 revealed that Ni^{2+} and Co^{2+} interact stronger with CO molecules than Mg^{2+} sites, as expected from the established d-orbital bonding models of CO to transition metals and the lack of π-back-bonding from main-group metals (Fig. 30).[178] The electron transfer from the open Ni^{2+} and Co^{2+} sites to the antibonding π-orbitals of COs was confirmed. As needed for stable M–CO interactions, the open Co^{2+} and Ni^{2+} sites enter into strong π-back-bonding with CO *via* electron transfer from the d-orbitals of the transition metal to the π^*-antibonding molecular orbitals of CO. The main-group metal Mg^{2+} cannot participate in such an electron transfer or orbital overlap with CO because of its lack of valence electrons (see also Section 4, CO adsorption).

Periodic DFT-D calculations at the B3LYP-D* level of theory were applied to calculate the heats of adsorption of CO on M-MOF-74 Mg^{2+}, Ni^{2+} and Zn^{2+} at 298 K.[245,249] The simulations at the B3LYP + D* level predicted heats of adsorption ΔH (Ni^{2+}, −41.9 kJ mol^{-1}; Mg^{2+}, −30 kJ mol^{-1}; Zn^{2+}, −24.8 kJ mol^{-1}) which underestimate the experimental data (Ni^{2+}, −59.7 kJ mol^{-1}; Mg^{2+}, −38.3 kJ mol^{-1}).[178,245,249] Sauer *et al.* showed that the hybrid MP2:B3LYP + D* method gives improved results, although the obtained values still deviate from the experiment (Ni^{2+}, −50.3 kJ mol^{-1}; Mg^{2+}, −41.2 kJ mol^{-1}; Zn^{2+}, −39.8 kJ mol^{-1}).

Computational adsorption of C_2H_2 on OMS

Wang *et al.* predicted that the strong C_2H_2 interaction with open OMS in the M-MOF-74 series is caused by the σ-donor/π-acceptor bonding between of C_2H_2 and suitable transition metal atoms, as established in organometallic chemistry.[234]

Fröba *et al.* pointed out the need for inclusion of a parameter adjustment based on *ab initio* calculations to describe the interaction of guest molecules with the OMS.[209] To account for electrostatic interactions between the sorbate and the OMS, point charges for the MOF were derived by fitting them to the DFT-PBE calculated electrostatic potential. This method revealed for HKUST-1 an isosteric heat of adsorption of −30 kJ mol^{-1} for C_2H_2 at low coverage, which deviates slightly from the experimental Q_{st}^{0} value (−30.4 to −39.0 kJ mol^{-1}).[209,261,262]

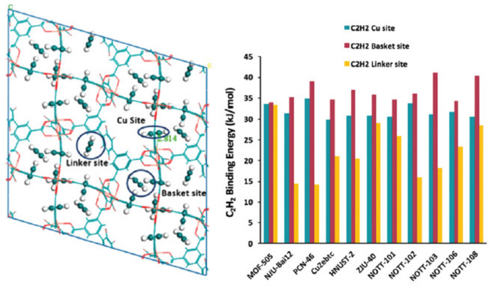

Fig. 31 Left: DFT optimized binding positions of C_2H_2 molecules in NOTT-108. Right: DFT calculated C_2H_2 binding energies for OMS (blue), basket pocket sites (red), and linker sites (yellow). Reproduced from ref. 263 permission from the American Chemical Society, copyright 2017.

Li *et al.* performed GCMC simulations and DFT calculations to study the C_2H_2 adsorption in a series of Cu^{2+} paddle-wheel MOFs, such as MOF-505, Nju-Bai12, PCN-46, ZJU-40 and NOTT-*X* (X = 101, 102, 103, 106, 108).[263] It was found that OMS, organic ligands and the functionalization of the ligands make an important contribution in promoting C_2H_2 storage capacity and the separation of C_2H_2 over CH_4 and CO_2 below 2 bar. Quantum-mechanical calculations were used to capture the interactions of C_2H_2 with the OMS. The corresponding terms were produced by fitting the DFT energy surface. Optimization of the ground state geometries was performed employing GGA exchange implemented with PBE. In all Cu^{2+} paddle-wheel MOFs, three adsorption sites for C_2H_2 were found (Fig. 31, left). These sites are referred to the open Cu^{2+} site (site I), the basket site, where three paddle-wheel clusters and three ligands form a basket (site II) and the sites which are mostly near the aromatic rings of the linker (site III). The basket site II was found to be the most preferred adsorption site for C_2H_2. For this basket-pocket site higher binding energies (−34.0 to −41.1 kJ mol^{-1}) than for site I (−33.7 to −29.9 kJ mol^{-1}) and for site III (−14.3 to −33.4 kJ mol^{-1}) were calculated using DFT (Fig. 31, right).[263]

Computational adsorption of CH_4 on OMS

Computational studies for the CH_4 adsorption behavior in the paddle-wheel MOFs $[M_3(btc)_2]$ (M = Cu^{2+}, Cr^{2+}) and PCN-14 indicate that the OMS are not the preferred adsorption sites for CH_4.[212,264,265]

Cavalcante *et al.* classified the Cu^{2+} sites in PCN-14 as weak methane adsorption sites.[265] GCMC simulated adsorption isotherms performed for HKUST-1 and PCN-14 at 150 K revealed an occupation of CH_4 at the open Cu^{2+} sites (1.67 and 0.05 bar). At 290 K over a pressure range of 0.01–35 bar no adsorption on these sites could be determined theoretically. Likewise, GCMC calculations show no energy barriers between weak and strong adsorption sites in PCN-14, allowing open Cu^{2+} sites to direct the CH_4 molecules to the neighboring adsorption sites. After all, it was reasoned that multiple adsorption sites and efficient linking between them can explain the high methane uptake in PCN-14.[265]

Brown *et al.* stated that, consequently, the strength of the CH_4 binding at the OMS in HKUST-1 and $[Cr_3(btc)_2]$ is caused by intermolecular interactions with adjacent CH_4 molecules adsorbed at the windows of the octahedral cages (primary sites) instead of an electronic interaction with the metal center.[264]

The values for the binding enthalpy for the open Cu^{2+} site in HKUST-1 was calculated to be -9.4 kJ mol^{-1} using the DFT-vdW-DF2+*U* method. Comparatively, a significantly higher value for the binding enthalpies at the windows of HKUST-1 (-21.8 kJ mol^{-1}) and $[Cr_3(btc)_2]$ (-21.5 kJ mol^{-1}) was calculated. The authors noted that the DFT calculations for $[Cr_3(btc)_2]$ fail to capture the multireference character of the Cr–Cr bond in the singlet ground state, and they argued that the detection of bond enthalpies at the open Cr^{2+} site is therefore unreliable. Furthermore, these simulations revealed no difference in the adsorption behavior of HKUST-1 and $[Cr_3(btc)_2]$, for the interaction with the respective OMS.[264] The type of the metal cation affects the adsorption mechanism only very little and the strong binding is due to a combination of structural features that are identical in both $[M_3(btc)_2]$ materials together with $CH_4\cdots CH_4$ vdW interactions. Hence, the uptake values for HKUST-1 and $[Cr_3(btc)_2]$ are similar.[264]

Düren *et al.* used DFT/CC-PES simulations to derive the favorable adsorption sites in HKUST-1.[212] With the intention to eliminate the ambiguity and inaccuracy that results from generic force fields, they applied a potential energy surface (PES) calculated by a hybrid DFT/*ab initio* method (DFT/CC) in the GCMC simulations. Here, the DFT/CC corrections were performed using PBE with the AVQZ basis set and CCSD(T)/CBS (complete basis set limit) calculations. The authors noted that simulation of CH_4 adsorption isotherms at 77 K and 87 K using the UFF-based GCMC method is not suitable to capture the CH_4 adsorption on the OMS. Instead, DFT/CC-PES simulations capture the shape of the experimental adsorption isotherm and the CH_4 adsorption sites including the OMS. This study revealed a population in the centers of the small pores at low CH_4 loading, followed by adsorption on the center of the windows to the small cavities and only at higher loading an occupancy of the OMS was observed.[212] According to the DFT/CC-PES, an occupancy of 96% was determined on the OMS, corresponding to 46.25 of the 48 OMS being occupied by CH_4. Also, the simulated distance between the CH_4 molecules and the open Cu^{2+} site of 3.097 Å agrees well with the experimental value (3.075 Å).

Furthermore, the fluid framework potential energy derived with DFT/CC-PES yields an interaction with the OMS, while this effect was not captured by the PES derived from the UFF force field.[212]

Separation

Independent of the open metal source, computational studies using DFT-derived non-polarizable force fields for the adsorption of dry $N_2/CO_2/CH_4$ gas mixtures reproduce for the whole M-MOF-74 series a higher CO_2 adsorption over CH_4 and N_2, with almost no N_2 adsorbed under natural gas purification conditions.[256] Smit *et al.* developed DFT-derived non-polarizable force fields to study the adsorption properties of the gas mixture CO_2/H_2O in M-MOF-74 considering the H_2O sensitivity of these frameworks. The use of this method allowed for a forecast how fast a CO_2 uptake will decrease in the presence of water. It could be detected that the CO_2 uptake decreases with increasing H_2O bonding energy. Thus, in Mg-MOF-74, with the highest DFT binding energy for H_2O (-66.9 kJ mol^{-1}), the H_2O uptake is greater than for CO_2, even when the mole fraction of H_2O in the gas mixture is only 0.1% at 313 K and 0.15 bar. In contrast, in Zn-MOF-74, with the weakest DFT-calculated H_2O binding energy (-46.3 kJ mol^{-1}), the H_2O uptake surpasses the CO_2 uptake only when the mole fraction of H_2O is above 2% (at 313 K and 0.15 bar). Thus, Zn-MOF-74 can tolerate the presence of 20-times more H_2O than Mg-MOF-74. The latter will be useless for carbon capture as most flue gases contain significantly more than 2% H_2O. The values for the other M-MOF-74 analogues lie in a range between 0.1% and 2%. Consequently, none of the M-MOF-74 frameworks will be applicable for CO_2 adsorption from moist gas streams.[256]

In summary, theoretical methods are used to calculate adsorption isotherms, heats of adsorption, binding geometries of adsorbates at the MOF surface *etc.* With adequate description of adsorbate-adsorbent interactions, quantum mechanical calculations of potential energy surfaces are able to reproduce experimental binding enthalpies. At the DFT-level, the inclusion of van der Waals interactions is crucial. The best results compared to the experiment are obtained through a combination of dispersion corrected DFT and high-level *ab initio* methods, as *e.g.* DFT-D and coupled cluster (CC) methods including complete basis set extrapolation. It is possible to achieve agreement between computational and experimental Q^0_{st} values for the heat of adsorption within 1–2 kJ mol^{-1} (Tables S1–S3 in ESI†). The deviation of 1–2 kJ mol^{-1} is within the experimental error, even if such Q^0_{st} values are unjustified reported with a decimal digit.[266–268]

4. Open metal site applications

"Application" can mean different things. In basic research it could be already considered an "application" that OMS allow for the defined post-synthetic modification of a different linker at the metal site. Further, the formation of an OMS is also the prerequisite for the "binding" of weakly coordinating adsorbates such as CO_2, H_2 *etc.* As outlined in the computational Section 3, these gas molecules bind most strongly to the OMS which forms the basis of "applying" OMS-MOFs for high gas uptake and separation (see below). At the same time, the structure elucidation of the binding mode of these adsorbed gas molecules in OMS-MOFs is also "applied" in structural studies.

In addition, we note that the following "applications" of OMS-MOFs (or MOFs at large) in gas sorption, catalysis and sensing are "potential applications", which are suggested from lab experiments and which have not yet been commercialized.

Noteworthy, this section only collects "applications" in connection with verified OMS formation and does not refer to work which only claims OMS effects.

Post functionalization of OMS in MOFs

By definition, post-functionalization refers to a chemical modification of the MOF after its synthesis. We emphasize again that the structure of the MOF should be preserved upon functionalization, which needs to be verified *e.g.* by powder X-ray diffraction, FT-IR spectroscopy and gas sorption experiments after the reaction.[12]

The general and basic strategy found in the literature for post-functionalization of OMS is a ligand coordination to the OMS. This ligand coordination is also named "grafting"[98,269,270] in the literature. Also the term "amination" is used,[271,272] when an amine ligand is coordinated to the OMS. The term "extended hook"[273] is found for bifunctional ligands, like ethylenediamine, where one end is anchored to the open metal sites on the framework and the other end is available as an additional functionality in the pore, for example to capture metal ions or clusters at the centers of the channels.[12,98,113,143,146,148,182,269–286]

Using post-functionalization *via* grafting a ligand to the open metal sites in MOFs can improve their performance in various applications, for example increase the gas uptake or catalytic activity. It should be evident that the quantification of the amount of grafted ligands to OMS is essential and can be carried out, for example, by MOF digestion and NMR analysis.

We note that the post-functionalization by ligand-coordination or -grafting to metal sites does not necessarily need to proceed *via* a proven or prepared OMS intermediate. A simple ligand exchange where the solvent–ligand at the metal atom in the MOF framework is replaced by the new (functional) ligand will also achieve this type of post-functionalization. If this ligand exchange proceeds through a more dissociative mechanism, that is, by the existing ligand dissociating first, then OMS will be a short-lived intermediate. However, ligand replacement in coordination chemistry can also occur *via* an associate mechanism through expansion of the coordination number.

In this section we will only discuss post-functionalization by ligand-coordination or -grafting which occurred *via* a verified OMS intermediate.

Post-functionalization of open Cr^{3+} sites

Kim *et al.*[143] reported on the post-functionalized MIL-101(Cr) compounds, CMIL-1 and CMIL-2, where the chiral pyridyl modified organocatalytic L-proline ligands L1 [(*S*)-*N*-(pyridin-3-yl)-pyrrolidine-2-carboxamide] and L2 [(*S*)-*N*-(pyridin-4-yl)-pyrrolidine-2-carboxamide] were coordinated to the open Cr^{3+} sites. The CMIL compounds showed catalytic activities in asymmetric aldol reactions and by comparison with the chiral ligands alone a much higher enantioselectivity. For the post-functionalization, the activated MOF and the new ligand were mixed together in anhydrous chloroform and refluxed under N_2 atmosphere for 24 h. The structure of MIL-101(Cr) did not change after grafting with the chiral ligands based on PXRD. The success of the grafting was based on FT-IR spectroscopy which showed characteristic bands of C═O at 1558 and 1695 cm^{-1}, and N–H stretching bands at 3189 and 3220 cm^{-1}, and on elemental analysis which suggested that ~1.8 chiral ligands per formula unit were incorporated inside the pores of CMILs. The BET surface area decreased from 3850 (for MIL-101(Cr)) to 1420 (for CMIL-1) and to 1375 $m^2\ g^{-1}$ (for CMIL-2), due to the incorporation of the organic molecules inside the pores.[143] Along the same lines, Ren *et al.*[113] grafted the chiral pyridyl modified L-proline derivative [(*S*)-1-formyl-*N*-(pyridin-3-yl)pyrrolidine-2-carboxamide] to the open Cr^{3+} sites of the MIL-101(Cr) framework. They used the same methods as Kim *et al.*,[143] to check the successful introduction of the ligand. The elemental analysis results indicated that 1.45 chiral ligands per formula unit are incorporated inside the pores of CMIL-101 and the BET surface area decreased from 2963 to 1258 $m^2\ g^{-1}$, due to of the immobilization of organic molecules inside the pores (Fig. 32).[113]

Furthermore, Jhung *et al.*[269] reported on MIL-101(Cr) with or without modification for the adsorptive removal of the artificial sweeteners saccharin, acesulfame and cyclamate. For the post-modification of MIL-101(Cr), the activated MIL and melamine or urea was mixed together in toluene solvent and refluxed for 12 hours. Under these conditions and low basicity, the amino groups of melamine or urea were grafted onto the open Cr^{3+} sites. FT-IR spectroscopy showed characteristic bands of N–H bending, C–N stretching, and N–H wagging at 1608 and 1265/1211 cm^{-1}, and 707 cm^{-1} and the BET surface area decreased from 3030 (for MIL-101(Cr)) to 1970 (for urea MIL-101) and to 1350 $m^2\ g^{-1}$ (for melamine MIL-101), indicating the successful introduction of urea and melamine into MIL-101(Cr). It must be noted that the study did not quantify the amount of grafting.[269] Moreover, Janiak *et al.*[138] grafted several glycols ethylene glycols and ethylenediamine onto MIL-100(Cr) and quantified the amount of grafting, by using solution NMR spectroscopy. The ^{1}H-NMR spectra showed signals of the deprotonated and deuterium exchanged ligand $C_6H_3(COO^-)_3$, (btc^{3-}) and the grafted reagents (Fig. 33) and the integration gave ranges of grafted glycols and amine in MIL-100(Cr) from 1.28 to 1.88 molar equivalents for each $[Cr_3(\mu_3\text{-}O)(F,OH)(btc)_2]$ formula unit.[138]

Post-functionalization of open Cu^{2+} sites

Liu *et al.*[98] reported on the grafting with pyridyl-salicylimine (Py-SI) to open metal sites in Cu-bdc MOF MOF-2 by stirring the ligand and activated Cu-bdc in dry toluene. Afterwards, a solution of $PdCl_2$, toluene and DMF was added to Cu-bdc/Py-SI to obtain a Pd@Cu-bdc/Py-SI catalyst for Suzuki coupling (Fig. 34). They based the successful grafting on SEM-EDX quantification of Cl, Pd, and N. To enhance the CO_2 capture in $H_3[(Cu_4Cl)_3(btt_{ri})_8]$ Long *et al.*[278] grafted *N*,*N*′-dimethylethylenediamine (mmen) to the Cu sites to yield $H_3[(Cu_4Cl)_3(btt_{ri})_8(mmen)_{12}]$.[287,288] However, half of the Cu-OMS were not grafted at all, as the grafting was successful only at the large pores. The grafted material did not collapse and retained the original structure according to PXRD. From N_2 sorption measurement the BET surface area decreased from 1770 $m^2\ g^{-1}$ to 870 $m^2\ g^{-1}$.[278] Rosseinsky *et al.*[274] described the binding of secondary amines to the coordination sites on the Cu^{2+} paddle-wheel MOF HKUST-1. The modified HKUST-1 was then exposed to NO to form a coordinated *N*-diazenium diolates (NONOates).[274]

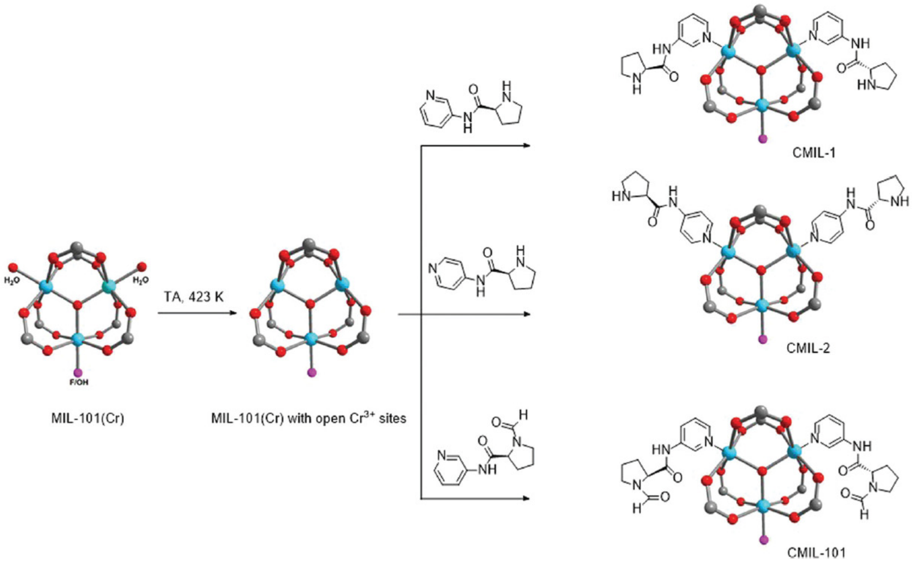

Fig. 32 Activation and post-modification with chiral ligands of MIL-101(Cr). Crystal structure information from ref. 149 (CSD-Refcode CIGXIA). Adapted from ref. 113 with permission of Elsevier BV., copyright 2017 and from ref. 143 with permission from the American Chemical Society, copyright 2009.

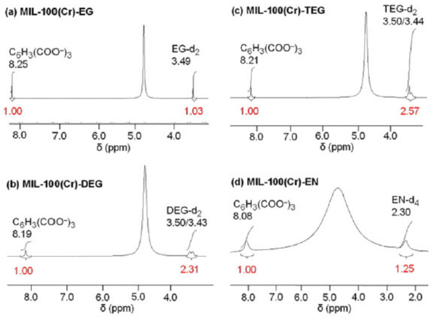

Fig. 33 ^{1}H NMR spectra (200 MHz) of modified MIL-101(Cr) after dissolution in D_2O/NaOD (EG = ethylene glycol, DEG = diethylene glycol, TEG = triethylene glycol, EN = ethylenediamine). Reproduced from ref. 138 with permission of Elsevier BV., copyright 2015.

Gas sorption

Gas adsorption, including harmful gases is an issue of constant interest in MOF chemistry.[79,289] The amount and affinity of the adsorbed gas depends on adsorbent (MOF) binding sites, surface area, porosity, temperature, pressure and the polarity of the adsorbate (gas).[290] MOFs have been widely studied with respect to the selective adsorption and separation of gases such as H_2, CO_2, CO, NO, C_2H_2, CH_4 and SO_2.[291,292] Open metal sites and large surface area in MOFs are two important parameters for adsorption capacity and efficiency. Stable MOFs with accessible open metal sites have a higher gas affinity and binding energy compared to the same MOF without OMS.[293] The somewhat higher porosity of OMS-MOFs also leads to a higher gas uptake. Gas adsorption to OMS is typically reflected in a steeper rise of the adsorption isotherm and a higher (negative) heat of adsorption (Q^0_{st}) at low loading compared to the same non-OMS MOF.[220] Such a steep rise and high Q^0_{st} reflects the affinity, that is preferential binding of the gas molecules to the free metal site. We note that the comparison of adsorption capacity or gas uptake values at $p/p_0 = 1$ or 1 bar absolute pressure is less meaningful since these values are largely determined by pore volume.[67,251]

In connection with gas sorption studies on OMS-MOFs, experimental high-resolution[70,155]/powder neutron diffraction[70,159,228,294–296] studies, synchrotron X-ray diffraction analysis[155,178,297,298] and near sites edge X-ray adsorption fine structure (NEXAFS)[299] spectroscopy were performed to obtain structural information of MOFs with OMS and to derive insight into the role of the OMS on the MOF–adsorbate interactions.[300]

One must admit that single crystal X-ray studies which require sizeable and good quality single crystals are seldom available for OMS-MOFs with adsorbates (see below for examples). We note that often MOF structures, *e.g.*, for HKUST-1, are reported with no solvent–ligand at the metal atom. Usually, the electron density which is associated with this solvent ligand then has not been refined or has been removed by the Squeeze option in the refinement procedure.[301–303] The knowledge about the interaction and dynamics between the OMS and adsorbate molecules is crucial for the design of frameworks with efficient gas capture possibilities. However, it is evident that in order to study OMS–adsorbate interactions by experimental structure methods, a fully activated sample without remaining coordinated solvent ligands on the metal atom is highly advantageous to induce and have only the adsorbate bound to the metal atoms.[155]

H_2 adsorption

In the early but superseded realm of hydrogen storage in MOFs metal–organic frameworks with open metal sites were seen as

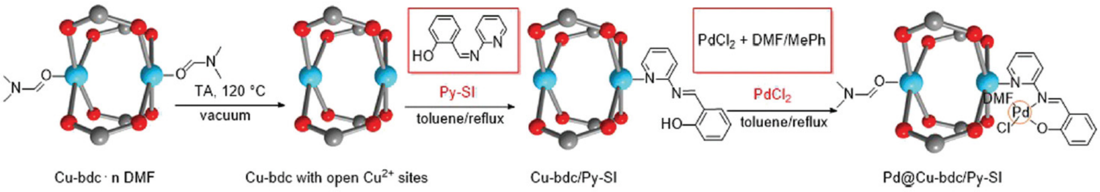

Fig. 34 Activation and grafting of [$Cu_2(bdc)_2(DMF)_2$] with pyridyl-salicylimine (Py-SI). Crystal structure information from ref. 128 (CSD-Refcode DIHVIB01). Adapted from ref. 98 with permission of Elsevier Inc., copyright 2016.

an important class for hydrogen sorption. The X-ray and neutron diffraction studies showed that OMS are the understandable primary location for adsorbed H_2 molecules. For OMS only the low pressure H_2 adsorption is relevant. Due to the good hydrogen affinity, they can slightly increase the H_2 uptake capacity and improve the isosteric heat of adsorption at low coverage (Q^0_{st}). However, due to the still relatively weak interactions with H_2, MOFs were not able not meet the gravimetric and volumetric storage targets.[86–88,91,304–306]

The most investigated series of metal–organic frameworks is the M-MOF-74 family consisting of, *e.g.*, [M_2(*p*-dobdc)], [M_2(*m*-dobdc)], [M_2(dobpdc)], and [M_2(olz)], which possess a high concentration of OMS, which can interact more strongly with the H_2 molecules. The isosteric heats of H_2 adsorption in [M_2(*p*-dobdc)] (M = Mg^{2+}, Mn^{2+}, Fe^{2+}, Co^{2+}, Ni^{2+}, Cu^{2+}, Zn^{2+}) indicated initial stronger binding sites and lower enthalpies of adsorption upon increasing adsorption. From the quantitative assessment of H_2 uptake a change in adsorption isotherm shape occurs upon reaching approx. one equivalent of H_2 per metal site. The isosteric heat dropped from about 8–13 kJ mol^{-1} (depending on the metal, see Fig. 35) to a lower value of about 5–6 kJ mol^{-1} after saturation of the stronger binding sites at a loading of ∼0.8 molecule H_2 per metal.[88,89,91,307–309] It can be noted that conversely the loading of ∼0.8 mol H_2 per mol metal may represent a quantification of the amount of formed OMS if the alternative of missing-metal defects or pore blocking can be excluded.

Based on neutron diffraction the presence of primary strong H_2/D_2 binding sites and several additional weaker binding sites was elucidated for M-MOF-74. Neutron diffraction studies with M-MOF-74 revealed metal-to-D_2 distances for the primary binding site of 2.20(1)–3.03 Å with $Ni^{2+} < Co^{2+} < Mg^{2+} < Fe^{2+} < Zn^{2+} < Mn^{2+} < Cu^{2+}$ (Fig. 36). The metal-to-D_2 bond distances correlate with the adsorption enthalpies, with ordering as $Cu^{2+} < Mn^{2+} \sim Zn^{2+} < Fe^{2+} < Mg^{2+} < Co^{2+} < Ni^{2+}$.[307,308]

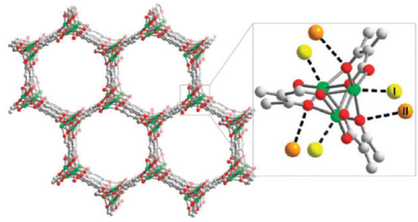

Fig. 36 View of the crystal structure of Mg-MOF-74 in the [001] direction. Atom color scheme: Mg green; C gray; O red. D_2 binding sites were determined by neutron diffraction: site I yellow; site II orange. Reproduced from ref. 308 with permission from The Royal Society of Chemistry, copyright 2011.

In isoreticular MOFs the Q^0_{st} ordering is $Mn^{2+} < Fe^{2+} < Co^{2+} < Ni^{2+}$ which is inversely proportional to the ionic radius of the metal ions which steadily drops from (high spin) Mn^{2+} to Ni^{2+} (Fig. 37).[88,310] As noted above for Fig. 35, the inflection points in Fig. 37 from ∼0.75 H_2/M in [Co_2(*m*-dobdc)] to ∼0.85 H_2/M in [Fe_2(*m*-dobdc)], may be interpretation as the fraction of OMS generated and available for H_2 binding. The inflection points are similar to the H_2-isosteric heat values for the M-MOF-74 series shown in Fig. 35.[88]

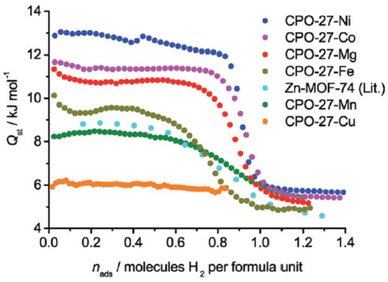

Fig. 35 Maximum H_2 isosteric heat of adsorption ($Q_{st,max}$) curves for M-MOF-74 (M = Mg, Mn, Fe, Co, Ni, Cu, Zn) (denoted in the figure as M-CPO-27). For M-MOF-74 a formula unit of [$M(C_4HO_3)$] was used here. Reproduced from ref. 89 with permission from The Royal Society of Chemistry, copyright 2015.

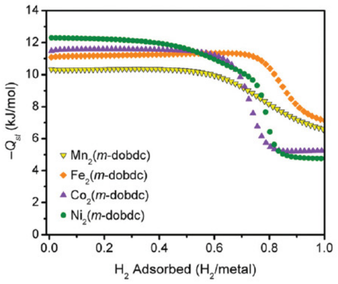

Fig. 37 H_2 isosteric heat of adsorption curves for [M_2(*m*-dobdc)] (M = Mn, Fe, Co, Ni). Reproduced from ref. 88 with permission from the American Chemical Society, copyright 2014.

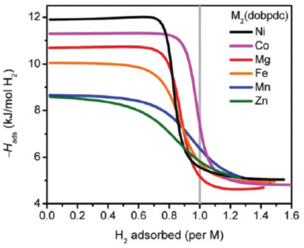

Fig. 38 H_2 isosteric heats of adsorption curves for $[M_2(dobpdc)]$ (M = Mg, Mn, Fe, Co, Ni, Zn). Reproduced from ref. 309 with permission from the American Chemical Society, copyright 2016.

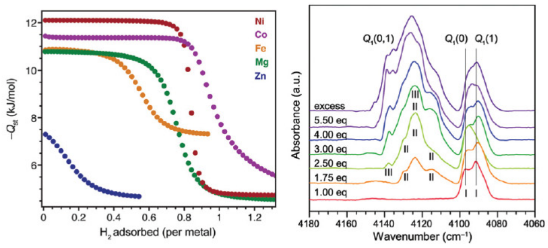

Fig. 39 Left: H_2 isosteric heat of adsorption curves for $[M_2(olz)]$ (M = Mg, Fe, Co, Ni, Zn). Right: IR absorption of H_2 in $[Mg_2(olz)]$ performed at 15 K. The equivalents (eq.) refer to the number of H_2 molecules per Mg^{2+}, and the spectral features corresponding to the distinct sites observed are denoted with Roman numerals. $Q(0)$ refers to *para*-H_2 and Q(1) to *ortho*-H_2 modes. The IR spectra indicate that H_2 is adsorbed at multiple sites as a function of loading. Reproduced from ref. 310 with permission from the American Chemical Society, copyright 2016.

In case of $[M_2(dobpdc)]$ the isosteric heat curve had the inflection point only for $[Mn_2(dobpdc)]$ and $[Co_2(dobpdc)]$ at an H_2 loading of one molecule per mol metal while for M = Mg^{2+}, Fe^{2+}, Ni^{2+}, Zn^{2+} the inflection point is at a lower loading than 1 eq. of H_2/M, as defects or intergrowth of crystallites may block some of the channels or the OMS are not quantitatively formed (Fig. 38). This can explain why Ni-MOF-74 displayed a higher H_2 uptake capacity at pressures up to approx. 300 mbar (at 77 K) than $[Ni_2(dobpdc)]$. While at the same time, $[Ni_2(dobpdc)]$ showed a higher gravimetric density of OMS (6.42 *vs.* 5.16 mmol g^{-1}) and a higher low-coverage isosteric heat. Noteworthy also Zn^{2+} showed the lowest value, due to its $3d^{10}$ electron configuration.[309]

The charge density at the metal sites and thus the H_2 binding enthalpies could be enhanced by replacing the linker *p*-dobdc^{4-} with *m*-dobdc^{4-}, thereby going from the M-MOF-74 to $[M_2(m\text{-}dobdc)]$ (M = Mn^{2+}, Fe^{2+}, Co^{2+}, Ni^{2+}) (Table 3). The stronger interaction between H_2 and the metal centers in the latter is evidenced by shorter M–H_2 contacts based on the results from powder neutron diffraction, inelastic spectroscopy and IR spectroscopy experiments.[88]

The MOFs, $[M_2(olz)]$ (M = Mg^{2+}, Fe^{2+}, Co^{2+}, Ni^{2+}, olz^{2-} = olsalazinate), exhibit the same SBU and ligand coordinating functionality as $[M_2(p\text{-}dobdc)]$.[310] The isosteric heats od adsorption values for $[M_2(olz)]$ are very similar to $[M_2(m\text{-}dobdc)]$ and $[M_2(dobpdc)]$ (Fig. 39, left).[310] The inflection points in the isosteric heat plot of Fig. 39, left indicate the amount of available OMS. For $[Co_2(olz)]$ the inflection point at 'H_2 adsorbed/metal' of about 1 shows near complete preceding activation and Co–OMS availability. The MOF $[Ni_2(olz)]$ and $[Mg_2(olz)]$ still have the inflection point at about 85% and 70% 'H_2 adsorbed/metal', respectively. A significant lower inflection point, *i.e.* OMS availability of about 0.6 'H_2 adsorbed/metal' is seen for $[Fe_2(olz)]$, which was explained with the milder activation conditions employed for this compound.

In situ IR spectroscopy was used to determine the nature of the $[Mg_2/Ni_2(olz)]$ interaction with H_2. To follow the binding of H_2 at the OMS the characteristic red-shift of the H–H stretching frequency can be used. IR spectra (Fig. 39, right) showed a doublet (4097 and 4091 cm^{-1}) at a loading of one H_2 per metal. The authors described that these are the pure vibrational modes of *ortho*-H_2 and *para*-H_2 bound to the OMS for 1 eq. H_2/M.[310]

The curves of H_2 isosteric heats of adsorption *versus* the amount of H_2 adsorbed/metal in Fig. 35, 37, 38 and 39, left allow to estimate the amount of available OMS. Thereby it can be assumed that '/metal' means total molar metal amount based on the sample mass and idealized formula unit. The isosteric heat of adsorption of H_2 data can be obtained from low-pressure H_2 isotherms at two different temperatures, *e.g.* 77 and 87 K using the Clausius–Clapeyron relation.

The H_2 amount at which the isosteric heat decreases (the inflection point), can be taken as an indicator for the amount and the accessibility of the OMS. If the inflection point is at 'H_2 adsorbed/metal' ≈ 1 then the framework was probably fully activated and all OMS were accessible to H_2. If the inflection point in the isosteric heat curve is at 'H_2 adsorbed/metal' <1, then part of the OMS is not accessible to H_2. This could be due incomplete activation that is incomplete solvent removal or missing-metal (or other) defects or pore-blocking in the channels which renders the metal sites inaccessible to gas molecules.

M-btt (M = Cr^{2+}, Mn^{2+}, Fe^{2+}, Cu^{2+}) was one of the first OMS MOF series which was studied for hydrogen storage (Table 3).[157–160,311] As noted above Fe-btt exhibits a higher isosteric heat of adsorption compared to Mn-btt, due to the smaller radius for Fe^{2+} (higher charge-to-radius ratio), giving a more polarizing binding site at the Fe ion.[309,311] Powder neutron diffraction of D_2-loaded Cr-btt[159] suggested only moderately strong Cr^{2+}–D_2 interactions from the rather long Cr–D_2 distance. However, the isosteric heat at low coverage was higher for Cr-btt compared to $[Cr_3(btc)_2]$[135] (Table 3). $[Cr_3(btc)_2]$, with the same paddle-wheel SBU as HKUST-1. It was suggested that the Cr$\equiv$Cr quadropole bond decreases the Lewis acidity of the Cr^{2+} centers.[157–160,311]

Paddle-wheel MOFs, like HKUST-1, NOTT-X, PCN-10,-11 with OMS feature in general comparatively low Q^0_{st} values of less than -7 kJ mol^{-1} (Table 3). It should be noted that tor Cu^{2+} in HKUST-1 and related MOFs its Jahn–Teller effect provides no strong driving force for coordination of gas molecules at the Cu^{2+} site.[135]

Accordingly, the series of NOTT-*X* (*X* = 100–107) MOFs with the paddle-wheel SBU showed isosteric heats of adsorption at low coverage in the range of 5.20 to 6.70 kJ mol^{-1} (Table 3) and the enthalpy of H_2 binding is influenced by pore size and the presence of additional aromatic rings not the OMS.[312]

Still, the paddle-wheel OMS-MOFs have a higher hydrogen affinity at low pressures in comparison to MOFs without OMS. The isosteric heat of adsorption in HKUST-1 (-4.5 kJ mol^{-1}, Table 3) is higher than in MOF-5 (-3.8 kJ mol^{-1}), due to the steep rise in the adsorption isotherm.[313]

In summary, open metal sites MOFs with M = Mg, Mn, Fe, Co, Ni are the most promising candidates for hydrogen sorption at low pressures, due to the higher enthalpy of adsorption of H_2 at these metal ions (isosteric heat of adsorption from about -10 to -13.5 kJ mol^{-1}). The isosteric heat of H_2 adsorption to the MOF pore wall is only around -3.8 kJ mol^{-1}.[313]

CO_2 adsorption

The interaction between CO_2 and OMS is generally more than 30 kJ mol^{-1}, giving a high CO_2 uptake at low relative pressure.[67,251,314] The binding affinity between the OMS and the CO_2 adsorbate is correlated with electrostatic interactions (CO_2 has a quadrupole moment).[315] The isostructural frameworks M-MOF-74 (M = Mg^{2+}, Mn^{2+}, Fe^{2+}, Co^{2+}, Ni^{2+}, Cu^{2+}, Zn^{2+}) have been extensively studied for their high performance in CO_2 storage.[52,70,316–319] Since these frameworks can be synthesized with different metals, they reflect both the role of each metal and the degree of Lewis acid interaction between the metal center and the CO_2 molecules. In particular, the presence of the stronger CO_2–OMS binding and a high density of OMS within the framework led to large CO_2 uptakes and makes this MOF group an interesting candidate for CO_2 adsorption.[52,97] Especially at low pressures (0.1–0.2 bar), which is the pressure region of interest in flue gas separation, these OMS-MOFs show high CO_2 uptakes.[55]

Kortrigh *et al.* applied 'near sites edge X-ray absorption fine structure' (NEXAFS) spectroscopy measurements at the Mg K-edge to study the interactions of Mg-MOF-74 with CO_2 molecules at open Mg^{2+} sites.[299] The authors associated the square pyramidal geometry at the open Mg^{2+} site with the appearance of a pre-edge peak in the Mg K-edge spectrum. A reduction in the intensity of this pre-edge feature, accompanied by a slight blue shift and an increase in intensity of the strongest major edge feature upon adsorption of CO_2, is interpreted as a recovery of the octahedral geometry around the Mg^{2+} cation with CO_2 coordination. This interpretation of the experimental results was supported with DFT calculations.[299]

Yildirim *et al.* showed by neutron powder diffraction measurements for the example of Mg-MOF-74, that the OMS in the M-MOF-74 series represent the primary adsorption sites.[228] Subsequently, the occupation of other CO_2 adsorption sites within the framework was later authenticated by neutron diffraction experiments and synchrotron X-ray diffraction measurements and was further supported by *in situ* ^{13}C NMR measurements.[70,178,294,320]

As is shown in Fig. 40 the CO_2 molecule assumes a bent end-on configuration when binding to metal atoms, as was detected for OMS in M-MOF-74 (Mg^{2+}, Mn^{2+}, Fe^{2+}, Co^{2+}, Cu^{2+}, Zn^{2+}) *via* powder neutron diffraction experiments.[70]

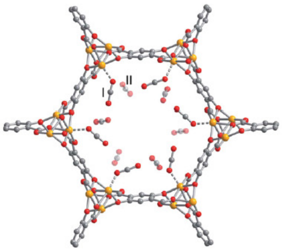

Fig. 40 View of a single channel in Fe-MOF-74 that is loaded with 1.5 CO_2 per iron(II) site. From the powder neutron diffraction data, there are two apparent CO_2 sites labelled as I and II in order of decreasing binding strength. Orange, grey, and red spheres represent Fe, C, and O atoms, respectively. Reproduced from ref. 70 with permission from The Royal Society of Chemistry, copyright 2014.

Moon *et al.* performed single-crystal X-ray diffraction experiments with CO_2 adsorbed single crystals of Mg-, Co- and Ni-MOF-74, to obtain insight into the CO_2 adsorption sites at the atomic level.[178] Also, two non-independent adsorption sites within the framework were found, which were assigned to the OMS (site A) and a secondary adsorption site between two OMS (site B) (Fig. 41).[178]

According to CO_2 adsorption isotherms at 298 K, the CO_2 capacity of Mg-, Co- and Ni-MOF-74 are 0.81, 1.30 and 1.67 mol mol^{-1}, respectively, at 0.1 bar.[178] The experimental obtained Q_{st}^0 values for CO_2 at OMS in the M-MOF-74 series are in the range from -39.0 to 47.0 kJ mol^{-1} for Mg^{2+} to -22.1 kJ mol^{-1} for Cu^{2+} following the order $Mg^{2+} > Ni^{2+} > Co^{2+} \sim Fe^{2+} > Mn^{2+} > Zn^{2+} > Cu^{2+}$.[52,70,71,222,297]

Adsorption of CO_2 at the OMS should also be reflected in the observation of an M–O(CO_2) 'bond' distance. Findings from single-crystal X-ray diffraction revealed short M–O(CO_2) bond distances, (Mg^{2+}–O(CO_2), 2.13(2) Å; Co^{2+}–O(CO_2), 2.27(2) Å; Ni^{2+}–O(CO_2), 2.08(6) Å), indicating the strong affinity for CO_2 molecules.[178] Single-crystal X-ray diffraction data for Mg- and Co-MOF-74 show interactions, of each O(CO_2) atom in site B with the C(CO_2) atom in site A, resulting in a T-shaped arrangement of adjacent CO_2 molecules (Fig. 41a and b). For the CO_2 molecule adsorbed on Ni-MOF-74, a slipped-parallel geometry was indicated (Fig. 41c).[178]

The values for the M–O(CO_2) distances determined *via* high-resolution powder neutron diffraction experiments were

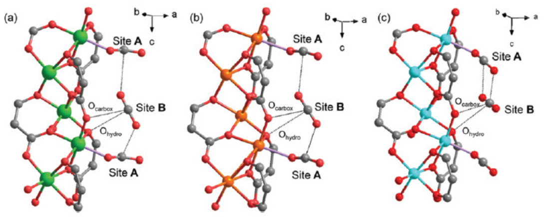

Fig. 41 Single-crystal X-ray structure of CO_2-adsorbed (a) Mg-MOF-74, (b) Co-MOF-74, and (c) Ni-MOF-74. Reproduced from ref. 178 with permission from the American Chemical Society, copyright 2019.

Mg^{2+}–O(CO_2), 2.27(1) Å; Co^{2+}–O(CO_2), 2.23(9) Å; Ni^{2+}–O(CO_2), 2.29(3) Å (taken at a temperature of 10 K) and differ only slightly from the single-crystal X-ray diffraction values.[70] The elongated M–O(CO_2) distances found for Mn^{2+} (2.51(3) Å), Cu^{2+} (2.86(3) Å) and Zn^{2+} (2.43(4) Å) analogues reflect their lower isosteric heats of adsorption. For Mn^{2+} this has been explained by its larger ionic radius.[70] It can be noted that for Cu^{2+} its Jahn–Teller effect together with an overall lower effective ionic charge of the Cu^{2+} ion provide no strong driving force for coordination of CO_2 molecule at the apical Cu^{2+} site in Cu-MOF-74.[297]

It has been shown that the adsorption capacity of CO_2 can vary depending on the metal species. Semilogarithmic plots of the adsorption isotherms depict a two-step adsorption, indicating a sequential occupation of the adsorption sites.[222,297,320,321] The first step at low loadings was assigned to the adsorption on the OMS (site A in Fig. 41).[297] Depending on the metal species, it occurs at increasing pressure in the order $Mg^{2+} < Ni^{2+} < Co^{2+} < Mn^{2+} < Zn^{2+} \ll Cu^{2+}$. At higher pressures the occupation of the secondary adsorption sites (site B in Fig. 41) occurs with the same metal order.[297]

A significantly lower Q^0_{st} value of -22.1 kJ mol^{-1} and a nearly linear uptake for CO_2 is evidence that there is no decisive preference for adsorbing CO_2 at the apical Cu^{2+} OMS or in the pores (Fig. 42).[70]

Further, the Cu–O–C(CO_2) angle was estimated to be 121°, while the M–O–C(CO_2) angles of the M-MOF-74 analogs are in the range of 145–150°.[297] The small bond angle for Cu-MOF-74 together with the weaker Cu–O interaction, indicates a strong influence of van der Waals interactions between CO_2 and the adjacent pore wall of the $dobdc^{4-}$ ligand.

The structure and dynamics of CO_2 molecules adsorbed to OMS were also examined by IR spectroscopy for the M-MOF-series.[322–325] Schmidt *et al.* observed *via* diffuse reflectance IR spectroscopy, that Mg-MOF-74 induces a blue shift in the asymmetric stretching vibration (ν_3 mode) of CO_2 adsorbed at the metal site, while the transition metal analogues cause a redshift (Fig. 43).[322] While the bonding to transitional metals occurs by electrostatic and charge transfer effects, the bonding to Mg^{2+} is almost exclusively due to electrostatic effects. Complete cancellation of contributions from the opposite local modes give rise to the observed frequency shift. This observation was explained by the absence of d-valence electrons in Mg^{2+}, so that no back bonding (electron donation to the CO_2 π^* orbital) is possible.[322]

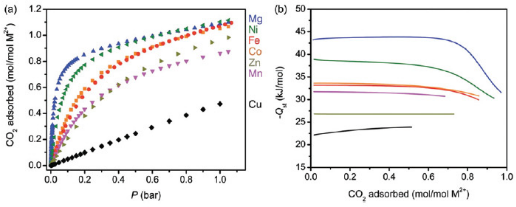

Fig. 42 Excess CO_2 adsorption isotherms for the M-MOF-74 series at 298 K. (b) Low coverage Q_{st} determined from CO_2 adsorption isotherms collected at 298, 308, and 318 K. Reproduced from ref. 70 with permission from The Royal Society of Chemistry, copyright 2014.

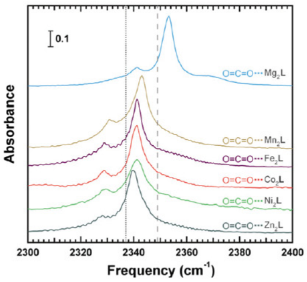

Fig. 43 Diffuse reflectance IR spectra of adsorbed CO_2 M-MOF-74 (M = Mg, Mn, Fe, Co, Zn) at 293 K. The dashed line at 2349 cm^{-1} marks the gas phase CO_2 ν_3 frequency and the dotted line at 2337 cm^{-1} marks the much weaker band involving the ν_3 transition of CO_2 in the first excited ν_2 level. Reproduced from ref. 322 with permission from the American Chemical Society, copyright 2015.

The dependency of the adsorption strength on the temperature in Mg-MOF-74 was investigated by Long *et al.*[326] Mg-MOF-74 shows an initial steep CO_2 uptake at low pressures which is characteristic for high CO_2 affinity. Huang *et al.* performed variable-temperature (VT) ^{17}O solid-state NMR spectroscopy (SSNMR) from 150 K to 403 K, to characterize the CO_2 adsorption capacity of MOFs as a function of the metal–CO_2 bond strength.[327] The authors stated that the CO_2 molecule is attached in a minimum energy configuration to the OMS, with a temperature-dependent angle Mg–O–C(CO_2) of *ca.* 120–130° (Fig. 44). Variable temperature ^{17}O SSNMR line shapes were interpreted by a wobbling of CO_2 about its axis and a hopping between different adsorption sites (Fig. 44). A reduced mobility of the CO_2 molecules at low temperatures leads to an increased interaction with the OMS and *vice versa*. With increasing temperature to about 403 K wobbling increases and remains in the fast motion regime (107 Hz), indicating that CO_2 moves through a larger space. On the other hand, the hopping angle decreases with increasing temperature, which was attributed to be a result of enhanced CO_2 motion along the length of the channels.

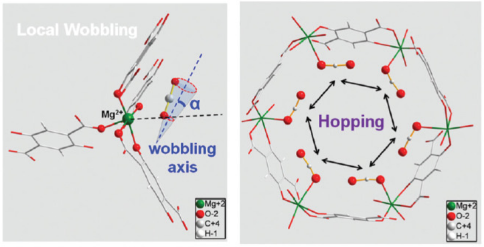

Fig. 44 Demonstration of the motion of adsorbed CO_2 molecules in Mg-MOF-74. For the adsorbed CO_2 two distinct motions were found: (left) localized wobbling, with precession of CO_2 around an angle α about the wobbling axis defined by its minimum energy configuration with respect to Mg; and (right) nonlocalized 6-fold hopping of adsorbed CO_2 between OMS. Reproduced from ref. 327 with permission from the American Chemical Society, copyright 2014.

In HKUST-1 two primary adsorption sites were revealed by the Fourier difference maps.[228] One adsorption site is associated to the open Cu^{2+} site and the other is associated to "the small cage window site, where the CO_2 sits in the four triangular-shaped openings into the small octahedral cage." Neutron diffraction measurement on the CO_2 adsorption in HKUST-1, for two different CO_2 loadings (1.07 and 1.47 CO_2/Cu), revealed that most CO_2 molecules prefer to adsorb on the open Cu^{2+} sites at low CO_2 concentration. The preferred adsorption on the OMS was associated with the higher electrostatic interaction between the OMS and the CO_2 quadrupole moment compared to an otherwise near vdW interaction between the organic framework walls and CO_2. Only with increased CO_2 loading, adsorption on the center of the small octahedral cage and the corner of the large cuboctahedral cage, was observed.[228]

Nachtigall *et al.* calculated the heat of adsorption from the CO_2 adsorption isotherm at 303 K of approx. -29 kJ mol^{-1} at low coverage. A slightly increase of heat of adsorption to approx. -32 kJ mol^{-1} was observed with higher loading (>8 mmol g^{-1}).[232]

Supported by DFT calculations, this behavior was explained as follows: The CO_2 molecules adsorb onto Cu^{2+} sites at low coverage. The adsorbed CO_2 molecules are tilted towards adjacent Cu^{2+} site, which leads to maximized lateral CO_2–CO_2 interactions. With increasing coverage (up to CO_2/Cu = 20 : 12, CO_2) the occupation takes place in the cage windows of small cages. Here, the CO_2 molecules in cage window sites are stabilized through lateral interactions with the CO_2 adsorbed at the Cu^{2+} site. At even higher coverages, CO_2 molecules adsorb in the center of small cages and in large cages. The increasing adsorption enthalpies which were found in the high-coverage regime, were attributed to lateral interactions between these molecules and those already adsorbed in Cu^{2+} sites and cage windows sites.[232]

For MIL-100(Cr), the isosteric heat of adsorption Q_{st}^{0} of -58 kJ mol^{-1} was calculated from CO_2 adsorption isotherms at 273, 298, and 323 K at low coverage.[328] Usually, the value for the heat of adsorption can be obtained from adsorption isotherms at two different temperatures by applying the Clausius–Clapeyron equation.[329] From variable-temperature infrared (VTIR) spectroscopy standard adsorption enthalpies for CO_2 can be obtained from analysis of IR spectra recorded over a temperature range while simultaneously measuring the equilibrium pressure inside a closed IR cell.[140] This study, revealed the following heats of adsorption for MIL-100(Cr) (-63 kJ mol^{-1}), MIL-100(V) (-54 kJ mol^{-1}) and MIL-100(Sc) (-48 kJ mol^{-1}).[140]

In comparison Férey *et al.* reported an adsorption enthalpy of -62 kJ mol^{-1} for MIL-100(Cr) from CO_2 adsorption isotherms coupled with microcalorimetric experiments, that is in good agreement with the value delivered form VTIR spectroscopy analysis.[251]

The asymmetric stretching vibration (ν_3 mode) of free CO_2 (2349 cm^{-1}) remains essentially invariant upon adsorption of CO_2 in for MIL-100(Cr) (2349 cm^{-1}), MIL-100(V) (2348 cm^{-1}) and MIL-100(Sc) (2352 cm^{-1}).[140] However, Palomino *et al.* did not take the vibration of free CO_2 as a reference but the value of 2341 cm^{-1} for carbon dioxide confined in the pores of silicalite.[330] Relative to this value of 2341 cm^{-1} the above blue-shifted values near 2350 cm^{-1} were interpreted as being due to a CO_2 adsorption onto open Cr^{3+}, V^{3+} and Sc^{3+} sites.[140]

Also, Férey *et al.* associated the strong ν_3-CO_2 band at 2351 cm^{-1} for MIL-100(Cr) after CO_2 adsorption with the formation of CO_2-coordinated species on the Lewis acid sites ($O{=}C{=}O\cdots Cr^{3+}$).[251] In addition, a weak band was observed at 1271 cm^{-1}, which is assigned to the $2\nu2$ overtone in Fermi resonance with the ν_1 mode near 1370 cm^{-1} and which is infrared-inactive for the free CO_2 molecule. It was also noted that CO_2 adsorption on MIL-100(Cr) with the aqua ligands still present on the Lewis acid sites did not exhibit the 2351 cm^{-1} band.[251]

Microcalorimetric experiments for MIL-100(Fe) were also performed, to investigate the energetics of interactions between iron sites and CO_2 during gravimetric measurements of adsorption.[142] Here, the heat of adsorption of CO_2 for MIL-100(Fe), lies in the range of -25 kJ mol^{-1} and -30 kJ mol^{-1}, for the sample (activated at 100 °C) where only Fe^{3+} sites are present and -35 kJ mol^{-1} for the partially reduced sample (activated at 250 °C) where Fe^{3+}/Fe^{2+} are present (see solvent removal strategies).[142]

The most recent computational studies through a periodic quantum mechanical hybrid HF/DFT approach of MIL-100(M^{3+}) structures with Cr^{3+} and Fe^{3+}, revealed that Cr^{3+} interacts strongly with the CO_2 molecule showing a short Cr^{3+}–(CO_2) distance (2.35 Å).[331] This was explained by the high electrostatic potential and the role of partly occupied d-orbitals (Fig. 45). In comparison Fe^{3+} shows a longer Fe–O(CO_2) distance (2.46 Å) and a smaller electrostatic potential thus leading to a weaker interaction energy.

Low-pressure adsorption isotherms on M-btt (M = Cr^{2+}, Mn^{2+}, Fe^{2+}, Cu^{2+}), at 298 K exhibit a steep initial rise, which is characteristic for the presence of highly polarizing adsorption sites (Fig. 46).[156] The steepest rise in the adoption isotherm was observed for Fe-btt, indicating a stronger interaction with CO_2 in comparison to its analogues. The calculated isosteric heats of adsorption at zero coverage were in the range of -51.2 kJ mol^{-1} to -30.7 kJ mol^{-1}, following the order $Fe^{2+} > Mn^{2+} > Cr^{2+} > Cu^{2+}$. Queen *et al.* showed, that the M–CO_2 adsorption strength is reflected in the increase in the

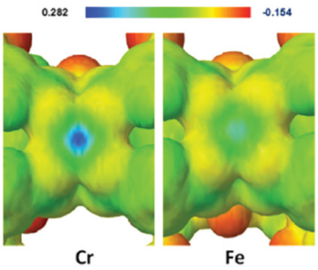

Fig. 45 Electrostatic potential of MIL-100 around the open Cr^{3+} and Fe^{3+} site. Reproduced from ref. 331 with permission from the American Chemical Society, copyright 2019.

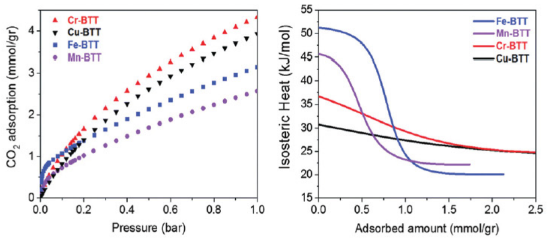

Fig. 46 Left: Excess CO_2 adsorption isotherms for M-btt (M = Cr^{2+}, Mn^{2+}, Fe^{2+}, Cu^{2+}) at 298 K. Right: Isosteric heats of adsorption, Q_{st}, plotted as a function of CO_2 loading. Reproduced from ref. 156 with permission from The Royal Society of Chemistry, copyright 2018.

bond distance range from 2.36(3) Å for Fe-btt to 2.60(3) Å for Cu-btt.[156]

Also, structural investigations *via* high-resolution powder neutron diffraction experiments of M-btt reveal the expected preferred adsorption of the guest molecules on the OMS (Fig. 47). However, it was pointed out[156] that Mn-btt is not suitable for these *in situ* diffraction experiments, as 83% of the OMS remained coordinated by methanol solvent molecules after activation (based on a previous X-ray analysis).[160]

In [Cu_2(dmcapz)] a steep uptake of 2.3 mmol g^{-1} was investigated at lower pressure, corresponding to the adsorption of one molecule CO_2 at each dinuclear Cu_2 unit.[100]

Furthermore, it has been shown, that the Cu^{2+} paddle wheel MOFs Cu-tdpat and Cu-Sp5, with both OMS and Lewis basic sites (LBS) within the linker, display an improved CO_2 adsorption capacity. The adsorption enthalpy at zero loading of -42.2 kJ mol^{-1} for Cu-tdpat and -43.1 kJ mol^{-1} for Cu-Sp5 was calculated from the CO_2 sorption data.[332] Feng *et al.* noted that these higher than expected (see above) adsorption enthalpies for Cu-tdpat and Cu-Sp5 are not only caused by the interaction with the open Cu^{2+} site, but also influenced by further adsorption sites (LBS and phenyl rings) as was investigated with room-temperature IR absorption measurements.[333]

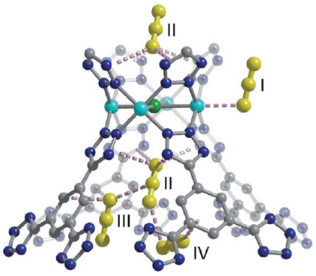

Fig. 47 View of the four different CO_2 adsorption sites within the MOFs Cu-btt as determined from Rietveld analysis of high-resolution powder neutron diffraction data. Cyan, grey, blue, and green spheres represent Cu, C, N, and Cl atoms, respectively, and yellow ball-and-stick models represent CO_2. Reproduced from ref. 156 with permission from The Royal Society of Chemistry, copyright 2018 (*cf.* to Fig. 27 for the adsorption sites identified by DFT calculations).

Zhu *et al.* found that in the framework of [Co_2(tzpa)(μ_3-OH)], the existence of accessible OMS, μ_3-OH groups, and uncoordinated carboxylate O sites, cause strong affinity towards CO_2.[181]

CO adsorption

MOFs with OMS have been proven to show a high heat of adsorption for CO at zero loading. In the literature the dipole moment of CO is sometimes invoked to explain the CO interaction with the metal at the OMS. We note however, that the dipole of CO is only 0.10 Debye with the negative end at the carbon atom. Instead and as can be expected from well-established metal–carbonyl chemistry, CO is an excellent ligand with strong covalent interaction to transition-metal atoms. When complete occupancy of the OMS has been achieved the dispersive forces between CO molecules and the organic pore walls of the network become effective. This leads to a decrease in the adsorption enthalpy. Based on the experimentally determined heat of adsorption for the M-MOF-74 series, it was found that the CO affinity for the OMS follows the order $Ni^{2+} > Co^{2+} \gg Mg^{2+} > Cu^{2+}$, indicating strong interaction of Ni^{2+} and Co^{2+} for CO molecules.[73,178]

The heat of adsorption values for CO in M-MOF-74 reflect the influence of the metal atom on the CO affinity. Moon *et al.* found the strongest affinity to CO for Ni^{2+}, reaching a Q^0_{st} value of -59.7 kJ mol^{-1}, followed by Co^{2+} with -55.5 kJ mol^{-1} and Mg^{2+} with a significantly lower value of -38.3 kJ mol^{-1} at 298 K (the lower value was explained due the lack of d-valence electrons in Mg^{2+} see above).[178] FT-IR analysis revealed stretching vibrations of CO bound to Co^{2+} at 2160 cm^{-1} and to Ni^{2+} at 2170 cm^{-1}, which compared with free CO at 2143 cm^{-1} would indicate only a σ-donor bond from CO to the metal with no metal-to-CO backbonding. No CO vibration was observed for Mg-MOF-74.[178]

It is noted that in comparison to the valence band for free CO at 2143 cm^{-1} the above higher wavenumbers indicate an only very weak M-to-CO back bonding, due to the relatively high metal 2+ oxidation state. CO is known to prefer to bind to metal atoms in low oxidation state (0 or even negative) as in neutral metal carbonyls or negative carbonyl metallates.[23,24]

To obtain insight into the CO adsorption sites at the atomic level, Moon *et al.* performed Single-crystal X-ray diffraction experiments with CO-adsorbed single crystals of Mg-, Co- and Ni-MOF-74. The CO molecules were bound to unsaturated transition metal centers with Co^{2+}/Ni^{2+}–CO bond distances of 2.151(2) and 2.147(3) Å, respectively, as seen before in metal carbonyls. As expected the $Mg^{2+}\cdots$CO distance for the non-classical main-group metal–carbonyl bond is much longer with 2.420(2) Å. Additional adsorbed CO molecules (at site B) show only van der Waals interactions to the metal-bound CO molecules at site A (Fig. 48).[178]

For Cu-MOF-74, an even low adsorption enthalpy of approx. -20 kJ mol^{-1} was indicated by variable temperature IR experiments.[73] Georgiev *et al.* observed the formation of carbonyls with the participation of Cu^{2+} sites, by the appearance of intense IR bands at 2153–2149 cm^{-1}. It was found that with low coverage, the carbonyl band dominates at 2153 cm^{-1}, which converts into

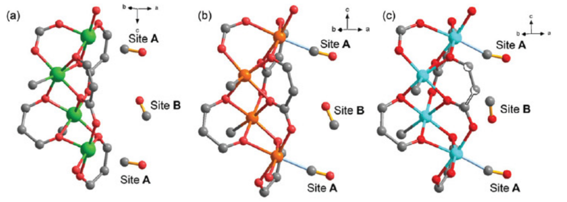

Fig. 48 Single-crystal X-ray crystal structure of CO-adsorbed (a) Mg-MOF-74, (b) Co-MOF-74, and (c) Ni-MOF-74. Reproduced from ref. 178 with permission from the American Chemical Society, copyright 2019.

a band at 2150 cm^{-1} with increased coverage. With further coverage increase, the band is additionally and gradually red-shifted. We note that this comparatively high wavenumber for the CO vibrations suggests very weak interactions with the Cu^{2+} adsorption site. Further a band at 2136 cm^{-1} was referred to physically adsorbed CO. Also, a small fraction of the copper ions was found in the Cu^{+} state, indicated by the weak IR band at 2120 cm^{-1}. Indeed, this band is the only one with remarkable stability towards outgassing.

The authors assumed, that the relatively constant intensity of this band indicates that the respective Cu^{+} sites are formed on specific structures, most probably at the external MOF surface.[73]

Kitagawa *et al.* noted accordingly, that despite the presence of open Cu^{2+} sites in [Cu$_2$(dmcapz)], the CO adsorption at 195 K is negligible for this compound.[100]

Lueking *et al.* performed *in situ* FTIR measurements on the paddle-wheel MOFs HKUST-1 and Cu-tdpat. FITR spectroscopy was able to detect interaction between CO and Cu^{2+} sites in HKUST-1.[334] Here, in 0.34 bar CO at 150 K, the CO vibration was observed at 2169 cm^{-1}. It should be evident that the high wavenumber signals again a non-classical metal carbonyl with a weak Cu$^{2+}\cdots$CO bond due to the non-existing π-back bonding (Fig. 49). Furthermore, CO vibrations at 2120 cm^{-1} were found, which were assigned to interactions of CO with Cu^{+}. After Ar purging, broad shoulders at 2156 cm^{-1} and 2191 cm^{-1} disappeared as excess CO was removed, while modes at 2172 cm^{-1} and 2120 cm^{-1} remained in the spectra. Also, the blue-shift from 2169 cm^{-1} to 2172 cm^{-1} in the CO–Cu^{2+} mode with removal of gaseous CO was attributed to a decrease in the number of CO interacting with the Cu^{2+}.

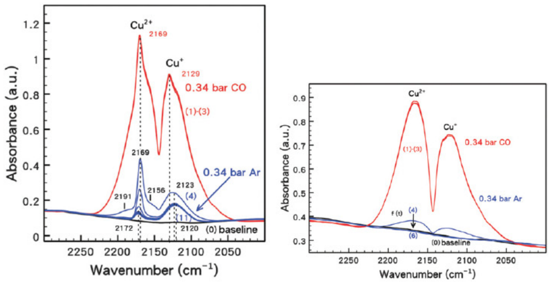

Fig. 49 Left: FTIR spectra of HKUST-1 at 150 K in 0.34 bar CO (1–3), and after 0.34 bar Ar purging to remove physisorbed CO (4–11). Right: FTIR spectra of Cu-tdpat at 150 K in excess CO exposure (1–3) and after Ar purging to remove gas phase CO (4–6). Reproduced from ref. 334 with permission from the Owner Societies, copyright 2015.

At the same time, the CO spectra of Cu-tdpat revealed no remaining Cu-adsorption after Ar purging for CO removal, despite the similar axial Cu^{2+} adsorption site as in HKUST-1.

Further investigations *via* temperature programmed desorption (TPD) measurements, showed a virtually identical profile of CO adsorbed to Cu-tdpat and HKUST-1, suggesting that CO adsorbs more strongly to the open metal site. Also, it was found that the amount of CO adsorbed at the axial Cu^{2+} sites of Cu-tdpat exceeds that of HKUST-1 up to temperatures above 150 K.[334] Gumma *et al.* examined the effect of the CO polarity and the electrostatic CO–OMS interactions on CO-loading in MIL-101(Cr) and HKUST-1, from CO adsorption measurements.[335] Low-pressure CO adsorption at 283 K revealed a high adsorption enthalpy of −48.2 kJ mol^{-1} for MIL-101(Cr) at zero loading. Despite the presence of open Cu^{2+} sites in HKUST-1, a comparatively weaker adsorption enthalpy of −23.4 kJ mol^{-1} was found at similar loading. The adsorption enthalpy decreases at an increased loading of about 6 mmol g^{-1} to −17.4 kJ mol^{-1}. The authors justified the higher adsorption enthalpy in MIl-101(Cr), with a stronger electrostatic contribution between Cr^{3+} and CO. The authors also suggested, that the Cu^{2+} cations in HKUST-1 are not fully accessible, because the coordinated solvent molecules from the synthesis were not completely removed.[335]

Férey *et al.* studied the interaction behavior of MIL-100(Fe) and CO in dependence of the activation conditions, (see above coordinated solvent removal strategies).[142] *In situ* IR spectroscopic analysis using CO as a probe allowed both the oxidation states of iron and the amount of OMS to be quantified. At room temperature, CO does not interact strongly with Fe^{3+} sites (weak band at 2190 cm^{-1}). An increase in the activation temperature leads to partial Fe^{3+} reduction to Fe^{2+} and to the appearance of two new bands at 2182 and 2173 cm^{-1} (that are still observed after desorption under vacuum). In the case, where only open Fe^{3+} sites are present the heat of adsorption is −39 kJ mol^{-1}. For the partially reduced sample, where both, open Fe^{2+} and Fe^{3+} sites are present the value of the heat of adsorption increases to about −51 kJ mol^{-1}. IR measurements revealed, that the higher value confirms the slightly stronger interaction of Fe^{2+} cations with CO over that of Fe^{3+} cations. Here, the weak interaction between the Fe^{3+} cations and CO are coincident with the weak band at 2190 cm^{-1}. The appearance of two CO valence bands at 2182 and 2173 cm^{-1}, was assigned to the adsorption on the open Fe^{2+}.[142]

NO adsorption

Open metal sites MOFs were applied for the specific nitric oxide (NO) adsorption and storage in view of the known good ligating properties of nitrosyl towards transition metal atoms. MOF have been investigated to store and to release NO, *e.g.* by exposure to water in connection to its pharmaceutical effect. NO is a biological signaling molecule, and is used *in vitro* and *in vivo* for anti-bacterial, anti-thrombotic and wound healing applications. MOFs are envisioned for the storage, delivery and biological activity of NO for these in healthcare applications. In part, this NO delivery is achieved on exposure of the MOF to moisture.[74,90]

The interaction of the NO with the open Cu^{2+} sites in HKUST-1 and with the Ni^{2+} and Co^{2+} sites in M-MOF-74 was reported by Morris *et al.*[90,336,337] They compared the NO sorption data of the three OMS-MOFs with MIL-53(Al/Cr) MOFs without OMS. Thereby, HKUST-1 (~3 mmol NO per g) and M-MOF-74 (M = Co, Ni; ~7 mmol NO per g) adsorbed high amounts of NO at RT in comparison to MIL-53 (<1 mmol g^{-1}). Moreover, the MOFs HKUST-1 and M-MOF-74 showed also large, and MIL-53 a small hysteresis on desorption of NO (Fig. 50).[90] The large hysteresis indicated the expected ligand binding of NO to OMS. HKUST-1 released only 1 μmol NO per g out of the ~3 mmol NO per g which underscore the NO chemisorption in this MOF. About 2.21 mmol g^{-1} is not desorbed when the NO pressure is reduced to almost zero.[90] This corresponds to ~1 NO per dicopper SBU in HKUST-1.[133,337]

In HKUST-1 Cu^{1+} sites can be formed *via* TA or photoreduction (see Section 2). The reduced open Cu^{1+} sites in HKUST-1 interact more strongly with NO in the presence of water, compared to the interaction of the higher oxidation state (Cu^{2+}) with NO.[338,339]

The nature of this Cu–NO interactions was investigated by XPS and NEXAFS with the latter showing a decrease of the intensity of the Cu^{1+} peak and an increase of the area of the Cu^{2+} peak with the introduction of NO (Fig. 51). This suggest that Cu^{1+} was oxidized by NO to form Cu^{2+}–NO^-. The reformed Cu^{2+} centers are then different (due to the bound NO) than the pristine Cu^{2+} in HKUST-1.[338,339] Zn-MOF-74[340] adsorbed approx. 5 mmol NO per g.[336] Hartmann and his co-workers[341] investigated the spectroscopic properties of NO adsorbed in M-MOF-74 (M = Co^{2+}, Ni^{2+}), by using low-temperature electron paramagnetic resonance (EPR) and IR spectroscopy. IR spectra showed the stretching frequency of NO (1878 cm^{-1} for free NO) for Ni-NO at 1838 cm^{-1} and for Co–NO adducts at 1797 cm^{-1}. These two bands were retained upon desorption at RT due to the good ligating action of NO with Co and Ni, again as expected from the good ligating action of NO towards transition metals.[341]

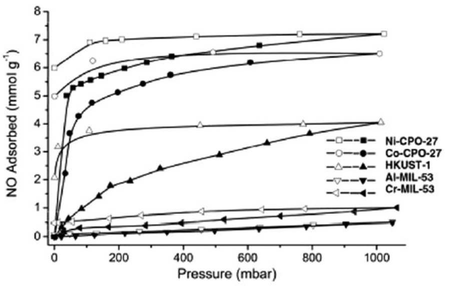

Fig. 50 The NO sorption isotherms of HKUST-1, M-MOF-74 (M = Ni, Co) (denoted in the figure as Ni/Co-CPO-27) and M-MIL-53 (M = Al; Cr) at RT. Reproduced from ref. 90 with permission of Elsevier Inc., copyright 2009.

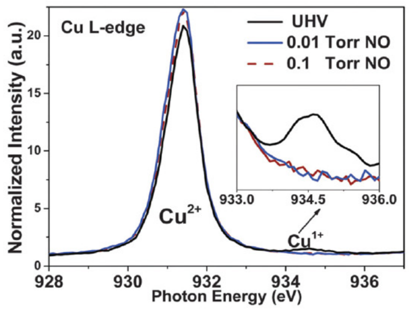

Fig. 51 Cu L-edge NEXAFS image in UHV and as a function of NO pressure in HKUST-1. Reproduced from ref. 338 with permission from The Royal Society of Chemistry, copyright 2014.

C_2H_2 sorption

Safe and efficient storage and separation of acetylene (C_2H_2) is a major challenge. Since highly reactive acetylenes explode at room temperature above a pressure of 2 atm, the industrial focus is on the development of low-pressure acetylene storage and separation methods.[342] MOFs provide an alternative solution for storing and depositing C_2H_2 at low pressures.[343] Especially MOFs with OMS could make an important contribution to C_2H_2 storage technology.[261,262,344–351]

OMS–MOFs show high values for the isosteric heats of adsorption for C_2H_2, from approx. −30.4 to −39.0 kJ mol^{-1} for HKUST-1, −41.0 kJ mol^{-1} for Mg-MOF-74, −45.0 kJ mol^{-1} for Co-MOF-74 to −45.0 to −46.5 kJ mol^{-1} for Fe-MOF-74 with the highest Q^0_{st} value.[209,261,262,351] Comparatively, the C_2H_2 adsorption enthalpies for MOFs without OMS such as MIL-53, MOF-5 and ZIF-8 are in the range of approx. −13 to −20 kJ mol^{-1}.[262]

Compared to non-OMS MOFs, Chen *et al.* attributed the Q^0_{st} value for HKUST-1 to the interaction of the Cu^{2+}–OMS with C_2H_2. The authors established the preferred interaction site between deuterated acetylene molecules and Cu^{2+} by neutron powder diffraction studies. Rietveld refinement of the neutron diffraction data revealed, that at a 0.62 C_2D_2 per Cu loading acetylene is adsorbed entirely at an open Cu^{2+} site. A linear orientation of the C_2H_2 molecule parallel to the O–Cu–O axis was found, with a Cu–C bonding distance of 2.62 Å. Adsorption at the entrance window of a small cage (cage window site), was found at an increased loading of 1.5 C_2D_2 per Cu. The authors concluded that these primary and secondary adsorption sites together cause the relatively high acetylene uptake of 201 cm^3 g^{-1} C_2H_2 for HKUST-1 at RT and 1 atm.[262]

CH_4 adsorption

CH_4 has technical relevance as the main component of natural gas. Increasing the storage capacity in a given volume or at a given pressure by adsorption in a (cheap and stable) porous material would be highly attractive. Referring to this, MOFs have been extensively studied and have been proven to be promising materials for methane storage.[352–357] A promising approach to increase the methane storage capacity was seen in

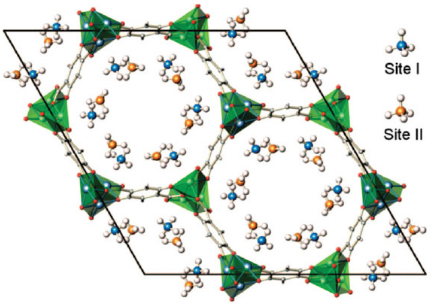

Fig. 52 Projection of the unit cell of Mg-MOF-74 with CH_4 adsorbed on site I and site II, as determined from neutron diffraction. Note that each metal ion is in contact to one methane molecule. Reproduced from ref. 294 with permission from the American Chemical Society, copyright 2009.

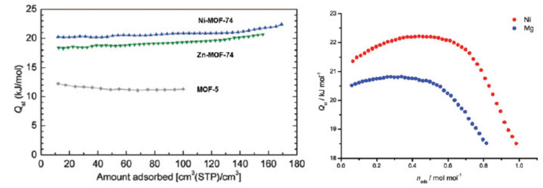

Fig. 53 Left: The experimental Q_{st} of Ni-MOF-74 and Zn-MOF-74, delivered from CH_4 adsorption isotherms at 270, 280, and 298 K. The Q_{st} of Mg-MOF-74, Mn-MOF-74, and Co-MOF-74 fall between the two curves and, thus, are not shown for clarity. The Q_{st} of MOF-5 are plotted for comparison. Reproduced from ref. 294 with permission from the American Chemical Society, copyright 2009. Right: Isosteric heat of adsorption of CH_4 in Ni-MOF-74 (red) and Mg-MOF-74 (blue) as a function of loading, calculated from the isotherms at 179 and 283 K. Reproduced from ref. 321 with permission from The Royal Society of Chemistry, copyright 2009.

the design of MOFs with suitable pore sizes and a high density of open metal sites, which can more strongly interact with CH_4 than the organic pore walls.[358–360]

In previous studies authors claim an influence of OMS in connection with increased adsorption capacity of CH_4.[361] Within the M-MOF-74 series, it was found that Ni-MOF-74 exhibits the highest Q^0_{st} at low CH_4 loading and adsorbs the largest amount of CH_4. According to neutron diffraction experiments, the OMS were identified as primary CH_4 adsorption sites (Fig. 52).[294] Physisorption of CH_4 on the OMS in Mg-MOF-74, was confirmed using neutron diffraction experiments with the experimental Mg···C distance of 3.4 Å. This distance is only slightly smaller than the experimental C···C distance of 3.45 Å for CH_4 adsorbed on a graphite surface. In Mg-MOF-74 the neighboring methane molecules on sites I and II have a C···C distance of ~3.73 Å, only slightly smaller than that in solid methane, suggesting that the adsorbed CH_4 molecules on site II has similar weak interactions with both the framework (mainly the C and O atoms on the organic linker) and the CH_4 molecules on site I (Fig. 52).[294]

However, also in this work, the heats of adsorption for M-MOF-74 (Mg^{2+}, Mn^{2+}, Co^{2+}, Ni^{2+}, Zn^{2+}), delivered from CH_4 adsorption isotherms (at 270, 280, and 298 K), are in the range of approx. -18.3 kJ mol^{-1} to -20.2 kJ mol^{-1}, with little variation with the metal and no variation with CH_4 loading (Fig. 53, left).[294] It must be noted that the absence of higher Q^0_{st} values at low loading speaks against an effect or significant interaction with OMS.

At the same time, the authors added, that in the case of methane, the M···C distance is largely constrained by the CH_4 geometry (a steric effect) and thus varies very little among different metals. This makes the CH_4 binding strength nearly independent of the open metal species. Therefore, we conclude that different from other adsorbates with dipole or quadrupole moment, CH_4 interacts only very weakly with OMS and not much stronger than with the organic pore walls.

Different to the finding of Yildirim *et al.*, where the methane heat of adsorption was almost constant for the whole loading range, Blom *et al.* highlighted a decrease from -20 to -22 kJ mol^{-1} to approx. -18.5 kJ mol^{-1} upon full occupancy for both Ni-MOF-74 and Mg-MOF-74 (Fig. 53, right). The heat of adsorption was calculated from the isotherms at 179 K and 283 K.[321]

Zhou *et al.* predicted for the paddle-wheel MOFs, HKUST-1, PCN-11 and PCN-14, that direct binding of a methane molecule to any Cu^{2+} site should be possible at room temperature and 35 bar, but this would then represent only a fraction of the total storage capacity in these MOFs.[358] The adsorption enthalpy for UTSA-20 from CH_4 adsorption isotherms at 200 K, 240 K, 270 K, and 300 K, was calculated to be -17.7 kJ mol^{-1} at zero coverage.[360] We note that it was not elucidated further if OMS had an influence on the heat of adsorption and if the heat of adsorption decreased after OMS coverage. The experimental determined heats of adsorption of $-17.1(5)$ kJ mol^{-1} for HKUST-1 and $-17.5(5)$ kJ mol^{-1} for [$Cr_3(btc)_2$], from CH_4 adsorption isotherms at room temperature and 35 bar are in a similar range.[264] In this experimental work, Brown *et al.* found for [$M_3(btc)_2$] (M = Cu^{2+}, Cr^{2+}), that at CD_4 loadings of 0.4, 0.7, the primary adsorption sites are around and within the small octahedral cage of the network and these adsorptions sites are favored over the open Cu^{2+} and Cr^{2+} sites, as assessed by situ neutron powder diffraction measurements. Additional nuclear density in the octahedral cages and at the OMS was discovered, both for HKUST-1 and for [$Cr_3(btc)_2$] at an increased loading (1.5 CD_4 per metal atom).[264]

SO_2 adsorption

Sulfur dioxide (SO_2) is an acidic and toxic gas in the atmosphere, which originates from both natural and anthropogenic source. The burning of fossil fuels and industrial processes contribute to the anthropogenic emissions. Although flue gas desulfurization (FGD) is in large parts (85–95%) carried out with established lime-stone absorption,[362,363] up to 150–450 ppm of residual SO_2 are emitted to the atmosphere, contributing a large part to the 80 Mt of worldwide anthropogenic SO_2 emissions from energy related sources in 2015.[364] New materials and processes to enhance FGD are desirable.[365–367] Open metal sites can act as sites for SO_2 adsorption.[368,369] In 2008, Yaghi *et al.*[79] reported on the dynamic adsorption capacity of *e.g.* HKUST-1 and Zn-MOF-74, which are potential OMS-MOFs.

The adsorption of SO_2 to open Cu^{2+} sites was reported for the paddle-wheel MOF MFM-170.[122] *In situ* synchrotron

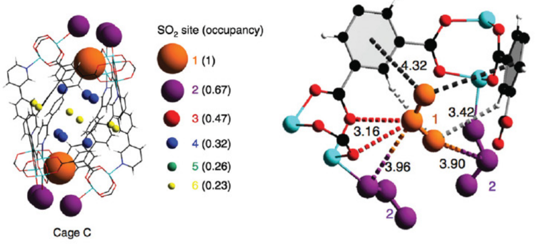

Fig. 54 Positions of SO_2 molecules in MFM-170 from *in situ* single-crystal X-ray diffraction. Left: Packing of SO_2 within cage C. Right: Intermolecular interactions between adsorbed SO_2 molecules and MFM-170 framework atoms. Single-colored dashed lines represent distances between adsorbed SO_2 molecules and framework atoms: red (O), blue (N), light grey (H), black (phenyl ring centroid). Dual-colored dashed lines represent intermolecular interactions between crystallographically distinct SO_2 molecules. Reproduced from ref. 122 with permission of Springer Nature, copyright 2019.

single-crystal X-ray diffraction experiments show the SO_2 coordination to OMS within a MOF for the first time. The preferred SO_2 adsorption site was found on a three-fold rotational axis in the triangular window of metal–organic cuboctahedra. The open Cu^{2+} sites represent the secondary adsorption sites, where the SO_2 molecule binds to the open Cu^{2+} site in an end-on mode [$O(SO_2)–Cu = 2.28(10)$ Å] with an occupancy of 0.67 (Fig. 54).

The authors showed *via* controlled desorption of SO_2 from MFM-170 that the open Cu^{2+} site is the most thermodynamically favored site. The diffraction data was collected under a dynamic vacuum at 298 K and desorption of SO_2 left the last adsorbate as the Cu^{2+}-bound SO_2 with an occupancy of 0.09. This suggests that the Cu^{2+} site is the thermodynamically strongest binding site, but (due to the Jahn–Teller effect) is still weak so that it is almost entirely desorbed on reduction of pressure.[122]

Separation

The separation of CO_2 from coal-gas exhaust gases and CH_4 from natural gas feeds is of great industrial importance. The selective adsorption or permeation of CO_2 is investigated in the context of CO_2 ("carbon") capture and sequestration,[315,370–373] or the CO_2 removal from natural gas ("natural gas sweetening", natural gas upgrading by removal of CO_2).[374–376] MOFs with OMS provide a distinct affinity for H_2, CO_2, CO, NO, and C_2H_2 due to specific OMS–adsorbate interactions. This was also evident from some of the earlier discussed theoretical studies. The presence of OMS in MOFs is a promising approach to enhance the CO_2 separation from gas mixtures with N_2 and CH_4 because of the high CO_2 adsorption energy to OMS (see above). The (calculated) adsorption enthalpy for CH_4 is about half the value for CO_2 and (see Tables S1 and S3 in ESI†). This explains the high selectivity of CO_2 over CH_4. OMS-MOFs can be used as solid adsorbents for selectively removing CO_2 (due to its large quadrupole moment and great polarizability) from dry gas mixtures with N_2 or CH_4.[71,178,321,332,333,377]

Single-crystal X-ray diffraction analysis and breakthrough experiments have been performed to investigate the role of OMS on the CO_2/CO or CO_2/CH_4 gas separation process.[178,378]

It has been shown that especially Mg-MOF-74 possesses high selectivity for CO_2 over CO and CH_4, since the main-group metal Mg^{2+} has no strong preference for CO (see above).[71,178] In breakthrough experiments with Mg-MOF-74 and a CO_2/CO gas mixture a longer breakthrough time for CO_2 than for CO was found, resulting in a high separation ability of CO_2 over CO.[178]

Furthermore, Mg-MOF-74 exhibits a high selectivity of CO_2 over CH_4.[71] Yaghi *et al.* showed that when Mg-MOF-74 is exposed to a gas mixture of CO_2/CH_4 in a ratio of 1 : 5, it only adsorbs CO_2. Breakthrough data revealed an CO_2 uptake of 8.9 wt% corresponding to 0.44 molecules of CO_2 per Mg^{2+} site before breakthrough. In comparison, for Zn-MOF-74, a CO_2 uptake of only 0.35 wt% was obtained under the same conditions.[71]

Schröder *et al.* have recently reported the coordination of SO_2 to open Cu^{2+} sites in MFM-170. MFM-170 provides high selectivity for SO_2.[122] The authors calculated the selectivity for equimolar mixtures of SO_2/CO_2, SO_2/N_2, SO_2/CO and SO_2/CH_4 from single-component isotherms at 298 K and 1 bar. Based on ideal adsorbed solution theory (IAST), high selectivity was proposed for SO_2/N_2 (944), followed by SO_2/CH_4 (260), SO_2/CO (203) and SO_2/CO_2 (35).[122]

A high adsorption capacity of OMS-MOFs was predicted for both CO_2 and C_2H_2, hence resulting in low C_2H_2/CO_2 selectivity (see the theoretical sections above).[209,234,351] Since the adsorption enthalpy of C_2H_2 is close to the one of CO_2 and the (calculated) adsorption enthalpy for CH_4 is about half (see Tables S1 and S3 in ESI†) this leads to an also high selectivity of C_2H_2 over CH_4.

Calero *et al.* noted, that among the OMS-MOFs Fe-MOF-74 shows the largest adsorption selectivity values for both C_2H_2/CH_4 and C_2H_2/CO_2 gas mixtures at 298 K and low pressure.[351]

Catalysis and photocatalysis

The utilization of heterogeneous MOF catalysts can offer a number of advantages over homogeneous metal catalysts, including easy separation, efficient recycling, minimization of metal traces in the product, and improved handling and process control. MOF catalysts also aim to exploit porosity and chemical tunability for reaction selectivity.[32,39] There are several strategies to implement catalytic activity in the MOFs structure. Catalytic sites can be incorporated into the bridging ligands or postsynthetically grafted onto the linker or the metal SBU of the MOF. Often MOF catalysts try to use their OMS as catalytically active centers. After formation, the OMS will act as a Lewis acid, and it will be available to accept electron density from any donor molecule that can be present.[379]

We note that there is a myriad of literature on MOF catalysis claiming the influence of OMS without proof. We did not include and will not comment this work here but have limited the noted work to cases with proven OMS effects. Such examples describing the use of MOF catalysts containing OMS have been published, with uses in the cyanosilylation of carbonyl compounds[380] or of benzaldehyde or acetone,[125] the Mukaiyama aldol condensation,[381] the organophosphorous ester hydrolysis,[382] the cycloaddition with propylene epoxide and other small substrates,[383] the isomerization of α-pinene oxide[384] or of glucose,[385] the conversion of citronellal into isopulegol,[384] as well as for the oxidation of alcohols[39,91] or various organic substrates[99] or for selective hydrogenations[38,153] and in photocatalysis.[386]

In 1994, Fujita *et al.*[387] demonstrated for the first time the utility of a 2D MOF [Cd(4,4′-bpy)$_2$(NO$_3$)$_2$], (bpy = bipyridine) as a heterogeneous Lewis acid catalyst, which promoted the cyanosilylation of aldehydes with shape selectivity. Kaskel *et al.*[125] showed that the open Cu^{2+} sites in HKUST-1 could catalyze the cyanosilylation of benzaldehyde or acetone. De Vos *et al.*[384] reported that activated HKUST-1 is a highly selective Lewis acid catalyst for the isomerization of α-pinene oxide to campholenic aldehyde, the cyclization of citronellal to isopulegol, and the rearrangement of α-bromoacetals due to its free Cu^{2+} coordination sites. Long *et al.*[381] described Mn-btt for the cyanosilylation of aromatic aldehydes with good conversion for small substrates and also substrate-size selectivity. Mn-btt can also be used to catalyze the Mukaiyama aldol reaction. The Lewis acid Cu^{2+} sites in the paddle-wheel MOF [Cu$_2$[(C$_{20}$H$_{12}$N$_2$O$_2$)(COO)$_4$]], with accessible acylamide groups[383] is a heterogeneous catalyst for carbon fixation *via* catalytic conversion of CO$_2$.

The OMS MOF MIL-101(Cr) was reported by Kaskel *et al.*[380] for the cyanosilylation of carbonyl compounds. The authors demonstrated that MIL-101(Cr) with open Cr^{3+} sites possess a higher Lewis acidity to yield a more active catalyst for the cyanosilylation reaction, in comparison to HKUST-1. OMS-MIL-101(Cr) showed a high yield of 98.5% at 313 K after 3 h, and the catalytic sites were immune to unwanted reduction by benzaldehyde.

Li *et al.*[39] generated a Pd/MIL-101(Cr) catalyst for the liquid-phase aerobic oxidation of various alcohols and analyzed the effect of OMS of the MOF-support on the reactivity of Pd nanoparticles for the alcohol oxidation. It was observed that after ethylenediamine grafting on the open Cr^{3+} sites the catalytic Pd activity was suppressed. The oxidation of cinnamyl alcohol indicated results that range from <3/98 to 99/99 (conv./sel%) in the order MIL-101(Cr) < 0.35% Pd/En-MIL-101(Cr) < 0.35% Pd/MIL-101(Cr). Accordingly, the use of 0.35% Pd/MIL-101 gave a complete conversion of cinnamyl alcohol to cinnamyl aldehyde within 0.5 h at 80 °C, while the amine grafted sample 0.35% Pd/En-MIL-101 showed only 45% yield of cinnamyl aldehyde within 3 h. After addition of a small amount of base additives (*e.g.* NaOH) to the system the activity increased (95% conversion of alcohol within 3 h). It can be deduced that the open Cr^{3+} sites play an imported role in the alcohol oxidation related to a promoting effect observed in MIL-101-supported metal nanoparticles for the conversions of aromatics.[388,389]

The MOFs TMU-10 and 12 with open Co^{2+} sites were studied by Morsali *et al.*[390] for the oxidative desulfurization reaction of a model oil, which was prepared by dissolving dibenzothiophene (DBT) in *n*-hexane. The Lewis acidic Co^{2+} sites in these structures successfully completed the quantitative desulfurization process after 6 h.

Kitagawa *et al.*[385] investigated the potential of MIL-101(Cr) derivatives for glucose isomerisation. In comparison to Amberlyst-15, a strongly acidic ion-exchange resin, MIL-100 and MIL-101 showed higher catalytic activity. Here, the catalytic activity can be modulated through the Lewis-acidity of the OMS by modification of the organic ligands with functional groups, like –NH$_2$, –(CH$_3$)$_2$, –NO$_2$ and –SO$_3$H. Electron donating –NH$_2$ and –(CH$_3$)$_2$ groups on the aromatic ring of the terephthalate, decrease the Lewis acidity of open Cr^{3+} sites and increase the electron density. Whereas electron-accepting –NO$_2$ and –SO$_3$H groups increase the Lewis acidity of OMS and decrease the electron density. The authors described also that MIL-100 and MIL-101 have though the same Lewis acidity, but different production yields of fructose, due to the differences in window size of the mesopores. MIL-101(Cr)–SO$_3$H provided a high conversion of glucose and selectively produced fructose.

Hatton *et al.*[382] investigated the modification of MIL-101(Cr) with dialkylaminopyridines (DAAP) for the hydrolytic degradation of organophosphorus esters such as diethyl-4-nitrophenyl phosphate (paraoxon). Different supernucleophilic DAAP ligands were coordinatively attaching onto part of the OMS of MIL-101. The authors showed, that the catalytic activity of the DAAP-modified MIL-101(Cr) was higher than activated MIL-101(Cr). Furthermore, the synergistic activation of the substrate by the Lewis acid Cr^{3+} sites and the electron-rich nucleophiles (DAAP) gave a Lewis acid–Lewis base activation mechanism.

For the selective semihydrogenation Luo *et al.* and co-workers[38] reported on Pd@Zn-MOF-74, which showed a high styrene selectivity of 92% at full conversion with a turnover frequency of 98.1 h^{-1} – compared to the selectivity of the Lindlar catalyst with 56%. The origin of ultrahigh selectivity, as proposed by DFT calculation, is due to a coordination of the C$\equiv$C bond of phenylacetylene to the open Zn(II) site.[38]

MIL-101(Fe) was studied for the photocatalytic CO$_2$ reaction by Li *et al.*[386] The authors demonstrated with *in situ* FT-IR studies that the open Fe sites are the photocatalytically active sites for this reaction. The adsorption of CO$_2$ directly onto the metal center activates the substrate for the photocatalytic CO$_2$ reduction reaction.

Morsali *et al.*[391] have reported the mixed-metal MOFs with open Cd sites for phenol degradation from aqueous solutions under UV and/or visible light irradiation. The authors compared the four TMU MOFs, [Zn(oba)(4-bpdh)$_{0.5}$], [Cd$_{0.15}$Zn$_{0.85}$(oba)(4-bpdh)$_{0.5}$], [Cd$_{0.3}$Zn$_{0.7}$(oba)(4-bpdh)$_{0.5}$] and [Cd(oba)(4-bpdh)]. The mixed metal-based MOFs with 15 and 30% Cd were photocatalytically more active than the just Cd or Zn containing MOF.

Hong *et al.*[111] explained that the activation temperature had an important effect on the catalytic activity for CO oxidation because more open metal sites available in HKUST-1 gave a higher CO activity, the catalytic activity then increased in the order HKUST-1-553 K < 443 K 473 K < 503 K < 523 K.

Sensing

Chemical materials for highly selective and sensitive detection of analytes in the gas and liquid phase are competitively investigated for applications in industrial processes, chemical threat detection, medical diagnostics, food quality control, occupational safety and environmental monitoring. Thereby Lewis acidic or basic sites in the ligands or OMS play an important role through their interactions with guest molecules for the selective recognition. Often luminescent MOFs (LMOFs) are utilized as sensor through the quenching or enhancement of their luminescence by the analyte. Mesoporous LMOFs allow also the sensing of larger molecules such as biologically active species.[392]

A few examples of porous MOFs with open metal sites have been investigated for their sensing properties. Morsali *et al.*[393] showed the potential of open Zn^{2+} sites in activated TMU-41, $[Zn_2(bdc)_{1.5}(L)]$ (L = pyridine 4-carboxylate) for the selective and recyclable luminescent sensing of MnO_4^-, $Cr_2O_7^{2-}$ and CrO_4^{2-}. Lobkovsky *et al.*[180] showed that the luminescent MOF $[Eu(btc)(H_2O)]$ after removal of the solvent molecules contained open Eu^{3+} sites, which could act as a highly selective sensor for small molecules, such as dimethyl formamide, acetone, and ethanol. For more practical use weakly coordinated 1-propanol molecules on the Eu^{3+} sites were replaced by DMF and acetone to gradually increase and decrease the fluorescence intensity, respectively.

The lanthanide MOF $[Eu_2(\mu_2\text{-pzdc})(\mu_4\text{-pzdc})(\mu_2\text{-ox})(H_2O)_4]$ (H_2pzdc = 2,5-pyrazinedicarboxylic acid, H_2ox = oxalic acid) was reported by Guillou *et al.*[394] for the recognition and sensing of acetone. After removal of the solvent molecules the MOF exhibited a high quenching effect with acetone.

Chen *et al.*[395] reported on the near infrared (NIR) luminescent Yb-MOF $[Yb(bpt)(H_2O)(DMF)_{1.5}(H_2O)_{1.25}]$ (bpt = biphenyl-3,4,5-tricarboxylate) for the sensing of small molecules. Activated [Yb(bpt)] showed typical NIR emission from the $^2F_{5/2} \rightarrow {}^2F_{7/2}$ transition of Yb^{3+} at 980 nm, when excited at 326 nm. In comparison to [Eu(btc)] the luminescence intensity of [Yb(bpt)] indicated even higher enhancing and quenching effects with DMF and acetone.

Dincă *et al.*[41] described the interaction of NH_3 with $[Zn_2(tcpe)]$ (tcpe = tetrakis(4-carboxyphenyl)ethylene) and $[Mg(H_2dhbdc)]$ (H_2dhbdc^{2-} = 2,5-dihyroxybenzene-1,4-dicarboxylate), which caused fluorescence shifts and turn-on luminescence responses over potential interferents such as water, methanol, amines, and other gases. The exposure of activated $[Zn_2(tcpe)]$ to ammonia, triethylamine, ethylenediamine, *N,N*-diethylformamide and water vapors shifted its emission maximum by up to 23 nm at room temperature. At 100 °C ammonia exposure led to a shift of the emission maximum from 487 to 511 nm, thus revealing a good selectivity for NH_3 detection. Based on *in situ* IR studies the authors verified the binding of NH_3 to the open Mg^{2+} sites in $[Mg(H_2dhbdc)]$.

5. Conclusions

The as-synthesized MOF will have initially all metal ions in its SBU in their fully coordinatively saturated state. This is the most stable metal coordination environment according to the usual metal coordination number, which is typically six (octahedral) or four (tetrahedral) for most 3d transition metal ions. Open metal sites in MOFs (OMS-MOFs) can be obtained by the removal of an initial labile terminal ligand, which may typically be a solvent molecule, from its coordinating metal atom. The procedure for this ligand removal with OMS generation is usually solvent exchange and removal, which may be generally termed "activation" and can be further differentiated into thermal, chemical or photothermal activation. Seldom noted, but definitely more important, is the at least partial reduction of the metal at the OMS upon its formation, as was already observed for HKUST-1 with Cu^{2+} to Cu^{1+} and MIL-100 with Fe^{3+} to Fe^{2+}; but such a reduction may also occur in many other OMS-MOFs.

OMS are often invoked but it is important to prove the presence of OMS by suitable analytical methods, such as NMR, TGA, FT-IR in connection with gas sorption studies. It is just becoming apparent that quantitative OMS generation cannot be taken for granted by "standard" activation protocols. Few studies have so far addressed the issue of OMS quantification and more such studies are needed to quantify the formed OMS.

The current characterization techniques for the detection and quantification of Lewis-acid sites in MOFs are gas or vapor adsorption, probe-molecule infrared spectroscopy and temperature-programmed desorption (TPD). The techniques are versatile but their application in OMS research remains limited. Most of the OMS work simply did not address the quantities of OMS formed. Also, further improvement and additional techniques are warranted. The NH_3-TPD technique, for example, has the limitation in quantifying OMS in the presence of Brønsted acid sites.

In MOF structures any change to the metal ions in the metal SBU must ensure the integrity of the network. Importantly, the MOF structure must not collapse, and their crystallinity and porosity should be preserved, that is, a labile terminal ligand should be removed without damage to the framework. Retention of the framework integrity is usually verified by PXRD.

It is the strength of theory that OMS can be easily studied regarding their electronic effects on the interactions with substrate molecules. The theory-based knowledge, how OMS interact with the guest molecules is needed along the experimental work for understanding the properties of OMS-MOFs. We note, however, that without additional parametrization, standard force fields are barely able to deliver accurate thermodynamic data. More accurate values for binding enthalpies are obtained through quantum mechanical calculation of potential energy surfaces, preferably using periodic boundaries. At the DFT-level, the inclusion of van der Waals interactions is crucial. The most accurate approach involves a combination of dispersion corrected DFT and high-level *ab initio* methods, as *e.g.* DFT-D and coupled cluster (CC) methods including complete basis set extrapolation. Theoretical studies support that OMS interactions with gaseous adsorbates are dispersion-driven for CH_4, involve electrostatic and dispersion for H_2, N_2, and CO_2, and contain a partially covalent (dative) bonding character with CO and C_2H_2.

The presence of OMS in the MOF causes enhanced interactions between the metal site and guest molecules. OMS are the primary adsorption sites for H_2, CO_2, CO, NO and C_2H_2 giving high heats of adsorption (Q_{st}). OMS are, however, not the primary adsorption site for CH_4 and possibly SO_2. The formation of an OMS is also the prerequisite for the "metal-binding" of weakly coordinating adsorbates such as CO_2 and H_2. Gas sorption studies on OMS-MOFs in connection with high-resolution/powder neutron diffraction studies, powder synchrotron X-ray diffraction analysis and near sites edge X-ray adsorption fine structure (NEXAFS) spectroscopy yielded structural information and insight into the role of the OMS on the MOF–adsorbate interactions.

The defined synthesis of OMS in MOFs is the basis for targeted functionalization through grafting, the coordination of weakly binding species and increased (supramolecular) interactions with guest molecules. The enhanced interactions can be highly effective on the MOF performance in the potential applications gas sorption and separation, catalysis and sensing. For example, MOFs with OMS are among the most promising solid adsorbents for selectively removing CO_2 from dry gas mixtures and have been described as highly active Lewis-acid catalysts.

Abbreviations

Ligands arranged alphabetically without protic H atoms

H_4abtc	3,3′,5,5′-Azobenzene-tetracarboxylic acid
H_4adip	5-Aminodiacetic isophthalic
H_4aobtc	Azoxybenzene-2,2′,3,3′-tetracarboxylic acid
H_2bbta	1*H*,5*H*-Benzene(1,2-*d*:4,5-*d*′)bistriazole
H_2bdc	Benzene-1,4-dicarboxylic acid/terephthalic acid
H_2bdc-NH_2	2-Aminoterephthalic acid
H_6bhb	3,3′,3″,5,5′,5″-Benzene-1,3,5-triyl-hexabenzoic acid
H_6btat	5,5′,5″-(Benzene-1,3,5-triyltris(anthracene-10,9-diyl))triisophthalic acid
4-bpdh	2,5-Bis(4-pyridyl)-3,4-diaza-2,4-hexadiene
H_3bpt	Biphenyl-3,4′,5-tricarboxylic acid
H_4bptc	1,1′-biphenyl-2,2′,6,6′-tetracarboxylic acid
H_3btc	Benzene-1,3,5-tricarboxylic acid/Trimesic acid
H_2btdd	Bis-(1*H*-1,2,3-triazolo-[4,5-*b*],[4′,5′-*i*])dibenzo-[1,4]-dioxine
H_3btt	5,5′,5″-(1,3,5-Phenylene)tris(1*H*-tetrazole)
H_3btt_{ri}	1,3,5-Tris(1*H*-1,2,3-triazol-5-yl)benzene
H_2dmcapz	3,5-Dimethyl-4-carboxypyrazole
H_4dobpdc	4,4′-Dioxidobiphenyl-3,3′-dicarboxylate
H_4(*p*-dobdc)	*para*-2,5-Dihydroxyterephthalic acid
H_4mbdpb	5-Methoxyl-1,3-bis(3,5-dicarboxylphenyl)-benzene
H_4mdip	5,5′-Methylenediisophthalate
H_4(*m*-dobdc)	*meta*-4,6-Dioxido-1,3-benzene-dicarboxylate
H_5n	2,5-Di(3,5-dicarboxylphenyl)-nicotinic acid
Hna	Nicotinic acid
H_2oba	4,4′-Oxybis(benzoic acid)
H_4olz	Olsalazine acid
H_2ox	Oxalic acid
H_2pyip	5-(Pyridin-3-yl)isophthalic acid
H_2pzdc	2,5-Pyrazinedicarboxylic acid
H_4sbtc	5-Sulfonyl-1,2,4-benzenetricarboxylic acid
H_2sip	5-Sulfoisophthalate
H_2sp_5-BF_4	1,3-Bis(4-carboxyphenyl)-4,5-dihydro-1*H*-imidazol-3-ium tetrafluoroborate
H_3tatb	4,4′,4″-*s*-Triazine-2,4,6-triyltribenzoate
H_4tcpe	Tetrakis(4-carboxyphenyl)ethylene
H_8tdcppy	1,3,6,8-Tetra(3,5-dicarboxyphenyl)pyrene
H_6tdpat	2,4,6-Tris(3,5-dicarboxylphenylamino)-1,3,5-triazine
H_3tzi	5-Tetrazolylisophthalic acid
H_3tzpa	5-(4-(Tetrazol-5-yl)phenyl)isophthalic acid
approx.	Approximately
BET	Brunauer–Emmett–Teller
BSS	Belof Stern Space
CA	Chemical activation
CAS	Confirmation of Acceptance for Studies
CC	Coupled cluster
CCDC	Cambridge crystallographic data center
CCSD	Coupled cluster singles and doubles
CCSD(T)	Coupled cluster singles, doubles with perturbative triples
CPO	Coordination polymer of Oslo
CSD	Cambridge structural database
CUS	Coordinatively unsaturated site(s)
D_2O/NaOD	Deuterium oxide/sodium deuteroxide solution
DCM	Dichloromethane
DFT	Density functional theory
DMF	*N*,*N*-Dimethylformamide
DSC	Differential scanning calorimetry
EDA	Energy decomposition analysis
EDX	Energy dispersive X-ray spectroscopy
EtOH	Ethanol
eq.	Equivalent
EXAFS	Extended X-ray absorption fine structure
FT-IR	Fourier transform infrared spectroscopy
GCMC	Grand Canonical Monte Carlo
HKUST	Hong Kong University of Science and Technology
IR	Infrared spectroscopy
MeCN	Acetonitrile
MeOH	Methanol
MIL	Materiaux de l'Institute Lavoisier
MOF(s)	Metal–organic framework(s)
NEXAFS	Near Edge X-ray Absorption Fine Structure
NMR	Nuclear magnetic resonance
NJFU	Nanjing Forestry University
NJU	Nanjing University
NONOates	*N*-Diazenium dialates
NOTT	University of Nottingham
OCS	Open coordination site(s)
OMS	Open metal site(s)
PA	Photothermal activation
PES	Potential energy surface
PBE	Perdew–Burke–Ernzernhof
PCN	Porous coordination network
PHAST(*)	Potentials with high accuracy, speed, and transferability; the * stands for the inclusion of the explicit polarization
PDOS	Partial density of states
P-XRD	Powder X-ray diffraction
Py-SI	Pyridyl-salicylimine

QM/MM	Combined quantum mechanical and molecular mechanical method
rht	Rhombicuboctahedral and trigonal, topology term
SBET	Surface area
SBU	Secondary building unit
$scCO_2$	Supercritical carbon dioxide
SCXRD	Single crystal X-ray diffraction
SE	Solvent exchange
SEM	Scanning electron microscope
SEM-EDX	Scanning Electron Microscopy/Energy Dispersive X-Ray Spectroscopy
soc	Square octahedral, topology term
TA	Thermal activation
TGA	Thermogravimetric analysis
TraPPe	Transferable Potentials for Phase Equilibria force Field
UiO	University in Oslo
UFF	Universal Force Field
UTSA	University of Texas at San Antonio
UV-Vis spectroscopy	Ultraviolet-visible spectroscopy
vdW	van der Waals
XPS	X-ray photoelectron spectroscopy
ZJU	Zhejiang University

Conflicts of interest

The authors declare no competing financial interest.

Acknowledgements

The authors gratefully acknowledge the financial support of the German Research Foundation (Deutsche Forschungsgemeinschaft, DFG) under grant no. Ja466/40-1 and project no. 396890929/GRK 2482.

References

1 S. R. Batten, N. R. Champness, X.-M. Chen, J. Garcia-Martinez, S. Kitagawa, L. Öhrström, M. O'Keeffe, M. P. Suh and J. Reedijk, *Pure Appl. Chem.*, 2013, **85**, 1715–1724.

2 S. R. Batten, N. R. Champness, X.-M. Chen, J. Garcia-Martinez, S. Kitagawa, L. Öhrström, M. O'Keeffe, M. P. Suh and J. Reedijk, *CrystEngComm*, 2012, **14**, 3001–3004.

3 M. E. Davis, *Nature*, 2002, **417**, 813–821.

4 Z. Ma, T. Kyotani, Z. Liu, O. Terasaki and A. Tomita, *Chem. Mater.*, 2001, **13**, 4413–4415.

5 C. Janiak and J. K. Vieth, *New J. Chem.*, 2010, **34**, 2366–2388.

6 V. Safarifard, S. Rodríguez-Hermida, V. Guillerm, I. Imaz, M. Bigdeli, A. Azhdari Tehrani, J. Juanhuix, A. Morsali, M. E. Casco and J. Silvestre-Albero, *Cryst. Growth Des.*, 2016, **16**, 6016–6023.

7 J. Dechnik, J. Gascon, C. J. Doonan, C. Janiak and C. J. Sumby, *Angew. Chem., Int. Ed.*, 2017, **56**, 9292–9310.

8 B. Li, H.-M. Wen, W. Zhou and B. Chen, *J. Phys. Chem. Lett.*, 2014, **5**, 3468–3479.

9 P. Serra-Crespo, E. V. Ramos-Fernandez, J. Gascon and F. Kapteijn, *Chem. Mater.*, 2011, **23**, 2565–2572.

10 J. Y. Lee, O. K. Farha, J. Roberts, K. A. Scheidt, S. T. Nguyen and J. T. Hupp, *Chem. Soc. Rev.*, 2009, **38**, 1450–1459.

11 Y.-B. Huang, J. Liang, X.-S. Wang and R. Cao, *Chem. Soc. Rev.*, 2017, **46**, 126–157.

12 A. Herbst and C. Janiak, *CrystEngComm*, 2017, **19**, 4092–4117.

13 K. Berijani and A. Morsali, *J. Catal.*, 2019, **378**, 28–35.

14 M. Bagheri, M. Y. Masoomi and A. Morsali, *ACS Catal.*, 2017, **7**, 6949–6956.

15 M. Bagheri, M. Y. Masoomi and A. Morsali, *Sens. Actuators, B*, 2017, **243**, 353–360.

16 P. Horcajada, R. Gref, T. Baati, P. K. Allan, G. Maurin, P. Couvreur, G. Férey, R. E. Morris and C. Serre, *Chem. Rev.*, 2012, **112**, 1232–1268.

17 Z.-G. Gu, D.-J. Li, C. Zheng, Y. Kang, C. Wöll and J. Zhang, *Angew. Chem., Int. Ed.*, 2017, **56**, 6853–6858.

18 F. Jeremias, D. Fröhlich, C. Janiak and S. K. Henninger, *New J. Chem.*, 2014, **38**, 1846–1852.

19 M. F. de Lange, K. J. Verouden, T. J. Vlugt, J. Gascon and F. Kapteijn, *Chem. Rev.*, 2015, **115**, 12205–12250.

20 D. Fröhlich, E. Pantatosaki, P. D. Kolokathis, K. Markey, H. Reinsch, M. Baumgartner, M. A. van der Veen, D. E. De Vos, N. Stock and G. K. Papadopoulos, *J. Mater. Chem. A*, 2016, **4**, 11859–11869.

21 H. Kummer, F. Jeremias, A. Warlo, G. Füldner, D. Fröhlich, C. Janiak, R. Gläser and S. K. Henninger, *Ind. Eng. Chem. Res.*, 2017, **56**, 8393–8398.

22 J. E. Huheey, E. A. Keiter and R. L. Keiter, *Inorganische Chemistry: Principles of Structure und Reactivity*, Harper Collines, New York, 4th edn, 1993.

23 C. Elschenbroich, *Organometallic*, Wiley-VCH Verlag GmbH & Co. KGaA, Weinheim, 3rd edn, 2006.

24 C. Janiak, H.-J. Meyer, D. Gudat and R. Alsfasser, *Riedel: Moderne Anorganische Chemie*, Walter de Gruyter GmbH & Co. KG, Berlin/Boston, 4th edn, 2012.

25 L. Beyer and J. A. Cornejo, *Koordinationschemie: Gundlagen – Synthesen – Anwendungen*, Vieweg + Teubner Verlag, Spinger Fachmedien Wiesbaden, 2012.

26 M. Bosch, M. Zhang and H.-C. Zhou, *Adv. Chem.*, 2014, **2014**, 182327.

27 M. C. Das, S. Xiang, Z. Zhang and B. Chen, *Angew. Chem., Int. Ed.*, 2011, **50**, 10510–10520.

28 M. Y. Masoomi, A. Morsali, A. Dhakshinamoorthy and H. Garcia, *Angew. Chem., Int. Ed.*, 2019, **58**, 15188–15205.

29 S.-i. Noro, S. Kitagawa, M. Yamashita and T. Wada, *Chem. Commun.*, 2002, 222–223.

30 Z. Zhang, S. Xiang, K. Hong, M. C. Das, H. D. Arman, M. Garcia, J. U. Mondal, K. M. Thomas and B. Chen, *Inorg. Chem.*, 2012, **51**, 4947–4953.

31 S. S. Y. Chui, S. M. F. Lo, J. P. H. Charmant, A. G. Orpen and I. D. Williams, *Science*, 1999, **283**, 1148–1150.

32 M. Eddaoudi, H. Li and O. Yaghi, *J. Am. Chem. Soc.*, 2000, **122**, 1391–1397.

33 O. M. Yaghi, C. E. Davis, G. Li and H. Li, *J. Am. Chem. Soc.*, 1997, **119**, 2861–2868.

34 M. Eddaoudi, D. B. Moler, H. Li, B. Chen, T. M. Reineke, M. O'Keefe and O. M. Yaghi, *Acc. Chem. Res.*, 2001, **34**, 319–330.

35 N. L. Rosi, J. Kim, M. Eddaoudi, B. Chen, M. O'Keeffe and O. M. Yaghi, *J. Am. Chem. Soc.*, 2005, **127**, 1504–1518.

36 J. W. Yoon, H. Chang, S.-J. Lee, Y. K. Hwang, D.-Y. Hong, S.-K. Lee, J. S. Lee, S. Jang, T.-U. Yoon, K. Kwac, Y. Jung, R. S. Pillai, F. Faucher, A. Vimont, M. Daturi, G. Férey, C. Serre, G. Maurin, Y.-S. Bae and J.-S. Chang, *Nat. Mater.*, 2017, **16**, 526–531.

37 L. Alaerts, M. Maes, M. A. van der Veen, P. A. Jacobs and D. E. De Vos, *Phys. Chem. Chem. Phys.*, 2009, **11**, 2903–2911.

38 H. Q. Wu, L. Huang, J. Q. Li, A. M. Zheng, Y. Tao, L. X. Yang, W. H. Yin and F. Luo, *Inorg. Chem.*, 2018, **57**, 12444–12447.

39 G. Chen, S. Wu, H. Liu, H. Jiang and Y. Li, *Green Chem.*, 2013, **15**, 230–235.

40 A. Verma, K. Tomar and P. K. Bharadwaj, *Inorg. Chem.*, 2017, **56**, 13629–13633.

41 N. B. Shustova, A. F. Cozzolino, S. Reineke, M. Baldo and M. Dincă, *J. Am. Chem. Soc.*, 2013, **135**, 13326–13329.

42 A. R. Kulkarni and D. S. Sholl, *J. Phys. Chem. C*, 2016, **120**, 23044–23054.

43 A. Luna-Triguero, J. M. Vicent-Luna, P. Gómez-Álvarez and S. Calero, *J. Phys. Chem. C*, 2017, **121**, 3126–3132.

44 A. Luna-Triguero, J. M. Vicent-Luna, A. Poursaeidesfahani, T. J. H. Vlugt, R. Sánchez-de-Armas, P. Gómez-Álvarez and S. Calero, *ACS Appl. Mater. Interfaces*, 2018, **10**, 16911–16917.

45 Y.-S. Bae, C. Y. Lee, K. C. Kim, O. K. Farha, P. Nickias, J. T. Hupp, S. B. T. Nguyen and R. Q. Snurr, *Angew. Chem., Int. Ed.*, 2012, **51**, 1857–1860.

46 J. Duan, M. Higuchi, J. Zheng, S.-I. Noro, I.-Y. Chang, K. Hyeon-Deuk, S. Mathew, S. Kusaka, E. Sivaniah, R. Matsuda, S. Sakaki and S. Kitagawa, *J. Am. Chem. Soc.*, 2017, **139**, 11576–11583.

47 Z. Liu, L. Lv, Y. He and Y. Feng, *CrystEngComm*, 2017, **19**, 2795–2801.

48 J.-W. Zhang, M.-C. Hu, S.-N. Li, Y.-C. Jiang, P. Qu and Q.-G. Zhai, *Chem. Commun.*, 2018, **54**, 2012–2015.

49 J.-W. Zhang, M.-C. Hu, S.-N. Li, Y.-C. Jiang and Q.-G. Zhai, *Chem. – Eur. J.*, 2017, **23**, 6693–6700.

50 H. He, D.-Y. Zhang, F. Guo and F. Sun, *Inorg. Chem.*, 2018, **57**, 7314–7320.

51 H. Kim and Y. Jung, *J. Phys. Chem. Lett.*, 2014, **5**, 440–446.

52 S. R. Caskey, A. G. Wong-Foy and A. J. Matzger, *J. Am. Chem. Soc.*, 2008, **130**, 10870–10871.

53 H. Oh, I. Savchenko, A. Mavrandonakis, T. Heine and M. Hirscher, *ACS Nano*, 2014, **8**, 761–770.

54 C.-X. Chen, S.-P. Zheng, Z.-W. Wei, C.-C. Cao, H.-P. Wang, D. Wang, J.-J. Jiang, D. Fenske and C.-Y. Su, *Chem. – Eur. J.*, 2017, **23**, 4060–4064.

55 M. Latroche, S. Suble, C. Serre, C. Mellot-Draznieks, P. L. Llewellyn, J.-H. Lee, J.-S. Chang, S. H. Jhung and G. Ferey, *Angew. Chem., Int. Ed.*, 2006, **45**, 8227–8231.

56 S. Ma and H.-C. Zhou, *J. Am. Chem. Soc.*, 2006, **128**, 11734–11735.

57 S. Ma, D. Yuan, J.-S. Chang and H.-C. Zhou, *Inorg. Chem.*, 2009, **48**, 5398–5402.

58 G.-J. Ren, Z. Chang, J. Xu, Z. Hu, Y.-Q. Liu, Y.-L. Xu and X.-H. Bu, *Chem. Commun.*, 2016, **52**, 2079–2082.

59 P. M. Forster, J. Eckert, B. D. Heiken, J. B. Parise, J. W. Yoon, S. H. Jhung, J.-S. Chang and A. K. Cheetham, *J. Am. Chem. Soc.*, 2006, **128**, 16846–16850.

60 F. Nouar, J. F. Eubank, T. Bousquet, L. Wojtas, M. J. Zaworotko and M. Eddaoudi, *J. Am. Chem. Soc.*, 2008, **130**, 1833–1835.

61 Y. Yan, X. Lin, S. Yang, A. J. Blake, A. Dailly, N. R. Champness, P. Hubberstey and M. Schröder, *Chem. Commun.*, 2009, 1025–1027.

62 Y. Yan, I. Telepeni, S. Yang, X. Lin, W. Kockelmann, A. Dailly, A. J. Blake, W. Lewis, G. S. Walker, D. R. Allan, S. A. Barnett, N. R. Champness and M. Schröder, *J. Am. Chem. Soc.*, 2010, **132**, 4092–4094.

63 X.-S. Wang, S. Ma, K. Rauch, J. M. Simmons, D. Yuan, X. Wang, T. Yildirim, W. C. Cole, J. J. López, A. de Meijere and H.-C. Zhou, *Chem. Mater.*, 2008, **20**, 3145–3152.

64 D. Liu, H. Wu, S. Wang, Z. Xie, J. Li and W. Lin, *Chem. Sci.*, 2012, **3**, 3032–3037.

65 T. Pham, K. A. Forrest, A. Hogan, B. Tudor, K. McLaughlin, J. L. Belof, J. Eckert and B. Space, *Cryst. Growth Des.*, 2015, **15**, 1460–1471.

66 G. Y. Yoo, W. R. Lee, H. Jo, J. Park, J. H. Song, K. S. Lim, D. Moon, H. Jung, J. Lim, S. S. Han, Y. Jung and C. S. Hong, *Chem. – Eur. J.*, 2016, **22**, 7444–7451.

67 W.-Y. Gao, S. Palakurty, L. Wojtas, Y.-S. Chen and S. Ma, *Inorg. Chem. Front.*, 2015, **2**, 369–372.

68 A. Masala, J. G. Vitillo, G. Mondino, C. A. Grande, R. Blom, M. Manzoli, M. Marshall and S. Bordiga, *ACS Appl. Mater. Interfaces*, 2017, **9**, 455–463.

69 J. M. Simmons, H. Wu, W. Zhou and T. Yildirim, *Energy Environ. Sci.*, 2011, **4**, 2177–2185.

70 W. L. Queen, M. R. Hudson, E. D. Bloch, J. A. Mason, M. I. Gonzalez, J. S. Lee, D. Gygi, J. D. Howe, K. Lee, T. A. Darwish, M. James, V. K. Peterson, S. J. Teat, B. Smit, J. B. Neaton, J. R. Long and C. M. Brown, *Chem. Sci.*, 2014, **5**, 4569–4581.

71 D. Britt, H. Furukawa, B. Wang, T. G. Glover and O. M. Yaghi, *Proc. Natl. Acad. Sci. U. S. A.*, 2009, **106**, 20637–20640.

72 P. Verma, R. Maurice and D. G. Truhlar, *J. Phys. Chem. C*, 2015, **119**, 28499–28511.

73 N. Drenchev, M. H. Rosnes, P. D. C. Dietzel, A. Albinati, K. Hadjiivanov and P. A. Georgiev, *J. Phys. Chem. C*, 2018, **122**, 17238–17249.

74 A. H. Khan, K. Peikert, F. Hoffmann, M. Fröba and M. Bertmer, *J. Phys. Chem. C*, 2019, **123**, 4299–4307.

75 J. Yang, B. Du, J. Liu, R. Krishna, F. Zhang, W. Zhou, Y. Wang, J. Li and B. Chen, *Chem. Commun.*, 2018, **54**, 14061–14064.

76 J. Pang, F. Jiang, M. Wu, C. Liu, K. Su, W. Lu, D. Yuan and M. Hong, *Nat. Commun.*, 2015, **6**, 7575.

77 C. Song, J. Jiao, Q. Lin, H. Liu and Y. He, *Dalton Trans.*, 2016, **45**, 4563–4569.

78 S. Xiang, W. Zhou, Z. Zhang, M. A. Green, Y. Liu and B. Chen, *Angew. Chem., Int. Ed.*, 2010, **49**, 4615–4618.

79 D. Britt, D. Tranchemontagne and O. M. Yaghi, *Proc. Natl. Acad. Sci. U. S. A.*, 2008, **105**, 11623–11627.

80 Y. He, W. Zhou, T. Yildirim and B. Chen, *Energy Environ. Sci.*, 2013, **6**, 2735–2744.

81 H. S. Koh, M. K. Rana, A. G. Wong-Foy and D. J. Siegel, *J. Phys. Chem. C*, 2015, **119**, 13451–13458.

82 M. Jorge, M. Fischer, J. R. B. Gomes, C. Siquet, J. C. Santos and A. E. Rodrigues, *Ind. Eng. Chem. Res.*, 2014, **53**, 15475–15487.

83 A. J. Rieth, Y. Tulchinsky and M. Dincă, *J. Am. Chem. Soc.*, 2016, **138**, 9401–9404.

84 Y.-H. Shih, K.-Y. Wang, B. Singco, C.-H. Lin and H.-Y. Huang, *Langmuir*, 2016, **32**, 11465–11473.

85 M. H. Weston, W. Morris, P. W. Siu, W. J. Hoover, D. Cho, R. K. Richardson and O. K. Farha, *Inorg. Chem.*, 2015, **54**, 8162–8164.

86 B. Chen, N. W. Ockwig, A. R. Millward, D. S. Contreras and O. M. Yaghi, *Angew. Chem., Int. Ed.*, 2005, **44**, 4745–4749.

87 Y. Yan, S. Yang, A. J. Blake and M. Schröder, *Acc. Chem. Res.*, 2014, **47**, 296–307.

88 M. T. Kapelewski, S. J. Geier, M. R. Hudson, D. Stück, J. A. Mason, J. N. Nelson, D. J. Xiao, Z. Hulvey, E. Gilmour, S. A. FitzGerald, M. Head-Gordon, C. M. Brown and J. R. Long, *J. Am. Chem. Soc.*, 2014, **136**, 12119–12129.

89 M. H. Rosnes, M. Opitz, M. Frontzek, W. Lohstroh, J. Peter Embs, P. A. Georgiev and P. D. C. Dietzel, *J. Mater. Chem. A*, 2015, **3**, 4827–4839.

90 N. J. Hinks, A. C. McKinlay, B. Xiao, P. S. Wheatley and R. E. Morris, *Microporous Mesoporous Mater.*, 2010, **129**, 330–334.

91 J. L. C. Rowsell and O. M. Yaghi, *J. Am. Chem. Soc.*, 2006, **128**, 1304–1315.

92 J. J. Goings, S. M. Ohlsen, K. M. Blaisdell and D. P. Schofield, *J. Phys. Chem. A*, 2014, **118**, 7411–7417.

93 J. Bentley, G. S. Foo, M. Rungta, N. Sangar, C. Sievers, D. S. Sholl and S. Nair, *Ind. Eng. Chem. Res.*, 2016, **55**, 5043–5053.

94 Z. R. Herm, E. D. Bloch and J. R. Long, *Chem. Mater.*, 2014, **26**, 323–338.

95 S. M. Chavan, G. C. Shearer, E. Bloch and S. Bordiga, *ChemPhysChem*, 2012, **13**, 445–448.

96 U. Böhme, B. Barth, C. Paula, A. Kuhnt, W. Schwieger, A. Mundstock, J. R. Caro and M. Hartmann, *Langmuir*, 2013, **29**, 8592–8600.

97 A. Ö. Yazaydın, R. Q. Snurr, T.-H. Park, K. Koh, J. Liu, M. D. LeVan, A. I. Benin, P. Jakubczak, M. Lanuza, D. B. Galloway, J. J. Low and R. R. Willis, *J. Am. Chem. Soc.*, 2009, **131**, 18198–18199.

98 S. Rostamnia, H. Alamgholiloo and X. Liu, *J. Colloid Interface Sci.*, 2016, **469**, 310–317.

99 J.-C. Wang, F.-W. Ding, J.-P. Ma, Q.-K. Liu, J.-Y. Cheng and Y.-B. Dong, *Inorg. Chem.*, 2015, **54**, 10865–10872.

100 E. Q. Procopio, T. Fukushima, E. Barea, J. A. R. Navarro, S. Horike and S. Kitagawa, *Chem. – Eur. J.*, 2012, **18**, 13117–13125.

101 H. K. Kim, W. S. Yun, M.-B. Kim, J. Y. Kim, Y.-Y. Bae, J. Lee and N. C. Jeong, *J. Am. Chem. Soc.*, 2015, **137**, 10009–10015.

102 J. Bae, J. S. Choi, S. Hwang, W. S. Yun, D. Song, J. Lee and N. C. Jeong, *ACS Appl. Mater. Interfaces*, 2017, **9**, 24743–24752.

103 J. S. Choi, J. Bae, E. J. Lee and N. C. Jeong, *Inorg. Chem.*, 2018, **57**, 5225–5231.

104 J. Bae, E. J. Lee and N. C. Jeong, *Chem. Commun.*, 2018, **54**, 6458–6471.

105 J. Espín, L. Garzón-Tovar, A. Carné-Sánchez, I. Imaz and D. Maspoch, *ACS Appl. Mater. Interfaces*, 2018, **10**, 9555–9562.

106 C.-D. Wu and M. Zhao, *Adv. Mater.*, 2017, **29**, 1605446.

107 R. Kitaura, G. Onoyama, H. Sakamoto, R. Matsuda, S.-I. Noro and S. Kitagawa, *Angew. Chem., Int. Ed.*, 2004, **43**, 2684–2687.

108 D.-M. Chen, J.-Y. Tian, C.-S. Liu and M. Du, *Chem. Commun.*, 2016, **52**, 8413–8416.

109 S. Rostamnia, H. Alamgholiloo, M. Jafari, R. Rookhosh and A. R. Abbasi, *Appl. Organomet. Chem.*, 2016, **30**, 954–958.

110 X. Liu, W. Fan, M. Zhang, G. Li, H. Liu, D. Sun, L. Zhao, H. Zhu and W. Guo, *Mater. Chem. Front.*, 2018, **2**, 1146–1154.

111 Q. Wenge, W. Yu, L. Chuanqiang, Z. Zongcheng, Z. Xuehong, Z. Guizhen, W. Rui and H. Hong, *Chin. J. Catal.*, 2012, **33**, 986–992.

112 S. Rostamnia and F. Mohsenzad, *Mol. Catal.*, 2018, **445**, 12–20.

113 J. Chen, X. Chen, Z. Zhang, Z. Bao, H. Xing, Q. Yang and Q. Ren, *Mol. Catal.*, 2018, **445**, 163–169.

114 F.-G. Xi, Y. Yang, H. Liu, H.-F. Yao and E.-Q. Gao, *RSC Adv.*, 2015, **5**, 79216–79223.

115 M. Vandichel, J. Hajek, F. Vermoortele, M. Waroquier, D. E. De Vos and V. Van Speybroeck, *CrystEngComm*, 2015, **17**, 395–406.

116 S. Nagarkar and S. K. Ghosh, *J. Chem. Sci.*, 2015, **127**, 627–633.

117 X.-S. Wang, S. Ma, P. M. Forster, D. Yuan, J. Eckert, J. J. López, B. J. Murphy, J. B. Parise and H.-C. Zhou, *Angew. Chem., Int. Ed.*, 2008, **47**, 7263–7266.

118 L. Du, Z. Lu, L. Xu and J. Zhang, *RSC Adv.*, 2017, **7**, 21268–21272.

119 H. Lyu, Q. Zhang, Y. Wang and J. Duan, *Dalton Trans.*, 2018, **47**, 4424–4427.

120 Y. Yan, D. I. Kolokolov, I. da Silva, A. G. Stepanov, A. J. Blake, A. Dailly, P. Manuel, C. C. Tang, S. Yang and M. Schröder, *J. Am. Chem. Soc.*, 2017, **139**, 13349–13360.

121 S. Ma, D. Sun, J. M. Simmons, C. D. Collier, D. Yuan and H.-C. Zhou, *J. Am. Chem. Soc.*, 2008, **130**, 1012–1016.

122 G. L. Smith, J. E. Eyley, X. Han, X. Zhang, J. Li, N. M. Jacques, H. G. W. Godfrey, S. P. Argent, L. J. McCormick McPherson, S. J. Teat, Y. Cheng, M. D. Frogley, G. Cinque, S. J. Day, C. C. Tang, T. L. Easun, S. Rudić, A. J. Ramirez-Cuesta, S. Yang and M. Schröder, *Nat. Mater.*, 2019, **18**, 1358–1365.

123 Z. Wei, W. Lu, H.-L. Jiang and H.-C. Zhou, *Inorg. Chem.*, 2013, **52**, 1164–1166.

124 M. V. Veidis, G. H. Schreiber, T. E. Gough and G. J. Palenik, *J. Am. Chem. Soc.*, 1969, **91**, 1859–1860.

125 K. Schlichte, T. Kratzke and S. Kaskel, *Microporous Mesoporous Mater.*, 2004, **73**, 81–88.

126 A. A. Talin, A. Centrone, A. C. Ford, M. E. Forster, V. Stavila, P. Haney, R. A. Kinney, V. Szalai, F. El Gabaly, H. P. Yoon, F. Léonard and M. D. Allendorf, *Science*, 2014, **342**, 66–69.

127 C. Prestipino, L. Regli, J. G. Vitillo, F. Bonino, A. Damin, C. Lamberti, A. Zecchina, P. L. Solari, K. O. Kongshaug and S. Bordiga, *Chem. Mater.*, 2006, **18**, 1337–1346.

128 A. A. Yakovenko, J. H. Reibenspies, N. Bhuvanesh and H.-C. Zhou, *J. Appl. Crystallogr.*, 2013, **46**, 346–353.

129 R. S. Kumar, S. S. Kumar and M. A. Kulandainathan, *Microporous Mesoporous Mater.*, 2013, **168**, 57–64.

130 Y. D. Liu, J. Kim, W.-S. Ahn and H. J. Choi, *Chem. Commun.*, 2012, **48**, 5635–5637.

131 J. Szanyi, M. Daturi, G. Clet, D. R. Baer and C. H. F. Peden, *Phys. Chem. Chem. Phys.*, 2012, **14**, 4383–4390.

132 C. Chen, T. Wu, D. Yang, P. Zhang, H. Liu, Y. Yang, G. Yang and B. Han, *Chem. Commun.*, 2018, **54**, 5984–5987.

133 S. Bordiga, L. Regli, F. Bonino, E. Groppo, C. Lamberti, B. Xiao, P. S. Wheatly, R. E. Morris and A. Zecchina, *Phys. Chem. Chem. Phys.*, 2007, **9**, 2676–2685.

134 L. J. Murray, M. Dincă, J. Yano, S. Chavan, S. Bordiga, C. M. Brown and J. R. Long, *J. Am. Chem. Soc.*, 2010, **132**, 7856–7857.

135 K. Sumida, J.-H. Her, M. Dincă, L. J. Murray, J. M. Schloss, C. J. Pierce, B. A. Thompson, S. A. FitzGerald, C. M. Brown and J. R. Long, *J. Phys. Chem. C*, 2011, **115**, 8414–8421.

136 M. Soo Lah and H. Chun, *Inorg. Chem.*, 1997, **36**, 1782–1785.

137 J. Jiang, Q. Wang, M. Zhang and J. Bai, *Cryst. Growth Des.*, 2017, **17**, 2223–2227.

138 M. Wickenheisser, F. Jeremias, S. K. Henninger and C. Janiak, *Inorg. Chim. Acta*, 2013, **407**, 145–152.

139 J. Yang, Y. Wang, L. Li, Z. Zhang and J. Li, *J. Colloid Interface Sci.*, 2015, **456**, 197–205.

140 C. P. Cabello, P. Rumori and G. T. Palomino, *Microporous Mesoporous Mater.*, 2014, **190**, 234–239.

141 J. W. Yoon, H. Chang, S.-J. Lee, Y. K. Hwang, D.-Y. Hong, S.-K. Lee, J. S. Lee, S. Jang, T.-U. Yoon, K. Kwac, Y. Jung, R. S. Pillai, F. Faucher, A. Vimont, M. Daturi, G. Férey, C. Serre, G. Maurin, Y.-S. Bae and J.-S. Chang, *Nat. Mater.*, 2017, **16**, 526–532.

142 J. W. Yoon, Y.-K. Seo, Y. K. Hwang, J.-S. Chang, H. Leclerc, S. Wuttke, P. Bazin, A. Vimont, M. Daturi, E. Bloch, P. L. Llewellyn, C. Serre, P. Horcajada, J.-M. Grenèche, A. E. Rodrigues and G. Férey, *Angew. Chem., Int. Ed.*, 2010, **49**, 5949–5952.

143 M. Banerjee, S. Das, M. Yoon, H. J. Choi, M. H. Hyun, S. M. Park, G. Seo and K. Kim, *J. Am. Chem. Soc.*, 2009, **131**, 7524–7525.

144 D.-Y. Hong, Y. K. Hwang, C. Serre, G. Férey and J.-S. Chang, *Adv. Funct. Mater.*, 2009, **19**, 1537–1552.

145 S. Bhattacharjee, C. Chen and W.-S. Ahn, *RSC Adv.*, 2014, **4**, 52500–52525.

146 S. M. Cohen, *Chem. Rev.*, 2012, **112**, 970–1000.

147 Q. Yang, Q. Xu and H. L. Jiang, *Chem. Soc. Rev.*, 2017, **46**, 4774–4808.

148 A. Herbst, A. Khutia and C. Janiak, *Inorg. Chem.*, 2014, **53**, 7319–7333.

149 P. Horcajada, S. Surblé, C. Serre, D.-Y. Hong, Y.-K. Seo, J.-S. Chang, J.-M. Grenèche, I. Margiolaki and G. Férey, *Chem. Commun.*, 2007, 2820–2822.

150 H. R. Moon, D.-W. Lim and M. P. Suh, *Chem. Soc. Rev.*, 2013, **42**, 1807–1824.

151 A. Dhakshinamoorthy and H. Garcia, *Chem. Soc. Rev.*, 2012, **41**, 5262–5284.

152 F. Schröder and R. A. Fischer, *Top. Curr. Chem.*, 2010, **293**, 77–113.

153 M. T. Zhao, K. Yuan, Y. Wang, G. D. Li, J. Guo, L. Gu, W. P. Hu, H. J. Zhao and Z. Y. Tang, *Nature*, 2016, **539**, 76–80.

154 H. Pan, X. Li, D. Zhang, Y. Guan and P. Wu, *J. Mol. Catal. A: Chem.*, 2013, **377**, 108–114.

155 S. Biswas, M. Maes, A. Dhakshinamoorthy, M. Feyand, D. E. De Vos, H. Garcia and N. Stock, *J. Mater. Chem.*, 2012, **22**, 10200–10209.

156 M. Asgari, S. Jawahery, E. D. Bloch, M. R. Hudson, R. Flacau, B. Vlaisavljevich, J. R. Long, C. M. Brown and W. L. Queen, *Chem. Sci.*, 2018, **9**, 4579–4588.

157 K. Sumida, S. Horike, S. S. Kaye, Z. R. Herm, W. L. Queen, C. M. Brown, F. Grandjean, G. J. Long, A. Dailly and J. R. Long, *Chem. Sci.*, 2010, **1**, 184–191.

158 M. Dincă, W. S. Han, Y. Liu, A. Dailly, C. M. Brown and J. R. Long, *Angew. Chem., Int. Ed.*, 2007, **46**, 1419–1422.

159 E. D. Bloch, W. L. Queen, M. R. Hudson, J. A. Mason, D. J. Xiao, L. J. Murray, R. Flacau, C. M. Brown and J. R. Long, *Angew. Chem., Int. Ed.*, 2016, **55**, 8605–8609.

160 M. Dincă, A. Dailly, Y. Liu, C. M. Brown, D. A. Neumann and J. R. Long, *J. Am. Chem. Soc.*, 2006, **128**, 16876–16883.

161 J. H. Cavka, S. Jakobsen, U. Olsbye, N. Guillou, C. Lamberti, S. Bordiga and K. P. Lillerud, *J. Am. Chem. Soc.*, 2008, **130**, 13850–13851.

162 J. Hajek, C. Caratelli, R. Demuynck, K. De Wispelaere, L. Vanduyfhuys, M. Waroquier and V. Van Speybroeck, *Chem. Sci.*, 2018, **9**, 2723–2732.

163 G. C. Shearer, S. Forselv, S. Chavan, S. Bordiga, K. Mathisen, M. Bjørgen, S. Svelle and K. P. Lillerud, *Top. Catal.*, 2013, **56**, 770–782.

164 P. M. Schoenecker, C. G. Carson, H. Jasuja, C. J. J. Flemming and K. S. Walton, *Ind. Eng. Chem. Res.*, 2012, **51**, 6513–6519.

165 L. Valenzano, B. Civalleri, S. Chavan, S. Bordiga, M. H. Nilsen, S. Jakobsen, K. P. Lillerud and C. Lamberti, *Chem. Mater.*, 2011, **23**, 1700–1718.

166 C. F. Macrae, I. J. Bruno, J. A. Chisholm, P. R. Edgington, P. McCabe, E. Pidcock, L. Rodriguez-Monge, R. Taylor, J. van de Streek and P. A. Wood, *J. Appl. Crystallogr.*, 2008, **41**, 466–470.

167 E. D. Bloch, L. J. Murray, W. L. Queen, S. Chavan, S. N. Maximoff, J. P. Bigi, R. Krishna, V. K. Peterson, F. Grandjean, O. Gary, J. Long, B. Smit, S. Bordiga, C. M. Brown and J. R. Long, *J. Am. Chem. Soc.*, 2011, **133**, 14814–14822.

168 M. H. Rosnes, D. Sheptyakov, A. Franz, M. Frontzek, P. D. C. Dietzel and P. A. Georgiev, *Phys. Chem. Chem. Phys.*, 2017, **19**, 26346–26357.

169 M. Märcza, R. E. Johnsen, P. D. C. Dietzel and H. Fjellvåg, *Microporous Mesoporous Mater.*, 2012, **157**, 62–74.
170 K. Lee, J. D. Howe, L.-C. Lin, B. Smit and J. B. Neaton, *Chem. Mater.*, 2015, **27**, 668–678.
171 E. Haldoupis, J. Borycz, H. Shi, K. D. Vogiatzis, P. Bai, W. L. Queen, L. Gagliardi and J. I. Siepmann, *J. Phys. Chem. C*, 2015, **119**, 16058–16071.
172 P. D. C. Dietzel, R. Blom and H. Fjellvåg, *Eur. J. Inorg. Chem.*, 2008, 3624–3632.
173 P. C. Dietzel, Y. Morita, R. Blom and H. Fjellvåg, *Angew. Chem., Int. Ed.*, 2005, **44**, 6354–6358.
174 F. Bonino, S. Chavan, J. G. Vitillo, E. Groppo, G. Agostini, C. Lamberti, P. D. C. Dietzel, C. Prestipino and S. Bordiga, *Chem. Mater.*, 2008, **20**, 4957–4968.
175 R. Sanz, F. Martínez, G. Orcajo, L. Wojtas and D. Briones, *Dalton Trans.*, 2013, **42**, 2392–2398.
176 M. Díaz-García and M. Sánchez-Sánchez, *Microporous Mesoporous Mater.*, 2014, **190**, 248–254.
177 T. Pham, K. A. Forrest, R. Banerjee, G. Orcajo, J. Eckert and B. Space, *J. Phys. Chem. C*, 2015, **119**, 1078–1090.
178 H. Kim, M. Sohail, K. Yim, Y. C. Park, D. H. Chun, H. J. Kim, S. O. Han and J.-H. Moon, *ACS Appl. Mater. Interfaces*, 2019, **11**, 7014–7021.
179 W. Wong-Ng, J. A. Kaduk, H. Wu and M. Suchomel, *Powder Diffr.*, 2012, **27**, 256–262.
180 B. Chen, Y. Yang, F. Zapata, G. Lin, G. Qian and E. B. Lobkovsky, *Adv. Mater.*, 2007, **19**, 1693–1696.
181 H.-H. Wang, L. Hou, Y.-Z. Li, C.-Y. Jiang, Y.-Y. Wang and Z. Zhu, *ACS Appl. Mater. Interfaces*, 2017, **9**, 17969–17976.
182 X.-F. Lu, P.-Q. Liao, J.-W. Wang, J.-X. Wu, X.-W. Chen, C.-T. He, J.-P. Zhang, G.-R. Li and X.-M. Chen, *J. Am. Chem. Soc.*, 2016, **138**, 8336–8339.
183 P.-Q. Liao, X.-Y. Li, J. Bai, C.-T. He, D.-D. Zhou, W.-X. Zhang, J.-P. Zhang and X.-M. Chen, *Chem. – Eur. J.*, 2014, **20**, 11303–11307.
184 P.-Q. Liao, H. Chen, D.-D. Zhou, S.-Y. Liu, C.-T. He, Z. Rui, H. Ji, J.-P. Zhang and X.-M. Chen, *Energy Environ. Sci.*, 2015, **8**, 1011–1016.
185 J. Zhang, J. T. Bu, S. Chen, T. Wu, S. Zheng, Y. Chen, R. A. Nieto, P. Feng and X. Bu, *Angew. Chem.*, 2010, **122**, 9060–9063.
186 http://www.incaweb.org/transit/iupacgcdir/overview.htm; retrieved February 2019.
187 H. Reinsch, *Eur. J. Inorg. Chem.*, 2016, 4290–4299.
188 L. Ma, A. Jin, Z. Xie and W. Lin, *Angew. Chem., Int. Ed.*, 2009, **48**, 9905–9908.
189 S. Barman, H. Furukawa, O. Blacque, K. Venkatesan, O. M. Yaghi, G.-X. Jin and H. Berke, *Chem. Commun.*, 2011, **47**, 11882–11884.
190 K. M. Patil, S. G. Telfer, S. C. Moratti, O. T. Qazvini and L. R. Hanton, *CrystEngComm*, 2017, **19**, 7236–7243.
191 E. Hastürk, C. Schlüsener, J. Quadbach, A. Schmitz and C. Janiak, *Microporous Mesoporous Mater.*, 2019, **280**, 277–287.
192 N. Sahiner and S. Demirci, *React. Funct. Polym.*, 2016, **105**, 60–65.
193 N. Sahiner and S. Demirci, *J. Appl. Polym. Sci.*, 2016, **133**, 44137.
194 X. Liu, S. Zhang, Y. Xing, S. Wang, P. Yang and H. Li, *New J. Chem.*, 2016, **40**, 9679–9683.
195 Z. Hu and D. Zhao, *CrystEngComm*, 2017, **19**, 4066–4081.
196 J. Jiang and O. M. Yaghi, *Chem. Rev.*, 2015, **115**, 6966–6997.
197 E. Pérez-Mayoral, Z. Musilová, B. Gil, B. Marszalek, M. Položij, P. Nachtigall and J. Čejka, *Dalton Trans.*, 2012, **41**, 4036–4044.
198 A. Vimont, H. Leclerc, F. Maugé, M. Daturi, J.-C. Lavalley, S. Surblé, C. Serre and G. Férey, *J. Phys. Chem. C*, 2007, **111**, 383–388.
199 C. V. Hidalgo, H. Itoh, T. Hattori, M. Niwa and Y. Murakami, *J. Catal.*, 1984, **85**, 362–369.
200 G. Centi, S. Perathoner, F. Trifiro, A. Aboukais, C. F. Aissi and M. Guelton, *J. Phys. Chem.*, 1992, **96**, 2617–2629.
201 F. Lónyi and J. Valyon, *Microporous Mesoporous Mater.*, 2001, **47**, 293–301.
202 D.-W. Kim, H.-G. Kim and D.-H. Cho, *Catal. Commun.*, 2016, **73**, 69–73.
203 A. H. Valekar., K.-H. Cho, S. K. Chitale, D.-Y. Hong, G.-Y. Cha, U.-H. Lee, D. W. Hwang, C. Serre, J.-S. Chang and Y. K. Hwang, *Green Chem.*, 2016, **18**, 4542–4552.
204 J. Kim, S.-N. Kim, H.-G. Jang, G. Seo and W.-S. Ahn, *Appl. Catal., A*, 2013, **453**, 175–180.
205 H. Jiang, Q. Wang, H. Wang, Y. Chen and M. Zhang, *ACS Appl. Mater. Interfaces*, 2016, **8**, 26817–26826.
206 J. N. Hall and P. Bollini, *Langmuir*, 2020, **36**, 1345–1356.
207 R. Poloni, K. Lee, R. F. Berger, B. Smit and J. B. Neaton, *J. Phys. Chem. Lett.*, 2014, **5**, 861–865.
208 M. Fischer, J. R. B. Gomes and M. Jorge, *Mol. Simul.*, 2014, **40**, 537–556.
209 M. Fischer, F. Hoffmann and M. Fröba, *ChemPhysChem*, 2010, **11**, 2220–2229.
210 T. Pham, K. A. Forrest, D. M. Franz, Z. Guo, B. Chen and B. Space, *Phys. Chem. Chem. Phys.*, 2017, **19**, 18587–18602.
211 J. Borycz, L.-C. Lin, E. D. Bloch, J. Kim, A. L. Dzubak, R. Maurice, D. Semrouni, K. Lee, B. Smit and L. Gagliardi, *J. Phys. Chem. C*, 2014, **118**, 12230–12240.
212 L. Chen, L. Grajciar, P. Nachtigall and T. Düren, *J. Phys. Chem. C*, 2011, **115**, 23074–23080.
213 B. Sun, S. Kayal and A. Chakraborty, *Energy*, 2014, **76**, 419–427.
214 K. S. Walton, A. R. Millward, D. Dubbeldam, H. Frost, J. J. Low, O. M. Yaghi and R. Q. Snurr, *J. Am. Chem. Soc.*, 2008, **130**, 406–407.
215 L. Chen, C. A. Morrison and T. Düren, *J. Phys. Chem. C*, 2012, **116**, 18899–18909.
216 S. Chen, Y. Shi and B. Gu, *AIChE J.*, 2018, **64**, 1383–1388.
217 T. Pham, K. A. Forrest and B. Space, *Phys. Chem. Chem. Phys.*, 2016, **18**, 21421–21430.
218 A. Kundu, K. Sillar and J. Sauer, *J. Phys. Chem. Lett.*, 2017, **8**, 2713–2718.
219 E. O. Fetisov, M. S. Shah, J. R. Long, M. Tsapatsis and J. I. Siepmann, *Chem. Commun.*, 2018, **54**, 10816–10819.
220 K. Yu, K. Kiesling and J. R. Schmidt, *J. Phys. Chem. C*, 2012, **116**, 20480–20488.

221 L. Grajciar, P. Nachtigall, O. Bludský and M. Rubeš, *J. Chem. Theory Comput.*, 2015, **11**, 230–238.

222 D. Yu, A. O. Yazaydin, J. R. Lane, P. D. C. Dietzel and R. Q. Snurr, *Chem. Sci.*, 2013, **4**, 3544–3556.

223 B. Vlaisavljevich, J. Huck, Z. Hulvey, K. Lee, J. A. Mason, J. B. Neaton, J. R. Long, C. M. Brown, D. Alfè, A. Michaelides and B. Smit, *J. Phys. Chem. A*, 2017, **121**, 4139–4151.

224 S. Grimme, *J. Comput. Chem.*, 2006, **27**, 1787–1799.

225 C. Zhou, L. Cao, S. Wei, Q. Zhang and L. Chen, *Comput. Theor. Chem.*, 2011, **976**, 153–160.

226 S. Kristyán and P. Pulay, *Chem. Phys. Lett.*, 1994, **229**, 175–180.

227 M. K. Rana, H. S. Koh, J. Hwang and D. J. Siegel, *J. Phys. Chem. C*, 2012, **116**, 16957–16968.

228 H. Wu, J. M. Simmons, G. Srinivas, W. Zhou and T. Yildirim, *J. Phys. Chem. Lett.*, 2010, **1**, 1946–1951.

229 S. Grimme, *J. Comput. Chem.*, 2004, **25**, 1463–1473.

230 S. Grimme, J. Antony, S. Ehrlich and H. Krieg, *J. Chem. Phys.*, 2010, **132**, 154104.

231 M. S. Gordon, Q. A. Smith, P. Xu and L. V. Slipchenko, *Annu. Rev. Phys. Chem.*, 2013, **64**, 553–578.

232 L. Grajciar, A. D. Wiersum, P. L. Llewellyn, J.-S. Chang and P. Nachtigall, *J. Phys. Chem. C*, 2011, **115**, 17925–17933.

233 A. L. Barnes, D. Bykov, D. I. Lyakh and T. P. Straatsma, *J. Phys. Chem. A*, 2019, **123**, 8734–8743.

234 X.-J. Hou, P. He, H. Li and X. Wang, *J. Phys. Chem. C*, 2013, **117**, 2824–2834.

235 K. Sillar, A. Kundu and J. Sauer, *J. Phys. Chem. C*, 2017, **121**, 12789–12799.

236 F. Darkrim and D. Levesque, *J. Chem. Phys.*, 1998, **109**, 4981.

237 J. L. Belof, A. C. Stern and B. Space, *J. Chem. Theory Comput.*, 2008, **4**, 1332–1337.

238 T. Pham, K. A. Forrest, K. McLaughlin, J. Eckert and B. Space, *J. Phys. Chem. C*, 2014, **118**, 22683–22690.

239 K. A. Forrest, T. Pham, K. McLaughlin, J. L. Belof, A. C. Stern, M. J. Zaworotko and B. Space, *J. Phys. Chem. C*, 2012, **116**, 15538–15549.

240 D. Franz, K. A. Forrest, T. Pham and B. Space, *Cryst. Growth Des.*, 2016, **16**, 6024–6032.

241 T. Pham, K. A. Forrest, J. Eckert and B. Space, *Cryst. Growth Des.*, 2016, **16**, 867–874.

242 J.-D. Chai and M. Head-Gordon, *Phys. Chem. Chem. Phys.*, 2008, **10**, 6615–6620.

243 R. Z. Khaliullin, E. A. Cobar, R. C. Lochan, A. T. Bell and M. J. Head-Gordon, *J. Phys. Chem. A*, 2007, **111**, 8753–8765.

244 Q. Yang and C. Zhong, *J. Phys. Chem. B*, 2006, **110**, 655–658.

245 L. Valenzano, B. Civalleri, K. Sillar and J. Sauer, *J. Phys. Chem. C*, 2011, **115**, 21777–21784.

246 G. Alonso, D. Bahamon, F. Keshavarz, X. Giménez, P. Gamallo and R. Sayós, *J. Phys. Chem. C*, 2018, **122**, 3945–3957.

247 J. J. Potoff and J. I. Siepmann, *AIChE J.*, 2001, **47**, 1676–1682.

248 A. L. Mullen, T. Pham, K. A. Forrest, C. R. Cioce, K. McLaughlin and B. Space, *J. Chem. Theory Comput.*, 2013, **9**, 5421–5429.

249 L. Valenzano, B. Civalleri, S. Chavan, G. T. Palomino, C. O. Arean and S. Bordiga, *J. Phys. Chem. C*, 2010, **114**, 11185–11191.

250 J. Park, H. Kim, S. S. Han and Y. Jung, *J. Phys. Chem. Lett.*, 2012, **3**, 826–829.

251 P. L. Llewellyn, S. Bourrelly, C. Serre, A. Vimont, M. Daturi, L. Hamon, G. De Weireld, J.-S. Chang, D.-Y. Hong, Y. K. Hwang, S. H. Jhung and G. Férey, *Langmuir*, 2008, **24**, 7245–7250.

252 C. Zhang, L. Wang, G. Maurin and Q. Yang, *AIChE J.*, 2018, **64**, 4089–4096.

253 M. Dion, H. Rydberg, E. Schröder, D. C. Langreth and B. I. Lundqvist, *Phys. Rev. Lett.*, 2004, **92**, 246401.

254 J. P. Perdew and Y. Wang, *Phys. Rev. B: Condens. Matter Mater. Phys.*, 1986, **33**, 8800–8802.

255 K. Lee, É. D. Murray, L. Kong, B. I. Lundqvist and D. C. Langreth, *Phys. Rev. B: Condens. Matter Mater. Phys.*, 2010, **82**, 081101.

256 R. Mercado, B. Vlaisavljevich, L.-C. Lin, K. Lee, Y. Lee, J. A. Mason, D. J. Xiao, M. I. Gonzalez, M. T. Kapelewski, J. B. Neaton and B. Smit, *J. Phys. Chem. C*, 2016, **120**, 12590–12604.

257 Y. Hijikata and S. Sakaki, *Inorg. Chem.*, 2014, **53**, 2417–2426.

258 W. You, Y. Liu, J. D. Howe and D. S. Sholl, *J. Phys. Chem. C*, 2018, **122**, 8960–8966.

259 L. Ding and A. Ö. Yazaydin, *J. Phys. Chem. C*, 2012, **116**, 22987–22991.

260 L. Valenzano, J. G. Vitillo, S. Chavan, B. Civalleri, F. Bonino, S. Bordiga and C. Lamberti, *Catal. Today*, 2012, **182**, 67–79.

261 Y. He, R. Krishna and B. Chen, *Energy Environ. Sci.*, 2012, **5**, 9107–9120.

262 S. Xiang, W. Zhou, J. M. Gallegos, Y. Liu and B. Chen, *J. Am. Chem. Soc.*, 2009, **131**, 12415–12419.

263 Y. Ji, L. Ding, Y. Cheng, H. Zhou, S. Yang, F. Li and Y. Li, *J. Phys. Chem. C*, 2017, **121**, 24104–24113.

264 Z. Hulvey, B. Vlaisavljevich, J. A. Mason, E. Tsivion, T. P. Dougherty, E. D. Bloch, M. Head-Gordon, B. Smit, J. R. Long and C. M. Brown, *J. Am. Chem. Soc.*, 2015, **137**, 10816–10825.

265 S. M. P. Lucena, P. G. M. Mileo, P. F. G. Silvino and C. L. Cavalcante, *J. Am. Chem. Soc.*, 2011, **133**, 19282–19285.

266 F. Jeremias, A. Khutia, S. K. Henninger and C. Janiak, *J. Mater. Chem.*, 2012, **22**, 10148–10151.

267 F. Jeremias, V. Lozan, S. K. Henninger and C. Janiak, *Dalton Trans.*, 2013, **42**, 15967–15973.

268 F. Jeremias, D. Fröhlich, C. Janiak and S. K. Henninger, *RSC Adv.*, 2014, **4**, 24073–24082.

269 P. W. Seo, N. A. Khan, Z. Hasan and S. H. Jhung, *ACS Appl. Mater. Interfaces*, 2016, **8**, 29799–29807.

270 V. Pentyala, P. Davydovskaya, M. Ade, R. Pohle and G. Urban, *Sens. Actuators, B*, 2016, **225**, 363–368.

271 N. Wang, A. Mundstock, Y. Liu, A. Huang and J. Caro, *Chem. Eng. Sci.*, 2015, **124**, 27–36.

272 J. S. Yeon, W. R. Lee, N. W. Kim, H. Jo, H. Lee, J. H. Song, K. S. Lim, D. W. Kang, J. G. Seo, D. Moon, B. Wiers and C. S. Hong, *J. Mater. Chem. A*, 2015, **3**, 19177–19185.

273 S.-T. Zheng, X. Zhao, S. Lau, A. Fuhr, P. Feng and X. Bu, *J. Am. Chem. Soc.*, 2013, **135**, 10270–10273.

274 M. J. Ingleson, R. Heck, J. A. Gould and M. J. Rosseinsky, *Inorg. Chem.*, 2009, **48**, 9986–9988.

275 S. Zhao, J. Mei, H. Xu, W. Liu, Z. Qu, Y. Cui and N. Yan, *J. Hazard. Mater.*, 2018, **351**, 301–307.
276 S. N. Kim, S.-T. Yang, J. Kim, J.-E. Park and W.-S. Ahn, *CrystEngComm*, 2012, **14**, 4142–4147.
277 M. Xu, S. Yuan, X.-Y. Chen, Y.-J. Chang, G. Day, Z.-Y. Gu and H.-C. Zhou, *J. Am. Chem. Soc.*, 2017, **139**, 8312–8319.
278 T. M. McDonald, D. M. D'Alessandro, R. Krishna and J. R. Long, *Chem. Sci.*, 2011, **2**, 2022–2028.
279 N. Al-Janabi, H. Deng, J. Borges, X. Liu, A. Garforth, F. R. Siperstein and X. Fan, *Ind. Eng. Chem. Res.*, 2016, **55**, 7941–7949.
280 X. Du, R. Fan, L. Qiang, K. Xing, H. Ye, X. Ran, Y. Song, P. Wang and Y. Yang, *ACS Appl. Mater. Interfaces*, 2017, **9**, 28939–28948.
281 B. M. Wiers, M.-L. Foo, N. P. Balsara and J. R. Long, *J. Am. Chem. Soc.*, 2011, **133**, 14522–14525.
282 H. Wang, J. Xu, D.-S. Zhang, Q. Chen, R.-M. Wen, Z. Chang and X.-H. Bu, *Angew. Chem., Int. Ed.*, 2015, **54**, 5966–5970.
283 D. Denysenko, M. Grzywa, J. Jelic, K. Reuter and D. Volkmer, *Angew. Chem., Int. Ed.*, 2014, **53**, 5832–5836.
284 E. Žunkovič, M. Mazaj, G. Mali, M. Rangus, T. Devic, C. Serre and N. Z. Logara, *J. Solid State Chem.*, 2015, **225**, 209–215.
285 Z. Wang and S. M. Cohen, *Chem. Soc. Rev.*, 2009, **38**, 1315–1329.
286 K. K. Tanabe and S. M. Cohen, *Chem. Soc. Rev.*, 2011, **40**, 498–519.
287 Z. R. Herm, J. A. Swisher, B. Smit, R. Krishna and J. R. Long, *J. Am. Chem. Soc.*, 2011, **133**, 5664–5667.
288 A. Demessence, D. M. D'Alessandro, M. L. Foo and J. R. Long, *J. Am. Chem. Soc.*, 2009, **131**, 8784–8786.
289 K. C. Kim, *J. Organomet. Chem.*, 2018, **854**, 94–105.
290 H. Frost, T. Düren and R. Q. Snurr, *J. Phys. Chem. B*, 2006, **110**, 9565–9570.
291 J.-R. Li, R. J. Kuppler and H.-C. Zhou, *Chem. Soc. Rev.*, 2009, **38**, 1477–1504.
292 A. Ö. Yazaydin, A. I. Benin, S. A. Faheem, P. Jakubczak, J. J. Low, R. R. Willis and R. Q. Snurr, *Chem. Mater.*, 2009, **21**, 1425–1430.
293 E. J. García, J. P. S. Mowat, P. A. Wright, J. Pérez-Pellitero, C. Jallut and G. D. Pirngruber, *J. Phys. Chem. C*, 2012, **116**, 26636–26648.
294 H. Wu, W. Zhou and T. Yildirim, *J. Am. Chem. Soc.*, 2009, **131**, 4995–5000.
295 W. L. Queen, C. M. Brown, D. K. Britt, P. Zajdel, M. R. Hudson and O. M. Yaghi, *J. Phys. Chem. C*, 2011, **115**, 24915–24919.
296 J. Getzschmann, I. Senkovska, D. Wallacher, M. Tovar, D. Fairen-Jimenez, T. Düren, J. M. van Baten, R. Krishna and S. Kaskel, *Microporous Mesoporous Mater.*, 2010, **136**, 50–58.
297 B. Pato-Doldán, M. H. Rosnes and P. D. C. Dietzel, *ChemSusChem*, 2017, **10**, 1710–1719.
298 M. I. Gonzalez, J. A. Mason, E. D. Bloch, S. J. Teat, K. J. Gagnon, G. Y. Morrison, W. L. Queen and J. R. Long, *Chem. Sci.*, 2017, **8**, 4387–4398.
299 W. S. Drisdell, R. Poloni, T. M. McDonald, J. R. Long, B. Smit, J. B. Neaton, D. Prendergast and J. B. Kortright, *J. Am. Chem. Soc.*, 2013, **135**, 18183–18190.
300 M. Asgari, R. Semino, P. Schouwink, I. Kochetygov, O. Trukhina, J. D. Tarver, S. Bulut, S. Yang, C. M. Brown, M. Ceriotti and W. L. Queen, *Eur. J. Inorg. Chem.*, 2019, 1147–1154.
301 A. L. Spek, Structure Validation in Chemical Crystallography, *Acta Crystallogr., Sect. B: Struct. Sci.*, 2009, **65**, 148–155.
302 R. B. Getman, Y.-S. Bae, C. E. Wilmer and R. Q. Snurr, *Chem. Rev.*, 2012, **112**, 703–723.
303 S. O. Odoh, C. J. Cramer, D. G. Truhlar and L. Gagliardi, *Chem. Rev.*, 2015, **115**, 6051–6111.
304 M. Paik Suh, H. J. Park, T. K. Prasad and D.-W. Lim, *Chem. Rev.*, 2012, **112**, 782–835.
305 H. W. Langmi, J. Ren, B. North, M. Mathe and D. Bessarabov, *Electrochim. Acta*, 2014, **128**, 368–392.
306 V. K. Peterson, Y. Liu, C. M. Brown and C. J. Kepert, *J. Am. Chem. Soc.*, 2006, **128**, 15578–15579.
307 P. D. C. Dietzel, B. Panella, M. Hirscher, R. Blom and H. Fjellva, *Chem. Commun.*, 2006, 959–961.
308 K. Sumida, C. M. Brown, Z. R. Herm, S. Chavan, S. Bordiga and J. R. Long, *Chem. Commun.*, 2011, **47**, 1157–1159.
309 D. Gygi, E. D. Bloch, J. A. Mason, M. R. Hudson, M. I. Gonzalez, R. L. Siegelman, T. A. Darwish, W. L. Queen, C. M. Brown and J. R. Long, *Chem. Mater.*, 2016, **28**, 1128–1138.
310 D. J. Levine, T. Runčevski, M. T. Kapelewski, B. K. Keitz, J. Oktawiec, D. A. Reed, J. A. Mason, H. Z. H. Jiang, K. A. Colwell, C. M. Legendre, S. A. FitzGerald and J. R. Long, *J. Am. Chem. Soc.*, 2016, **138**, 10143–10150.
311 K. Sumida, D. Stück, L. Mino, J.-D. Chai, E. D. Bloch, O. Zavorotynska, L. J. Murray, M. Dinca, S. Chavan, S. Bordiga, M. Head-Gordon and J. R. Long, *J. Am. Chem. Soc.*, 2013, **135**, 1083–1091.
312 X. Lin, I. Telepeni, A. J. Blake, A. Dailly, C. M. Brown, J. M. Simmons, M. Zoppi, G. S. Walker, K. M. Thomas, T. J. Mays, P. Hubberstey, N. R. Champness and M. Schröder, *J. Am. Chem. Soc.*, 2009, **131**, 2159–2171.
313 B. Panella, M. Hirscher, H. Pütter and U. Müller, *Adv. Funct. Mater.*, 2006, **16**, 520–524.
314 C. Chen, Y.-R. Lee and W.-S. Ahn, *J. Nanosci. Nanotechnol.*, 2016, **16**, 4291–4301.
315 Z. Zhang, Y. Zhao, Q. Gong, Z. Li and J. Li, *Chem. Commun.*, 2013, **49**, 653–661.
316 L.-C. Lin, J. Kim, X. Kong, E. Scott, T. M. McDonald, J. R. Long, J. A. Reimer and B. Smit, *Angew. Chem., Int. Ed.*, 2013, **52**, 4410–4413.
317 C. Chen, X. Feng, Q. Zhu, R. Dong, R. Yang, Y. Cheng and C. He, *Inorg. Chem.*, 2019, **58**, 2717–2728.
318 P. D. C. Dietzel, R. E. Johnsen, H. Fjellvåg, S. Bordiga, E. Groppo, S. Chavan and R. Blom, *Chem. Commun.*, 2008, 5125–5127.
319 R. M. Marti, J. D. Howe, C. R. Morelock, M. S. Conradi, K. S. Walton, D. S. Sholl and S. E. Hayes, *J. Phys. Chem. C*, 2017, **121**, 25778–25787.

320 X. Kong, E. Scott, W. Ding, J. A. Mason, J. R. Long and J. A. Reimer, *J. Am. Chem. Soc.*, 2012, **134**, 14341–14344.

321 P. D. C. Dietzel, V. Besikiotis and R. Blom, *J. Mater. Chem.*, 2009, **19**, 7362–7370.

322 S. A. FitzGerald, J. M. Schloss, C. J. Pierce, B. Thompson, J. L. C. Rowsell, K. Yu and J. R. Schmidt, *J. Phys. Chem. C*, 2015, **119**, 5293–5300.

323 J. G. Vitillo and G. Ricchiardi, *J. Phys. Chem. C*, 2017, **121**, 22762–22772.

324 Y. Yao, N. Nijem, J. Li, Y. J. Chabal, D. C. Langreth and T. Thonhauser, *Phys. Rev. B: Condens. Matter Mater. Phys.*, 2012, **85**, 064302.

325 N. Nijem, P. Canepa, L. Z. Kong, H. H. Wu, J. Li, T. Thonhauser and Y. J. Chabal, *J. Phys.: Condens. Matter*, 2012, **24**, 424203.

326 J. A. Mason, K. Sumida, Z. R. Herm, R. Krishna and J. R. Long, *Energy Environ. Sci.*, 2011, **4**, 3030–3040.

327 W. D. Wang, B. E. G. Lucier, V. V. Terskikh, W. Wang and Y. Huang, *J. Phys. Chem. Lett.*, 2014, **5**, 3360–3365.

328 J. Yang, H. Bai, F. Zhang, J. Liu, J. Winarta, Y. Wang and B. Mu, *J. Chem. Eng. Data*, 2019, **64**, 5814–5823.

329 J. Moellmer, A. Moeller, F. Dreisbach, R. Glaeser and R. Staudt, *Microporous Mesoporous Mater.*, 2011, **138**, 140–148.

330 B. Bonelli, B. Civalleri, B. Fubini, P. Ugliengo, C. O. Areán and E. Garrone, *J. Phys. Chem. B*, 2000, **104**, 10978–10988.

331 M. D'Amore, B. Civalleri, I. J. Bush, E. Albanese and M. Ferrabone, *J. Phys. Chem. C*, 2019, **123**, 28677–28687.

332 I. Kochetygov, S. Bulut, M. Asgari and W. L. Queen, *Dalton Trans.*, 2018, **47**, 10527–10535.

333 B. Li, Z. Zhang, Y. Li, K. Yao, Y. Zhu, Z. Deng, F. Yang, X. Zhou, G. Li, H. Wu, N. Nijem, Y. J. Chabal, Z. Lai, Y. Han, Z. Shi, S. Feng and J. Li, *Angew. Chem., Int. Ed.*, 2012, **51**, 1412–1415.

334 C.-Y. Wang, P. Ray, Q. Gong, Y. Zhao, J. Li and A. D. Lueking, *Phys. Chem. Chem. Phys.*, 2015, **17**, 26766–26776.

335 P. Chowdhury, S. Mekala, F. Dreisbach and S. Gumma, *Microporous Mesoporous Mater.*, 2012, **152**, 246–252.

336 A. C. McKinlay, B. Xiao, D. S. Wragg, P. S. Wheatley, I. L. Megson and R. E. Morris, *J. Am. Chem. Soc.*, 2008, **130**, 10440–10444.

337 B. Xiao, P. S. Wheatley, X. Zhao, A. J. Fletcher, S. Fox, A. G. Rossi, I. L. Megson, S. Bordiga, L. Regli, K. M. Thomas and R. E. Morris, *J. Am. Chem. Soc.*, 2007, **129**, 1203–1209.

338 N. Nijem, H. Bluhm, M. L. Ng, M. Kunz, S. R. Leone and M. K. Gilles, *Chem. Commun.*, 2014, **50**, 10144–10147.

339 M. Todaro, G. Buscarino, L. Sciortino, A. Alessi, F. Messina, M. Taddei, M. Ranocchiari, M. Cannas and F. M. Gelardi, *J. Phys. Chem. C*, 2016, **120**, 12879–12889.

340 P. D. C. Dietzel, R. E. Johnson, R. Blom and H. Fjellvag, *Chem. – Eur. J.*, 2008, **14**, 2389–2397.

341 B. Barth, M. Mendt, A. Pöppl and M. Hartmann, *Microporous Mesoporous Mater.*, 2015, **216**, 97–110.

342 R. Matsuda, R. Kitaura, S. Kitagawa, Y. Kubota, R. V. Belosludov, T. C. Kobayashi, H. Sakamoto, T. Chiba, M. Takata, Y. Kawazoe and Y. Mita, *Nature*, 2005, **436**, 238–241.

343 X. Rao, J. Cai, J. Yu, Y. He, C. Wu, W. Zhou, T. Yildirim, B. Chen and G. Qian, *Chem. Commun.*, 2013, **49**, 6719–6721.

344 Z. Zhang, S. Xiang and B. Chen, *CrystEngComm*, 2011, **13**, 5983–5992.

345 L. Zhang, K. Jiang, Y. Li, D. Zhao, Y. Yang, Y. Cui, B. Chen and G. Qian, *Cryst. Growth Des.*, 2017, **17**, 2319–2322.

346 T. Xia, J. Cai, H. Wang, X. Duan, Y. Cui, Y. Yang and G. Qian, *Microporous Mesoporous Mater.*, 2015, **215**, 109–115.

347 C. Song, J. Hu, Y. Ling, Y. Feng, D.-L. Chen and Y. He, *Dalton Trans.*, 2015, **44**, 14823–14829.

348 X. Duana, Y. Heb, Y. Cuia, Y. Yanga, R. Krishna, B. Chen and G. Qian, *RSC Adv.*, 2014, **4**, 23058–23063.

349 X. Duan, Y. Zhou, R. Lv, B. Yu, H. Chen, Z. Ji, Y. Cui, Y. Yang and G. Qian, *J. Solid State Chem.*, 2018, **260**, 31–33.

350 L. Zhang, C. Zou, M. Zhao, K. Jiang, R. Lin, Y. He, C.-D. Wu, Y. Cui, B. Chen and G. Qian, *Cryst. Growth Des.*, 2016, **16**, 7194–7197.

351 A. Luna-Triguero, J. M. Vicent-Luna, R. M. Madero-Castro, P. Gómez-Álvarez and S. Calero, *ACS Appl. Mater. Interfaces*, 2019, **11**, 31499–31507.

352 A. A. Fomkin, A. Y. Tsivadze, O. E. Aksyutin, A. G. Ishkov, A. A. Pribylov, A. V. Shkolin, I. E. Men'shchikov, K. V. Romanov, R. V. Teterevlev, U. Müller, L. Arnold and M. Piontek, *Prot. Met. Phys. Chem. Surf.*, 2018, **54**, 347–353.

353 M. K. Taylor, T. Runčevski, J. Oktawiec, M. I. Gonzalez, R. L. Siegelman, J. A. Mason, J. Ye, C. M. Brown and J. R. Long, *J. Am. Chem. Soc.*, 2016, **138**, 15019–15026.

354 F. Gándara, H. Furukawa, S. Lee and O. M. Yaghi, *J. Am. Chem. Soc.*, 2014, **136**, 5271–5274.

355 Y. Peng, V. Krungleviciute, I. Eryazici, J. T. Hupp, O. K. Farha and T. Yildirim, *J. Am. Chem. Soc.*, 2013, **135**, 11887–11894.

356 M. Zhang, W. Zhou, T. Pham, K. A. Forrest, W. Liu, Y. He, H. Wu, T. Yildirim, B. Chen and B. Space, *Angew. Chem., Int. Ed.*, 2017, **56**, 11426–11430.

357 Y. He, W. Zhou, G. Qian and B. Chen, *Chem. Soc. Rev.*, 2014, **43**, 5657–5678.

358 H. Wu, J. M. Simmons, Y. Liu, C. M. Brown, X.-S. Wang, S. Ma, V. K. Peterson, P. D. Southon, C. J. Kepert, H.-C. Zhou, T. Yildirim and W. Zhou, *Chem. – Eur. J.*, 2010, **16**, 5205–5214.

359 V. J. Witherspoon, R. Mercado, E. Braun, A. Mace, J. Bachman, J. R. Long, B. Blümich, B. Smit and J. A. Reimer, *J. Phys. Chem. C*, 2019, **123**, 12286–12295.

360 Z. Guo, H. Wu, G. Srinivas, Y. Zhou, S. Xiang, Z. Chen, Y. Yang, W. Zhou, M. O'Keeffe and B. Chen, *Angew. Chem., Int. Ed.*, 2011, **50**, 3178–3181.

361 W. Zhou, *Chem. Rec.*, 2010, **10**, 200.

362 J.-Y. Lee, T. C. Keener and Y. J. J. Yang, *Air Waste Manage. Assoc.*, 2012, **59**, 725–732.

363 R. K. Srivastava and W. J. Jozewicz, *Air Waste Manage. Assoc.*, 2011, **51**, 1676–1688.

364 International Energy Agency, *World Energy Outlook 2016*, IEA Publications, Paris, 2016.

365 Y. Zhang, P. Zhang, W. Yu, J. Zhang, J. Huang, J. Wang, M. Xu, Q. Deng, Z. Zeng and S. Deng, *ACS Appl. Mater. Interfaces*, 2019, **11**, 10680–10688.

366 B. Brandt, A. Nuhnen, M. Lange, J. Möllmer, O. Weingart and C. Janiak, *ACS Appl. Mater. Interfaces*, 2019, **11**, 17350–17358.
367 D. Dietrich, C. Licht, A. Nuhnen, S.-P. Höfert, L. De Laporte and C. Janiak, *ACS Appl. Mater. Interfaces*, 2019, **11**, 19654–19667.
368 T. G. Glover, G. W. Peterson, B. J. Schindler, D. Britt and O. M. Yaghi, *Chem. Eng. Sci.*, 2011, **66**, 163–170.
369 J. B. DeCoste, T. J. Demasky, M. J. Katz, O. K. Farha and J. T. A. Hupp, *New J. Chem.*, 2015, **39**, 2396–2399.
370 K. Sumida, D. L. Rogow, J. A. Mason, T. M. McDonald, E. D. Bloch, Z. R. Herm, T.-H. Bae and J. R. Long, *Chem. Rev.*, 2012, **112**, 724–781.
371 J. Liu, P. K. Thallapally, B. P. McGrail, D. R. Brown and J. Liu, *Chem. Soc. Rev.*, 2012, **41**, 2308–2322.
372 J.-R. Li, Y. Ma, M.-C. McCarthy, J. Sculley, J. Yu, H.-K. Jeong, P. B. Balbuena and H.-C. Zhou, *Coord. Chem. Rev.*, 2011, **225**, 1791–1823.
373 X. Lu, D. Jin, S. Wei, Z. Wang, C. An and W. Guo, *J. Mater. Chem. A*, 2015, **3**, 12118–12132.
374 Z. Y. Yeo, T. L. Chew, P. W. Zhu, A. R. Mohamed and S.-P. Chai, *J. Nat. Gas Chem.*, 2012, **21**, 282–298.
375 A. K. Datta and P. K. Sen, *J. Membr. Sci.*, 2006, **283**, 291–300.
376 B. Seoane, J. Coronas, I. Gascon, M. E. Benavides, O. Karvan, J. Caro, F. Kapteijn and J. Gascon, *Chem. Soc. Rev.*, 2015, **44**, 2421–2454.
377 S. Nandi, R. Maity, D. Chakraborty, H. Ballav and R. Vaidhyanathan, *Inorg. Chem.*, 2018, **57**, 5267–5272.
378 P. Mishra, S. Edubilli, B. Mandal and S. Gumma, *J. Phys. Chem. C*, 2014, **118**, 6847–6855.
379 J. N. Hall and P. Bollini, *React. Chem. Eng.*, 2019, **4**, 207–222.
380 A. Henschel, K. Gedrich, R. Kraehnert and S. Kaskel, *Chem. Commun.*, 2008, 4192–4194.
381 S. Horike, M. Dincă, K. Tamaki and J. R. Long, *J. Am. Chem. Soc.*, 2008, **130**, 5854–5855.
382 S. Wang, L. Bromberg, H. Schreuder-Gibson and T. A. Hatton, *ACS Appl. Mater. Interfaces*, 2013, **5**, 1269–1278.
383 P.-Z. Li, X.-J. Wang, J. Liu, H. S. Phang, Y. Li and Y. Zhao, *Chem. Mater.*, 2017, **29**, 9256–9261.
384 L. Alaerts, E. Ségiun, H. Poelman, F. Thibault-Starzyk, P. A. Jacobs and D. E. De Vos, *Chem. – Eur. J.*, 2006, **12**, 7353–7363.
385 G. Akiyama, R. Matsuda, H. Sato and S. Kitagawa, *Chem. – Asian J.*, 2014, **9**, 2772–2777.
386 D. Wang, R. Huang, W. Liu, D. Sun and Z. Li, *ACS Catal.*, 2014, **4**, 4254–4260.
387 M. Fujita, Y. J. Kwon, S. Washizu and K. Ogura, *J. Am. Chem. Soc.*, 1994, **116**, 1151–1152.
388 H. Liu, Y. W. Li, H. Jiang, C. Vargas and R. Luque, *Chem. Commun.*, 2012, **48**, 8431–8433.
389 H. Liu, Y. W. Li, R. Luque and H. Jiang, *Adv. Synth. Catal.*, 2011, **353**, 3107–3113.
390 M. Y. Masoomi, M. Bagheri and A. Morsali, *Inorg. Chem.*, 2015, **54**, 11269–11275.
391 M. Y. Masoomi, M. Bagheri, A. Morsali and P. C. Junk, *Inorg. Chem. Front.*, 2016, **3**, 944–951.
392 T. Rasheed and F. Nabeel, *Coord. Chem. Rev.*, 2019, **401**, 213065.
393 N. Abdollahi and A. Morsali, *Anal. Chim. Acta*, 2019, **1064**, 119–125.
394 D. Ma, W. Wang, Y. Li, J. Li, C. Daiguebonne, G. Calvez and O. Guillou, *CrystEngComm*, 2010, **12**, 4372–4377.
395 Z. Guo, H. Xu, S. Su, J. Cai, S. Dang, S. Xiang, G. Qian, H. Zhang, M. O'Keeffe and B. Chen, *Chem. Commun.*, 2011, **47**, 5551–5553.

Electronic Supplementary Material (ESI) for Chemical Society Reviews.

Coordinatively Unsaturated Metal Sites (Open Metal Sites) in Metal-Organic Frameworks: Design and Applications†

Ülkü Kökçam-Demir,[§a] Anna Goldman,[§a] Leili Esrafili,[b] Maniya Gharib,[b] Ali Morsali[§b,*]
Oliver Weingart[c] and Christoph Janiak [§a,*]

[a] Institut für Anorganische Chemie und Strukturchemie, Heinrich-Heine-Universität Düsseldorf, D-40204 Düsseldorf Germany. Email: janiak@hhu.de

[b] Department of Chemistry, Faculty of Sciences, Tarbiat Modares University, P.O. Box 14115-175, Tehran, Islamic Republic of Iran. Email: morsali_a@modares.ac.ir

[c] Institut für Theoretische Chemie und Computerchemie, Heinrich-Heine-Universität Düsseldorf, D-40204 Düsseldorf Germany. Email: Oliver.Weingart@hhu.de

† § These authors contributed equally.

E-mail addresses: Uelkue.Koekcam@hhu.de, Anna.Goldman@hhu.de, leiliesrafili@gmail.com, mania.gha1990@gmail.com, morsali_a@modares.ac.ir Oliver.Weingart@hhu.de, janiak@hhu.de,

Table S 1 Calculated binding energies −ΔE and isosteric heats of adsorption (−ΔH, $-Q_{st}$) values for CO_2 in relation to the different OMS, using computational methods in comparison to $-Q_{st}^{0}$ values from experimental studies.

MOF	M-MOF-74								HKUST-1
OMS	**Mg**	**Cr**	**Mn**	**Fe**	**Co**	**Ni**	**Cu**	**Zn**	**Cu**
Exp.	39.0-47.0 [1,2,3,4,6,17]	/	31.7-31.9[6,17]	33.2-34.3[6,17]	33.6-37.0[3,4,6,17]	38.6-41.0[3,4,6,17]	22.1-24.0[6,17]	26.8-30.6[1,6,17]	29.0[5]
MP2	40.5[6]		30.3[6]	24.2[6]	29.7[6]	31.2[6]	16.2[6]	29.7[6]	
LDA	54.3[6] (51.2)[7]		38.4[6]	38.1[6]	42.5[6] (36.6)[7]	43.1[6]	31.0[6]	40.2[6]	(30.6)[7] 32.7[8]
GGA-PW91	23.9[6]		13.3[6]	9.4[6]	10.6[6]	12.5[6]	6.0[6]	12.6[6]	
GGA-PBE	(20.2)[7]				(8.3)[7]	(8.8)[7]			(9.4)[7]
Hybrid-GGA B3LYP	23.9[6] 27.1[9]		12.1[6]	4.5[6]	7.0[6]	11.6[6]	3.5[6]	11.8[6]	
DFT-D2	(39.7)[7]				(29.0)[7]	(30.6)[7]			(18.5)[7]
PBE-D2	40.5[10]		33.8[10]	33.9[10]	33.7[10]	36.9[10]	27.1[10]	30.5[10]	21.0[11]
PBE-D3	39.7[10]		34.6[10] 32.4[12]	34.5[10]	33.9[10] 29.5[12]	36.7[10] 32.3[12]	28.0[10] 21.5[12]	31.8[10]	21.0[11]
PBE-D3 BJ	40.5[10]		35.5[10]	35.3[10]	34.5[10]	37.4[10]	27.8[10]	31.0[10]	
B3LYP-D*	(37.9)[13,14]					(35.5)[14]		(31.7)[14]	
ωB97X-D	(44.9)[9]								
optB88-vdW	(52.8)[7] 53.1[10]	46.2[10]		46.5[10]	(39.9)[7] 46.7[10]	(43.1)[7] 51.0[10]	37.9[10]**	41.6[10]	
optB86b-vdW	52.5[10] (53.9)[7]	45.9[10]		46.1[10]	46.6[10] (40.4)[7]	50.7[10] (45.6)[7]	37.5[10]	41.3[10]	28.0[11] (25.4)[7]
vdW-DF	(40.5)[15]								
PBE-vdW	(58.3)[15]								
optPBE-vdW	(57.2)[7]				(43.7)[7]	(46.6)[7]			(27.7)[7]
revPBE-vdW	(47.3)[7]				(37.2)[7]	(37.8)[7]			(23.3)[7]
rPW86-vdW	(46.2)[7]				(32.5)[7]	(34.5)[7]			(21.5)[7]

vdW-DF2	(37.4)^{15} (44.7)^{16}	38.1^{10}		38.1^{10}	37.7^{10}	41.5^{10}	30.9^{10}	34.0^{10}	22.0^{11}
vdW-DF2 + U	(40.9)^{17} (41.0)^{29}		(33.9)^{17} (27.0)^{29}	(34.1)^{17} (34.0)^{29}	(33.8)^{17} (34.0)^{29}	(37.3)^{17} (34.0)^{29}	(27.1)^{17} (37.0)^{29}	(30.2)^{17} (27.0)^{29}	(30.0)^{29}
rev-vdW-DF2	43.6^{10}		37.0^{10}	37.3^{10}	37.4^{10}	41.3^{10}	28.2^{10}	32.1^{10}	
B3LYP+D*/MP2	(42.7)^{14}					(40.5)^{14}		(39.0)^{14}	
DFT/CC									28.0^{11}
QM/MM DFT/MP2	48.2^{6}		37.2^{6}	32.2^{6}	37.0^{6}	39.1^{6}	23.9^{6}	37.0^{6}	
GCMC PHAST*									30^{18}
MOF	**M-btt**								
Exp.		36.7^{19}		51.2^{19}			30.7^{19}		
vdW-DF+ U		(36.6)^{19}		(51.7)^{19}			(29.4)19		

Table S 2 Calculated $-\Delta E$ and ($-\Delta H$, $-Q_{st}$) values for H_2 in relation to the different OMS, using computational methods in comparison to $-Q_{st}^0$ from experimental studies.

MOF	**M-MOF-74**							
OMS	**Mg**	**Cr**	**Mn**	**Fe**	**Co**	**Ni**	**Cu**	**Zn**
Exp.	10.1-10.7^{20,24}		8.8^{21,24}	9.7^{21}	10.7^{21,24}	12.9-13.5^{22,23,24}	6.1^{28}	8.5-8.8^{24},^{25}
DL	(6.5)^{20}							
BSS	(6.0)^{20}							
BSSP	(10.9)^{20}				(12.4)^{26}	(14.0)^{26}	(6.5)^{27}	(8.7)^{26}
LDA	24.8^{24}		22.4^{24}		35.6^{24}	39.0^{24}		22.0^{24}
GGA-PBE	12.4^{24}		11.1^{24}		12.8^{24}	15.0^{24}		10.5^{24}
PBE+D			13.9^{28}				11.3^{28}	
vdW-DF2	(10.0)^{29}	(6.0)^{29}	(8.0)^{29}	(9.0)^{29}	(9.0)^{29}	(10.0)^{29}	(6.0)^{29}	(8.0)^{29}
MOF	**MOF-505**							
Exp.							6.1^{24,30}	
PBE							13.4^{31}	

Table S 3 Calculated −ΔE and (−ΔH, $-Q_{st}$) values for C_2H_2, CO, CH_4 in relation to the different OMS, using computational methods in comparison to $-Q_{st}^0$ from experimental studies.

C_2H_2									
MOF	**M-MOF-74**								
OMS	**Mg**	**Cr**	**Mn**	**Fe**	**Co**	**Ni**	**Cu**	**Zn**	
Exp.	41.0[32]			45.0-46.5[32,33]	45.0[32]				30.4-39.0[32,34]
DFT-PBE									(30.0)[35]
vdW-DF2	(38.0)[29]	(31.0)[29]	(38.0)[29]	(37.0)[29]	(36.0)[29]	(37.0)[29]	(20.0)[29]	(35.0)[29]	
	Cu-paddle-wheel-MOFs								
MOF	**MOF-505**	**PCN-46**	**NJU-Bai12**	**ZJU-40**	**NOT-101**	**NOT-102**	**NOT-103**	**NOT-106**	**NOT-108**
Exp.	24.7[38,36]			34.5[38,37]	37.1[38,36]	22.0[38,37]	30.8[38,36]		
GCMC	(27.7)[38]	(24.1)[38]	(22.9)[38]	(23.9)[38]	(23.8)[38]	(24.7)[38]	(23.3)[38]	(25.5)[38]	(26.2)[38]
PBE	33.6[38]	34.8[38]	31.4[38]	30.8[38]	30.7[38]	33.7[38]	31.2[38]	31.8[38]	30.8[38]
CO									
MOF	**M-MOF-74**								
OMS	**Mg**	**Cr**	**Mn**	**Fe**	**Co**	**Ni**	**Cu**	**Zn**	
Exp.	38.0[3]				55.5[3]	59.7[3]			
B3LYP-D*	(30.0)[14]					(41.9)[14]		(24.8)[14]	
vdW-DF2	(35.0)[29]	(20.0)[29]	(29.0)[29]	(30.0)[29]	(30.0)[29]	(34.0)[29]	(16.0)[29]	(25.0)[29]	
B3LYP+D*/MP 2	(41.2)[14]					(50.3)[14]		(39.8)	
MOF	**MIL-101**								
Exp.									
ωB97X-D		(37.4)[9]							
CH_4									
MOF	**M-MOF-74**								
Exp.	18.2[6]		18.2[6]		19.2[6]	19.0[6]		18.3[39]	
vdW-DF2+U	(19.0)[29]	(14.0)[29]	(19.0)[29]	(19.0)[29]	(18.0)[29]	(19.0)[29]	(14.0)[29]	(19.0)[29]	
MOF	**HKUST-1**								
DFT/CC-PES							13.23[40]		

4

---

1 J. M. Simmons, H. Wu, W. Zhou and T. Yildirim, E*nergy Environ. Sci.*, 2011, **4**, 2177–2185.
2 D. Britt, H. Furukawa, B. Wang, T. G. Glover and O. M. Yaghi, *PNAS*, 2009, **106**, 20637–20640.
3 H. Kim, M. Sohail, K. Yim, Y. C. Park, D. H. Chun, H. J. Kim, S. O. Han and J.-H. Moon, *ACS Appl. Mater. Interfaces*, 2019, **11**, 7014-7021.
4 S. R. Caskey, A. G. Wong-Foy and A. J. Matzger, *J. Am. Chem. Soc.*, 2008, **130**, 10870-10871.
5 L. Grajciar, A. D. Wiersum, P. L. Llewellyn, J.-S. Chang and P. Nachtigall, *J. Phys. Chem. C*, 2011, **115**, 17925–17933.
6 D. Yu, A. O. Yazaydin, J. R. Lane, P. D. C. Dietzel and R. Q. Snurr, *Chem. Sci.*, 2013, **4**, 3544–3556.
7 M. K. Rana, H. S. Koh, J. Hwang and D. J. Siegel, J. Phys. Chem. C, 2012, **116**, 16957–16968.
8 H. Wu, J. M. Simmons, G. Srinivas, W. Zhou and T. Yildirim, *J. Phys. Chem. Lett.*, 2010, **1**, 1946–1951.
9 K. Yu, K. Kiesling and J. R. Schmidt, *J. Phys. Chem. C*, 2012, **116**, 20480–20488.
10 B. Vlaisavljevich, J. Huck, Z. Hulvey, K. Lee, J. A. Mason, J. B. Neaton, J. R. Long, C. M. Brown, D. Alfè, A. Michaelides and B. Smit, *J. Phys. Chem. A*, 2017, **12**1, 4139–4151.
11 L. Grajciar, P. Nachtigall, O. Bludský and M. Rubeš, J. Chem. Theory Comput., 2015, **11**, 230–238.
12 E. Haldoupis, J. Borycz, H. Shi, K. D. Vogiatzis, P. Bai, W. L. Queen, L. Gagliardi and J. I. Siepmann, *J. Phys. Chem. C*, 2015, **119**, 16058-16071.
13 L. Valenzano, B. Civalleri, S. Chavan, G. T. Palomino, C. O. Arean and S. Bordiga, *J. Phys. Chem. C*, 2010, **114**, 11185–11191.
14 L. Valenzano, B. Civalleri, K. Sillar and J. Sauer, *J. Phys. Chem. C,* 2011, **115**, 21777–21784.
15 R. Poloni, B. Smit and J. B. Neaton, *J. Phys. Chem. A*, 2012, **116**, 4957–4964.
16 G. Alonso, D. Bahamon, F. Keshavarz, X. Giménez, P. Gamallo and R. Sayós, *J. Phys. Chem. C*, 2018, **122**, 3945–3957.
17 W. L. Queen, M. R. Hudson, E. D. Bloch, J. A. Mason, M. I. Gonzalez, J. S. Lee, D. Gygi, J. D. Howe, K. Lee, T. A. Darwish, M. James, V. K. Peterson, S. J. Teat, B. Smit, J. B. Neaton, J. R. Long and C. M. Brown, *Chem. Sci.*, 2014, **5**, 4569–4581.
18 T. Pham, K. A. Forrest, D. M. Franz, Z. Guo, B. Chen and B. Space, P*hys. Chem. Chem. Phys.*, 2017, **19**, 18587–18602.
19 M. Asgari, S. Jawahery, E, D. Bloch, M. R. Hudson, R. Flacau, B. Vlaisavljevich, J. R. Long, C. M. Brown and W. L. Queen, *Chem. Sci.*, 2018, **9**, 4579-4588.
20 T. Pham, K. A. Forrest, K. McLaughlin, J. Eckert and B. Space, *J. Phys. Chem. C*, 2014, **118**, 22683–22690.
21 D. Gygi, E. D. Bloch, J. A. Mason, M. R. Hudson, M. I. Gonzalez, R. L. Siegelman, T. A. Darwish, W. L. Queen, C. M. Brown and J. R. Long, *Chem. Mater.*, 2016, **28**, 1128–1138.
22 P. D. C. Dietzel, P. A. Georgiev, J. Eckert, R. Blom, T. Strassle and T. Unruh, Chem. Commun., 2010, **46**, 4962–4964.
23 J. G. Vitillo, L. Regli, S. Chavan, G. Ricchiardi, G. Spoto, P. D. C. Dietzel, S. Bordiga, and A. Zecchina, *J. Am. Chem. Soc.*, 2008, **130**, 8386–8396.
24 W. Zhou, H. Wu and T. Yildirim, *J. Am. Chem. Soc.*, 2008, **130**, 15268–15269.
25 Y. Liu, H. Kabbour, C. M. Brown, D. A. Neumann and C. C. Ahn, *Langmuir*, 2008, **24**, 4772–4777.
26 T. Pham, K. A. Forrest, R. Banerjee, G. Orcajo, J. Eckert and B. Space, *J. Phys. Chem. C*, 2015, **119**, 1078-1090.
27 T. Pham, K. A. Forrest, J. Eckert and B. Space, *Cryst. Growth Des.*, 2016, **16**, 867–874.
28 M. H. Rosnes, M. Opitz, M. Frontzek, W. Lohstroh, J. Peter Embs, P. A. Georgiev and P. D. C. Dietzel, J. *Mater. Chem. A*, 2015, **3**, 4827-4839.
29 K. Lee, J. D. Howe, L.-C. Lin, B. Smit and J. B. Neaton, Chem. Mat., 2015, **27**, 668-678.
30 Y. Yan, X. Lin, S. Yang, A. J. Blake, A. Dailly, N. R. Champness, P. Hubberstey and M. Schröder, *Chem. Commun.*, 2009, 1025-1027.
31 Q. Yang and C. Zhong, *J. Phys. Chem. B*, 2006, **110**, 655-658.
32 Y. He, R. Krishna and B. Chen, *Energy Environ. Sci.*, 2012, **5**, 9107–9120.
33 A. Luna-Triguero, J. M. Vicent-Luna, R. M. Madero-Castro, P. Gómez-Álvarez and S. Calero, *ACS Appl. Mater. Interfaces*, 2019, **11**, 31499–31507.
34 S. Xiang, W. Zhou, J. M. Gallegos, Y. Liu and B. Chen, *J. Am. Chem. Soc.*, 2009, **131**, 12415–12419.
35 M. Fischer, F. Hoffmann and M. Fröba, *ChemPhysChem*, 2010, **11**, 2220–2229.
36 Y He, B. Li, M. O'Keeffe and B. Chen, Chem. Soc. Rev., 2014, **43**, 5618–5656.
37 H.-M. Wen, H. Wang, B. Li, Y. Cui, H. Wang and G. Qian, *Inorg. Chem.*, 2016, **55**, 7214–7218.
38 Y. Ji, L. Ding, Y. Cheng, H. Zhou, S. Yang, F. Li and Y. Li, *J. Phys. Chem. C*, 2017, **121**, 24104–24113.
39 H.Wu, W. Zhou and T. Yildirim, *J. am. Chem. Soc.*, 2009, **131**, 4995–5000.
40 L. Chen, L. Grajciar, P. Nachtigall and T. Düren, *J. Phys. Chem. C*, 2011, **115**, 23074–23080.

3.2 Veröffentlichung als Co-Autorin

3.2.1 Wassersorptionsuntersuchungen

Im Folgenden werden zu der Veröffentlichung eine kurze Zusammenfassung und eine Beschreibung der Eigenanteile gegeben. Es wurden PXRDs und Wassersorptionsisothermen aufgenommen.

Rana Dalapati,[a] Ülkü Kökçam-Demir,[b] Christoph Janiak[b], Shyam Biswas*[a],

The effect of functional groups in the aqueous-phase selective sensing of Fe(III) ions by thienothiophene-based zirconium metal-organic frameworks and the design of molecular logic gates;

Dalton Trans., 2018, **47**, 1159–1170.
DOI: 10.1039/C7DT04130F, Referenz [207]

In dieser Arbeit wird die solvothermale Synthese von vier Zr-basierten MOFs mit Thienothiophen-basierten Liganden vorgesellt. Die Liganden wurden systematisch mit Methyl- und Phenylgruppen zur Abstimmung des Fluoreszenz- und hydrophoben Verhaltens der MOFs modifiziert. Diese Thienothiophen-basierten MOFs zeigen eine hohe Selektivität und Sensitivität beim Nachweis von Fe^{3+}-Ionen in rein wässrigem Medium.

Tabelle 2 Ergebnisse der H_2O-Sorptionsmessungen von 1´, 2´, 3´, 4´. Reproduziert von Ref. 207 mit Genehmigung, The Royal Society of Chemistry, © 2018.

MOF	**Water loading ($g \cdot g^{-1}$)**	
	at $p/p_0 = 0.5$	at $p/p_0 = 0.9$
1´	0.30	0.39
2´	0.21	0.35
3´	0.06	0.31
4´	0.04	0.16

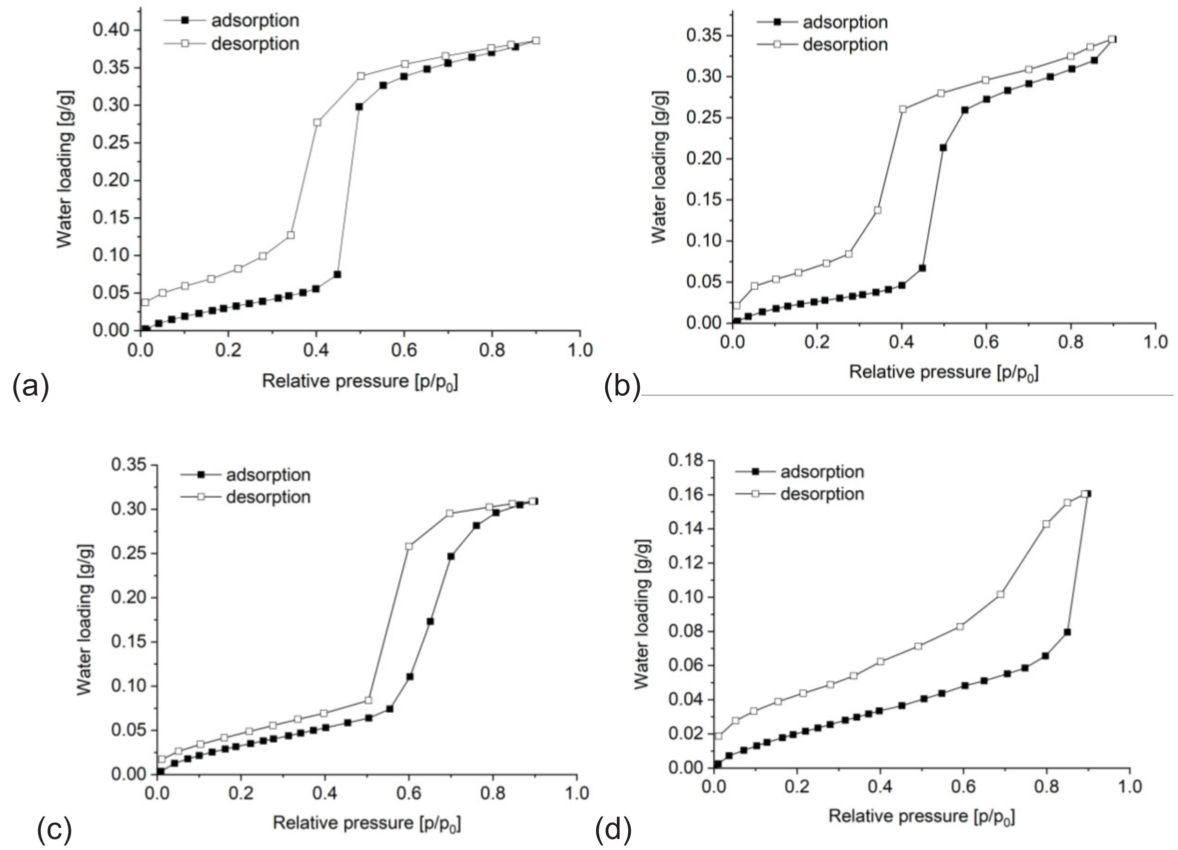

(a) (b) (c) (d)

Abbildung 20 H_2O-Sorptionsisothermen von (a) 1´, (b) 2´, (c) 3´ und (d) 4´ bei 20 °C. Reproduziert von Ref. 207 mit Genehmigung, The Royal Society of Chemistry, © 2018.

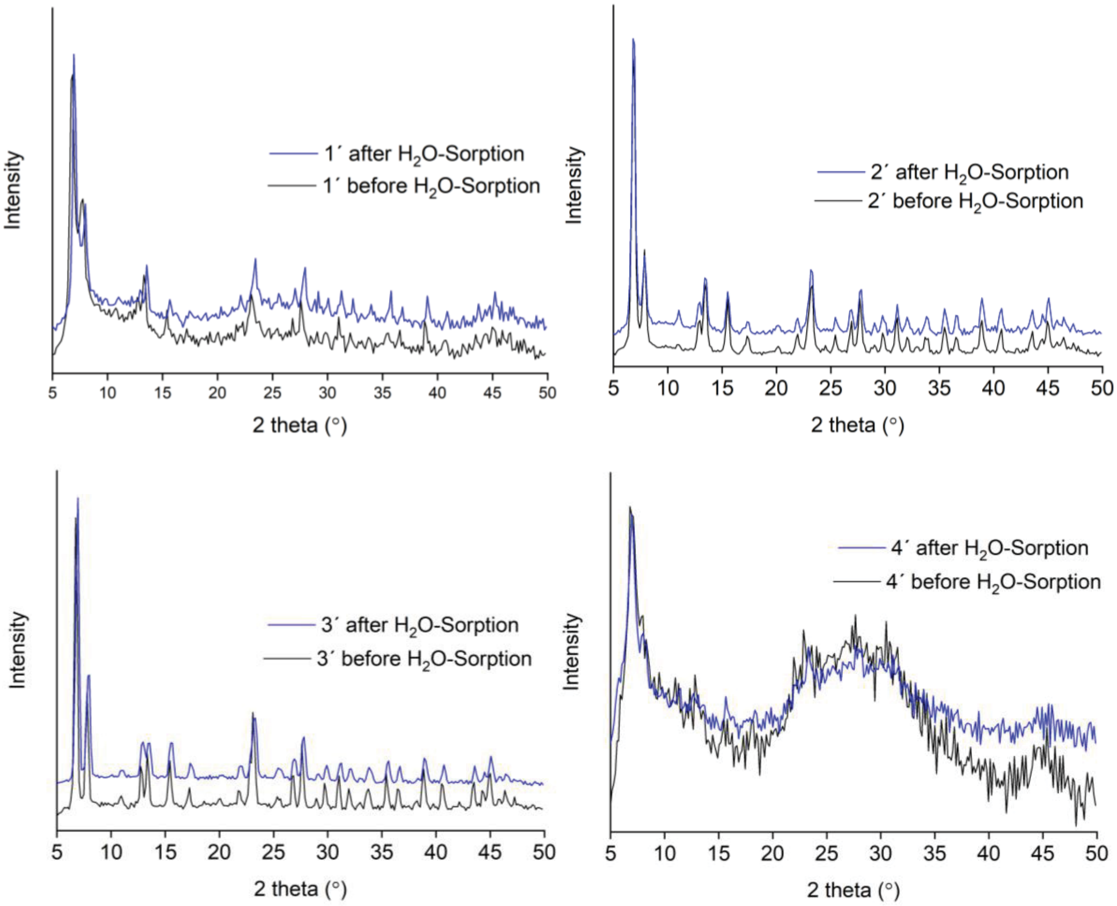

Abbildung 21 PXRDs von 1´, 2´, 3´, 4´ vor und nach den Wassersorptionsmessungen. Reproduziert von Ref. 207 mit Genehmigung, The Royal Society of Chemistry, © 2018.

Anteil an der Publikation:

- Die Probenvorbereitung und Messung der Proben 1´, 2´, 3´, 4´mittels PXRD, Stickstoff- und Wassersorption.
- Die Auswertung, Darstellung und Interpretation der PXRD- und Wassersorptions-Ergebnisse.
- Die Verschriftlichung des Abschnitts „*Hydrophobic properties*“; insbesondere PXRD- und Wassersorptions-Ergebnisse.
- Die Anfertigung der Tabelle 1 „*Water loading* (g·g^{-1})“.
- Die Überarbeitung und Korrektur des Abschnitts „*Hydrophobic properties*“ erfolgte durch Herrn Prof. Dr. Christoph Janiak.
- Die Durchsicht und Korrektur des finalen Manuskriptes als Co-Autorin.

3.2.2 Strukturuntersuchungen mittels Röntgenpulverdiffraktometrie

Im Rahmen dieser Dissertation wurde das Röntgenpulverdiffraktometer *Bruker D2 PHASER* durch mich betreut. Für verschiedene Veröffentlichungen wurden Materialien mittels Röntgenpulverdiffraktometrie untersucht. Im Folgenden werden zu diesen Veröffentlichungen eine kurze Zusammenfassung gegeben, PXRDs dargestellt und die jeweiligen Eigenanteilen aufgelistet. Die Publikationen werden in zeitlich chronologischer Reihenfolge aufgezeigt.

Mathias Getzlaff, Miriam Leifels, Paula Weber, Ülkü Kökçam-Demir, Christoph Janiak,

Magnetic nanoparticles in toner material;

Nano-Structures & Nano-Objects, 2020, **22,** 100462.
DOI: 10.1016/j.nanoso.2020.100462, Referenz [208]

In dieser Arbeit werden verschiedene Tonermaterialien, die in Drucker bzw. Kopierer verwendet werden, hinsichtlich Materialzusammensetzung, Form, Größe und Kristallinität untersucht. Es wird gezeigt, dass aus den Tonermaterialien magnetische Nanopartikeln erhalten werden können.

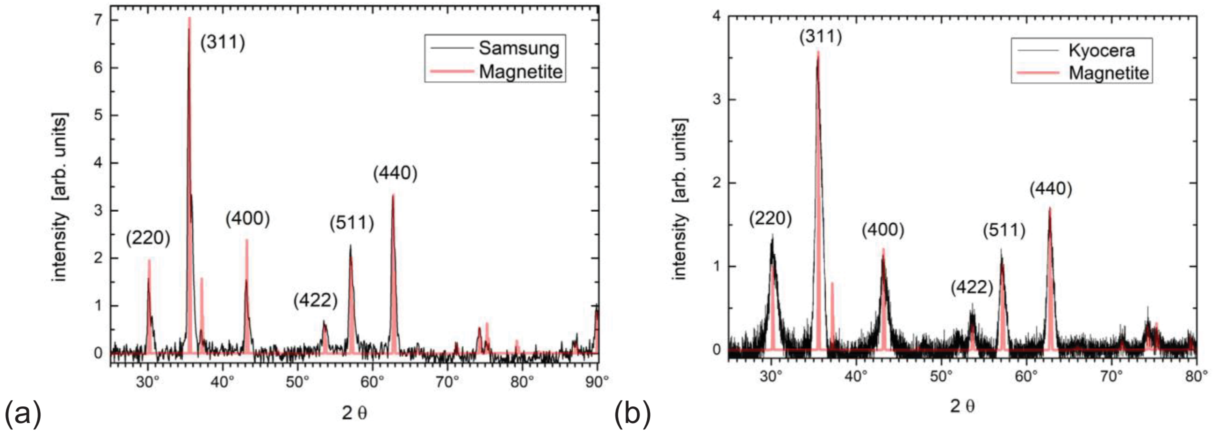

Abbildung 22 PXRDs von (a) Samsung, (b) Kyrocera Tonermaterialien nach Hintergrundsubtraktion und Magnetit (RRUFF ID: R061111.9). Nachdruck von Ref. 208 mit Genehmigung, Elsevier B.V., © 2020.

Anteile an der Publikation:

- Die Probenvorbereitung und Durchführung der PXRD-Messungen.
- Recherche: PXRD von Magnetit, RRUFF ID: R061111.9.
- Die Durchsicht und Korrektur des finalen Manuskriptes als Co-Autorin.

Philippe Belle Ebanda Kedi, Chick Christian Nanga, Awawou Paboudam Gbambie, Vandi Deli, Francois Eya'ane Meva, Hamza Elsayed Ahmed Mohamed, Agnes Antoinette Ntoumba, Moise Henri Julien Nko'o, Ülkü Kökçam-Demir, Bastian Moll, Houatchaing Kouemegne Armelle Michelle, Peter Teke Ndifon, Emmanuel Albert Mpondo Mpondo, Alain Bertrand Dongmo, Christoph Janiak, Malik Maaza,

Biosynthesis of Silver Nanoparticles from Microsorum Punctatum (L.) Copel Fronds Extract and an In-Vitro Anti-Inflammation Study;

J. Nanotechnol. Res., 2020, **2**, 025–041.
DOI: 10.26502/jnr.2688-85210014, Referenz [209]

In dieser Arbeit wird die Synthese von Silber-Nanopartikeln (AgNPs) unter Verwendung des Pflanzenextraktes *Microsorum punctatum* vorgestellt. Die entstandenen Partikeln wurden auf die entzündungshemmende Wirkung hin untersucht. Es konnte eine positive Wirkung gegenüber Proteindenaturierung festgestellt werden.

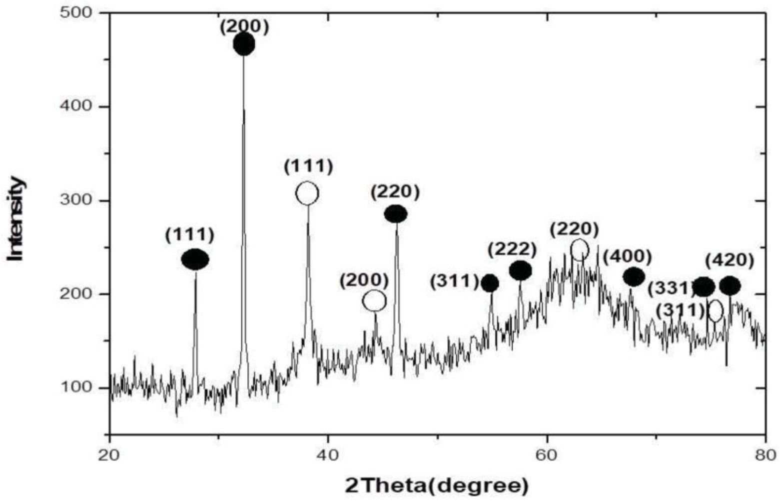

Abbildung 23 PXRD von Silber-Nanopartikeln. Nachdruck von Ref. 209 mit Genehmigung, Fortune Journals, © 2020.

Anteile an der Publikation:

- Unterstützung bei den PXRD-Messungen an der Heinrich-Heine-Universität.
- Die Durchsicht und Korrektur des finalen Manuskriptes als Co-Autorin.

Dana Bejan, Lucian Gabriel Bahrin, Sergiu Shova, Narcisa Laura Marangoci, Ülkü Kökçam-Demir, Vasile Lozan, Christoph Janiak,

New Microporous Lanthanide Organic Frameworks. Synthesis, Structure, Luminescence, Sorption, and Catalytic Acylation of 2-Naphthol;

Molecules, 2020, **25**, 3055.
DOI: 10.3390/molecules25133055, Referenz [210]

In dieser Arbeit werden die Synthesen von neuen Lanthan-, Cerium-, Neodym-, Europium-, Gadolinium-, Dysprosium- und Holmium-basierten Metall-organischen Gerüstverbindungen mit dem 1,3,5-Tris(4-carboxyphenyl)-2,4,6-trimethylbenzol-Liganden (H_3L) vorgestellt. Mittels Röntgeneinkristalldiffraktometrie konnten neue dreidimensionale MOFs mit der Summenformel $[LnL(H_2O)_2]_n \cdot xDMF \cdot yH_2O$ (Ln = La, Ce, Nd) aufgeklärt werden. Diese Ln-MOFs zeigen eine permanente Porosität mit spezifischen Oberflächen bis 400 $m^2 \cdot g^{-1}$, eine thermische Stabilität bis 500 °C und weisen katalytische Aktivitäten auf.

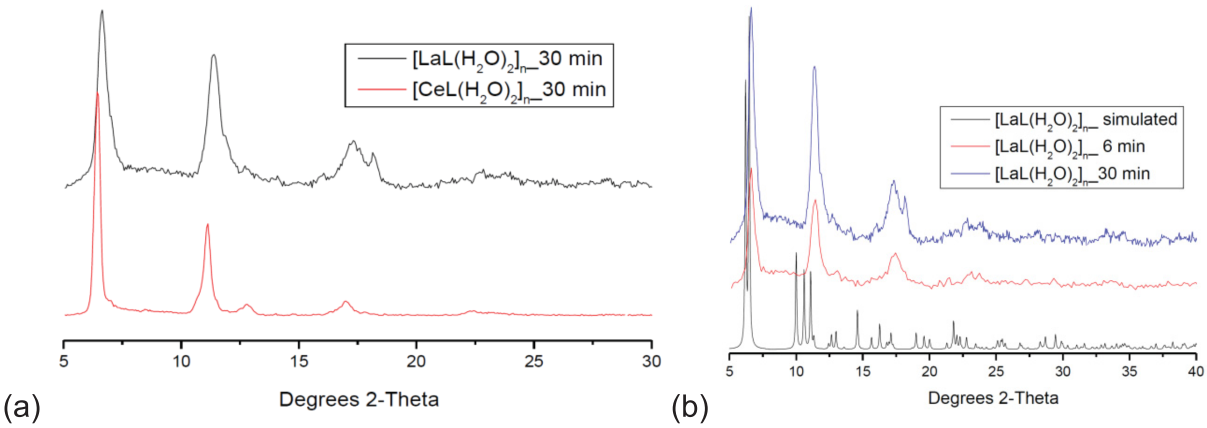

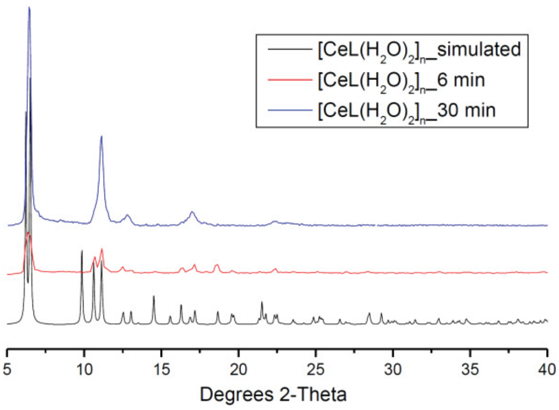
$[CeL(H_2O)_2]_n$_simulated
$[CeL(H_2O)_2]_n$_6 min
$[CeL(H_2O)_2]_n$_30 min
5
10
15
20
25
30
35
40
Degrees 2-Theta

(c)

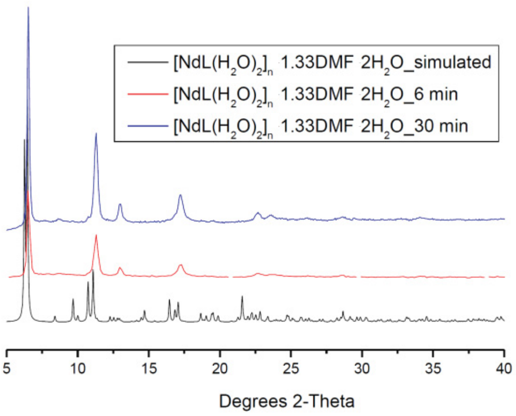
$[NdL(H_2O)_2]_n$ 1.33DMF $2H_2O$_simulated
$[NdL(H_2O)_2]_n$ 1.33DMF $2H_2O$_6 min
$[NdL(H_2O)_2]_n$ 1.33DMF $2H_2O$_30 min
5
10
15
20
25
30
35
40
Degrees 2-Theta

(d)

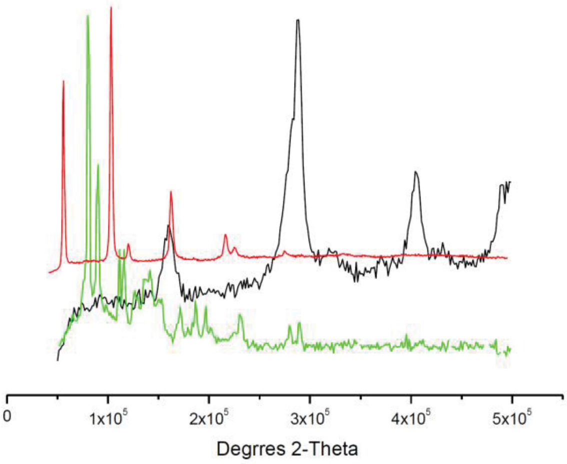
0
$1x10^5$
$2x10^5$
$3x10^5$
$4x10^5$
$5x10^5$
Degrres 2-Theta

(e)

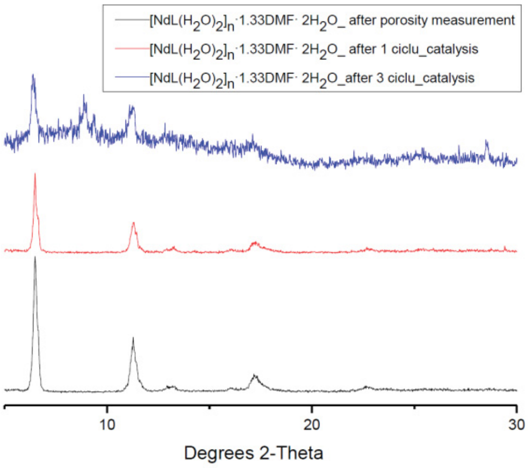
$[NdL(H_2O)_2]_n \cdot$1.33DMF$\cdot$ $2H_2O$_ after porosity measurement
$[NdL(H_2O)_2]_n \cdot$1.33DMF$\cdot$ $2H_2O$_ after 1 ciclu_catalysis
$[NdL(H_2O)_2]_n \cdot$1.33DMF$\cdot$ $2H_2O$_after 3 ciclu_catalysis
10
20
30
Degrees 2-Theta

(f)

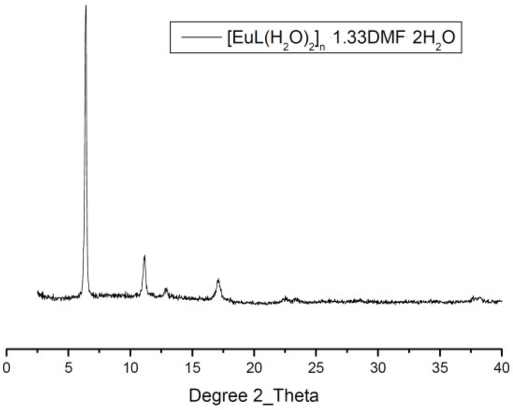
$[EuL(H_2O)_2]_n$ 1.33DMF $2H_2O$
0
5
10
15
20
25
30
35
40
Degree 2_Theta

(g)

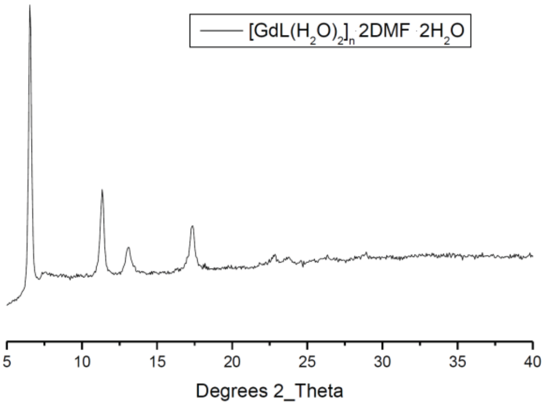
$[GdL(H_2O)_2]_n$ 2DMF $2H_2O$
5
10
15
20
25
30
35
40
Degrees 2_Theta

(h)

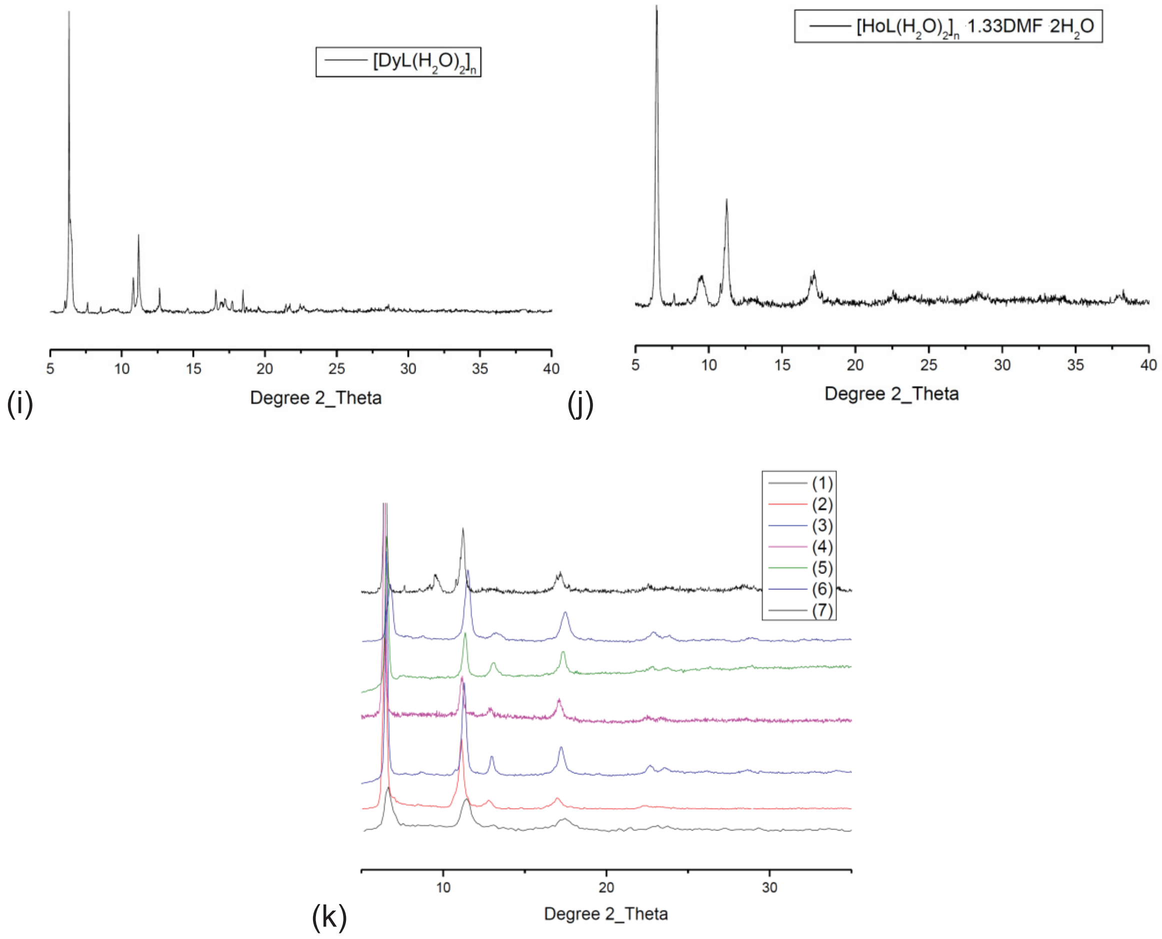

Abbildung 24 PXRDs von Ln-MOFs (a bis k). Nachdruck von Ref. 210 mit Genehmigung, MDPI, © 2020.

Anteile an der Publikation:

- Die Probenvorbereitung und Durchführung der PXRD-Messungen.
- Unterstützung bei der Auswertung der PXRDs an der Heinrich-Heine-Universität.
- Die Durchsicht und Korrektur des finalen Manuskriptes als Co-Autorin.

Phillipe Belle Ebanda Kedi, Berthe Ngangue Etah, Vandi Deli, Awawou Paboudam Gbambie, Agnes Antoinette Ntoumba, Ülkü Kökçam-Demir, Bastian Moll, Hamza Elsayed Ahmed Mohamed, Judith Caroline Ngo Nyobe, Chick Christian Nanga, Jean Yves Sikapi Fouda, Loick Pradel Kojom Foko, Emmanuel Edmond Tchoumbi, Armelle Michelle Houatchaing, Yvon Kevin Dimitri Manfred Kotto Modi, Francois Eya'ane Meva, Peter Teke Ndifon, Alain Bertrand Dongmo, Malik Maaza, Siegfried Didier Dibong, Emmanuel Albert Mpondo Mpondo, Christoph Janiak,

In vitro and in vivo anti-inflammatory activity of green synthesized silver nanoparticles from the aqueous bark extract of Mangifera indica Linn. (Anacardiaceae);

Int. J. Green Herbal Chem., 2020, **9**, 345–360.
DOI: 10.24214/IJGHC/HC/9/3/34560, Referenz [211]

In dieser Arbeit wird die Synthese von Silber-Nanopartikeln (AgNPs) unter Verwendung des Rindenextraktes *Mangifera indica* (MI) vorgestellt.

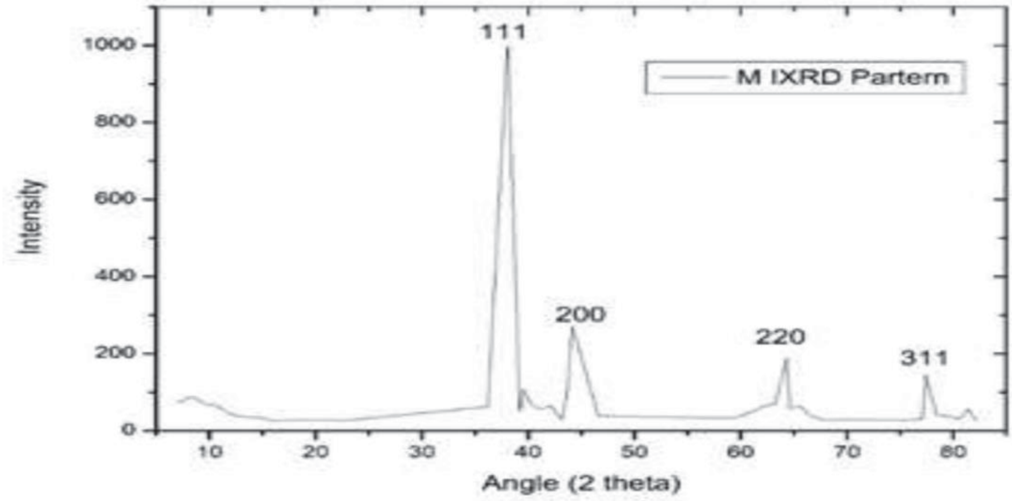

Abbildung 25 PXRD von MI-AgNPs. Nachdruck von Ref. 211 mit Genehmigung, IJGHC, © 2020.

Anteile an der Publikation:

- Unterstützung bei den PXRD-Messungen an der Heinrich-Heine-Universität.
- Die Durchsicht und Korrektur des finalen Manuskriptes als Co-Autorin.

Mohammed Enamullah, Kazi Saima Banu, Mohammed Anwar Hossain, Ülkü Kökçam-Demir,

High-spin bis[(S or R)-N-1-(Ar)ethyl-salicylaldiminato-κ^{2}N,O]-Λ/Δ-iron(II): Combined studies of syntheses, spectroscopy, diastereoselection, electrochemistry, paramagnetic, thermal, PXRD and DFT/TDDFT;

J. Mol. Struct., 2020, **1199**, 126947.
DOI: 10.1016/j.molstruc.2019.126947, Referenz [212]

In dieser Arbeit werden *high-spin* Bis[(*S* oder *R*)-N-1-(Ar)ethyl-salicylaldiminato-κ2N,O]-Λ/Δ-Eisen(II) Komplexe {Ar = C_6H_5 (Fe*S*L_1 oder Fe*R*L_1), *p*-OMeC_6H_4 (Fe*S*L_2 oder Fe*R*L_2) und *p*-BrC_6H_4 (Fe*S*L_3 oder Fe*R*L_3)} durch die Reaktion von (*S* oder *R*)-N-1-(Ar)ethyl-salicylaldimin (*S* oder *R*-HL) mit Eisen(II)-chlorid vorgestellt.

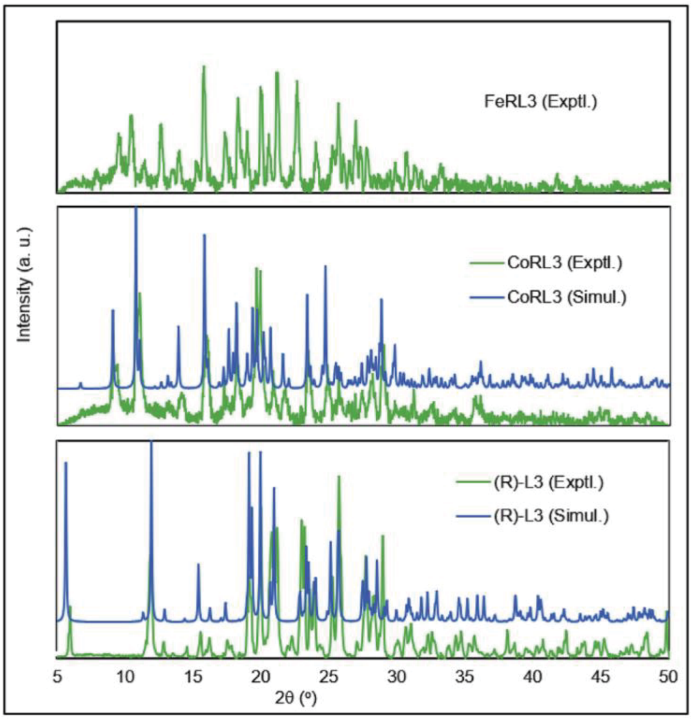

Abbildung 26 PXRDs von (*R*)-L_3, Co*R*L_3 und Fe*R*L_3. Nachdruck von Ref. 212 mit Genehmigung, Elsevier B.V., © 2019.

Anteile an der Publikation:

- Unterstützung bei den PXRD-Messungen an der Heinrich-Heine-Universität.

- Die Durchsicht und Korrektur des finalen Manuskriptes als Co-Autorin.

Mathias Getzlaff, Miriam Leifels, Paula Weber, Ülkü Kökçam-Demir, Christoph Janiak,

Nanoparticles in toner material;

SN Appl. Sci., 2019, **1:489**.
DOI: 10.1007/s42452-019-0501-9, Referenz [213]

In dieser Arbeit werden verschiedene Tonermaterialien, die in Drucker bzw. Kopierer, verwendet werden, hinsichtlich Materialzusammensetzung, Form, Größe und Kristallinität untersucht. Es wird gezeigt, dass aus den Tonermaterialien Siliciumdioxid- und amorphe Kohlenstoff-Nanopartikeln erhalten werden können.

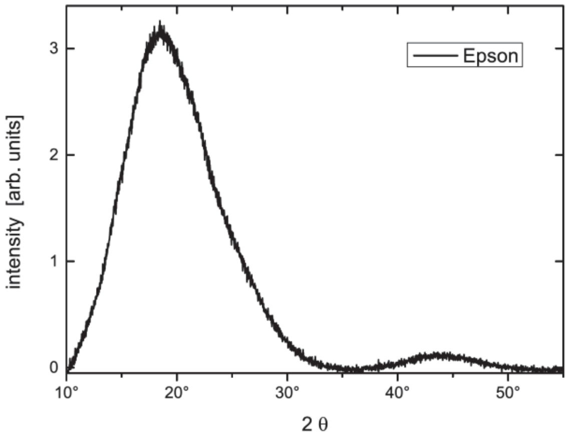

Abbildung 27 PXRDs von Epson – Tonermaterial nach Hintergrundsubtraktion. Nachdruck von Ref. 213 mit Genehmigung, SN Applied Sciences, © 2019.

Anteile an der Publikation:

- Die Probenvorbereitung und Durchführung der PXRD-Messung.
- Die Durchsicht und Korrektur des finalen Manuskriptes als Co-Autorin.

Francois Eya'ane Meva, Joel Olivier Avom Mbeng, Cecile Okalla Ebongue, Carsten Schlüsener, Ülkü Kökçam-Demir, Agnes Antoinette Ntoumba, Phillipe Belle Ebanda Kedi, Etienne Elanga, Evrard-Rudy Njike Loudang, Moise Henri Julien Nko'o, Edmond Tchoumbi, Vandi Deli, Christian Chick Nanga, Emmanuel Albert Mpondo Mpondo, Christoph Janiak,

Stachytarpheta cayennensis Aqueous Extract, a New Bioreactor towards Silver Nanoparticles for Biomedical Applications;

J. Biomater. Nanobiotechnol., 2019, **10**, 102–119.
DOI: 10.4236/jbnb.2019.102006, Referenz [214]

In dieser Arbeit wird die Synthese und Charakterisierung von Silber-Nanopartikeln vorgestellt. Die Silber-Nanopartikeln wurden unter Verwendung des wässrigen Extrakts von *Stachytarpheta cayennensis* hergestellt und auf die entzündungshemmende und antioxidativen Eigenschaften hin analysiert.

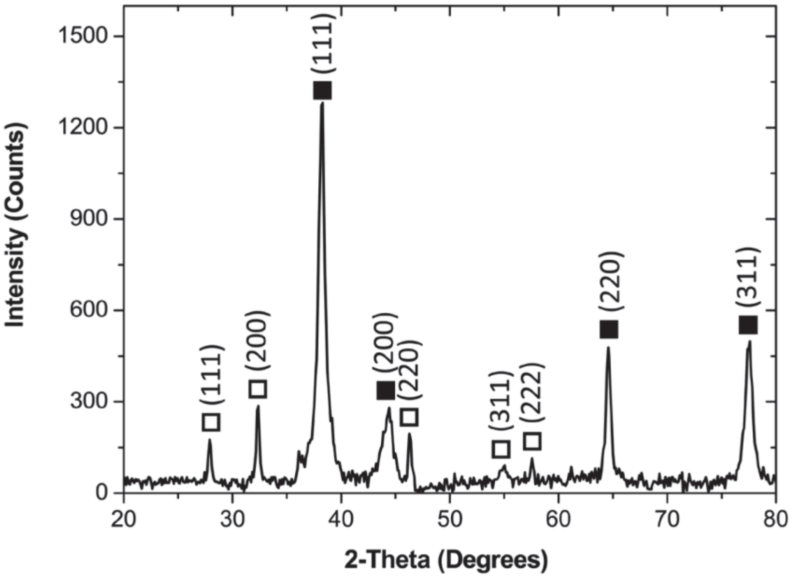

Abbildung 28 PXRD von Silber-Nanopartikeln. Nachdruck von Ref. 214 mit Genehmigung, Scientific Research Publishing Inc., © 2019.

Anteile an der Publikation:

- Unterstützung bei den PXRD-Messungen an der Heinrich-Heine-Universität.
- Die Durchsicht und Korrektur des finalen Manuskriptes als Co-Autorin.

Francois Eya'ane Meva, Agnes Antoinette Ntoumba, Philippe Belle Ebanda Kedi, Edmond Tchoumbi, Alexa Schmitz, Laura Schmolke, Maximilian Klopotowski, Bastian Moll, Ülkü Kökçam-Demir, Emmanuel Albert Mpondo Mpondo, Leopold Gustave Lehman, Christoph Janiak,

Silver and palladium nanoparticles produced using a plant extract as reducing agent, stabilized with an ionic liquid: sizing by X-ray powder diffraction and dynamic light scattering;

J. Mater. Res. Technol., 2019, **8**, 1991–2000.
DOI: 10.1016/j.jmrt.2018.12.017, Referenz [215]

In dieser Arbeit wird die Synthese und Charakterisierung von Silber- und Palladium-Nanopartikeln vorgestellt. Die Nanopartikeln wurden unter Verwendung des wässrigen Avocado-Pflanzenextrakts von *Persea americana* (PA) hergestellt. Zur Stabilisierung der Nanopartikeln wurde die ionische Flüssigkeit 1-Ethyl-3-Methylimidazolium Tosylat ([EMIm][Tos]) zugegeben.

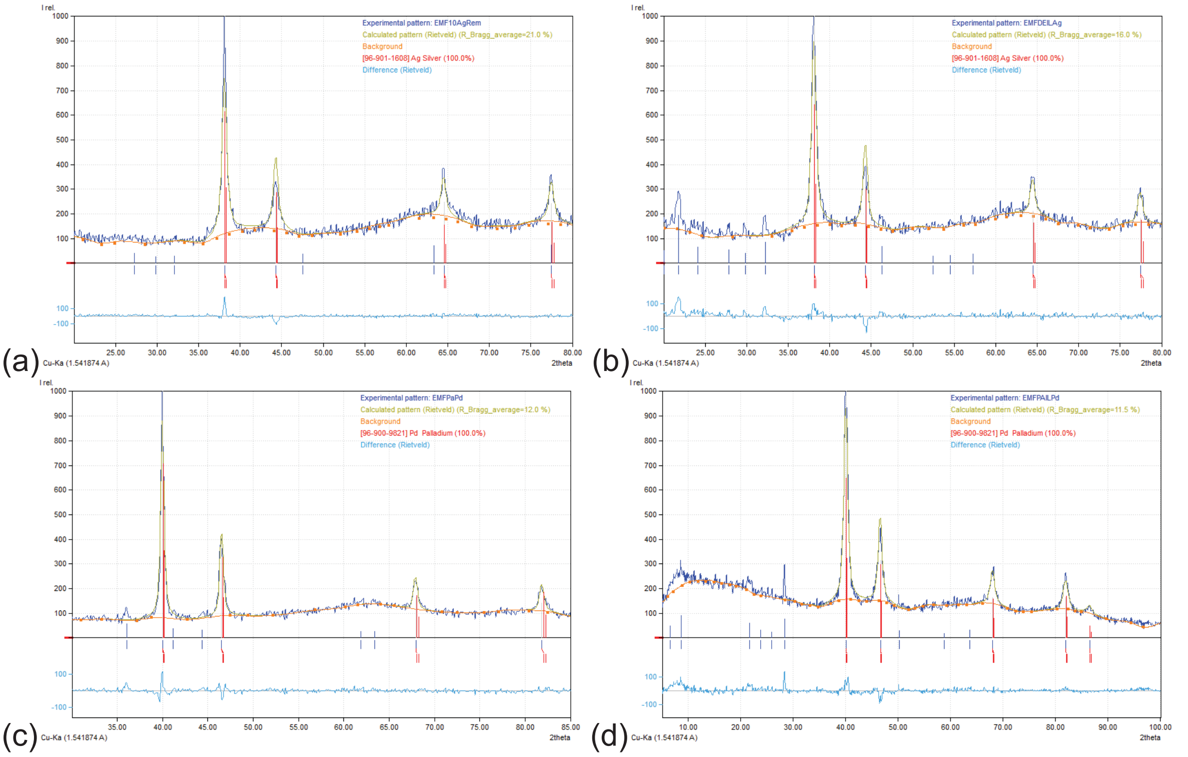

Abbildung 29 PXRDs von (a) EMF10AgRem, (b) EMFDEILAg, (c) EMFPaPd und (d) EMFPAILPd. Nachdruck von Ref. 215 mit Genehmigung, Elsevier Editora Ltda., © 2019.

Anteile an der Publikation:

- Unterstützung bei den PXRD-Messungen an der Heinrich-Heine-Universität.
- Die Durchsicht und Korrektur des finalen Manuskriptes als Co-Autorin.

Bernd Engelkamp, Mhamed El Achhab, Björn Fischer, Ülkü Kökçam-Demir, Klaus Schierbaum,

Combined Galvanostatic and Potentiostatic Plasma Electrolytic Oxidation of Titanium in Different Concentrations of H_2SO_4,

Metals, 2018, **8**, 386.
DOI: 10.3390/met8060386, Referenz [216]

In dieser Arbeit wird die plasmaelektrolytische Oxidation von Titan vorgestellt.

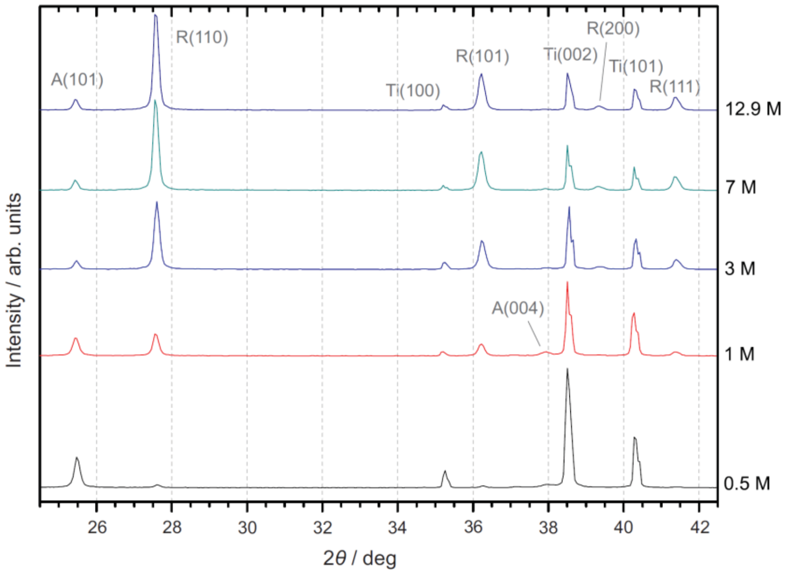

Abbildung 30 PXRDs von Proben mit unterschiedlicher H_2SO_4-Konzentration. Nachdruck von Ref. 216 mit Genehmigung, MDPI, © 2018.

Anteile an der Publikation:

- Unterstützung bei den PXRD-Messungen an der Heinrich-Heine-Universität.
- Die Durchsicht des finalen Manuskriptes als Co-Autorin.

4 Unveröffentlichte Ergebnisse

In den folgenden Kapiteln werden weitere Ergebnisse dargestellt und diskutiert. Diese Ergebnisse wurden bislang nicht in wissenschaftlichen Veröffentlichungen publiziert.

4.1 Weitere Untersuchungen zu Al-MOFs Kompositen

Al-MOF-GO Komposite wurden in der Veröffentlichung „*Improving porosity and water uptake of aluminum metal-organic frameworks (Al-MOFs) as graphite oxide (GO) composites*“ in Kapitel 3.1.1 dargestellt. Hierzu werden in Kapitel 4.1.1 ergänzende Ergebnisse zur Untersuchung der thermischen Stabilität von GO in Syntheselösungen und -bedingungen aufgezeigt und beschrieben.

Des Weiteren werden in Kapitel 4.1.2 in Anlehnung an die Veröffentlichung in Kapitel 3.1.1 neue Komposite aus MIL-100(Al) mit Aeroperl® und Aerosil® dargestellt.

4.1.1 Thermische Stabilität von Graphitoxid in Lösung

Über die thermische Stabilität von GO im Vakuum bei verschiedenen Temperaturen wurde bereits in Kapitel 3.1.1 berichtet.

Um die thermische Stabilität von GO in Syntheselösungen zu untersuchen, wurde das GO zunächst mit Wasser, wie bei der Synthese von MIL-100(Al) und MIL-100(Al)-GO Kompositen, versetzt und bei 60 °C, 100 °C, 140 °C und 190 °C für je 10 Minuten in der Mikrowelle behandelt und anschließend getrocknet. Zusätzlich wurde das GO mit einem Lösungsmittelgemisch aus Wasser und DMF (4:1), wie bei der Synthese von CAU-10-H und CAU-10-H-GO Kompositen, versetzt und bei 60 °C, 100 °C, 135 °C und 180 °C für jeweils 24 h unter Rückfluss erhitzt und getrocknet.

Im Anschluss wurden PXRDs (Abbildung 31) und IR-Spektren (Abbildung 32) aufgenommen.

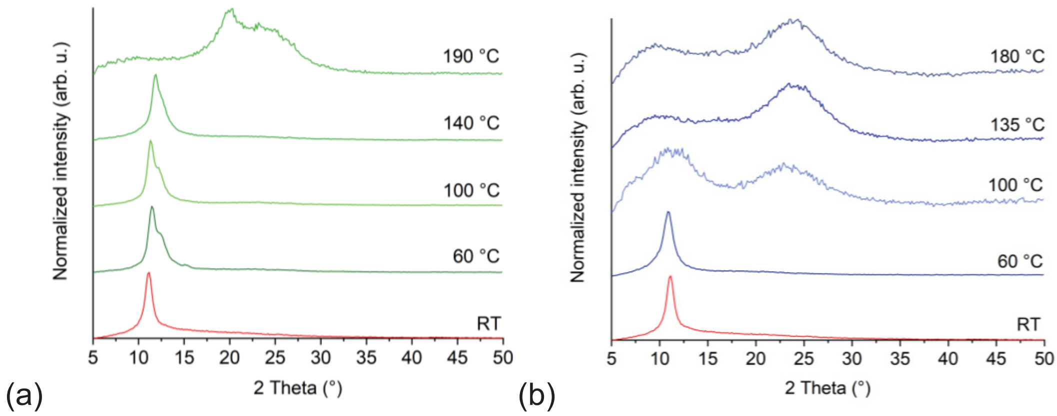

Abbildung 31 PXRDs von (a) GO, welches bei unterschiedlichen Temperaturen in Wasser für 10 min in der Mikrowelle zur Reaktion gebracht wurde, (b) GO, welches bei unterschiedlichen Temperaturen in einer Wasser/DMF-Lösung (4:1) unter Rückfluss erhitzt wurde. Das rote Diffraktogramm ist von GO, welches bei Raumtemperatur gelagert wurde.

Die PXRDs in Abbildung 31a zeigen ab 60 °C eine Verbreitung des Reflexes bei ca. 11 ° 2 Theta und bei 190 °C eine Veränderung des Diffraktogrammes im Vergleich zu unbehandeltem GO (rotes Diffraktogramm). Der Reflex bei ca. 23 ° 2 Theta wird TRGO (thermisch reduziertes GO) zugeschrieben. Die PXRDs in Abbildung 31b zeigen ab 100 °C die Veränderungen der Diffraktogramme und das Entstehen von TRGO. In Abbildung 32a,b werden die IR-Spektren gezeigt.

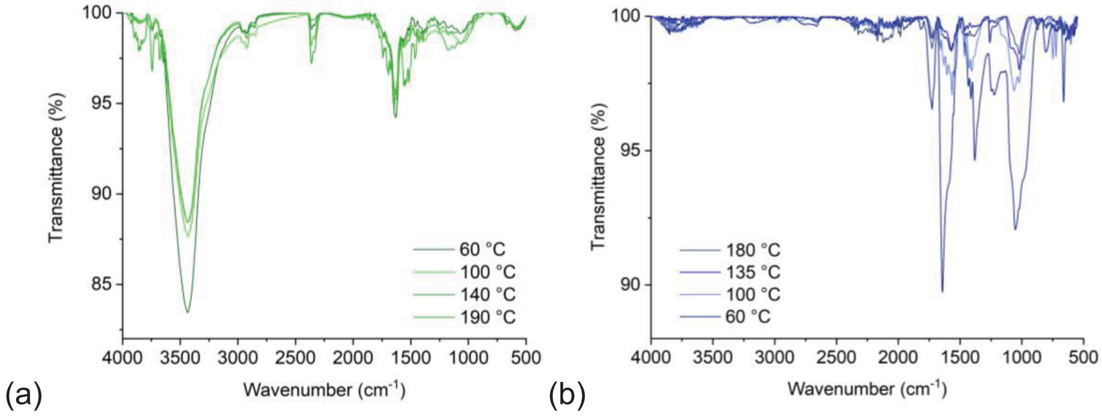

Abbildung 32 IR-Spektren von (a) GO, welches bei unterschiedlichen Temperaturen in Wasser für 10 min in der Mikrowelle zur Reaktion gebracht wurde und (b) GO, welches bei unterschiedlichen Temperaturen in einer Wasser/DMF-Lösung (4:1) unter Rückfluss erhitzt wurde.

Anteile an den Ergebnissen – Thermische Stabilität von Graphitoxid in Lösung:

- Thermische Untersuchungen von GO in Lösungsmitteln (analog zur Synthese von MIL-100(Al) und MIL-100(Al)-GO Kompositen wurden eigenständig durchgeführt; analog zur Synthese von CAU-10-H und CAU-10-H-GO Kompositen wurden von Herrn Marco Bengsch (Bachelorarbeit) durchgeführt. Die Auswertung und Darstellung der PXRD und IR-Ergebnisse wurden eigenständig vorgenommen.
- Die GO-Synthese nach der Hummers Methode wurde von Herrn Dr. Niels Tannert durchgeführt. Die Auswertung, Darstellung und Verschriftlichung der Ergebnisse wurden eigenständig vorgenommen.
- Die eigenständige Konzipierung, Erstellung der Abbildungen, Aufarbeitung und Verschriftlichung der kompletten experimentellen Ergebnisse.
- Im Rahmen seiner Bachelorarbeit hat Herr Marco Bengsch an den Ergebnissen zeitweise mitgewirkt.

4.1.2 Komposite aus MIL-100(Al) mit Aeroperl® und Aerosil®

Analog zu den MIL-100(Al)-GO Kompositen[205] wurden zwei weitere MIL-100(Al)-Komposite mit pyrogenen Kieselsäuren, Aeroperl® 300/30[217] und Aerosil® 300,[218] hergestellt. Aeroperl® 300/30 und Aerosil® 300 sind Silica-Materialien mit hydrophilen Eigenschaften. Aeroperl® 300/30 weist eine BET-Oberfläche von 270 bis 330 $m^2 \cdot g^{-1}$ bei einem Porenvolumen von 1.5 bis 1.9 $mL \cdot g^{-1}$ und einen Siliciumdioxid (SiO_2) Gehalt von ≥ 99.0% auf.[217] Aerosil® 300 weist ebenfalls eine BET-Oberfläche von 270 bis 330 $m^2 \cdot g^{-1}$ und einen SiO_2 Gehalt von > 99.8% auf.[218]

Die Komposite aus MIL-100(Al) mit Aeroperl® und Aerosil® wurden mit fünf verschiedenen Aeroperl®- und Aerosil®-Anteilen (von 2 bis 21 Gew.-%) hergestellt. Zur Identifizierung der synthetisierten Komposite wurden PXRDs aufgenommen, welche in Abbildung 33 mit dem simulierten Diffraktogramm von MIL-100(Al), den Diffraktogrammen von Aeroperl® und Aerosil® und dem Diffraktogramm von reinem MIL-100(Al) dargestellt sind.

Im weiteren Verlauf werden die Komposite MIL-100(Al)-Aeroperl und MIL-100(Al)-Aerosil bezeichnet. Aeroperl® wird mit AP und Aerosil® mit AS abgekürzt.

Die Diffraktogramme der MIL-100(Al)-AP und MIL-100(Al)-AS Komposite stimmen mit dem simulierten Diffraktogramm von MIL-100(Al) und dem Diffraktogramm von reinem MIL-100(Al) überein.

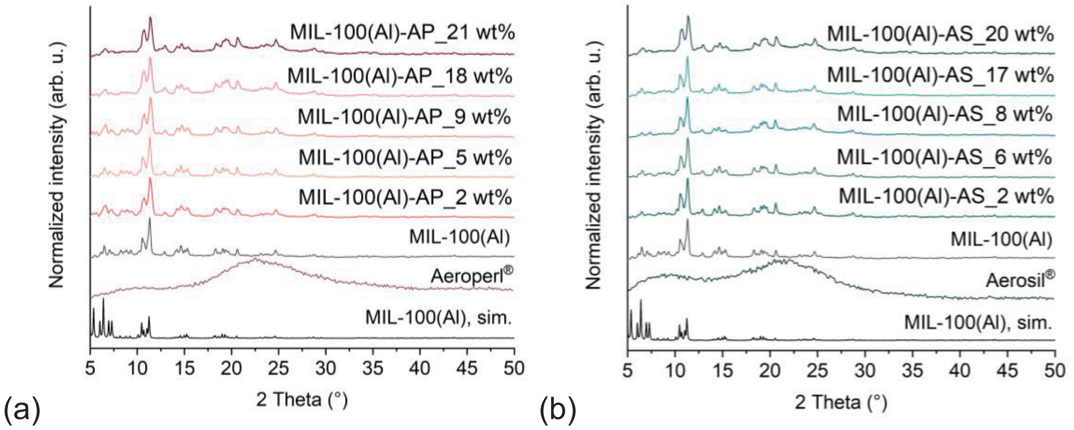

Abbildung 33 PXRDs von MIL-100(Al) (simuliert; CCDC 789872, CSD-Refcode BUSPIP),[145] Aeroperl®, Aerosil®, MIL-100(Al), (a) MIL-100(Al)-AP_2, 5, 9, 18, 21 Gew.-% und (b) MIL-100(Al)-AS_2, 6, 8, 17, 20 Gew.-% Kompositen.

Die Morphologien der hergestellten Komposite wurden über REM-Aufnahmen untersucht. Abbildung 34 zeigt exemplarische REM-Aufnahmen von MIL-100(Al)-AP und MIL-100(Al)-AS Kompositen mit > 20 Gew.-% AP und AS.

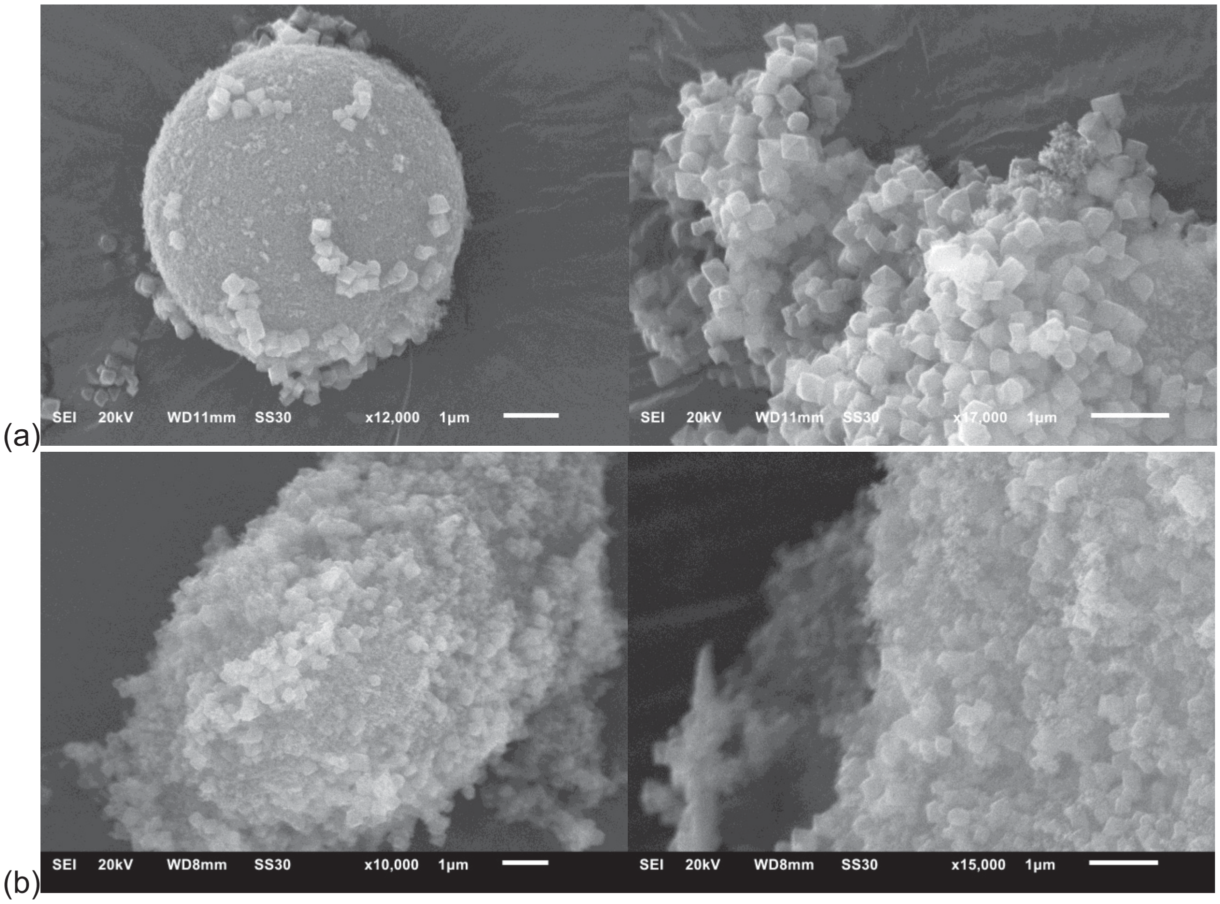

Abbildung 34 REM-Aufnahmen von (a) MIL-100(Al)-AP (> 20 Gew.-%) und (b) MIL-100(Al)-AS (> 20 Gew.-%) Kompositen.

Die spezifischen BET-Oberflächen von MIL-100(Al)-AP und MIL-100(Al)-AS Kompositen wurden mittels N_2-Sorption (Abbildung 35) untersucht. Zusammenfassend lässt sich festhalten, dass im Vergleich zu reinem MIL-100(Al) bei MIL-100(Al)-AP Komposit mit 21 Gew.-% AP die BET-Oberfläche um 8% gesteigert werden konnte.

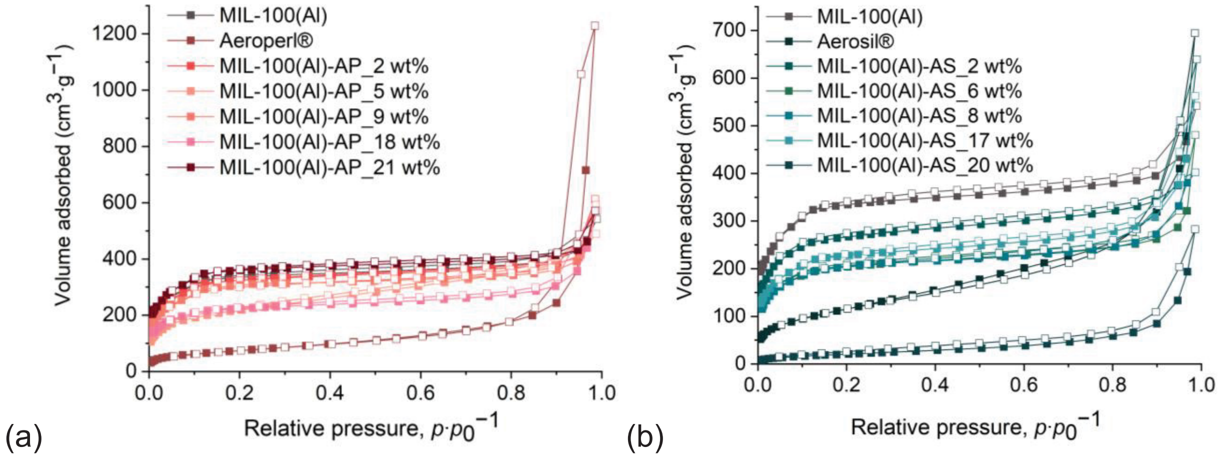

Abbildung 35 N_2-Sorptionsisothermen von MIL-100(Al), (a) MIL-100(Al)-AP_2, 5, 9, 18, 21 Gew.-% und (b) MIL-100(Al)-AS_2, 6, 8, 17, 20 Gew.-% Kompositen.

Des Weiteren wurden H_2O-Sorptionsisothermen von MIL-100(Al)-AP und MIL-100(Al)-AS Kompositen aufgenommen (Abbildung 36). Bei MIL-100(Al)-AP Komposit mit 5 Gew.-% AP konnte eine Steigerung der Wasseraufnahme um 12% im Vergleich zu reinem MIL-100(Al) erzielt werden.

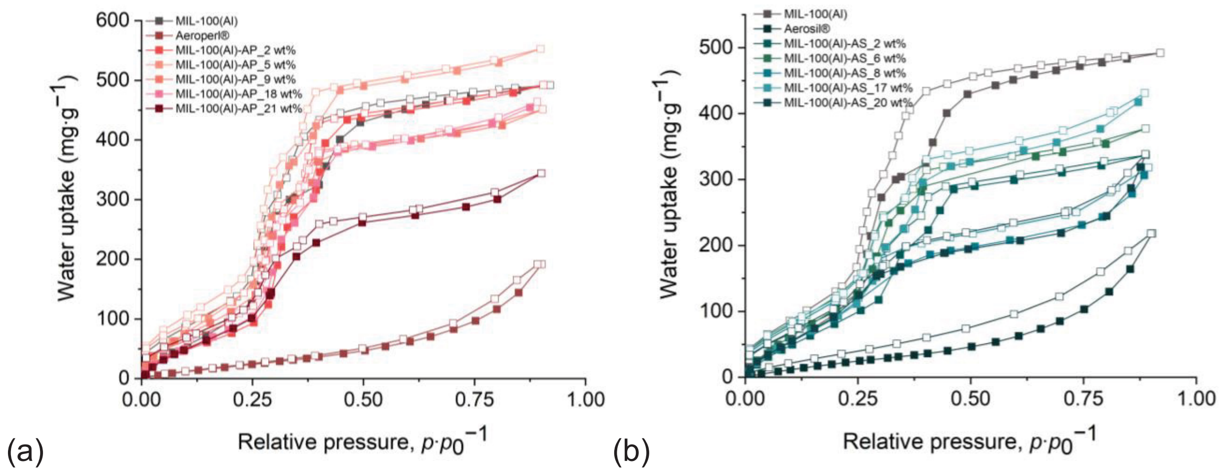

Abbildung 36 H_2O-Sorptionsisothermen von MIL-100(Al), (a) MIL-100(Al)-AP_2, 5, 9, 18, 21 Gew.-% und (b) MIL-100(Al)-AS_2, 6, 8, 17, 20 Gew.-% Kompositen.

Die N_2- und H_2O- Sorptionsergebnisse von MIL-100(Al)-AP und -AS Kompositen sind in Tabelle 3 zusammengefasst.

Tabelle 3 Ergebnisse der N_2- und H_2O-Sorptionsmessungen von MIL-100(Al)-AP und MIL-100(Al)-AS Kompositen.

Probe[a]	S (BET) ($m^2\cdot g^{-1}$)[b]	$V_{\mathrm{pore(total)}}$ ($cm^3\cdot g^{-1}$)[c]	$V_{\mathrm{pore(micro)}}$ ($cm^3\cdot g^{-1}$)[d]	Wasseraufnahme ($mg\cdot g^{-1}$) at $p\cdot p_0^{-1}$ =		
				0.3	**0.5**	**0.9**
Aeroperl®	271	0.55	-	29	47	191
Aerosil®	433	0.63	-	29	46	218
MIL-100(Al) Lit.	1576 [148]	n/a [148]	n/a [148]	≤ 200 [146]	≤ 400 [146]	500 [27,146]
MIL-100(Al)	1317	0.67	0.44	273	429	492
MIL-100(Al)-AP_2	1277	0.63	0.42	190	438	492
MIL-100(Al)-AP_5	803	0.64	0.12	271	490	553
MIL-100(Al)-AP_9	1197	0.60	0.43	239	390	452
MIL-100(Al)-AP_18	856	0.55	0.27	178	389	464
MIL-100(Al)-AP_21	1418	0.67	0.48	145	262	344
MIL-100(Al)-AS_2	1027	0.58	0.32	117	290	337
MIL-100(Al)-AS_6	779	0.44	0.25	183	290	377
MIL-100(Al)-AS_8	783	0.51	0.27	172	198	318
MIL-100(Al)-AS_17	881	0.58	0.28	146	326	431
MIL-100(Al)-AS_20	81	0.21	-	157	194	338

[a] In MIL-100(Al)-AP_*x* oder MIL-100(Al)-AS_*x* bezieht sich "*x*" auf das Gew.-% von AP oder AS im Komposit (siehe präparativen Teil). Bspw. weist MIL-100(Al)-AP_2 einen AP-Anteil von 2 Gew.-% im Komposit auf.

[b] N_2-Sorptionsisothermen wurden bei 77 K durchgeführt. Die BET-Oberflächen S(BET) wurden aus fünf Adsorptionspunkten im Druckbereich von $0.04 < p\cdot p_0^{-1} < 0.1$ für MIL-100(Al) und $0.02 < p\cdot p_0^{-1} < 0.1$ für MIL-100(Al)-AP_*x* und MIL-100(Al)-AS_*x* Kompositen ermittelt.

[c] Das totale Porenvolumen, $V_{\mathrm{pore(total)}}$ wurde aus den Daten der N_2-Sorptionsisotherme bei 77 K ($p\cdot p_0^{-1} = 0.95$ für MIL-100(Al) und Komposite) für Poren ≤ 20 nm berechnet.

[d] Das Mikroporenvolumen, $V_{\mathrm{pore(micro)}}$ bezieht sich nur auf die Mikroporen und wurde nach der $V\!-\!t$ Methode mit der *thickness* Methode "DeBoer" im Bereich von $0.2 < p\cdot p_0^{-1} < 0.4$ für MIL-100(Al), MIL-100(Al)-AP_*x* und MIL-100(Al)-AS_*x* Kompositen erhalten.

Alle Werte sind gerundet.

Anteile an den Ergebnissen – MIL-100(Al)-AP und MIL-100(Al)-AS Komposite:

- Eigenständige Synthese von MIL-100(Al), MIL-100(Al)-AP und MIL-100(Al)-AS Kompositen sowie die Auswertung und Darstellung der Ergebnisse.
- Eigenständige analytische Untersuchungen mittels PXRD, Stickstoff- und Wassersorption sowie die Auswertung und Darstellung der experimentellen Ergebnisse.
- PXRDs, Stickstoff- und Wassersorptionsisothermen von reinem Aeroperl® und Aerosil® wurden von Herrn Dr. Niels Tannert aufgenommen.
- Die REM Untersuchungen wurden von Frau Dr. Sandra Nießing und Herrn Dr. Carsten Schlüsener durchgeführt und dargestellt. Die Auswertung und Verschriftlichung der Ergebnisse wurden eigenständig vorgenommen.
- Die eigenständige Konzipierung, Erstellung der Abbildungen, Aufarbeitung und Verschriftlichung der kompletten experimentellen Ergebnisse und Verschriftlichung der theoretischen Zusammenhänge.
- Umfassende und eigenständige Literaturrecherche.

5 Experimentalteil

5.1 Allgemeine Hinweise

Alle Versuche wurden unter atmosphärischen Bedingungen durchgeführt. Zur Reinigung wurden alle verwendeten Glasgeräte für mindestens 24 h in Kaliumhydroxid/Isopropanol aufbewahrt und für mindestens 2 bis 3 h in verd. HCl-Bad neutralisiert. Anschließend wurden die Glasgeräte mit deionisiertem (deion.) Wasser gewaschen und im Trockenschrank bei 60 °C getrocknet.

5.2 Verwendete Chemikalien

Alle kommerziell erworbenen Chemikalien wurden ohne Aufreinigung eingesetzt (Tabelle 4).

Tabelle 4 Übersicht über die verwendeten Chemikalien mit Angabe des Herstellers und der Reinheit.

Chemikalie	**Formel**	**Hersteller**	**Reinheit [%]**
1,3-Benzoldicarbonsäure (H_2BDC)	$C_8H_6O_4$	Alfa Aesar	99
1,3,5-Benzoltricarbonsäure (H_3BTC)	$C_9H_6O_6$	abcr GmbH	98
Aeroperl® 300/30	–	Evonik	> 99
Aerosil® 300	–	Evonik	> 99.8
Aluminium(III)chlorid-Hexahydrat	$AlCl_3 \cdot 6H_2O$	Janssen Chemicals	99
Aluminium(III)nitrat-Nonahydrat	$Al(NO_3)_3 \cdot 9H_2O$	Alfa Aesar	98–102
Ethanol	C_2H_6OH	Aldrich	p.a.
Graphitpulver	–	Alfa Aesar	99
Kaliumpermanganat	$KMnO_4$	Grüssing GmbH	99
Natriumnitrat	$NaNO_3$	PanReac AppliChem	99
N,*N*-Dimethylformamid (DMF)	C_3H_7NO	Fischer Chemical	p.a.
SAPO-34	–	Clarinat	–
Schwefelsäure	H_2SO_4	VWR Chemicals	95–97
Wasserstoffperoxid	H_2O_2	Chemsolute	30

5.3 Geräte und Parameter

Infrarotspektroskopie (IR-Spektroskopie). Die IR-Spektren wurden an einem Bruker Tensor 37 FT-IR-Spektrometer (Bruker Optics, Ettlingen, Germany) im Bereich von 4000 cm^{-1} bis 400 cm^{-1} und im ATR/KBr-Modus (Platinum ATR-QL, Diamond) durchgeführt.

Mikrowelle. Für die Mikrowellenreaktionen wurde die Discover SP Mikrowelle der Firma CEM verwendet.

Rasterelektronenmikroskop (REM). Die REM-Aufnahmen wurden an einem JEOL JSM-6510LV QSEM Advanced Elektronenmikroskop (Jeol, Akishima, Japan) mit einer LaB_6-Kathode (5–20 keV) aufgenommen.

Röntgenpulverdiffraktometrie (PXRD). Die Röntgenpulverdiffraktogramme wurden bei Umgebungstemperatur an einem D2 Phaser der Firma Bruker (300 W, 30 kV, 10 mA; Bruker, Billerica, US) unter Nutzung von Cu-Kα Strahlung (λ = 1.54182 Å) im Bereich von $5° < 2\theta < 50°$ mit einer Abtastrate von 0.1501 bis 0.0548 °/s aufgenommen. Die Diffraktogramme wurden auf einem *low-background silicon sample holder* durchgeführt. Die Auswertung der Diffraktogramme erfolgte mithilfe der Software Match! der Firma Crystal Impact in der Version 3.3.0.

Stickstoffsorptionsmessungen (N_2-Sorption). N_2-Physisorptionsisothermen (Reinheit 99.9990%, 5.0) wurden an einem NOVA 4000e der Firma Quantachrome bei 77 K durchgeführt. Die Proben wurden vor den Messungen im Vakuum ($<10^{-2}$ mbar) bei materialspezifischen Temperaturen für ein paar Stunden entgast. Die BET-Oberflächen wurden mit Rouquerol-Plots ($r > 0.998$) berechnet.

Vakuumofen. Die Trocknung der Produkte erfolgte im VACUTHERM Vakuumofen der Firma Heraeus.

Wassersorptionsmessungen (H_2O-Sorption). H_2O-Sorptionsisothermen wurden an einem Vapor Sorption Analyzer (VStar4) und an einem Autosorb iQ MP der Firma Quantachrome bei 293 K gemessen. Die Proben wurden vor den Messungen an einem

FloVac Degasser im Vakuum ($<10^{-3}$ mbar) bei materialspezifischen Temperaturen für ein paar Stunden entgast.

Zentrifuge. Zentrifugiert wurde im EBA 8S der Firma Hettich mit einer maximalen Drehzahl von 6000 rpm.

5.4 Präparativer Teil

5.4.1 Thermische Stabilität von Graphitoxid in Lösung

Graphitoxid

Graphitoxid wurde durch die Hummers-Methode[171] hergestellt. Dabei wurden Graphitpulver (5.0 g) und Natriumnitrat ($NaNO_3$, 5.0 g) in Schwefelsäure (H_2SO_4, >230 mL) dispergiert. Die Suspension wurde gerührt und in einem Eisbad auf 0 °C abgekühlt. Anschließend wurde Kaliumpermanganat ($KMnO_4$, 30.1 g) langsam über einen Zeitraum von 30 min zugegeben. Nach 60 min Rühren im Eisbad wurde die Suspension bei Raumtemperatur für 48 h weiter gerührt. Nach 48 h wurden deion. Wasser (1500 mL) und Wasserstoffperoxid (H_2O_2, 120 mL) zugegeben und über Nacht weiter gerührt. Der Ansatz wurde durch Zentrifugation getrennt. Nach mehrmaligem Waschen mit Wasser (5x), zentrifugieren (5x) und Soxhlet-Extraktion mit Wasser wurde Graphitoxid erhalten.

Graphitoxid in Lösung

(1) Es wurden insgesamt vier analoge Ansätze hergestellt. Je zwei Spatelspitzen Graphitoxid wurden mit 2 mL Wasser versetzt und 5 min bei Raumtemperatur gerührt. Anschließend wurden die Suspensionen in der Mikrowelle für 10 min bei 60 °C, 100 °C, 140 °C und 190 °C zur Reaktion gebracht (Einstellungen: 150 W, 20 bar). Alle Ansätze wurden zentrifugiert, der Überstand abdekantiert und der Rückstand bei 60 °C im Vakuumofen über Nacht getrocknet.

PXRDs: Abbildung 31a, **IR-Spektren**: Abbildung 32a

(2) Es wurden insgesamt vier analoge Ansätze hergestellt. Je zwei Spatelspitzen Graphitoxid wurden mit 5 mL einer Lösung aus Wasser und DMF (4:1) versetzt und für 24 h bei 60 °C in den Ofen gestellt. Die drei weiteren Ansätze wurden bei 100 °C, 135 °C und 180 °C für 24 h unter Rückfluss erhitzt. Alle Ansätze wurden zentrifugiert, der Überstand abdekantiert und der Rückstand bei 60 °C im Vakuumofen über Nacht getrocknet.

PXRDs: Abbildung 31b, **IR-Spektren**: Abbildung 32b

5.4.2 Komposite aus MIL-100(Al) mit Aeroperl® und Aerosil®

Synthese von MIL-100(Al)

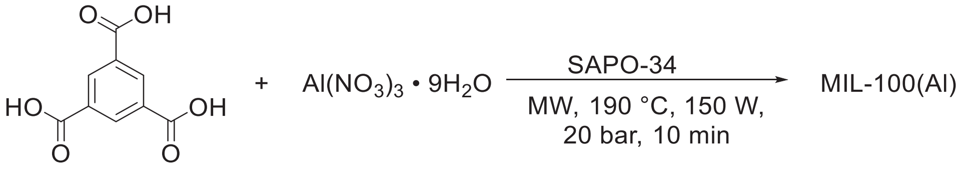

Abbildung 37 Schematische Darstellung der Synthese von MIL-100(Al). SAPO-34 wurde als Induktionsreagenz zur schnelleren und kontrollierten Synthese von MIL-100(Al) verwendet.[148]

Die mikrowellen-unterstützte Synthese von MIL-100(Al) basiert auf der Veröffentlichung von Qui et al.[148] Alle Parameter wurden aus dieser Veröffentlichung modifiziert. In einem 10 mL Mikrowellenröhrchen wurden 132 mg (0.35 mmol) $Al(NO_3)_3 \cdot 9H_2O$, 61.2 mg (0.29 mmol) Trimesinsäure (H_3BTC) und 3.1 mg (0.05 mmol) SAPO-34 mit 2 mL deion. Wasser versetzt und 5 min bei Raumtemperatur gerührt. Anschließend wurde die Suspension in der Mikrowelle für 10 min bei 190 °C zur Reaktion gebracht (Einstellungen: 150 W, 20 bar). Das Produkt wurde zentrifugiert, der Überstand abdekantiert und der Rückstand mit DMF (3 x 2 mL) und Ethanol (3 x 2 mL) gewaschen. Anschließend wurde das Produkt bei 120 °C für 3 h im Vakuumofen getrocknet.

PXRD: Abbildung 33, **N_2-Sorptionsisotherme**: Abbildung 35, **H_2O-Sorptionsisoterme**: Abbildung 36, **N_2- und H_2O-Sorptionsdaten**: Tabelle 3

Tabelle 5 Synthesedaten von MIL-100(Al).

Probe	Edukt	Menge (mg)	Ausbeute (mg; %)
MIL-100(Al)	$Al(NO_3)_3 \cdot 9H_2O$	132	22.3; 27
	H_3BTC	61.2	
	SAPO-34	3.1	

Synthese von MIL-100(Al)-Aeroperl

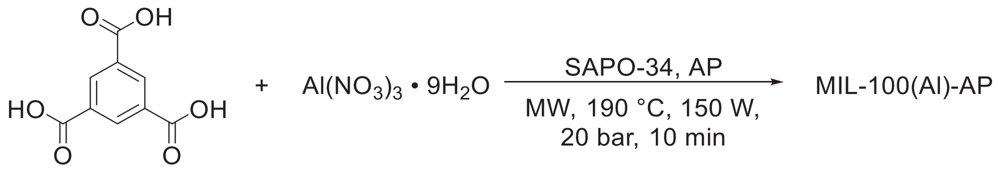

Abbildung 38 Schematische Darstellung der Synthese von MIL-100(Al)-AP Kompositen.

In einem 10 mL Mikrowellenröhrchen wurden 0.4, 1.2, 2, 4, 6 mg Aeroperl®, 132 mg (0.35 mmol) $Al(NO_3)_3 \cdot 9H_2O$, 61.2 mg (0.29 mmol) Trimesinsäure (H_3BTC) und 3.1 mg (0.05 mmol) SAPO-34 mit 2 mL deion. Wasser versetzt und 5 min bei Raumtemperatur gerührt. Anschließend wurde die Suspension in der Mikrowelle für 10 min bei 190 °C zur Reaktion gebracht (Einstellungen: 150 W, 20 bar). Das Produkt wurde zentrifugiert, der Überstand abdekantiert und der Rückstand mit DMF (3 x 2 mL) und Ethanol (3 x 2 mL) gewaschen. Anschließend wurde das Produkt bei 120 °C für 3 h im Vakuumofen getrocknet. Aeroperl (Gew.-%) wurde wie folgt berechnet: (Masse AP) / (Masse MOF-AP) × 100%. Es resultierten 2, 5, 9, 18, 21 Gew.-% AP. Die Proben wurden folgendermaßen bezeichnet: MIL-100(Al)-AP_*x* (x = 2, 5, 9, 18, 21 Gew.-%).

PXRDs: Abbildung 33a, **REMs**: Abbildung 34a, **N_2-Sorptionsisothermen**: Abbildung 35a, **H_2O-Sorptionsisotermen**: Abbildung 36a, **N_2- und H_2O-Sorptionsdaten**: Tabelle 3

Tabelle 6 Synthesedaten von MIL-100(Al)-AP Kompositen.

Probe	Edukt	Menge (mg)	Ausbeute (mg; %)	AP (wt%)
MIL-100(Al)-AP_2	$Al(NO_3)_3 \cdot 9H_2O$	132	20.9; 26	1.91 = 2
	H_3BTC	61.2		
	SAPO-34	3.1		
	AP	0.4		
MIL-100(Al)-AP_5	$Al(NO_3)_3 \cdot 9H_2O$	132	22.1; 27	5.43 = 5
	H_3BTC	61.2		
	SAPO-34	3.1		
	AP	1.2		
MIL-100(Al)-AP_9	$Al(NO_3)_3 \cdot 9H_2O$	132	21.5; 26	9.30 = 9
	H_3BTC	61.2		
	SAPO-34	3.1		
	AP	2		
MIL-100(Al)-AP_18	$Al(NO_3)_3 \cdot 9H_2O$	132	22.0; 27	18.18 = 18
	H_3BTC	61.2		
	SAPO-34	3.1		
	AP	4		
MIL-100(Al)-AP_21	$Al(NO_3)_3 \cdot 9H_2O$	132	28.6; 35	20.98 = 21
	H_3BTC	61.2		
	SAPO-34	3.1		
	AP	6		

Synthese von MIL-100(Al)-Aerosil

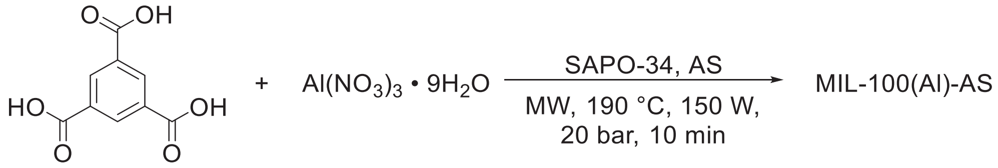

Abbildung 39 Schematische Darstellung der Synthese von MIL-100(Al)-AS Kompositen.

In einem 10 mL Mikrowellenröhrchen wurden 0.4, 1.2, 2, 4, 6 mg Aerosil®, 132 mg (0.35 mmol) $Al(NO_3)_3{\cdot}9H_2O$, 61.2 mg (0.29 mmol) Trimesinsäure (H_3BTC) und 3.1 mg (0.05 mmol) SAPO-34 mit 2 mL deion. Wasser versetzt und 5 min bei Raumtemperatur gerührt. Anschließend wurde die Suspension in der Mikrowelle für 10 min bei 190 °C zur Reaktion gebracht (Einstellungen: 150 W, 20 bar). Das Produkt wurde zentrifugiert, der Überstand abdekantiert und der Rückstand mit DMF (3 x 2 mL) und Ethanol (3 x 2 mL) gewaschen. Anschließend wurde das Produkt bei 120 °C für 3 h im Vakuumofen getrocknet. Aerosil (Gew.-%) wurde wie folgt berechnet: (Masse AS) / (Masse MOF-AS) × 100%. Es resultierten ca. 2, 6, 8, 17, 20 Gew.-% AS. Die Proben wurden folgendermaßen bezeichnet: MIL-100(Al)-AS_*x* (x = 2, 6, 8, 17, 20 Gew.-%).

PXRDs: Abbildung 33b, **REM**: Abbildung 34b, **N_2-Sorptionsisothermen**: Abbildung 35b, **H_2O-Sorptionsisotermen**: Abbildung 36b, **N_2- und H_2O-Sorptionsdaten**: siehe Tabelle 3

Tabelle 7 Synthesedaten von MIL-100(Al)-AS Kompositen.

Probe	Edukt	Menge (mg)	Ausbeute (mg; %)	AS (wt%)
MIL-100(Al)-AS_2	$Al(NO_3)_3 \cdot 9H_2O$	132	21.4; 26	1.87 = 2
	H_3BTC	61.2		
	SAPO-34	3.1		
	AS	0.4		
MIL-100(Al)-AS_6	$Al(NO_3)_3 \cdot 9H_2O$	132	21.7; 27	5.53 = 6
	H_3BTC	61.2		
	SAPO-34	3.1		
	AS	1.2		
MIL-100(Al)-AS_8	$Al(NO_3)_3 \cdot 9H_2O$	132	25.0; 31	8.00 = 8
	H_3BTC	61.2		
	SAPO-34	3.1		
	AS	2		
MIL-100(Al)-AS_17	$Al(NO_3)_3 \cdot 9H_2O$	132	23.5; 29	17.02 = 17
	H_3BTC	61.2		
	SAPO-34	3.1		
	AS	4		
MIL-100(Al)-AS_20	$Al(NO_3)_3 \cdot 9H_2O$	132	30.0; 37	20.00 = 20
	H_3BTC	61.2		
	SAPO-34	3.1		
	AS	6		

6 Zusammenfassung und Ausblick

In der vorliegenden Dissertation wurden zwei Ziele, die Synthese und Charakterisierung von MOF Kompositen und das Verfassen eines Reviews, verfolgt. Die daraus resultierenden Ergebnisse wurden in Form von Veröffentlichungen in internationalen Fachjournalen publiziert, siehe Kapitel 3.1.1 und 3.1.2.[205,206]

Im ersten Teil dieser Dissertation konnten im Rahmen einer Veröffentlichung neue Forschungsergebnisse zu MOF Kompositen vorgestellt werden.[205] Hierbei wurden neue Al-MOF-GO Komposite aus literaturbekannten Al-MOFs, MIL-100(Al) und CAU-10-H, mit Graphitoxid dargestellt. Dabei wurden MIL-100(Al)-GO und CAU-10-H-GO Komposite aus 2 bis 16 Gew.-% GO erfolgreich synthetisiert. Die *in situ* Synthesen wurden zum einen unter Mikrowellenbestrahlung (MIL-100(Al) und Komposite) und zum anderen unter Rückflussbedingungen (CAU-10-H und Komposite) durchgeführt. Die erhaltenen Materialien wurden anhand analytischer Methoden wie IR-Spektroskopie, PXRD, REM, Stickstoff- und Wassersorption umfassend charakterisiert. Im Vergleich zu den reinen Al-MOFs, MIL-100(Al) und CAU-10-H, konnten MIL-100(Al)-GO und CAU-10-H-GO Komposite mit höherer spezifischer BET-Oberfläche und Wasseraufnahme hergestellt werden (Abbildung 40).[205] Dies lässt auf eine gute Wechselwirkung zwischen MOF und GO-Schichten mit der Bildung einer zusätzlichen Grenzfläche schließen.[205]

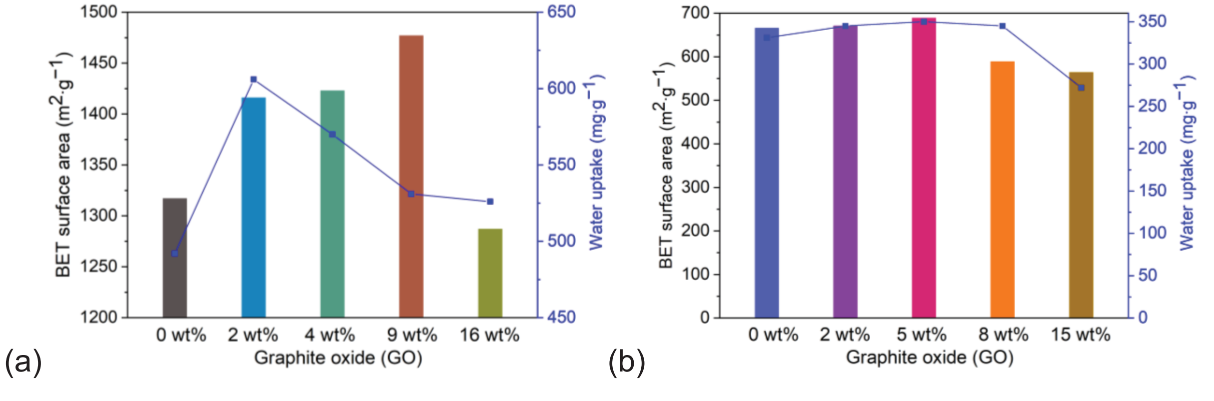

Abbildung 40 Graphische Darstellung der spezifischen BET-Oberflächen und der Wasseraufnahmen von (a) MIL-100(Al), MIL-100(Al)-GO_2, 4, 9, 16 Gew.-% Kompositen und (b) CAU-10-H, CAU-10-H-GO_2, 5, 8, 15 Gew.-% Kompositen. Reproduziert von Ref. 205 mit Genehmigung, Elsevier Inc., © 2021.

Im Einzelnen konnte eine Zunahme der spezifischen BET-Oberfläche von 8 bis 12% und eine Zunahme des Gesamtporenvolumens von 7 bis 10 % bei MIL-100(Al)-GO Kompositen mit 2, 4 und 9 Gew.-% GO erzielt werden. Bei CAU-10-H-GO Kompositen mit 2 und 5 Gew.-% GO wurde eine Zunahme des Gesamtporenvolumens von 4 bis 7% gegenüber dem reinen CAU-10-H beobachtet (Abbildung 40).[205]

Weiterhin konnte gezeigt werden, dass das MIL-100(Al)-GO Komposit mit 2 Gew.-% GO eine um 23% erhöhte Wasseraufnahme im Vergleich zu reinem MIL-100(Al) aufweist. Bei höheren GO-Anteilen wie bei MIL-100(Al)-GO Kompositen mit 4, 9 und 16 Gew.-% GO resultierten um 7 bis 16% erhöhte Wasseraufnahmen. Im Gegensatz dazu zeigten die CAU-10-H-GO Komposite mit 2, 5 und 8 Gew.-% GO nur eine um 4 bis 6% erhöhte Wasseraufnahme (Abbildung 40). Des Weiteren wurde in allen vier CAU-10-H-GO Kompositen mit 2, 5, 8 ,15 Gew.-% GO eine hydrophile Verschiebung der S-förmigen Wasseraufnahme zu einem niedrigen relativen Druck ($p{\cdot}p_0^{-1}$ = ~0.15) im Vergleich zu reinem CAU-10-H ($p{\cdot}p_0^{-1}$ = ~0.17) beobachtet (Abbildung 41).[205]

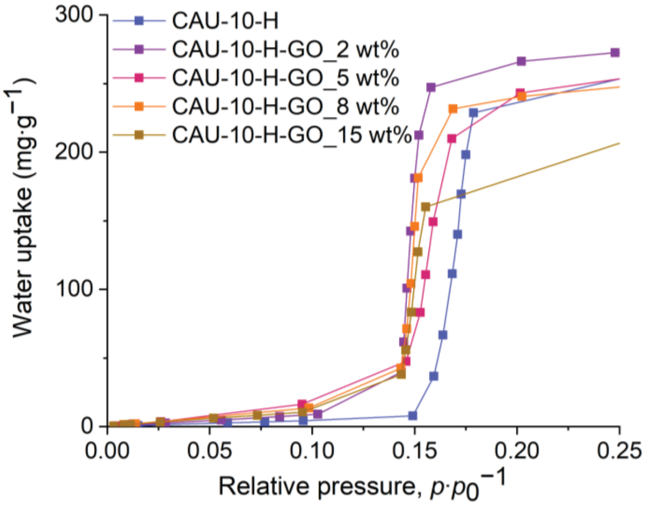

Abbildung 41 H_2O-Adsorptionsisothermen von CAU-10-H und CAU-10-H-GO_2, 5, 8, 15 Gew.- % Kompositen. Nachdruck von Ref. 205 mit Genehmigung, Elsevier Inc., © 2021.

Ferner wurde gezeigt, dass die MIL-100(Al)-GO_2, 4 Gew.-% und CAU-10-GO_2, 5 Gew.-% Komposite nahezu unveränderte Wasseraufnahmen nach fünf Adsorptions- und Desorptionszyklen aufweisen (Abbildung 42).[205]

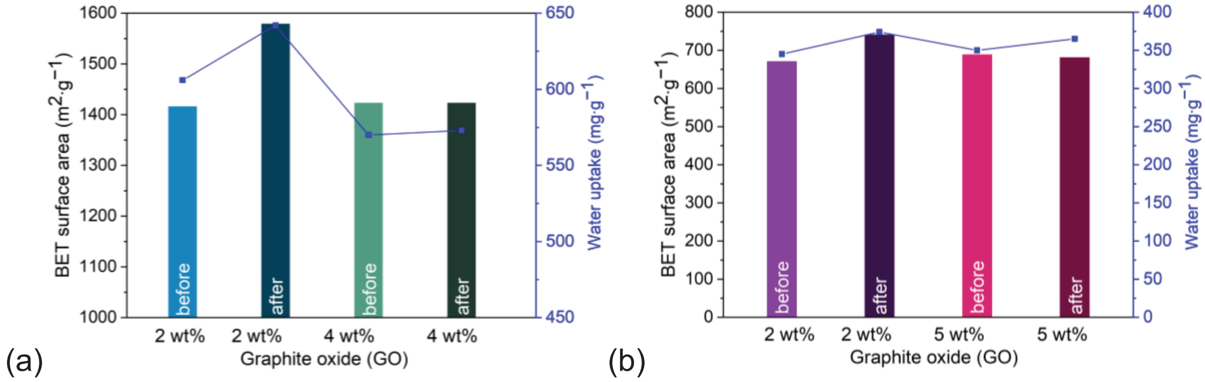

Abbildung 42 Graphische Darstellung der spezifischen BET-Oberflächen und der Wassersorptionsergebnissen von (a) MIL-100(Al)-GO_2, 4 Gew.-% Kompositen und (b) CAU-10-H-GO_2, 5 Gew.-% Kompositen vor und nach fünf Ad- und Desorptionszyklen.[205]

Im zweiten Teil dieser Dissertation konnte anhand der Fachliteratur eine umfangreiche theoretische Zusammenfassung zu den Synthesestrategien, den Eigenschaften, den Computerstudien und den Anwendungen von MOFs mit offenen Metallstellen gegeben werden.[206] Es wurde eine Vielzahl an MOFs mit OMS, wie bspw. HKUST-1 (M = Cu^{2+}), MIL-100 (M = Sc^{3+}, V^{3+}, Cr^{3+}, Fe^{3+}), MOF-74 (M = Mg^{2+}, Fe^{2+}, Co^{2+}, Ni^{2+}, Cu^{2+}, Zn^{2+}, Cd^{2+}), UiO-66 (M = Zr^{4+}) etc., aufgezeigt.[206]

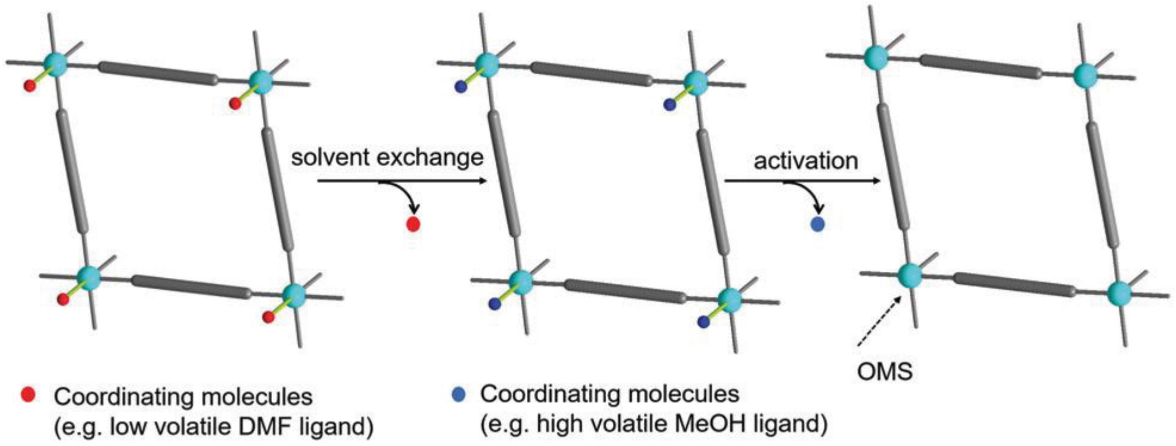

Abbildung 43 Schematische Darstellung zur Generierung von OMS in MOF durch Lösungsmittelaustausch eines weniger flüchtigen Lösungsmittels (z.B. DMF) mit einem leicht flüchtigen Lösungsmittel (z.B. MeOH) und anschließende Aktivierung. Nachdruck von Ref. 206 mit Genehmigung, The Royal Society of Chemistry, © 2020.

Unter Synthesestrategien sind Verfahren, im Allgemeinen Aktivierungsmethoden, zur Generierung bzw. Erzeugung von offenen Metallstellen in MOFs gemeint. Offene Metallstellen in MOFs können durch die Entfernung von koordinierten labilen Lösungsmittelmolekülen, wie Wasser, Alkoholen, Acetonitril oder DMF, generiert werden. Hierbei kommen die Aktivierungsmethoden wie der Lösungsmittelaustausch und die thermische, chemische oder photochemische Aktivierung zum Einsatz. Dabei ist es besonders wichtig, dass die MOF-Struktur nicht kollabiert und ihre Eigenschaften wie Kristallinität und Porosität beibehält (Abbildung 43). Die Überprüfung läuft im Allgemeinen mittels PXRD ab.[206]

Um das Vorhandensein von offenen Metallstellen bestätigen zu können, sind weitere analytische Methoden wie die Kernspinresonanzspektroskopie (engl. *nuclear magnetic resonance*, NMR), die thermogravimetrische Analyse (TGA), die FT-IR-Spektroskopie in Zusammenhang mit Gassorptionsstudien heranzuziehen. Zur Quantifizierung von OMS in MOFs, d.h. zur Bestimmung der relativen Menge (Prozentsatz) an Lewis-Säure Stellen oder offenen Metallstellen in MOFs, können Techniken wie die Gas- oder Dampfadsorption, die IR-Spektroskopie und die temperaturprogrammierte Desorption gewählt werden. Es stellte sich heraus, dass diese Techniken bislang nur in wenigen OMS-Arbeiten Anwendung finden. Die Computerstudien können als Grundlage zur Untersuchung der Interaktion von offenen Metallstellen mit verschiedenen Gastmolekülen, die nicht aus Experimenten abgeleitet werden können, und zur Vorhersage der Sorptionseigenschaften dienen. Hierbei liefert eine Kombination der dispersionskorrigierten DFT (engl. *density functional theory*) und *high-level ab-initio* Methoden, wie z.B. das DFT-D und das CC (engl. *coupled cluster*) Verfahren, den genauesten Ansatz.[206]

Das Vorhandensein von OMS in MOFs führt zur Verstärkung der Wechselwirkungen zwischen den freien Koordinationsstellen am Metall und den Gastmolekülen. Diese Eigenschaft bewirkt eine breite Anwendung in Gassorption, Separation, Katalyse oder Sensorik. Bspw. sind offene Metallstellen primäre Adsorptionsstellen für diverse Gase wie Wasserstoff, Kohlenstoff- oder Sticktoffmonoxid.[206]

Literaturverzeichnis

1 O.M. Yaghi, H. Li, *J. Am. Chem. Soc.*, 1995, **117**, 10401–10402.

2 O.M. Yaghi, G. Li. H. Li, *Nature*, 1995, **378**, 703–706.

3 C. Janiak, *Dalton Trans.*, 2003, 2781–2804.

4 C. Janiak, J.K. Vieth, *New J. Chem.*, 2010, **34**, 2366–2388.

5 S.R. Batten, N.R. Champness, X.-M. Chen, J. Garcia-Martinez, S. Kitagawa, L. Öhrström, M. O'Keeffe, M.P. Suh, J. Reedijk, *CrystEngComm*, 2012, **14**, 3001–3004.

6 H.-C. Zhou, S. Kitagawa, *Chem. Soc. Rev.*, 2014, **43**, 5415–5418.

7 S.R. Batten, N.R. Champness, X.-M. Chen, J. Garcia-Martinez, S. Kitagawa, L. Öhrström, M. O'Keeffe, M.P. Suh, J. Reedijk, *Pure Appl. Chem.*, 2013, **85**, 1715–1724.

8 R.A. Fischer, I. Schwedler, *Angew. Chem.*, 2014, **126**, 7209–7214.

9 O.K. Farha, I. Eryazici, N.C. Jeong, B.G. Hauser, C.E. Wilmer, A.A. Sarjeant, R.Q. Snurr, S.T. Nguyen, A.Ö. Yazaydın, *J. Am. Chem. Soc.*, 2012, **134**, 15016–15021.

10 H. Li, M. Eddaoudi, M. O´Keeffe, O.M. Yaghi, *Nature*, 1999, **402**, 276–279.

11 M. Eddaoudi, J. Kim, N. Rosi, D. Vodak, J. Wachter, M. O´Keeffe, O.M. Yaghi, *Science*, 2002, **295**, 469–474.

12 J. Dechnik, J. Gascon, C.J. Doonan, C. Janiak, C.J. Sumby, *Angew. Chem., Int. Ed.*, 2017, **56**, 9292–9310.

13 B. Li, H.-M. Wen, W. Zhou, B. Chen, *J. Phys. Chem. Lett.*, 2014, **5**, 3468–3479.

14 P. Serra-Crespo, E.V. Ramos-Fernandez, J. Gascon, F. Kapteijn, *Chem. Mater.*, 2011, **23**, 2565–2572.

15 J.-R. Li, J. Sculley, H.-C. Zhou, *Chem. Rev.*, 2012, **112**, 869–932.

16 V. Safarifard, S. Rodríguez-Hermida, V. Guillerm, I. Imaz, M. Bigdeli, A. Azhdari Tehrani, J. Juanhuix, A. Morsali, M.E. Casco, J. Silvestre-Albero, *Cryst. Growth Des.*, 2016, **16**, 6016–6023.

17 J.Y. Lee, O.K. Farha, J. Roberts, K.A. Scheidt, S.T. Nguyen, J.T. Hupp, *Chem. Soc. Rev.*, 2009, **38**, 1450–1459.

18 J.T. Hupp, *Chem. Soc. Rev.*, 2009, **38**, 1450–1459.

19 Y.-B. Huang, J. Liang, X.-S. Wang, R. Cao, *Chem. Soc. Rev.*, 2017, **46**, 126–157.

20 D. Farrusseng, S. Aguado, C. Pinel, *Angew. Chem., Int. Ed.*, 2009, **48**, 7502–7513.

21 M. Yoon, R. Srirambalaji, K. Kim, *Chem. Rev.*, 2012, **112**, 1196–1231.

22 A. Herbst, C. Janiak, *CrystEngComm*, 2017, **19**, 4092–4117.

23 Z. Ma, T. Kyotani, Z. Liu, O. Terasaki, A. Tomita, *Chem. Mater.*, 2001, **13**, 4413–4415.

24 M.E. Davis, *Nature*, 2002, **417**, 813–821.

25 G. Férey, *Chem. Soc. Rev.*, 2008, **37**, 191–214.

26 S.K. Henninger, H.A. Habib, C. Janiak, *J. Am. Chem. Soc.*, 2009, **131**, 2776–2777.

27 F. Jeremias, D. Fröhlich, C. Janiak, S.K. Henninger, *New J. Chem.*, 2014, **38**, 1846–1852.

28 M.F. de Lange, K.J. Verouden, T.J. Vlugt, J. Gascon, F. Kapteijn, *Chem. Rev.*, 2015, **115**, 12205–12250.

29 D. Fröhlich, E. Pantatosaki, P.D. Kolokathis, K. Markey, H. Reinsch, M. Baumgartner, M.A. van der Veen, D.E. De Vos, N. Stock, G.K. Papadopoulos, *J. Mater. Chem. A*, 2016, **4**, 11859–11869.

30 H. Kummer, F. Jeremias, A. Warlo, G. Füldner, D. Fröhlich, C. Janiak, R. Gläser, S.K. Henninger, *Ind. Eng. Chem. Res.*, 2017, **56**, 8393–8398.

31 Z.-G. Gu, D.-J. Li, C. Zheng, Y. Kang, C. Wöll, J. Zhang, Angew. *Chem., Int. Ed.*, 2017, **56**, 6853–6858.

32 P. Horcajada, R. Gref, T. Baati, P.K. Allan, G. Maurin, P. Couvreur, G. Férey, R.E. Morris, C. Serre, *Chem. Rev.*, 2012, **112**, 1232–1268.

33 Y. Cui, Y. Yue, G. Qian, B. Chen, *Chem. Rev.*, 2012, **112**, 1126–1162.

34 C. Wang, T. Zhang, W. Lin, *Chem. Rev.*, 2012, **112**, 1084–1104.

35 L.E. Kreno, K. Leong, O.K. Farha, M. Allendorf, R.P. Van Duyne, J.T. Hupp, *Chem. Rev.*, 2012, **112**, 1105–1125.

36 H.B. Tanh Jeazet, C. Staudt, C. Janiak, *Dalton Trans.*, 2012, **41**, 14003–14027.

37 M.T. Kapelewski, T. Runčevski, J.D. Tarver, H.Z.H. Jiang, K.E. Hurst, P.A. Parilla, A. Ayala, T. Gennett, S.A. FitzGerald, C.M. Brown, J.R. Long, *Chem. Mater.*, 2018, **30**, 8179–8189.

38 M.P. Suh, H.J. Park, T.K. Prasad, D.-W- Lim, *Chem. Rev.*, 2012, **112**, 782–835.

39 C. Pettinari, A. Tombasi, *MRS Energy Sustain.*, 2020. DOI: 10.1557/mre.2020.30.

40 K. Sumida, D.L. Rogow, J.A. Mason, T.M. McDonald, E.D. Bloch, Z.R. Herm, T.-H. Bae, J.R. Long, *Chem. Rev.*, 2012, **112**, 724–781.

41 C. Duan, Y. Yu, J. Xiao, Y. Li, P. Yang, F. Hu, H. Xi, *Green Energy Environ.*, 2021, **6**, 33–49.

42 B. Wang, L.-H. Xie, X. Wang, X.-M. Liu, J. Li, J.-R. Li, *Green Energy Environ.*, 2018, **3**, 191–228.

43 H. Furukawa, K.E. Cordova, M. O´Keeffe, O.M. Yaghi, *Science*, 2013, **341**, 1230444.

44 H.-C. Zhou, J.R. Long, O.M. Yaghi, *Chem. Rev.*, 2012, **112**, 673–674.

45 I. Thomas-Hillman, A. Laybourn, C. Dodds, S.W. Kingman, *J. Mater. Chem. A*, 2018, **6**, 11564–11581.

46 A. Schoedel, Z. Ji, O.M. Yaghi, *Nat. Energy*, 2016, **1**, 16034–16046.

47 Merck, Können winzige Stoffe den Planeten grüner machen? Verfügbar unter: https://www.merckgroup.com/de/research/science-space/envisioning-tomorrow/scarcity-of-resources/mof.html, Zugegriffen: 17.02.2021.

48 S. Kitagawa, *Angew. Chem. Int. Ed.*, 2015, **54**, 10686–10687.

49 (a) Intergovernmental Panel on Climate Change (IPCC), 2018, Summary for Policymakers. In: Global Warming of 1.5°C. An IPCC Special Report on the impacts of global warming of 1.5°C above pre-industrial levels and related global greenhouse gas emission pathways, in the context of strengthening the global response to the threat of climate change, sustainable development, and efforts to eradicate poverty. Verfügbar unter: https://www.ipcc.ch/site/assets/uploads/sites/2/2019/05/SR15_SPM_version_report_LR.pdf, Zugegriffen: 09.02.2021. (b) Intergovernmental Panel on Climate Change (IPCC), 2018, 1.5 °C globale Erwärmung, Zusammenfassung für politische Entscheidungsträger, ISBN: 978-3-89100-051-9, deutsche Übersetzung durch deutsche IPCC-Koordinierungsstelle, Bonn, 2018. Verfügbar unter: https://www.ipcc.ch/site/assets/uploads/2020/07/SR1.5-SPM_de_barrierefrei.pdf, Zugegriffen: 09.02.2021.

50 Greenpeace, Februar 2019, Klimawandel – das Tempo steigt, Verursacht der Mensch die Erderwärmung? Verfügbar unter:

https://www.greenpeace.de/themen/klimawandel/verursacht-der-mensch-die-erderwarmung, Zugegriffen: 09.02.2021.

51 Umweltbundesamt (UBA), 27.11.2019, Ist Atomstrom wirklich CO2-frei? Verfügbar unter: https://www.umweltbundesamt.de/service/uba-fragen/ist-atomstrom-wirklich-co2-frei, Zugegriffen: 09.10.2021.

52 Greenpeace, Welche Treibhausgase verursachen den Klimawandel? CO_2 & Co. Verfügbar unter: https://www.greenpeace.de/themen/klimawandel/welche-treibhausgase-verursachen-die-erderw%C3%A4rmung, Zugegriffen: 12.02.2021.

53 mdr Wissen, 22.01.2020, Wer stösst am meisten aus? Die Top 5 der CO_2-Verursacher Deutschland nach Sektoren. Verfügbar unter: https://www.mdr.de/wissen/deutschland-top-fuenf-klima-emissionen-100.html, Zugegriffen: 09.02.2021.

54 Umweltbundesamt (UBA), 30.07.2020, Emissionsquellen. Verfügbar unter: https://www.umweltbundesamt.de/themen/klima-energie/treibhausgas-emissionen/emissionsquellen#energie-stationar, Zugegriffen: 10.02.2021.

55 Umweltbundesamt (UBA), 01.04.2020, Lachgas und Methan. Verfügbar unter: https://www.umweltbundesamt.de/themen/boden-landwirtschaft/umweltbelastungen-der-landwirtschaft/lachgas-methan, Zugegriffen: 10.02.2021.

56 Intergovernmental Panel on Climate Change (IPCC), 2008: Klimaänderung 2007, Synthesebericht, ISBN: 978-3-00-025397-3, deutsche Übersetzung durch deutsche IPCC-Koordinierungsstelle, Berlin, 2008. Verfügbar unter: https://www.ipcc.ch/site/assets/uploads/2018/08/IPCC2007-SYR-german.pdf, Zugegriffen: 12.02.2021.

57 N. Podbregar, K. Schwanke, H. Frater, Wetter Klima Klimawandel, Wissen für eine Welt im Umbruch, ISBN: 978-3-540-79291-8, e-ISBN: 978-3-540-79292-5, Springer-Verlag Berlin, 2009.

58 Umweltbundesamt (UBA), 26.06.2020, Atmosphärische Treibhausgas-Konzentrationen. Verfügbar unter: https://www.umweltbundesamt.de/daten/klima/atmosphaerische-treibhausgas-konzentrationen#kohlendioxid-, Zugegriffen: 12.02.2021.

59 United Nations Framework Convention on Climate Change (UNFCCC), The Paris Agreement. Verfügbar unter: https://unfccc.int/process-and-meetings/the-paris-agreement/the-paris-agreement, Zugegriffen: 12.02.2021.

60 Europäische Union (EU), Klimapolitik, Übereinkommen von Paris. Verfügbar unter: https://ec.europa.eu/clima/policies/international/negotiations/paris_de, Zugegriffen: 12.02.2021.

61 Bundesministerium für Wirtschaft und Energie (BMWi), Klimaschutz, Abkommen von Paris. Verfügbar unter: https://www.bmwi.de/Redaktion/DE/Artikel/Industrie/klimaschutz-abkommen-von-paris.html, Zugegriffen: 12.02.2021.

62 Bundesministerium für Umwelt (BMU), Naturschutz und nukleare Sicherheit, Die Klimakonferenz in Paris. Verfügbar unter: https://www.bmu.de/themen/klima-energie/klimaschutz/internationale-klimapolitik/pariser-abkommen/, Zugegriffen: 12.02.2021.

63 Bundesministerium für Umwelt (BMU), Naturschutz und nukleare Sicherheit, Klimaschutzplan 2050, Klimapolitische Grundsätze und Ziele der Bundesregierung, Berlin, 2016. Verfügbar unter: https://www.bmu.de/fileadmin/Daten_BMU/Download_PDF/Klimaschutz/klimaschutzplan_2050_bf.pdf, Zugegriffen: 12.02.2021.

64 Bundesministerium für Wirtschaft und Energie (BMWi), 28.01.2021, Klimaschutz, Treibhausgas-Emissionen in Deutschland in Millionen Tonnen CO_2-Äquivalente. Verfügbar unter: https://www.bmwi.de/Redaktion/DE/Infografiken/Energie/fortschrittsbericht-co2-emissionen.html, Zugegriffen: 12.02.2021.

65 Bundesministerium für Wirtschaft und Energie (BMWi), Mai 2017, Langfristszenarien für die Transformation des Energiesystems in Deutschland, Modul 10.a: Reduktion der Treibhausgasemissionen Deutschlands um 95% bis 2050, Grundsätzliche Überlegungen zu Optionen und Hemmnissen, Projekt: Fraunhofer ISI, Consentec GmbH, Institut für Energie und Umweltforschung (ifeu). Verfügbar unter: https://www.bmwi.de/Redaktion/DE/Downloads/B/berichtsmodul-10-a-bericht-reduktion-

der-treibhausgasemissionen-deutschlands-langfassung.pdf?__blob=publicationFile&v=4, Zugegriffen: 12.02.2021.

66 NewClimate Institute, 2019, 1.5 °C Was Deutschland tun muss. Verfügbar unter: https://newclimate.org/wp-content/uploads/2019/03/Deutschland_1.5_Web.pdf, Zugegriffen: 12.02.2021.

67 A. Hildebrandt, Klimawandel in der Wirtschaft, Warum wir ein Bewusstsein für Dringlichkeit brauchen, ISBN: 978-3-662-60394-9, e-ISBN: 978-3-662-60395-6, Springer-Verlag, Berlin, 2020.

68 Europäische Union (UN), Europäischer Rat, 22.12.2020, Maßnahmen der EU gegen den Klimawandel. Verfügbar unter: https://www.consilium.europa.eu/de/policies/climate-change/, Zugegriffen: 12.02.2021.

69 International Energy Agency (IEA), International Council of Chemical Associations (ICCA), DECHEMA, 2013, Technology Roadmap: Energy and GHG Reductions in the chemical industry via Catalytic Processes. Verfügbar unter: https://dechema.de/dechema_media/Downloads/Positionspapiere/IndustrialCatalysis/Chemical_Roadmap_2013_Final_WEB-called_by-dechema-original_page-136220-original_site-dechema_eV-view_image-1.pdf, Zugegriffen: 24.02.2021.

70 International Council of Chemical Associations (ICCA), 2019, Enabling the Future, Chemistry innovations for a low-carbon society. Verfügbar unter: https://icca-chem.org/wp-content/uploads/2020/05/Enabling-the-Future.pdf, Zugegriffen: 16.02.2021.

71 Verband der chemischen Industrie e.V. (VCI), September 2019, Auf dem Weg zu einer treibhausgasneutralen chemischen Industrie in Deutschland, Studie: DECHEMA, FutureCamp. Verfügbar unter: https://www.vci.de/vci/downloads-vci/publikation/2019-10-09-studie-roadmap-chemie-2050-treibhausgasneutralitaet-kurzfassung.pdf, Zugegriffen: 12.02.2021.

72 Verband der chemischen Industrie e.V. (VCI), 09.10.2019, Eine treibhausgasneutrale Chemie ist technologisch möglich. Verfügbar unter: https://www.vci.de/presse/pressemitteilungen/treibhausgasneutrale-chemie-technologisch-moeglich-vci-studie-potenzial-und-voraussetzungen-fuer-starke-co2-minderung-chemieindustrie.jsp, Zugegriffen: 12.02.2021.

73 Verband der chemischen Industrie e.V. (VCI), 30.06.2020, „Chemistry4Climate“ für eine treibhausgasneutrale Chemie. Verfügbar unter: https://www.vci.de/themen/energie-klima/klimaschutz/chemistry4climate-fuer-eine-treibhausgasneutrale-chemie.jsp, Zugegriffen: 12.02.2021.

74 Europäische Kommission, CORDIS Forschungsergebnisse der EU, Aktenzeichen 227608, letzte Aktualisierung 11.05.2018. Verfügbar unter: https://cordis.europa.eu/article/id/227608-membrane-co2-filtration-for-power-stations/de, Zugegriffen: 30.07.2021.

75 A. Zulys, F. Yulia, N. Muhadzib, Nasruddin, *Ind. Eng. Chem. Res.*, 2021, **60**, 37–51.

76 L. Xu, C.-Y. Xing, D. Ke, L. Chen, Z.-J. Qiu, S.-L. Zeng, B.-J. Li, S. Zhang, *ACS Appl. Mater. Interfaces*, 2020, **12**, 3032–3041.

77 H. Wu, X.Y. Kong, X. Wen, S.-P. Chai, E.C. Lovell, J. Tang, Y.H. Ng, *Angew. Chem. Int. Ed.*, 2021, 60, 8455–8459.

78 chemie.de – Das Chemie Fachportal vom Labor bis zum Prozess, 04.02.2021, Neuartiger Photokatalysator verwandelt Kohlendioxid in Licht effektiv in Methan als Kraftstoff. Verfügbar unter: https://www.chemie.de/news/1169743/neuartiger-photokatalysator-verwandelt-kohlendioxid-mit-licht-effektiv-in-methan-als-kraftstoff.html, Zugegriffen: 22.02.2021.

79 S.S.Y. Chui, S.M.F. Lo, J.P.H. Charmant, A.G. Orpen, I.D. Williams, *Science*, 1999, **283**, 1148–1150.

80 M. Eddaoudi, H. Li and O.M. Yaghi, *J. Am. Chem. Soc.*, 2000, **122**, 1391–1397.

81 O.M. Yaghi, C.E. Davis, G. Li and H. Li, *J. Am. Chem. Soc.*, 1997, **119**, 2861–2868.

82 S. Kaskel, *Chem. Ing. Tech.*, 2010, **82**, 1019–1023.

83 M. Eddaoudi, D.B. Moler, H. Li, B. Chen, T.M. Reineke, M. O’Keeffe, O.M. Yaghi, *Acc. Chem. Res.*, 2001, **34**, 319–330.

84 J. Kim, B. Chen, T. M. Reineke, H. Li, M. Eddaoudi, D.B. Moler, M. O´Keeffe, O.M. Yaghi, *J. Am. Chem. Soc.*, 2001, **123**, 8239–8247.

85 D.J. Tranchemontagne, J.L. Mendoza-Cortés, M. O´Keeffe, O.M. Yaghi, *Chem. Soc. Rev.*, 2009, **38**, 1257–1283.

86 M. Mozafari, Metal-Organic Frameworks for Biomedical Applications, Chapter 2 – Secondary building units of MOFs (by A. Schoedel), *Elsevier Inc.*, 2020, 11–44.

87 S. Bauer, N. Stock, *Chem. Unserer Zeit*, 2008, **42**, 12–19.

88 C. Janiak, J. K. Vieth, *New J. Chem.*, 2010, **34**, 2366–2388.

89 G. Férey, *Chem. Mater.*, 2001, **13**, 3084–3098.

90 O.M. Yaghi, M. O´Keeffe, N.W. Ockwig, H.K. Chae, M. Eddaoudi, J. Kim, *Nature*, 2003, **423**, 705–714.

91 G. Férey, C. Mellot-Draznieks, C. Serre, F. Millange, J. Dutour, S. Surblé, I. Margiolaki, *Science*, 2005, **309**, 2040–2042.

92 T. Loiseau, C. Serre, C. Huguenard, G. Fink, F. Taulelle, M. Henry, T. Bataille, G. Férey*, Chem. Eur. J.*, 2004, **10**, 1373–1382.

93 W. Lu, Z. Wei, Z.-Y. Gu, T.-F. Liu, J. Park, J. Park, J. Tian, M. Zhang, Q. Zhang, T. Gentle III, M. Bosch, H.-C. Zhou, *Chem. Soc. Rev.*, 2014, **43**, 5561–5593.

94 Y. Gao, K. Liu, R. Kang, J. Xia, G. Yu, S. Deng, *J. Hazard. Mater.*, 2018, **359**, 248–257.

95 G. Férey, C. Serre, *Chem. Soc. Rev.*, 2009, **38**, 1380–1399.

96 Z. Mai, D. Liu, Cryst. *Growth Des.*, 2019, **19**, 7439–7462.

97 N.W. Ockwig, O. Delgado-Friedrichs, M. O´Keeffe, O.M. Yaghi, *Acc. Chem. Res.*, 2005, **38**, 176–182.

98 S. Brunauer, P.H. Emmett, E. Teller, *J. Am. Chem. Soc.*,1938, **60**, 309–319.

99 M. Thommes, K. Kaneko, A.V. Neimark, J.P. Olivier, F. Rodriguez-Reinoso, J. Rouquerol, K.S.W. Sing, *Pure Appl. Chem.*, 2015, **87**, 1051–1069.

100 M. Mozafari, Metal-Organic Frameworks for Biomedical Applications, Chapter 7 – Hydrothermal synthesis of MOFs (by W. Chen, L. Du, C. Wu), *Elsevier Inc.*, 2020, 141–157.

101 N. Stock, S. Biswas, *Chem. Rev.*, 2012, **112**, 933–969.

102 F.X. Llabrés i Xamena, J. Gascon, Metal Organic Frameworks as Heterogeneous Catalysts, Chapter 2 – Synthesis of MOFs (by N. Stock, H. Reinsch, L.-H. Schilling), *The Royal Society of Chemistry*, 2013, 9–30.

103 M. Safaei, M.M. Foroughi, N. Ebrahimpoor, S. Jahani, A. Omidi, M. Khatami, *Trends Anal. Chem.*, 2019, **118**, 401–425.

104 M. Mozafari, Metal-Organic Frameworks for Biomedical Applications, Chapter 9 – Electrochemical synthesis of MOFs (by A. Ghoorchian, A. Afkhami, T. Madrakian, M. Ahmadi), *Elsevier Inc.*, 2020, 177–195.

105 P.A. Bayliss, I.A. Ibarra, E. Pérez, S. Yang, C.C. Tang, M. Poliakoff, M. Schröder, *Green Chem.*, 2014, **16**, 3796–3802.

106 W. Xu, J. Dong, J. Li, J. Li, F. Wu, *J. Chem. Soc., Chem. Commun.*, 1990, 755–756.

107 S. Gökpinar, T. Diment, C. Janiak, *Dalton Trans.*, 2017, **46**, 9895–9900.

108 N. Tannert, S. Gökpinar, E. Hastürk, S. Nießing, C. Janiak, *Dalton Trans.*, 2018, **47**, 9850–9860.

109 S. Waitschat, M.T. Wharmby, N. Stock, *Dalton Trans.*, 2015, **44**, 11235–11240.

110 K.K. Gangu, S. Maddila, S.B. Mukkamala, S.B. Jonnalagadda, *Inorg. Chim. Acta*, 2016, **446**, 61–74.

111 M. Rubio-Martinez, C. Avci-Camur, A.W. Thornton, I. Imaz, D. Maspoch, M. R. Hill, *Chem. Soc. Rev.*, 2017, **46**, 3453–3480.

112 J. Klinowski, F.A. Almeida Paz, P. Silva, J. Rocha, *Dalton Trans.*, 2011, **40**, 321–330.

113 S.L. James, C.J. Adams, C. Bolm, D. Braga, P. Collier, T. Friščić, F. Grepioni, K.D. M. Harris, G. Hyett, W. Jones, A. Krebs, J. Mack, L. Maini, A. Guy Orpen, I.P. Parkin, W.C. Shearouse, J.W. Steed, D.C. Waddell, *Chem. Soc. Rev.*, 2012, **41**, 413–447.

114 M. Mozafari, Metal-Organic Frameworks for Biomedical Applications, Chapter 8 – Microwave synthesis of metal-organic frameworks (by R.F. Mendes, J. Rocha, F.A. Almeida Paz), *Elsevier Inc.*, 2020, 159–176.

115 D. Dallinger, *Chem. Unserer Zeit*, 2013, **47**, 356–366.

116 CEM, Theorie zum Mikrowellen-Aufschluss. Verfügbar unter: https://cem.de/theorie-zum-mikrowellen-aufschluss, Zugegriffen: 09.10.2021.

117 J. Bentley, G.S. Foo, M. Rungta, N. Sangar, C. Sievers, D.S. Sholl, S. Nair, *Ind. Eng. Chem. Res.*, 2016, **55**, 5043–5053.

118 E.Q. Procopio, T. Fukushima, E. Barea, J.A.R. Navarro, S. Horike, S. Kitagawa, *Chem. – Eur. J.*, 2012, **18**, 13117–13125.

119 H.K. Kim, W.S. Yun, M.-B. Kim, J.Y. Kim, Y.-Y. Bae, J. Lee, N.C. Jeong, *J. Am. Chem. Soc.*, 2015, **137**, 10009–10015.

120 J. Espín, L. Garzón-Tovar, A. Carné-Sánchez, I. Imaz, D. Maspoch, *ACS Appl. Mater. Interfaces*, 2018, **10**, 9555–9562.

121 C.-D. Wu, M. Zhao, *Adv. Mater.*, 2017, **29**, 1605446.

122 R. Kitaura, G. Onoyama, H. Sakamoto, R. Matsuda, S.-I. Noro, S. Kitagawa, *Angew. Chem., Int. Ed.,* 2004, **43**, 2684–2687.

123 R. Allmann, Röntgenpulverdiffraktometrie, Rechengestützte Auswertung, Phasenanalyse und Strukturbestimmung, ISBN: 978-3-540-43967-7, e-ISBN: 978-3-642-56079-8, Springer-Verlag Berlin Heidelberg, 2003. DOI: 10.1007/978-3-642-56079-8.

124 K.S.W. Sing, D.H. Everett, R.A.W. Haul, L. Moscou, R.A. Pierotti, J. Rouquérol, T. Siemieniewska, *Pure Appl. Chem.*, 1985, **57**, 603–619.

125 M. Thommes, *Chem. Ing. Tech.*, 2010, **82**, 1059–1073.

126 M. Krüger, A.K. Inge, H. Reinsch, Y.-H. Li, M. Wahiduzzaman, C.-H. Lin, S.-L. Wang, G. Maurin, N. Stock, *Inorg. Chem.*, 2017, **56**, 5851–5862.

127 A. Samokhvalov, *Coord. Chem. Rev.*, 2018, **374**, 236–253.

128 H. Reinsch, B. Marszałek, J. Wack, J. Senker, B. Gil, N. Stock, *Chem. Commun.*, 2012, **48**, 9486–9488.

129 F. Jeremias, D. Fröhlich, C. Janiak, S.K. Henninger, *RSC Adv.*, 2014, **4**, 24073–24082.

130 H. Reinsch, M.A. van der Veen, B. Gil, B. Marszalek, T. Verbiest, D. de Vos, N. Stock, *Chem. Mater.*, 2013, **25**, 17–26.

131 H. Reinsch, S. Waitschat, N. Stock, *Dalton Trans.*, 2013, **42**, 4840–4847.

132 D. Lenzen, J. Zhao, S.-J. Ernst, M. Wahiduzzaman, A.K. Inge, D. Fröhlich, H. Xu, H.-J. Bart, C. Janiak, S. Henninger, G. Maurin, X. Zou, N. Stock, *Nature Commun.*, 2019, **10**, 3025.

133 D. Fröhlich, S.K. Henninger, C. Janiak, *Dalton Trans.*, 2014, **43**, 15300–15304.

134 M.F. de Lange, T. Zeng, T.J.H, Vlugt, J. Gascon, F. Kapteijn, *CrystEngComm.*, 2015, **17**, 5911–5920.

135 D. Lenzen, P. Bendix, H. Reinsch, D. Fröhlich, H. Kummer, M. Möllers, P.P.C. Hügenell, R. Gläser, S. Henninger, N. Stock, *Adv. Mater.*, 2018, **30**, 1705869

136 C.B.L. Tschense, N. Reimer, C.-W. Hsu, H. Reinsch, R. Siegel, W.J. Chen, C.-H. Lin, A. Cadiau, C. Serre, J. Senker, N. Stock, *Z. Anorg. Allg. Chem.*, 2017, **643**, 1600–1608.

137 N. Tannert, S.J. Ernst, C. Jansen, H.-J. Bart, S.K. Henninger, C. Janiak, *J. Mater. Chem. A*, 2018, **6**, 17706–17712.

138 A. Cadiau, J.S. Lee, D. Damasceno Borges, P. Fabry, T. Devic, M.T. Wharmby, C. Martineau, D. Foucher, F. Taulelle, C.-H. Jun, Y.K. Hwang, N. Stock, M.F. de Lange, F. Kapteijn, J. Gascon, G. Maurin, J.-S. Chang, C. Serre, *Adv. Mater.*, 2015, **27**, 4775–4780.

139 S.K. Henninger, F. Jeremias, H. Kummer, C. Janiak, *Eur. J. Inorg. Chem.*, 2012, 2625–2634.

140 D.M. Steinert, S.-J. Ernst, S.K. Henninger, C. Janiak, *Eur. J. Inorg. Chem.*, 2020, 4502–4515.

141 E. Hastürk, S.-J. Ernst, C. Janiak, *Curr. Opinion Chem. Eng.*, 2019, **24**, 26–36.

142 S. Gökpinar, S.-J. Ernst, E. Hastürk, M. Möllers, I. El Aita, R. Wiedey, N. Tannert, S. Nießing, S. Abdpour, A. Schmitz, J. Quodbach, G. Füldner, S.K. Henninger, C. Janiak, *Ind. Eng. Chem. Res.*, 2019, **58**, 21493–21503.

143 Y.I. Aristov, *Appl. Therm. Eng.*, 2013, **50**, 1610–1618.

144 A. Khutia, H.U. Rammelberg, T. Schmidt, S.K. Henninger, C. Janiak, *Chem. Mater.*, 2013, **25**, 790–798.

145 C. Volkringer, D. Popov, T. Loiseau, G. Férey, M. Burghammer, C. Riekel, M. Haouas, F. Taulelle, *Chem. Mater.*, 2009, **21**, 5695–5697.

146 F. Jeremias, A. Khutia, S.K. Henninger, C. Janiak, *J. Mater. Chem.*, 2012, **22**, 10148–10151.

147 A. García Márquez, A. Demessence, A.E. Platero-Prats, D. Heurtaux, P. Horcajada, C. Serre, J.-S. Chang, G. Férey, V.A. de La Peña-O'Shea, C. Boissière, *Eur. J. Inorg. Chem.*, 2012, **2012**, 5165–5174.

148 M. Qiu, Q. Guan, W. Li, *Cryst. Growth Des.*, 2016, **16**, 3639–3646.

149 C. Schlüsener, M. Xhinovci, S.-J. Ernst, A. Schmitz, N. Tannert, C. Janiak, *Chem. Mater.*, 2019, **31**, 4051–4062.

150 N. Tannert, C. Jansen, S. Nießing, C. Janiak, *Dalton Trans.*, 2019, **48**, 2967–2976.

151 C. Schlüsener, D.N. Jordan, M. Xhinovci, T.J. Matemb Ma Ntep, A. Schmitz, B. Giesen, C. Janiak, *Dalton Trans.*, 2020, **49**, 7373–7383.

152 J. Canivet, A. Fateeva, Y. Guo, B. Coasne, D. Farrusseng, *Chem. Soc. Rev.*, 2014, **43**, 5594–5617.

153 L.D. O'Neill, H. Zhang, D. Bradshaw, *J. Mater. Chem.*, 2010, **20**, 5720–5726.

154 M.D. Rowe, D.H. Thamm, S.L. Kraft, S.G. Boyes, *Biomacromolecules*, 2009, **10**, 983–993.

155 M. Arnold, P. Kortunov, D.J. Jones, Y. Nedellec, J. Kärger, J. Caro, *Eur. J. Inorg. Chem.*, 2007, 60–64.

156 J. Gascon, S. Aguado, F. Kapteijn, *Microporous Mesoporous Mater.*, 2008, **113**, 132–138.

157 Y. Liu, Z. Ng, E.A. Khan, H.-K. Jeong, C.-B. Ching, Z. Lai, *Microporous Mesoporous Mater.*, 2009, **118**, 296–301.

158 Y. Yoo, H.-K. Jeong, *Chem. Commun.*, 2008, 2441–2443.

159 S. Hermes, D. Zacher, A. Baunemann, C. Wöll, R.A. Fischer, *Chem. Mater.*, 2007, **19**, 2168–2173.

160 S.J. Yang, J.Y. Choi, H.K. Chae, J.H. Cho, K.S. Nahm, C.R. Park, *Chem. Mater.*, 2009, **21**, 1893–1897.

161 M. Jahan, Q. Bao, J.-X. Yang, K.P. Loh, *J. Am. Chem. Soc.*, 2010, **132**, 14487–14495.

162 C. Petit, T.J. Bandosz, *Adv. Funct. Mater.*, 2011, **21**, 2108–2117.

163 C. Petit, T.J. Bandosz, *Dalton Trans.*, 2012, **41**, 4027–4035.

164 D. Bradshaw, A. Garai, J. Huo, *Chem. Soc. Rev.*, 2012, **41**, 2344–2381.

165 I. Ahmed, S.H. Jhung, *Mater. Today*, 2014, **17**, 136–146.

166 J. Yan, Y. Yu, C. Ma, J. Xiao, Q. Xia, Y. Li, Z. Li, *Appl. Therm. Eng.*, 2015, **84**, 118–125.

167 F. Barroso-Bujans, S. Cerveny, A. Alegría, J. Colmenero, *Carbon*, 2010, **48**, 3277–3286.

168 A. Buchsteiner, A. Lerf, J. Pieper, *J. Phys. Chem. B*, 2006, **110**, 22328–22338.

169 B. Kartick, S.K. Srivastava, *J. Nanosci. Nanotechnol.*, 2011, **11**, 8586–8592.

170 C. Petit, B. Mendoza, T.J. Bandosz, *ChemPhysChem*, 2010, **11**, 3678–3684.

171 W.S. Hummers, R.E. Offeman, *J. Am. Chem. Soc.*, 1958, **80**, 1339.

172 S.K. Srivastava, J. Pionteck, *J. Nanosci. Nanotechnol.*, 2015, **15**, 1984–2000.

173 S. Park, J. An, I. Jung, R.D. Piner, S.J. An, X. Li, A. Velamakanni, R.S. Ruoff, *Nano Lett.*, 2009, **9**, 1593–1597.

174 C. Petit, T.J. Bandosz, *Adv. Mater.*, 2009, **21**, 4753–4757.

175 E. Elsayed, H. Wang, P.A. Anderson, R. Al-Dadah, S. Mahmoud, H. Navarro, Y. Ding, J. Bowen, *Microporous Mesoporous Mater.*, 2017, **244**, 180–191.

176 I. Ahmed, N.A. Khan, S.H. Jhung, *Inorg. Chem.*, 2013, **52**, 14155–14161.

177 C. Petit, L. Huang, J. Jagiello, J. Kenvin, K.E. Gubbins, T.J. Bandosz, *Langmuir*, 2011, **27**, 13043–13051.

178 Y. Li, J. Miao, X. Sun, J. Xiao, Y. Li, H. Wang, Q. Xia, Z. Li, *Chem. Eng. J.*, 2016, **298**, 191–197.

179 Y. Zhao, H. Ding, Q. Zhong, *Appl. Surf. Sci.*, 2013, **284**, 138–144.

180 C. Petit, T.J. Bandosz, *Adv. Funct. Mater.*, 2010, **20**, 111–118.

181 X. Liu, H. Zhou, Y. Zhang, Y. Liu, A. Yuan, *Chin. J. Chem.*, 2012, **30**, 2563–2566.

182 Y. Zheng, S. Zheng, H. Xue, H. Pang, *Adv. Funct. Mater.*, 2018, **28**, 1804950.

183 C. Petit, J. Burress, T.J. Bandosz, *Carbon*, 2011, **49**, 563–572.

184 S. Liu, L. Sun, F. Xu, J. Zhang, C. Jiao, F. Li, Z. Li, S. Wang, Z. Wang, X. Jiang, H. Zhou, L. Yang, C. Schick, *Energy Environ. Sci.*, 2013, **6**, 818–823.

185 Z. Bian, J. Xu, S. Zhang, X. Zhu, H. Liu, J. Hu, *Langmuir*, 2015, **31**, 7410–7417.

186 A. Policicchio, Y. Zhao, Q. Zhong, R.G. Agostino, T.J. Bandosz, *ACS Appl. Mater. Interfaces*, 2014, **6**, 101–108.

187 W. Huang, X. Zhou, Q. Xia, J. Peng, H. Wang, Z. Li, *Ind. Eng. Chem. Res.*, 2014, **53**, 11176–11184.

188 Z. Bian, X. Zhu, T. Jin, J. Gao, J. Hu, H. Liu, *Microporous Mesoporous Mater.*, 2014, **200**, 159–164.

189 A.M. Ebrahim, J. Jagiello, T.J. Bandosz, *J. Mater. Chem. A*, 2015, **3**, 8194–8204.

190 C. Petit, B. Mendoza, T.J. Bandosz, *Langmuir*, 2010, **26**, 15302–15309.

191 F. Xu, Y. Yu, J. Yan, Q. Xia, H. Wang, J. Li, Z. Li, *Chem. Eng. J.*, 2016, **303**, 231–237.

192 X. Zhou, W. Huang, J. Liu, H. Wang, Z. Li, *Chem. Eng. Sci.*, 2017, **167**, 98–104.

193 A. Taheri, E.G. Babakhani, J. T. Darian, *Energy Fuels*, 2017, **31**, 8792–8802.

194 X. Zhou, W. Huang, J. Shi, Z. Zhao, Q. Xia, Y. Li, H. Wang, Z. Li, *J. Mater. Chem. A*, 2014, **2**, 4722–4730.

195 X. Sun, Y. Li, H. Xi, Q. Xia, *RSC ADV.*, 2014, **4**, 56216–56223.

196 X. Sun, Q. Xia, Z. Zhao, Y. Li, Z. Li, *Chem. Eng. J.*, 2014, **239**, 226–232.

197 X. Zhou, W. Huang, J. Miao, Q. Xia, Z. Zhang, H. Wang, Z. Li, *Chem. Eng. J.*, 2015, **266**, 339–344.

198 Z.H. Huang, G. Liu, F. Kang, *ACS Appl. Mater. Interfaces*, 2012, **4**, 4942–4947.

199 C. Petit, T.J. Bandosz, *J. Mater. Chem.*, 2009, **19**, 6521–6528.

200 A.R. Noorpoor, S. Nazari Kudahi, *J. Environ. Chem. Eng.*, 2016, **4**, 1081–1091.

201 Y. Cao, Y. Zhao, Z. Lv, F. Song, Q. Zhong, *J. Ind. Eng. Chem.*, 2015, **27**, 102–107.

202 S. Castarlenas, C. Téllez, J. Coronas, *J. Membr. Sci.*, 2017, **526**, 205–211.

203 H. Zhou, J. Zhang, J. Zhang, X. Yan, X. Shen, A. Yuan, *Int. J. Hydrog. Energy*, 2015, **40**, 12275–12285.

204 J. Zhang, D. Ji, H. Zhou, X. Yan, A. Yuan, *J. Nanosci. Nanotechnol.*, 2017, **17**, 1400–1406(7).

205 Ü. Kökçam-Demir, N.Tannert, M. Bengsch, A. Spieß, C. Schlüsener, S. Nießing, C. Janiak, *Microporous Mesoporous Mater.*, 2021, **326**, 111352.

206 Ü. Kökçam-Demir, A. Goldman, L. Esrafili. M. Gharib, A. Morsali, O. Weingart, C. Janiak, *Chem. Soc. Rev.*, 2020, **49**, 2751–2798.

207 R. Dalapati, Ü. Kökçam-Demir, C. Janiak, S. Biswas, *Dalton Trans.*, 2018, **47**, 1159–1170.

208 M. Getzlaff, M. Leifels, P. Weber, Ü. Kökçam-Demir, C. Janiak, *Nano-Structures & Nano-Objects*, 2020, **22**, 100462.

209 P.B. Ebanda Kedi, C.C. Nanga, A.P. Gbambie, V. Deli, F. Eya’ane Meva, H.E.A. Mohamed, A.A. Ntoumba, M.H.J. Nko’o, Ü. Kökçam-Demir, B. Moll, H.K. Armelle Michelle,

P. Teke Ndifon, E.A. Mpondo Mpondo, A.B. Dongmo, C. Janiak, M. Maaza, *J. Nanotechnol. Res.*, 2020, **2**, 025–041.

210 D. Bejan, L.G. Bahrin, S. Shova, N. L. Marangoci, Ü. Kökçam-Demir, V. Lozan, C. Janiak, *Molecules*, 2020, **25**, 3055.

211 P.B. Ebanda Kedi, B. Ngangue Etah, V. Deli, A. Paboudam Gbambie, A.A. Ntoumba, Ü. Kökçam-Demir, B. Moll, H.E.A. Mohamed, J.C. Ngo Nyobe, C.C. Nanga, J.Y. Sikapi Fouda, L.P. Kojom Foko, E.E. Tchoumbi, A.M. Houatchaing, Y.K.D. M. Kotto Modi, F. Eya'ane Meva, P. Teke Ndifon, A.B. Dongmo, M. Maaza, S. Didier Dibong, E.A. Mpondo Mpondo, C. Janiak, *Int. J. Green Herbal Chem.*, 2020, **9**, 345–360.

212 M. Enamullah, K.S. Banu, M.A. Hossain, Ü. Kökçam-Demir, *J. Mol. Struct.*, 2020, **1199**, 126947.

213 M. Getzlaff, M. Leifels, P. Weber, Ü. Kökçam-Demir, C. Janiak, *SN Appl. Sci.*, 2019, **1:489**.

214 F. Eya'ane Meva, J.O. Avom Mbeng, C. Okalla Ebongue, C. Schlüsener, Ü. Kökçam-Demir, A.A. Ntoumba, P.B. Ebanda Kedi, E. Elanga, E.-R. Njike Loudang, M.H.J. Nko'o, E. Tchoumbi, V. Deli, C.C. Nanga, E.A. Mpondo Mpondo, C. Janiak, *J. Biomater. Nanobiotechnol.*, 2019, **10**, 102–119.

215 F. Eya'ane Meva, A.A. Ntoumba, P.B. Ebanda Kedi, E. Tchoumbi, A. Schmitz, L. Schmolke, M. Klopotowski, B. Moll, Ü. Kökçam-Demir, E.A. Mpondo Mpondo, L.G. Lehman, C. Janiak, *J. Mater. Res. Technol.*, 2019, **8**, 1991–2000.

216 B. Engelkamp, M. El Achhab, B. Fischer, Ü. Kökçam-Demir, K. Schierbaum, *Metals*, 2018, **8**, 386.

217 Evonik Operations GmbH, Produktinformation AEROPERL® 300/30, April 2021. Verfügbar unter: https://products-re.evonik.com/www2/uploads/productfinder/AEROPERL-30030-DE.pdf, Zugegriffen: 05.10.2021.

218 Evonik Operations GmbH, Produktinformation AEROSIL® 300, April 2021. Verfügbar unter: https://products-re.evonik.com/www2/uploads/productfinder/AEROSIL-300-DE.pdf, Zugegriffen: 05.10.2021.